HEMI-LABILE, REDOX ACTIVE METALLODITHIOLATES AS LIGANDS FOR BIOINSPIRED PROTON REDUCTION CATALYSTS

A Dissertation

by

POKHRAJ GHOSH

Submitted to the Office of Graduate and Professional Studies of
Texas A&M University
in partial fulfillment of the requirements for the degree of

DOCTOR OF PHILOSOPHY

Chair of Committee,	Marcetta Y. Darensbourg
Committee Members,	Francois P. Gabbai
	Paul A. Lindahl
	Kim R. Dunbar
	Perla B. Balbuena
Head of Department,	Simon W. North

December 2017

Major Subject: Chemistry

ABSTRACT

The versatile organometallic type active sites in biology that harbor intact metallo-sulfur units are key inspirations for synthetic biomimetic studies. Salient features of such active sites, *viz*., the propitious positioning of the pendant amine-base over the distal iron in the H-cluster of [FeFe]-H_2ase, are 'design-directives' in the development of small molecule catalysts. The Dubois catalyst, featuring such a pendant amine, achieves turnovers over 100,000 s^{-1} and serves as a testament to the success of such systems. Although the active site of [NiFe]-H_2ase is devoid of such a pendant amine, it uses terminal cysteinyl-thiolates in this capacity.

As a synthetic chemist, I used several MN_2S_2 metallodithiolates, as intact metoalloligands, to bind $[Cp^RFe(CO)]^+$ or $\{Fe(NO)_2\}^{9/10}$ receiver units, via bridging thiolates. These mono- and bidentate hetero/homobimetallic complexes emulate core features of [NiFe]-H_2ase active site. Despite lack of terminal thiolates or pendant amine, the bidentate complexes showed H^+ reduction electrocatalysis to produce H_2. Hence the obvious question was how did these electrocatalysts work? Extensive collaborations with Prof. M. B. Hall and co-worker Dr. Shengda Ding, suggested e^-/H^+ induced rearrangement of S-bridged bimetallics that allowed HER. Thus, these stable bidentate complexes undergo bidentate/monodentate hemi-lability to develop *in situ* pendant base features, reminiscent of the enzyme active sites. The free thiolate in the monodentate

bound bimetallics displayed stoichiometric binding of protons and Ph_3PAu^+ (as a proton analogue), and other electrophiles to support the claim.

The versatility of the metallodithiolates ligands, as surrogates of conventional phosphines and carbenes, was also shown in their monodentate binding capabilities with $[Fe^IFe^I]$, $[Fe^I[Fe(NO)]^{II}]$ and $[(\mu\text{-}H)Fe^{II}Fe^{II}]$ systems, as [FeFe]-H_2ase bioinspired trimetallics.

DEDICATION

To my parents, whose unconditional love and selfless sacrifice in my upbringing knows no bounds.

ACKNOWLEDGEMENTS

It's an honor and sheer privilege to learn chemistry from one of the pioneers in the field of bioinorganic chemistry, Prof. Marcetta Y. Darensbourg, an accomplished scientist, an exceptional advisor, and above all a steadfast mentor and guide. I admire her dedication and perseverance in research and teaching, the attributes of a great researcher, the qualities I desire to emulate in my career. Graduate school is tough and demanding, your friendly demeanor and humble attitude made it easy for me to approach you for any assistance. You have been very supportive and encouraging, and gave me the freedom to work on a lot a research projects. I sincerely thank you for helping me grow as a research scientist. I would like to thank my committee members, Prof. Francois P. Gabbai, Prof. Paul A. Lindahl, Prof. Kim R. Dunbar and Prof. Perla B. Balbuena for serving on my committee and showing interest in my work. I would like to thank Prof. Don Darensbourg for advising me when necessary, during the course of my research.

It is impossible to work in a synthetic chemistry lab without getting help from your colleagues. I would like to thank all the past and present members in the Darensbourg lab. I was lucky to learn Schlenk line techniques from Dr. Chung-Hung Hsieh (Mark), an exceptional synthetic inorganic chemist. Thank you Mark for mentoring me and laying the foundation of my synthetic skills as I first joined the MYD group. Randara, thank you so much for being there as a friend and a senior. You have helped and supported me immensely when I went through some excruciating times

during my graduate school. I was lucky to share the lab with Hamid and Ning Wang. I cherish our friendship and also would like to thank both of you for helping me and advising me in my research. Rachel, thank you for being a good friend and colleague. I would like to thank all the undergraduate students who have worked with me, Nicholas Zaibaq, Rubi Bohmer, Zach, Aron, Heechang (Anthony) and particularly Manuel and Yicheng. I appreciate the hard work that all of you did working with me. I would also like to thank Ethel and Abbey for assisting me in various official and administrative work. I would also like to thank my collaborators, Prof. M. B. Hall, Dr. N. Bhuvanesh, Dr. C. Popescu, Dr. A. M. Lunsford, Dr. S. Ding for their contributions to my research.

During my M.Sc. days in IIT Guwahati, India, I am proud to mention the names of many professors, especially Dr. Biplab Mondal, who taught the bioinorganic chemistry course. Having joined his lab as a Masters' degree student was the turning point in my career as I became passionate about inorganic chemistry. I still remember the joy that I felt when my first coauthored paper was published from his lab. I would also like to thank Prof. T. Punniyamurthy, Prof. B. K. Patel and Prof. A. K. Mishra for allowing me to work in your labs and recommending me to join TAMU.

During my undergraduate course in Presidency College, I had the opportunity to learn chemistry from some eminent professors like, Dr. A. K. Sarkar, Dr. G. Chatterjee, Dr. D. Mondal, Dr. G. K. Kar, Dr. B. C. Kundu, Dr. S. Ghosh and many others. Thank you all for laying the foundation of Chemistry in me. I would also like to thank Dr. Hrishikesh Chatterjee and Dr. Pulak Ganguly of Narendrapur Ramakrishna Mission

College for their valuable teachings and motivating me to pursue further studies in Chemistry.

My liking for Chemistry took shape when Dr. Moumita Ghosh and Sri Brahma Roy taught me during my high-school days. Thank you for inspiring me in the field of Chemistry.

I would also like to thank Sayantika, my friends and well-wishers.

Nevertheless, it is my parents, whose selfless sacrifice, dedication, and unconditional love in my upbringing, makes me what I am today. I am ever so grateful and indebted to you. Whatever I am today is because of you. After all, it is the temperament of an elysian harmony of nature, that has silently synthesized the moments, joined the dots, for the humble submission of my dissertation.

NOMENCLATURE

H_2ase	Hydrogenase
ACS	Acetyl-Coenzyme A Synthase
DNIC	Dinitrosyl iron complex
RRE	Roussin's Red Ester
NHC	N-heterocyclic carbene
IMes	1,3-Dimesitylimidazole-2-ylidene
IMe	1,3-Dimethylimidazole-2-ylidene
pdt	1,3-Propanedithiolate
dmpdt	2,2-Dimethylpropanedithiolate
adt	2-Aza-1,3-propanedithiolate
bme-dach	bis(N,N'-2-mercapto-2-methylpropyl)-1,5-diazocycloheptane
bme-daco	bis(N,N'-2-mercapto-2-methylpropyl)-1,5-diazocyclooctane
bme-dame	2,2'-(ethane-1,2-diylbis(methylazanediyl))diethanemercaptol
BArF	Tetrakis(3,5-bis(trifluoromethyl)phenyl)borate
Fc	Ferrocene
Fc^+	Ferrocenium
Cp	Cyclopentadienyl
Cp*	Pentamethylcyclopentadienyl
HER	Hydrogen evolution reaction
TOF	Turnover frequency

TON	Turnover number
KIE	Kinetic isotope effect
CV	Cyclic voltammetry
IR	Infrared spectroscopy
NMR	Nuclear magnetic resonance
EPR	Electron paramagnetic resonance
ESI-MS	Electrospray ionization mass spectroscopy
XRD	X-ray diffraction
GC	Gas chromatography
TFA	Trifluoroacetic acid
DCM	Dichloromethane
THF	Tetrahydrofuran
ACN	Acetonitrile
SI	Supporting information
PNNL	Pacific Northwest National Lab

CONTRIBUTORS AND FUNDING SOURCES

Contributors

This work was supervised by a dissertation committee consisting of Professors Marcetta Y. Darensbourg [advisor], Francois P. Gabbai, Paul A. Lindahl, Kim R. Dunbar of the Department of Chemistry and Perla B. Balbuena of the Department of Chemical Engineering.

The experimental work in this dissertation was completed by the student, in collaboration with Dr. Nattamai Bhuvanesh (Chapters III, IV, V, VI, VII and VIII) and Dr. Jason A. Denny (Chapter VI) for X-ray crystallography studies, Dr. Codrina V. Popescu (Chapter III) for Mössbauer studies, Prof. Michael B. Hall and Dr. Shengda Ding (Chapters III, V and VII) for computational studies, Dr. Rachel B. Chupik (Chapters V and VI), Dr. Chung-Hung Hsieh (Chapters V, VI, VII and VIII), Dr. Allen M. Lunsford (Chapter III), Dr. Ning Wang (Chapters III and IV), Manuel Quiroz (Chapters IV, V and VIII), and Dr. Tiankun Zhao for assisting in experimental work.

Funding Sources

This work was made possible in part by the financial support of National Science Foundation under Grant Numbers CHE-1266097, CHE-1665258, the Robert A. Welch Foundation under Grant Numbers A-0924 and the Qatar National Research Fund under Grant Number NPRP 6-1184-1-22.

Its contents are solely the responsibility of the authors and do not necessarily represent the official views of the funding agencies.

TABLE OF CONTENTS

Page

LIST OF FIGURES

Page

LIST OF TABLES

Page

CHAPTER I

INTRODUCTION AND LITERATURE REVIEW

It all started when a sugar-beet factory located nearby the Great Ouse river in the cathedral city of Ely in Cambridgeshire, England, caused serious river pollution by dumping their factory effluents. Apart from the legal prosecutions and damage to the fisheries, a surprisingly positive outcome of the pollution was the discovery of "hydrogenase" by Marjory Jane Stephenson and her coworker, L. H. Stickland. Albeit, discouraged from scientific research involving bacteria, Stephenson nevertheless, took a keen interest in the biochemistry behind the pollution and formulated the problem in her public talk "How microbes live or some aspects of bacterial physiology".[1] According to her, the microbes that thrived on the sugar-beet waste did not produce alcohol, unlike yeasts, but lived via a metabolic pathway that made gases – hydrogen, carbon dioxide, and methane. She demonstrated that their microbial cultures could chemically reduce methylene blue, in a Thunberg tube, in the presence of hydrogen and not nitrogen as a plebeian alternative. Thus, they established that the microbes contained an enzyme which was widespread in *E. coli*, could activate hydrogen, justifying their appellation of 'hydrogenase'.[1]

And so began the quest for hydrogenases from the 1930s.

In 1934, Green and Stickland demonstrated the reversibility of the reaction carried out by hydrogenases. They found that the equilibrium point for the hydrogen-

induced reduction of methyl viologen was the same whether colloidal palladium or a bacterial suspension of hydrogenase was used as the catalyst. They quantified their results over a wide range of hydrogen partial pressures and H^+ ion concentrations and found that the calculated electrochemical potential was identical to that of a standard hydrogen electrode.[2]

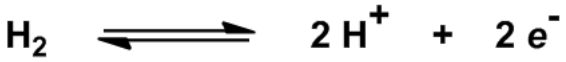

In 1901, Pakes and Jollyman had already reported the formation of hydrogen by eneterobacteria from formate.[3] Later in 1932, Stephcnson and Stickland quantified the production of one mole of hydrogen per mole of formate and formulated the following reaction pathway:[4]

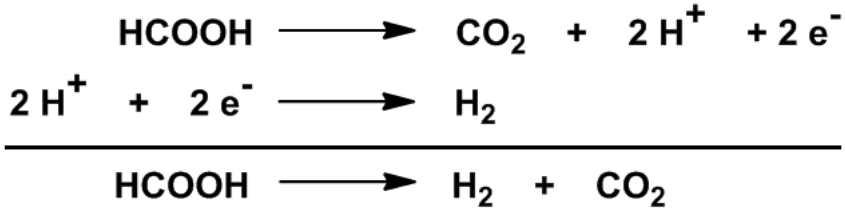

Although an investigation of the aforementioned mechanism using heavy water, by Farkas and Yudkin,[5] was inconclusive due to an exchange reaction between H_2O and HD, to produce HOD and H_2, Kempncr and Kubowitz from Warburg's laboratory in 1934, showed the inhibiting effect of cyanide and CO on hydrogen formation by *Clostridium butyricum*.[6-7] A decade later, Papenheimer and Shaskan reported that *Clostridium welehii* grown from iron-deficient cultures showed very little hydrogen

production and formed lactic acid rather than n-butyric and acetic acids as the metabolites of glucose fermentation.[8]

The 1930's through 1970's saw a great surge in the biological studies of a wide variety of bacteria, alga and other microbes featuring hydrogenase, nitrogenase, formic hydrogenlyase, methanogens etc. The connection of hydrogenase with nitrogen fixation was shown by P. W. Wilson in the 1930s when he deduced that dihydrogen acted as a competitive inhibitor for nitrogen fixation and the presence of hydrogenase in *Azotobacter* in 1942.[9-10]

The first mechanism of hydrogenase enzyme action using cell-free extracts of *Proteus vulgaris* was shown by Rittenberg in 1953.[11] Through kinetic studies, he demonstrated the isotope exchange between H_2 and D_2O. He also formulated that cells in H_2O solution allowed the conversion of para hydrogen to ortho hydrogen, which did not occur in similar cells in D_2O.[11] Similar studies on H/D exchange and para/ortho hydrogen conversion were shown four decades later by Berlier, Lespinat and Dimon using gas chromatographic-mass spectrometric techniques.[12] Rittenberg's significant work was followed by the isolation and a 35-fold purification of the *Desulfovibrio desulfuricans* in 1960,[13] which was shown to be the key enzyme in the isolation of the active site of [FeFe]-H_2ase some four decades later.[14] The late 1960's reported some important contributions from A. I. Krasna regarding the reactivity of hydrogenases in presence of visible and ultraviolet light.[15-16]

The 1970's marked the seminal works from Haschke and Campbell where they characterized and isolated *Desulfovibrio vulgaris* showing the presence of iron(II) in an enzyme with a molecular weight of 41,000.[17] Later, works from Legall, *et al*. and Mortenson showed the evidence of a non-heme iron[18] in the active site and the presence of iron-sulfur clusters.[19-21] This heralded the advent of EPR studies on the ubiquitous electron-transfer proteins containing iron-sulfur clusters.[19-20, 22] A pool of eminent spectroscopists and biochemists like A. J. Bearden, R. Cammack, H. Beinert and R. H. Sands showed keen interest in understanding the role of redox activity and electron transfer in the Fe-S proteins present in the photosynthetic electron-transfer chain, mitochondrial respiratory chain and membrane bioenergetics.[19-20, 22] In 1972, Multani and Mortenson reported the circular dichroism spectra of hydrogenase from *Clostridium pasterurianum* W5.[23]

During this time bio-inspired inorganic model complexes of Fe-S clusters by Richard Holm came into effect.[19, 22] This field of study was revolutionized by his epoch-making contributions that lasted over half a century and produced eminent scientists as his coworkers in the field of inorganic and organometallic chemistry. An interesting work by Yates *et al*., published in Nature 1976, showed the synergistic relationship of hydrogenase and nitrogenase in which the H_2 evolved by Azotobacter nitrogenase was oxidized by a hydrogenase to release more reducing power for metabolism. The presence of acetylene, on the other hand, inhibited the activity.[24] This observation would have immense effect on the recent interesting works by Hoffmann *et al*. in understanding the mechanism of nitrogenase.[25] In 1978, A. I. Krasna published a paper in Methods in

Enzymology about oxygen-stable hydrogenase and its assay.[26] Several membrane bound hydrogenases were also isolated during this time.[27] Workshops in Göttingen published a compendia titled "Hydrogenases: their catalytic activity, structure and function".[28]

The 1980's commenced some decisive works on the presence of Ni in hydrogenases using Electron Paramagnetic resonance spectroscopy (EPR) spectroscopy.[29] The requirement of nickel, cobalt, molybdenum for the growth of *Methanobacterium thermoautotrophicum* was first established by R. K. Thauer in 1979.[30] Later, presence of Ni was proven by isotope substitution experiments in some pioneering EPR studies by Albracht, Graf and Thauer in 1982.[29, 31-32] EPR became a predominant tool in the hydrogenase evolutionary history which ear-marked the scientific community with key publications such as, "Evidence for nickel and a three iron-center in the hydrogenase of *Desulfovibrio desulfuricans*" by H. J. Kruger *et al*.,[33] "Unambiguous identification of nickel EPR signal in ^{61}Ni-enriched *Desulfovibrio gigas* hydrogenase"[34] and "The presence of redox-sensitive nickel in the periplasmic hydrogenase from *Desulfovibrio gigas"*[35] by J. J. Moura *et al*., "Hydrogenase from *Vibrio succinogenes*, a nickel protein" by G. Unden *et al*., etc., all in 1982. A selenocysteine containing hydrogenase was discovered by S. Yamazaki during this year.[36]

A wide variety of spectroscopic studies were also carried out during this time as more and more hydrogenases were isolated from multiple microorganisms.[29] Although they differed considerably in metal content, molecular composition, specific activity, oxygen sensitivity etc., a striking similarity was the presence of Fe-S clusters in all.[37]

Important spectroscopic contributions from M. W. W. Adams, B. M. Hoffman and E. Munck in EPR, Mossbauer and electron nuclear double resonance of the oxidized bidirectional hydrogenase from *Clostridium pasteurianum* W5 was published in the Journal of Biological Chemistry in December 1984.[29, 37-39] Using EPR spectroscopy, J. LeGall from University of Georgia, showed possible intermediate species, a transient appearance of the so-called Ni-C state and proposed catalytic cycle of the enzyme.[29, 37, 40]

Mid-1980 onwards, immense efforts were extended towards the isolation, cloning, sequencing and encoding of genes for hydrogenases and nitrogenases.[41-45] Although a 4 Å resolution single crystal structure of [NiFe]-hydrogenase was obtained by T. Yagi, H. Inokuchi *et al*. in 1987 from *Desulfovibrio vulgaris*,[46] a high resolution crystal structure was first obtained by Fontecilla-Camps a decade later, from *Desulfovibrio gigas*.[47] During this time proton-induced X-ray emission[48] and X-ray absorption spectroscopy[49] were used to analyze metal composition and detect new iron-sulfur clusters in hydrogenase II by K. L. Kovacs *et al*. and M. W. W. Adams and K. E. Stockley *et al*., respectively.[29, 50] Cyanide inactivation of hydrogenase was re-investigated by L. C. Seefeldt and D. J. Arp.[51]

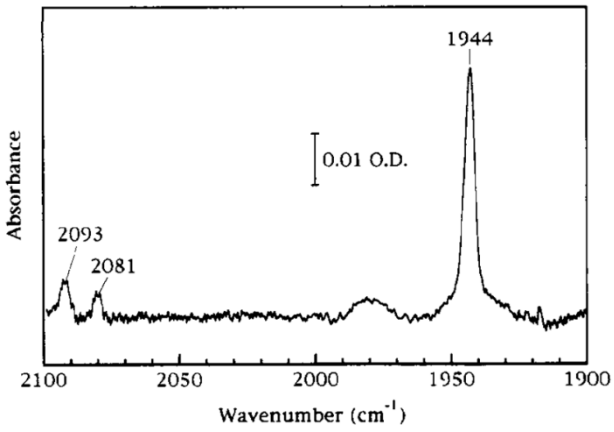

Figure I-1. IR spectrum of oxidized [NiFe]-H_2ase from *Chromatium vinosum* at 20 K.[52] (Reprinted with permission from Bagley, K. A.; Van Garderen, C. J.; Chen, M.; Woodruff, W. H.; Duin, E. C.; Albracht, S. P. J. *Biochemistry* **1994**, *33*, 9229. Copyright **1994** American Chemical Society)

Various redox-intermediates of the [NiFe]-hydrogenases from *Desulfovibrio gigas* were detected using Mossbauer, EPR, and mass-spectrometric studies as building blocks for obtaining a unified catalytic cycle.[29] Fast forwarding to 1994, interesting results from IR spectroscopy were reported by Bagley, Albracht, Woodruff, *et al*. from their studies on hydrogenase from *Chromatium vinosum*.[29, 52] Three stretching frequencies were reported at 2093 (w), 2081 (w) and 1944 (s) which although initially thought to be artifacts, were later identified as two CN's and CO, respectively, Figure I-1.[37, 52] Later, through X-ray crystallography of the [NiFe]-H_2ase from *Desulfovibrio gigas* by Fontecilla-Camps in 1995, the active site was clarified and the diatomic ligands CN's and CO could be located on the Fe.[47] Several X-ray structures of the [NiFe]-H_2ase isolated from numerous microorganisms by various groups were determined from 1995 onwards.

The finding of the ν(CO) and ν(CN) stretching frequencies from the enzyme showed close similarities with the ν(CN): 2094, 2088 cm^{-1} and ν(CO): 1949 cm^{-1} stretching frequencies from the organometallic complex, $[\eta^5\text{-}(C_5H_5)Fe(CN)_2CO]^-$, analyzed for comparison by Marcetta and Donald Darensbourg, in 1998, Figure I-2.[37, 52, 55] This remarkable similarity showed great insights about the organometallic nature of the [NiFe]-H_2ase active site and heralded the development of small molecules as models through synthetic inorganic and organometallic chemistry. The next two decades saw a surge in the development of synthetic biomimetics.[56-57] Over 1800 research articles are present in the literature involving model complexes from various research groups worldwide. Amongst eminent researchers who have made significant contributions in understanding *vis-á-vis* expanding the bio-inorganic frontiers in this field are organometallic chemists like Marcetta Y. Darensbourg, Tom Rauchfuss, Chris Pickett, and theoretical chemists like Mike B. Hall.[56-58]

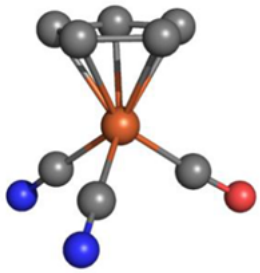

Figure I-2. Ball and stick rendition of the crystal structure of $[\eta^5\text{-}(C_5H_5)Fe(CN)_2CO]^-$.[55]

In 1998, the X-ray crystal structure of the [FeFe]-H_2ase (CpI) from *Clostridium pasteurianum* was reported by Peters, Seefeldt *et al*.[59] It showed an overall similarity and distinct differences in the coordination geometry of the Fe centers. Later in 2007, a third type of hydrogenase containing a single Fe center was reported by S. Shima and R. K. Thauer, [Fe]-H_2ase.[60] Some notable reviews that marked the next two decades highlighting the enormity of the research that lasted for almost 90 years are mentioned in Table I-1.[29, 37, 43-45, 58, 61-65] A timeline showing selected landmarks in hydrogenase research is shown in Figure I-3. My sincerest apologies to all whose contributions are not included here or in the write-up.

Table I-1. List of notable reviews that marked the next two decades highlighting the enormity of the research that lasted for almost 90 years.

Title	Reference
Catalytic Properties of Hydrogenases	Karyakin *et al*. *Russ. Chem. Rev.* **1986**, *55*, 867
Reactions with molecular hydrogen in microorganisms: Evidence for a purely organic hydrogenation catalyst	Thauer *et al*. *Chem. Rev*. **1996**, *96*, 3031
Occurrence, classification, and biological function of hydrogenases: An overview	Vignais *et al*. *Chem. Rev.* **2007**, *107*, 4206
Activation and inactivation of hydrogenase function and the catalytic cycle: Spectroelectrochemical studies	De Lacey *et al*. *Chem. Rev*. **2007**, *107*, 4304
Structure/function relationship of [FeFe]- and [NiFe]-H_2ase	Fontecilla-Camps *et al*. *Chem. Rev*. **2007,** *107*, 4273
Computational studies of [NiFe] and [FeFe] hydrogenase	Siegbahn *et al*. *Chem. Rev*. **2007**, *107*, 4414
Hydrogen: An overview	Lubitz *et al*. *Chem. Rev*. **2007**, *107***,** 3900
[NiFe] and [FeFe] hydrogenases studied by advanced magnetic resonance techniques	Lubitz *et al*. *Chem. Rev*. **2007**, *107***,** 4331
Investigating and exploiting the electrocatalytic properties of hydrogenases	Vincent *et al*. *Chem. Rev*. **2007**, *107***,** 4366
The Bioorganometallic Chemistry of Hydrogenase	Darensbourg *et al*. Wiley-VCH Verlag GmbH & Co. KGaA: **2014**; pp 239
Hydrogenase	Lubitz *et al*. *Chem. Rev*. **2014**, *114***,** 4081

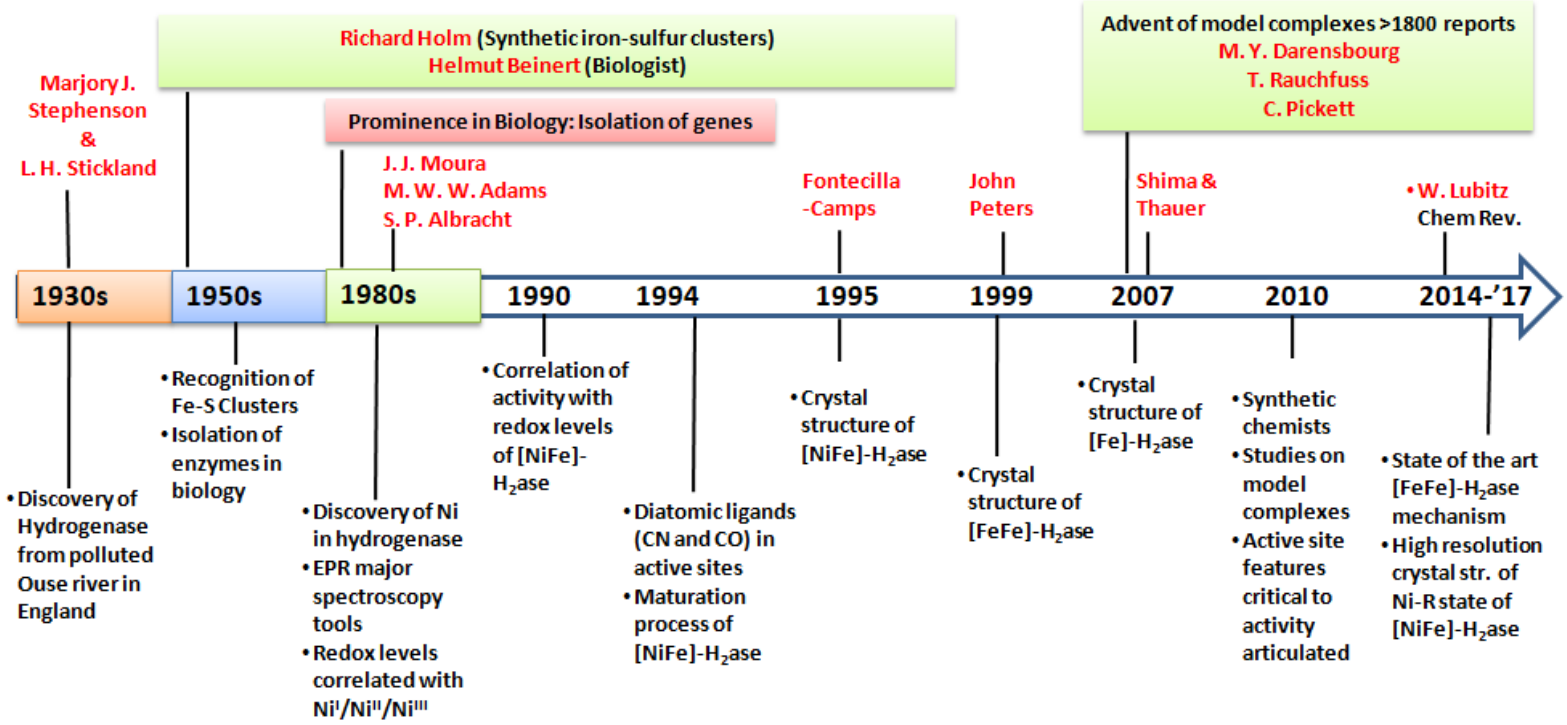

Figure I-3. A timeline showing selected landmarks in hydrogenase research.[66] Disclaimer: My sincerest apologies to all whose contributions are not included here or in the write-up.

Understanding the Mechanism of [NiFe]-H_2ase

The catalytic cycle that was proposed for the [NiFe]-H_2ase in 2001 is summarized below.[54] The activation step involved the reduction of the Ni by an external electron donor. The metal ions Ni^{II} and Fe^{II} within the active site are assumed to react with bound H_2 or as a hydride. It was presumed that the hydrogen was bound to the Fe^{II}. An e^- transfer to the 4Fe4S would oxidize Ni^{II} to Ni^{III} with a release of hydron from H_2 to maintain charge neutrality, resulting in a hydride-bound iron. A series of electron transfer takes place from the proximal cluster, hydride (reducing Ni^{III} to Ni^{I}), and from the nickel to the proximal [4Fe-4S]. This was followed by a transfer of a second electron from the cluster to the acceptor protein, converting the enzyme to the NiSR state. Two hydrons are also transferred to the solution.[54]

As mentioned earlier a wide variety of spectroscopic tools have been rigorously applied over decades of research to access the electronic structure and dynamical aspects of the catalytic cycle. These include FTIR (Fourier-transform infrared spectroscopy), XAS (X-ray absorption), Mossbauer and in particular various pulsed EPR spectroscopic techniques like ENDOR (electron-nuclear double resonance).[29, 37] Recent years saw the use of spohisticated spectroscopic methods including, SEIRA (surface enhanced infrared absorption), resonance Raman and NRVS (nuclear vibrational resonance spectroscopy).[37] FTIR spectroscopy has been instrumental in assigning diatomic ligands CN^- and CO, on the iron center, in the range of 2100-2040 cm^{-1} and 1970-1900 cm^{-1}, respectively.[52] The obtained wavenumbers are sensitive to the oxidation state of iron and provide insight regarding its electron density during the catalytic cycle.[37] Studies with

^{57}Fe enriched [NiFe]-H$_2$ase showed a very weak signal from EPR studies. This shows iron remains as low spin, diamagnetic Fe(II) in all redox states.[37]

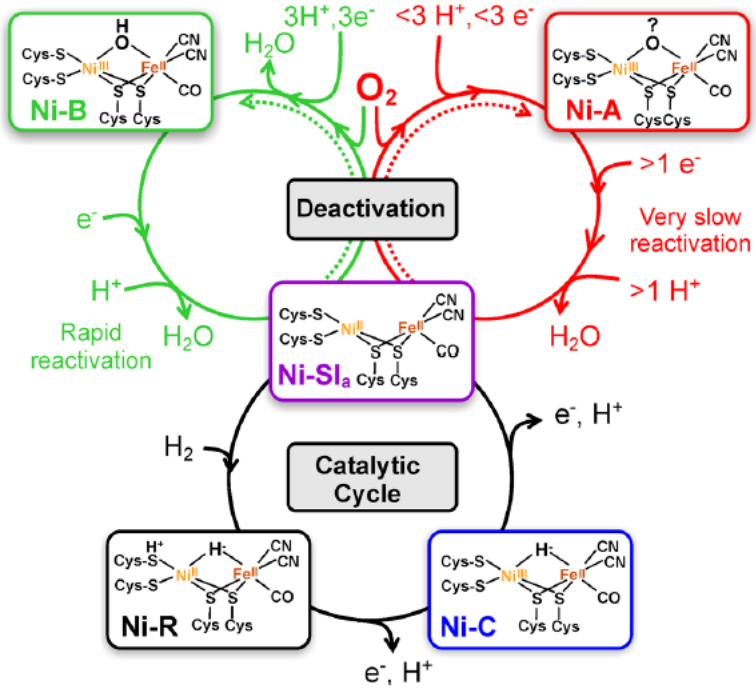

Figure I-4. The complete catalytic cycle of [NiFe]-H$_2$ase with deactivation/reactivation mechanism.[37] (Reprinted with permission from (Lubitz, W.; Ogata, H.; Rüdiger, O.; Reijerse, E. *Chem. Rev.* **2014,** *114* (8), 4081-4148). Copyright **2014** American Chemical Society.)

The spectroscopic tools have been instrumental in defining various isolated states to obtain a state-of-the art catalytic cycle with redox scheme.[37] The main function of [NiFe]-H$_2$ase is biased towards dihydrogen activation. The different states involved in the catalytic cycle along with the deactivation/reactivation mechanism of [NiFe]-H$_2$ase is shown in Figure I-4. The different states and their properties are summarized below:[37]

Ni-A state:[37]

- Inactive oxidized unready state (requires longer time for activation) that passes through **Ni-SU** state prior to the catalytic cycle.
- Oxidation states: five-coordinate, EPR active, Ni^{III} and six-coordinate Fe^{II}.
- The exact identity of the oxygenic bridge is unknown.
- Absent in oxygen-tolerant hydrogenases.

Ni-B state:[37]

- Inactive oxidized ready state (can be activated in seconds) that passes through **Ni-SI$_r$** state prior to the catalytic cycle.
- Oxidation states: five-coordinate Ni^{III} and six-coordinate Fe^{II}.
- Presence of a oxo-bridge between two metals (Ni···Fe distance is 2.7 Å); HYSCORE (hyperfine sublevel correlation) and ENDOR studies identified the bridging oxygenic ligand as μ-OH^-.

Using ESEEM (electron spin echo envelope modulation) spectroscopy, a *nitrogen* coupling, showing hyperfine and quadrupole features, has been detected for Ni-A and Ni-B states. Although nitrogen is not directly bound to the NiFe center, it has been interpreted that a H-bond from a highly conserved histidine unit with the axial cysteine is responsible for fine tuning the electronic properties.[37 67-68]

Ni-SI$_a$ state:[37]

- Reduction of the **Ni-A** and **Ni-B** states generate **Ni-SU** (silent unready) and **Ni-Si$_r$** (silent ready) states, respectively.
- A four cordinate Ni^{II} is proposed with no bridging ligand.
- The spin state of Ni^{II}, S = 0 (LS) or S = 1 (HS), is ambiguous as the state is EPR silent.
- Theoretical calculations predict a Ni···Fe distance of 2.8 Å or greater.
- EPR silent **Ni-SCO** state is formed in presence of CO.

Ni-C state:[37]

- The EPR active catalytic state forms with H_2 activation and plays a conspicuous role in the catalytic H_2 turnover.
- Presence of an exchangable proton was shown by ENDOR studies from Brian Hoffmann.[69]
- This state shows a formal Ni^{III}-H^-, which is two electron more reduced than the oxidized **Ni-A** and **Ni-B** states**.**
- The H-bond interaction of histidine moeity with the axial cysteine is present as indicated by EPR studies showing hyperfine and quadrupole coupling from the ^{14}N.
- Reacts with CO at low temperatures under light and forms various CO inhibited, EPR active **Ni-L** states.[70]

Ni-R state:[37]

- Addition of one e^- to the **Ni-C** state produces the fully reduced **Ni-R** state which exists in three isolectronic forms.
- Oxidation state: five coordinate, EPR silent Ni^{II} with spin states, S= 0 or S =1.
- A 0.89 Å resolution crystal structure of this state showed a slightly assymetric hydride bridge between Ni (1.58 Å) and Fe (1.78 Å) and a terminal protonated cysteine-S. The Ni···Fe distance of 2.58 Å.[71]

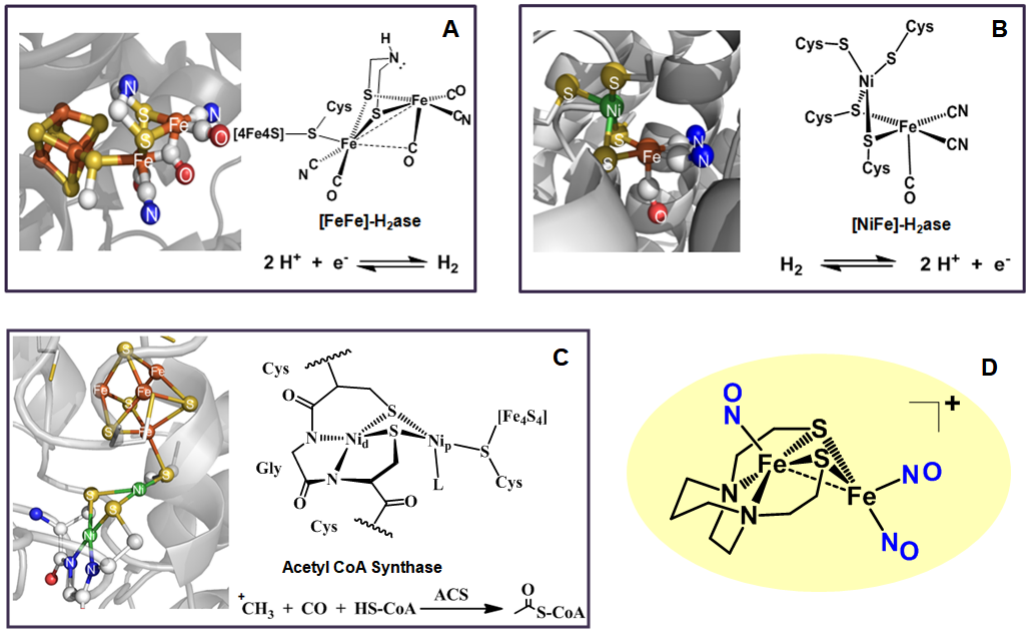

Figure I-5. The active sites of A) [FeFe]-[59], B) [NiFe]-H_2ase[47] and C) acetyl CoA synthase[72-73] in their protein backbone, respectively; their chemdraw representations are shown alongside. D) Diirontrinitrosyl catalyst, synthesized in the Darensbourg lab, inspired from the three enzyme active sites.[74]

Having identified the significance of the various states in the catalytic cycle and the deactivation/reactivation steps of the [NiFe]-H_2ase,[37] the importance of cis-dithiolate

bridged NiFe bimetallics as mediators for reversible proton-electron coupling stands out. The fact that noble metals like Pt are efficient catalysts for dihydrogen production/activation, cost-effective alternatives using base-metals are of primary importance for sustainable catalysis.[56, 75] The [NiFe]-H_2ase story provides an efficent guide as to how Mother Nature does it.[75]

"What I cannot create, I do not understand"-Richard Feynman. As a synthetic inorganic chemist, my goal in the Darensbourg lab was to 'create' [NiFe]-H_2ase active-site mimics, as small molecule models, to 'understand' their function. In fact my research endeavors included inspirations not only from the [NiFe]-H_2ase active site, but also from other organometallic-type bimetallic active sites like [FeFe]-H_2ase[59] and acetyl CoA synthase (ACS).[73] Their active site features are shown in Figure I-5 and are briefly described below.

Unlike [NiFe]-H_2ase, [FeFe]-H_2ase has a predilection for dihydrogen production. The active site of the [FeFe]-H_2ase enzyme contains two iron atoms coordinated to five diatomic ligands, Figure I-5A. The diiron construct is bridged by an aza-dithiolate linker (S-CH_2-N(H)-CH_2-S).[37] The 2-Fe subsite uses a cysteine sulfur to bind to the protein and redox-active 4Fe4S cluster. Each iron center is bound to two terminal diatomic ligands, CO and CN. The low valent, low spin oxidation states displayed by the diiron contruct are stabilized by the aptly chosen pi-acid diatomic ligands like CO and CN. A third CO resides in a semi-bridging position between the two iron centers, which allows the proximal iron, (the one in near vicinity to the 4Fe4S cluster), a square pyramidal geometry and the second iron, the distal iron, an inverted square pyramidal geometry.

The unique geometry is expected to be stabilized by the protein super structure, with bulky, hydrophobic groups found in the second coordination sphere of the enzyme. This creates an 'open site' on the distal iron, that is responsible for proton binding, as a hydride, assisted by the azadithiolate linker which in turn acts as the mediator for proton relay to the distal iron center.[59] The functional role of the azadithiolate linker has been attested by numerous molecular catalysts that have been synthesized with a pendant base, like the famous Dubois' catalyst.[76]

Intact metallodithiolate ligands of the type, NiN_2S_2, where the tetradentate N_2S_2 ligand is reminiscent of the tripeptide motif (cysteine-glucine-cysteine), is also utilized by nature to bind a second nickel via the bridging *cis*-dithiolates, as seen in the active site of acetyl CoA synthase (ACS), Figure I-5C.[72-73] The second nickel, stabilized by a redox-active 4Fe4S cluster, featuring an open site (presumed to be water), is the site for organometallic transformations. Its function is to catalyze the conversion of CoASH, methyl and CO to H_3C-C(O)-SCoA.[72-73]

Although differing in their functions, the active sites of the three metalloenzymes deleniate a common $M(\mu\text{-}SR)_2M'$ core. A 'metallodithiolate-as-ligand' approach is the basis of my research. Synthetic chemists develop tools that are readily available. Pursutant to the iron dinitrosyl unit, the proton reduction catalyst based on $Fe_2(NO)_3$ complex,[74] Figure I-6D, my synthetic efforts were directed towards binding different metallodithiolate ligands with $FeCp^R(CO)$ or $Fe(NO)_2$ receiver units. Chapters III, IV and V of my dissertation show the synthesis of such dithiolate-bridged MFe bimetallics. These bimetallic complexes showed electrocatalysis for proton reduction. A

collaboration with Prof. M. B. Hall and Dr. Shengda Ding, TAMU, related possible intermediates generated from electrocatalysis with computational mechanistic studies. The possiblity of a metallodithiolate serving as an internal pendant base, governed by the concept of hemi-lability, for proton abstraction, was a key feature that led to a hydride/proton coupling for H_2 production.

In Chapters VI and VIII, metallodithiolates bound to an iron dinitrosyl unit and a diiron subunit, respectively, as monodentate bound species were synthesized to verify the basicity/nuclephilicity of the free thiolate with protons, gold-phosphonium ions and other electrophiles. Chapter VII is synthetic foray in isolating diirontrinitrosyl complexes in three redox states showing the efficiency of nitrosyls as electron buffers. Finally, a concluding Chapter IX, addresses open questions about isolating intermediates in a proposed catalytic cycle, improving ligand design to ameliorate electrocatalytic efficiency etc., to materialize an ultimate objective of bio-inspired base-metal catalysis.

CHAPTER II

GENERAL EXPERIMENTAL DETAILS FOR CHAPTERS III-VIII

General Methods and Techniques

All reactions and operations were carried out on a double-manifold Schlenk vacuum line or in a glovebox under a N_2 or Ar atmosphere. Acetonitrile, benzene, dichloromethane, hexane, pentane, methanol, benzene, diethylether, and toluene were freshly purified by MBraun Manual Solvent Purification System packed with Alcoa F200 activated alumina desiccant. The known complexes (NO)Fe(bme-dach)[77-78], bme-dach,[79] (NO)Co(bme-dach),[77-78] Ni(bme-dach),[79] (O≡V)(bme-dach),[80] (NO)Fe(bme-daco)[77], bme-daco,[81] (NO)Co(bme-daco),[77] Ni(bme-daco),[81] $[Co(bme\text{-}daco)]_2$,[82] $[Zn(bme\text{-}daco)]_2$,[83] $[Fe(bme\text{-}daco)]_2$,[82] (NO)Fe(bme-dame)[84], bme-dame,[85] $[(\eta^5\text{-}C_5Me_5)Fe(CO)_3][PF_6]$,[86] $[Fe(bme\text{-}dame)]_2$,[85] $(\eta^5\text{-}C_5H_5)Fe(CO)_2I$,[87] $(\eta^5\text{-}C_5H_5)Fe(CO)_2(THF)$,[87] NO_g,[88] (μ-pdt)$[Fe_2(CO)_6]$,[89] (μ-dmpdt)$[Fe_2(CO)_6]$,[90] (μ-adt)$[Fe_2(CO)_6]$,[91] Ni(bme-daco)$W(CO)_4$,[78, 92] Ni(bme-daco)$W(CO)_5$,[92] $Fe(CO)_2(NO)_2$,[93]

[#]Parts of this chapter were reproduced with permission from:
Ding, S.; Ghosh, P.; Lunsford, A. M.; Wang, N.; Bhuvanesh, N.; Hall, M. B.; Darensbourg, M. Y. *J. Am. Chem. Soc.*, **2016**, *138*, 12920-12927. Copyright **2016** American Chemical Society.
Ghosh, P.; Quiroz, M.; Wang, N.; Bhuvanesh, N.; Darensbourg, M. Y., *Dalton Trans.* 2017, ***46***, 5617-5624.
Ghosh, P.; Ding. S.; Chupik, R. B.; Hsieh, C. –H.; Quiroz, M.; Bhuvanesh, N.; Hall, M. B.; Darensbourg, M. Y. *Chem. Sci.* **2017** (DOI: 10.1039/C7SC03378H) .

NaBArF,[94] (THF)W(CO)$_5$,[92] [Fe(CO)$_3$NO][18-Crown-6],[93] (μ-pdt)(μ-H)[Fe(CO)$_2$(PMe$_3$)][PF$_6$],[95] [(IMes)Fe(NO)$_3$][BF$_4$],[96] [(IMe)Fe(NO)$_3$][BF$_4$],[96] (μ-pdt)[(CO)$_3$FeFe(NO)(CO)(IMe)][BF$_4$],[97] were synthesized by published procedures. The following materials were of reagent grade and were used as purchased from Sigma–Aldrich or Alfa-Aesar or Strem or TCI or Acros Chemicals: KEt$_3$BH, CoCp$_2$, CoCp*$_2$, ferrocene, Fc$^+$[PF$_6$], propanedithiol, PMe$_3$, PPh$_3$, HBF$_4$.Et$_2$O, CF$_3$COOH, ^{13}CO, CH$_3$COOH, (PPh$_3$)AuCl, C$_6$H$_5$CH$_2$Br, C$_2$H$_5$I, CH$_3$I, KBr, NaBr, , [NO][BF$_4$], [n-Bu$_4$N][PF$_6$], AgBF$_4$, HPLC-grade acetonitrile. The gases, ^{12}CO, N$_2$, Ar, H$_2$, CH$_4$, were purchased from Praxair.

Physical Measurements

Infrared spectra (IR) were recorded on a Bruker Tensor 37 Fourier transform IR (FTIR) spectrometer. Solution IR spectra were obtained using a CaF$_2$ cell with a 0.2 mm path length. Mass spectrometry (ESI-MS) was performed by the Laboratory for Biological Mass Spectrometry at Texas A&M University. ^{1}H, ^{13}C and ^{19}F NMR spectra were recorded on an Inova 500 MHz superconducting NMR instrument operating at 500 MHz and 125.72 MHz respectively or a Mercury 300 MHz NMR operating at 300 MHz and 75.43 MHz respectively. ^{1}H spectra were referenced to residual protonated solvent and ^{13}C spectra were referenced to deuterated solvent. X-Band Bruker 300E spectrometer was used to measure CW EPR spectrum at 9.3701 GHz frequency at 298 or 77 or 4 K. SpinCount developed by Prof. M. P. Hendrich of Carnegie Mellon University was used to simulate the spectra. OriginPro 8 SR4 v8.0951 (B951) developed by OriginLab Corporation was used for deconvolution of IR spectra. Elemental analyses

were performed by Atlantic Microlab, Inc., Norcross, GA. The low field Mössbauer spectroscopy was done by Dr Codrina Popescu from the Colgate University.

X-ray Diffraction Analyses

The crystal structures in general were measured at low temperatures (150 or 110 K) by BRUKER APEX 2 X-ray (three-circle) diffractometer with Mo sealed X-ray tube (K_α = 0.70173Å). New instruments were also used to measure single crystals using BRUKER Quest X-ray (fixed-Chi geometry) diffractometer with Mo-Iμs X-ray tube (K_α = 0.71073Å) and BRUKER Venture X-ray (kappa geometry) diffractometer with Cu-Iμs X-ray tube (K_α = 1.5418Å). The structures were refined by weighted least squares refinement on F^2. At idealized positions, hydrogen atoms were placed and fixed isotropic displacement parameters were used to refine them. For all non-hydrogen atoms, anisotropic displacement parameters were employed. The final data presentation and structure plots were generated in Olex2.

Electrochemistry

Cyclic voltammograms (CVs) were recorded on a BAS-100A electrochemical analyzer or CHI600E electrochemical analyzer (HCH instruments, Inc.) using a three-electrode cell: the working electrode was a glassy carbon disk electrode (0.071 cm^2), the reference electrode was a Vycor-tipped glass tube with $Ag/AgNO_3$; and the counter electrode was a straight platinum wire. The glassy carbon working electrode was polished with 3 μm diamond paste and then sonicated in ultrapure (Millipore) water for 10 min. The glassy carbon electrode was polished in between each electrochemical scan.

Solutions were deaerated by an Ar purge for 5−10 min, and a blanket of Ar was maintained over the solution while performing the measurements. All experiments were performed at room temperature in CH_3CN solutions, 2.0 mM in analyte, and 0.1 M [n-Bu_4N][PF_6] as supporting electrolyte. Ferrocene, Fc, served as the internal reference, and all potentials are reported relative to the Fc/Fc^+ couple at 0.00 V.

A custom made three-necked truncated conical shaped flask with an outlet port/gas inlet was the apparatus used for bulk electrolysis experiments. A Ni-Cr-coiled wire counter electrode, a $Ag/AgNO_3$ reference electrode, and a 3 mm glassy carbon working electrode were placed in the necks of the cell. The Ni-Cr-coiled wire placed in a glass tube with a medium glass frit served as the counter electrode. A glass tube containing a Ag wire immersed in a 1 mM solutions of $AgNO_3$ in MeCN separated from the main solution by a Vycor frit was the make-up of the reference electrode. To the electrochemical cell 10 mL of 0.1 M [n-Bu_4N][PF_6] in CH_3CN was added and then purged with Ar to deplete O_2. To the cell $2x10^{-5}$ mol of the appropriate catalyst and 50 equivalents of trifluoroacetic acid were added. To ensure that the experiment was under catalytic conditions, a cyclic voltammogram was recorded. After 30 minutes of bulk electrolysis performed at -1.80 V vs Fc/Fc^+, 1 mL of methane was added as the internal standard.

Determination of Overpotential

The overpotential for the complexes was determined by the method determined by Appel and Helm.[98] Overpotential is defined as the difference between the

thermodynamic potential (E_{H+}) and the catalytic half wave potential ($E_{cat/2}$).[99-100] The value of E_{H+} is +0.65 V (vs $Fc^{0/+}$ = 0.0 V) in 100 mM trifluoroacetic acid (TFA) in CH_3CN solvent. The potential where the catalytic current (i_{cat}) corresponds to half of its value is defined as the catalytic half wave potential ($E_{cat/2}$). A representative example for the **CoFe*'** complex, from Chapter IV, is shown in Figure II-1.

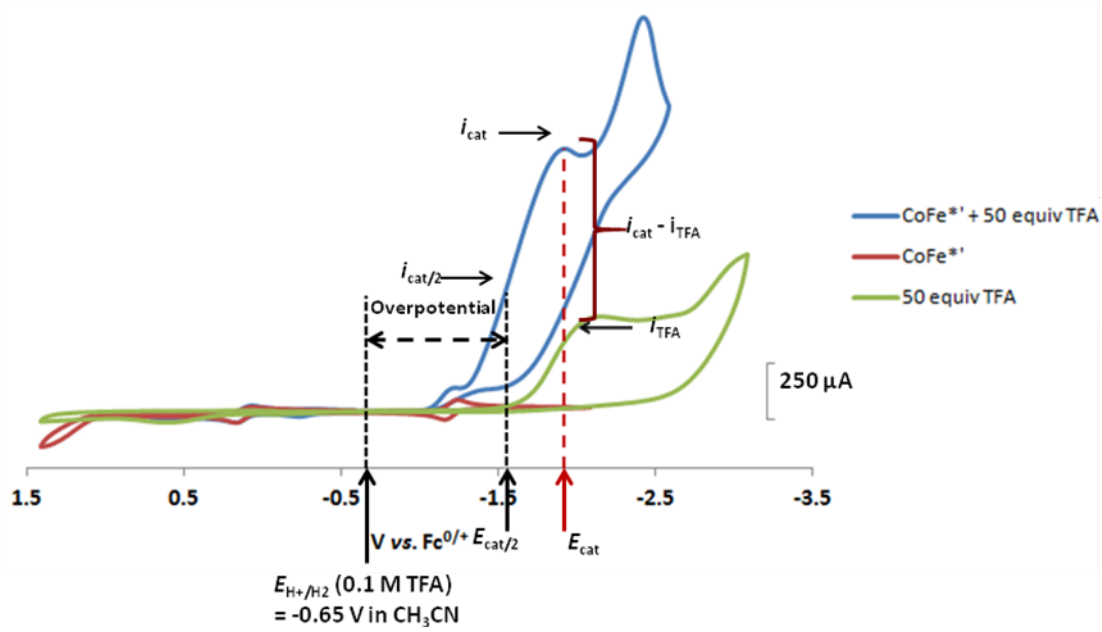

Figure II-1. Using a representative example from Chapter IV, overlay of cyclic voltammograms of **Co-Fe*'** (red trace), **Co-Fe*'** with 50 equivalents of TFA (blue trace) and 50 equivalents of TFA without catalyst (olive trace). Graphical representation for the calculation of $E_{cat/2}$, net catalytic current (i_{cat}-i_{TFA}) and overpotential is also illustrated.

Calculation of Turnover Frequency (TOF)

TOF frequency was calculated according to the modified equation as published by the Darensbourg group. The general form of the equation that uses i_{cat} (Eq. 1) was modified to compensate for the background acid contribution by subtracting the i_{TFA}

(Eq 2). The pictorial representation for the corrected catalytic contribution is shown in Figure II-1

$TOF = 1.94\ (V^{-1}) \times \nu\ (Vs^{-1}) \times [i_{cat}/i_p]^2$ (Eq. 1)[99]

$TOF = 1.94\ (V^{-1}) \times \nu\ (Vs^{-1}) \times [(i_{cat}-i_{TFA})/i_p]^2$ (Eq. 2)

ν = scan rate

i_{cat} = total current measured upon adding acid (TFA) to the catalyst

i_{TFA} = background current measured from the acid (TFA) at the potential of i_{cat}

i_p = current measured from the catalyst in absence of acid

i_{cat}-i_{TFA} = corrected current response from the catalyst only.

Gas Chromatography

Gas identification was accomplished with an Agilent Trace 1300 GC equipped with a thermal conductivity detector and a custom-made 120 cm stainless steel column packed with Carbosieve-II from Sigma-Aldrich. The carrier gas was Ar, and throughout the entire separation, the column was kept at 200 °C, while the detector was at 250 °C. Identification and quantification of H_2 produced from bulk electrolysis was accomplished by withdrawing 200 µL of the headspace using a 0.5 mL Valco Precision Sampling Syringe, Series A-2 equipped with a Valco Precision Sampling syringe needle with a 5 point side port. H_2 is the first peak to elute from the column at 1.28 min, followed by N_2/O_2 at 2.52 min, and finally CH_4 at 4.09 min. We posit that the peak at ca. 2.3 min in the gas chromatograms is due to N_2/O_2 from the atmosphere that contaminated the needle of the gas-tight syringe prior to the insertion of the head space gas into the gas chromatograph.

Quantification of H_2 produced was accomplished by determining the relative response factor of H_2 and the internal standard, CH_4. This was done by preparing vials containing varying amounts of H_2 with one mL of CH_4 and plotting the $\frac{\text{area of } H_2}{\text{area of } CH_4}$ vs. $\frac{\text{mL of } H_2}{\text{mL of } CH_4}$, Figure II-2. The calibration curve had the linear equation of y = 2.9757x + 0.0226 with R^2 value of 0.9987.

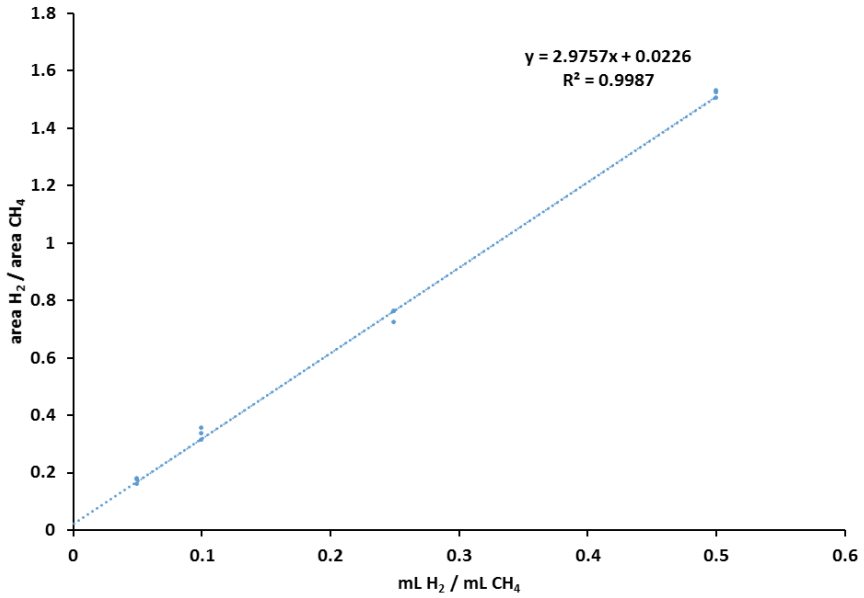

Figure II-2. Calibration curve used in the quantification of H_2 produced during electrolysis. This was generated by preparing vials containing varying amounts of H_2 with one mL of CH_4 and plotting the (area of H_2/area of CH_4) vs. (mL of H_2/mL of CH_4).

Experimental Details for Chapter III

Synthesis of [η^5-CpFe(CO)(bme-dach)Fe(NO)][BF_4], Fe-Fe'$^+$. A solution of $CpFe(CO)_2I$ (256 mg, 1.00 mmol) and $AgBF_4$ (195 mg, 1.00 mmol) in dichloromethane (20 mL) was stirred for 30 min at room temperature in absence of light and then filtered through a football cannula. (bme-dach)Fe(NO) (304 mg, 1.00 mmol) was added into the

filtrate, and the solution was stirred under UV lamp irradiation. The reaction was monitored by changes in the IR spectrum. On completion of the reaction, the resulting solution was evaporated to dryness under vacuum, and the residue was chromatographed on a silica column with CH_2Cl_2/CH_3OH (20:1, v/v) as eluent. Recrystallization in CH_2Cl_2/hexane at -35 °C afforded X-ray quality crystals of **Fe-Fe'**$^+$ as the BF_4^- salts. IR (CH_2Cl_2, cm^{-1}): ν(CO) 1935; ν(NO) 1717. ESI-MS$^+$: m/z 452.9932 (Calc. for $[M]^+$, 452.9931). Elem. Anal. Calc. for $C_{15}H_{23}BFe_2F_4N_3O_2S_2$: C, 33.36; H, 4.29; N, 7.78. Found: C, 33.04; H, 4.13; N, 7.19%.

Synthesis of [η^5-CpFe(CO)(bme-dach)Ni][BF$_4$], Ni-Fe'$^+$. In a manner similar to that of the above, complex **Ni-Fe'**$^+$ was synthesized using (bme-dach)Ni (277 mg, 1.00 mmol). Recrystallization in CH_2Cl_2/hexane at -35 °C afforded X-ray quality crystals of **Ni-Fe'**$^+$as the BF_4^- salts.IR (CH_2Cl_2, cm^{-1}): ν(CO) 1930. ESI-MS$^+$: m/z 424.9940 (calculated for $[M]^+$, 424.9960). Elem. Anal. Calc. for $C_{15}H_{23}BNiFeF_4N_3O_2S_2$: C, 35.13; H, 4.52; N, 5.46. Found: C, 35.10; H, 4.46; N, 5.46%.

Synthesis of [η^5-CpFe(CO)$_2$(bme-dach)Ni][BF$_4$], Ni-Fe"$^+$. A solution of $CpFe(CO)_2I$ (128 mg, 0.50 mmol) and $AgBF_4$ (97 mg, 0.50 mmol) in dichloromethane (20 mL) was stirred for 30 min at room temperature in absence of light and then filtered through a football cannula. A sonicated solution of (bme-dach)Ni (139 mg, 0.50 mmol) in dichloromethane was added into the filtrate. The solution was stirred in the dark for 3 h. On completion of the reaction, the resulting solution was evaporated to dryness under vacuum, washed with 20 mL (x 3) diethyl ether and redissolved in dichloromethane. The red colored solution was filtered through celite to remove unreacted (bme-dach)Ni and

the solution was recrystallized in CH_2Cl_2/hexane at -35 °C affording X-ray quality crystals of **Ni-Fe"**$^+$ as BF_4^- salts. IR (CH_2Cl_2, cm^{-1}): ν(CO) 2044, 1999. ESI-MS^+: m/z 452.9700 (Calc. for $[M]^+$, 452.9904).

Synthesis of [η^5-CpFe(CO)$_2$(bme-dach)Fe(NO)][BF$_4$], Fe-Fe"$^+$. In a manner similar to that of **Ni-Fe"**$^+$, complex **Fe-Fe"**$^+$ was synthesized using (bme-dach)Fe(NO) (152 mg, 0.50 mmol). IR (CH_2Cl_2, cm^{-1}): ν(CO) 2045, 2002; ν(NO) 1691. ESI-MS^+: m/z 480.8721 (calculated for $[M]^+$, 480.8982).

Turnover Frequency Data for Chapter III

The turnover frequency data of complexes, **Fe-Fe'**$^+$ and **Ni-Fe'**$^+$, in various equivalents of TFA, are shown in Tables II-1 and 2, respectively.

Table II-1. Values used for the calculation of TOF for **Fe-Fe'**$^+$ at various TFA concentrations in CH_3CN at a scan rate of 200 mV/s. Due to the appearance of the catalytic peak at -1.66 V, the value for i_p with no added acid was taken from the first reduction at -1.19 V. The kinetic isotope effect (KIE) was measured using 150 ul d_1-TFA and the TOF calculated in a similar fashion.

Acid (uL)	i_{cat} (A)	i_{acid} (A)	i_{cat}-i_{acid} (A)	TOF	KIE
0	3.75473E-05	0	3.75473E-05	0.00	
50	0.0013328	0.0006989	0.0006339	55.30	
150	0.0024215	0.0017145	0.0007070	68.79	
200	0.0029315	0.0022295	0.0007020	67.82	
d_1-TFA					
0	4.95958E-05	0.0000000	4.95958E-05	0.00	
150	0.00214944	0.00160215	0.00054729	47.25	1.46

Table II-2. Values used for the calculation of TOF for **Ni-Fe'**$^{+}$ at various TFA concentrations in CH_3CN at a scan rate of 200 mV/s. The kinetic isotope effect (KIE) was measured using 200 μL d_1-TFA and the TOF calculated in a similar fashion.

Acid (uL)	i_{cat} (A)	i_{acid} (A)	i_{cat}-i_{acid} (A)	TOF	KIE
0	0.0000558	0.0000000	0.0000558	0.00	
50	0.0009905	0.0004540	0.0005365	35.85	
100	0.0016305	0.0010011	0.0006294	49.35	
150	0.0021535	0.0015155	0.0006380	50.70	
200	0.0026368	0.0019941	0.0006426	51.43	
250	0.0031208	0.0024732	0.0006476	52.24	
d_1-TFA					
0	0.000059414	0.0000000	0.000059414	0.00	
200	0.00248022	0.0019302	0.00055002	33.25	1.56

Experimental Details for Chapter IV

Synthesis of [(η^5-C_5H_5)Fe(CO)$_2$(bme-dach)Co(NO)][BF_4], Co-Fe''. A solution of $CpFe(CO)_2I$ (256 mg, 1.00 mmol) and $AgBF_4$ (195 mg 1.00 mmol) in CH_2Cl_2 (20 mL) was stirred for 30 min in the dark at room temperature and then filtered through celite. The filtrate was added to a solution of (NO)Co(bme-dach) (307 mg, 1.00 mmol) in CH_2Cl_2 (20 mL) and stirred in the dark for 3 h. The resulting solution was then redissolved in CH_2Cl_2 after it was dried under vacuum and washed with 20 mL (x 3) diethyl ether. The solution was filtered through celite to filter any unreacted starting material and X-ray quality crystals for complex **Co-Fe''** were obtained by layering a

CH_2Cl_2 solution of the product with hexanes. IR (CH_2Cl_2, cm^{-1}): ν(CO) 2045, 2001; ν(NO) 1632; ESI-MS^+: *m/z* 483.95 (Calc. for $[M]^+$, 483.96).

Synthesis of [(η^5-C_5H_5)Fe(CO)(bme-dach)Co(NO)][BF_4], Co-Fe'. A solution of $CpFe(CO)_2I$ (256 mg, 1.00 mmol) and $AgBF_4$ (195 mg 1.00 mmol) in CH_2Cl_2 (20 mL) was stirred for 30 min in the dark at room temperature and then filtered through celite. The filtrate was added to a solution of (NO)Co(bme-dach) (307 mg, 1.00 mmol) in CH_2Cl_2 (20 mL) and the solution was stirred under UV lamp irradiation. IR spectrum was used to monitor the reaction. Upon completion of the reaction, the product was purified through a silica column with CH_2Cl_2/CH_3OH (20:1, v/v) as the eluent. X-ray quality crystals for complex **Co-Fe'** were also obtained by layering a CH_2Cl_2 solution of the product with hexanes. IR (CH_2Cl_2, cm^{-1}): ν(CO) 1934; ν(NO) 1650; ESI-MS^+: *m/z* 455.99 (Calc. for $[M]^+$, 455.99). Elem. Anal. Calc'd (found) for $C_{15}H_{23}BCoFeF_4N_3O_2S_2$ (MW = 543 g mol^{-1}): C, 33.17 (33.25); H, 4.27 (4.29); N, 7.74 (7.65).

Synthesis of [(η^5-C_5Me_5)Fe(CO)(bme-dach)Co(NO)][PF_6], Co-Fe*'. A solution of (NO)Co(bme-dach) (307 mg, 1.00 mmol) and $[Fe(Cp^*)(CO)_3]PF_6$ (419 mg, 1.00 mmol) in CH_2Cl_2 (25 mL) were stirred under UV lamp irradiation. The dark purple reaction mixture was monitored by IR spectroscopy. Once the reaction was completed, the dark purple product was purified by passing through a silica gel column with CH_2Cl_2/CH_3OH (10:1, v/v) as the eluent. X-ray quality crystals for complex **Co-Fe*'** were obtained by layering a CH_2Cl_2 solution of the product with hexanes. IR (CH_2Cl_2, cm^{-1}): ν(CO) 1907; ν(NO) 1647; ESI-MS^+: *m/z* 526.13 (Calc. for $[M]^+$, 526.07). Anal. Calc'd

(found) for $C_{20}H_{33}CoF_6FeN_3O_2PS_2$ (MW = 671 g mol^{-1}): C, 35.78 (36.31); H, 4.95 (5.16); N, 6.26 (5.83).

Synthesis of [(η^5-C_5Me_5)Fe(CO)(bme-dach)Ni][PF_6], Ni-Fe*'. In a similar manner to that of complex **Co-Fe*',** complex **Ni-Fe*'** was prepared by using Ni(bme-dach) (276 mg, 1.00 mmol) and $[Fe(Cp^*)(CO)_3]PF_6$ (419 mg, 1.00 mmol) in CH_2Cl_2 (25 mL) which was stirred under UV lamp irradiation. The tan reaction mixture was monitored by changes in the IR spectrum and X-ray quality crystals were obtained by layering a CH_2Cl_2 solution of the product with hexanes. IR (CH_2Cl_2, cm^{-1}): ν(CO) 1905; ESI-MS^+: *m/z* 495.06 (Calc. for $[M]^+$, 495.07). Anal. Calc'd (found) for $C_{20}H_{33}F_6FeN_2NiOPS_2$ (MW = 640 g mol^{-1}): C, 37.47 (36.99); H, 5.19 (5.38); N, 4.37 (4.31).

Turnover Frequency Data for Chapter IV

The turnover frequency data of complexes, Ni-**Fe*'**, **Co-Fe*'** and **Co-Fe'**, in various equivalents of TFA, are shown in Tables II-3, 4 and 5, respectively.

Table II-3. TOF calculation of **Ni-Fe*'** at various concentrations of TFA at scan rate of 0.2 V/s in CH_3CN. The value of i_p was considered at the appearance of the catalytic event at -1.91 V as the first reduction event.

Acid (µL)	i_{cat} (mA)	i_{TFA} (mA)	i_{cat}-i_{TFA} (mA)	TOF (s^{-1})
0	0.072	0.000	0.072	0.000
50	0.991	0.664	0.326	7.99
100	1.849	1.247	0.602	27.12
150	2.288	1.677	0.611	27.94
200	2.600	1.943	0.657	32.31

Table II-4. TOF calculation of **Co-Fe*'** at various concentrations of TFA at scan rate of 0.2 V/s in CH_3CN. The value of i_p was considered at the appearance of the catalytic event at -1.19 V as the first reduction event.

Acid (µL)	i_{cat} (mA)	i_{TFA} (mA)	i_{cat}-i_{TFA} (mA)	TOF (s^{-1})
0	0.053	0.000	0.053	0.000
50	1.184	0.665	0.518	36.56
100	1.907	1.218	0.689	64.69
150	2.299	1.608	0.691	65.06

Table II-5. TOF calculation of **Co-Fe'** at various concentrations of TFA at scan rate of 0.2 V/s in CH_3CN. The value of i_p was considered at the appearance of the catalytic event at -1.12 V as the first reduction event.

Acid (µL)	i_{cat} (mA)	i_{TFA} (mA)	i_{cat}-i_{TFA} (mA)	TOF (s^{-1})
0	0.056	0.000	0.056	0.00
50	1.007	0.454	0.553	37.91
100	1.539	0.848	0.690	59.23
150	1.897	1.125	0.772	74.08
200	2.105	1.307	0.076	79.15

Experimental Details for Chapter V

Syntheses of $[NiN_2S_2•Fe(NO)_2(CO)]$, [Ni-Fe(CO)] and **[Ni(bme-daco)•$Fe(NO)_2$], $[Ni\text{-}Fe]^0$.** A solution of Ni(bme-daco) (0.29g, 0.10 mmol) in 15 mL THF was anaerobically added to a freshly trapped orange solution of $Fe(CO)_2(NO)_2$ (0.11mmol) in 15 mL THF and was stirred for 10 min at room temperature in absence of

light. The reaction was monitored by changes in the IR spectrum for appropriate shift of the ν(CO) and ν(NO) stretching frequencies for the formation of **[Ni-Fe(CO)]**. IR (THF, cm^{-1}): ν(CO) 2006; ν(NO) 1734, 1690. **$[Ni\text{-}Fe]^0$** was synthesized upon heating **[Ni-Fe(CO)]** solution at 40 ^oC for 20 min or by stirring under UV light for 5 to 10 min. The course of the reaction should be monitored by IR spectrum as overheating or excess irradiation leads to decomposition. Upon completion of the reaction, the resulting brown solution was filtered over dry celite and was partially kept under vacuum to remove excess $Fe(CO)_2(NO)_2$. The concentrated brown THF solution was recrystallized by layering with hexane at – 35 ^oC to afford brown X-ray quality crystals. IR (THF, cm^{-1}): ν(NO) 1681 (m), 1630 (s). ESI-MS^+: *m/z* 405.9870 (Calc. for [M], 405.9731).

Synthesis of $[NiN_2S_2{\bullet}Fe(NO)_2][BF_4]$, $[Ni\text{-}Fe]^+$ or **$[Ni(bme\text{-}daco){\bullet}Fe(NO)_2]_2[BF_4]_2$, $[Ni_2\text{-}Fe_2]^{2+}$.** Reactants Ni(bme-daco) (0.29 g, 0.10 mmol), $[Fe(CO)_3(NO)]^-Na^+(18\text{-}C\text{-}6)^3$ (0.47 g, 0.10 mmol) and $[NO]BF_4$ (0.23 g, 0.20 mmol) were stirred in 20 mL CH_2Cl_2 for 5 h under N_2. The reaction was monitored by IR spectrum. Upon completion the purple reaction mixture was concentrated to around ~ 5 mL and was precipitated by adding pentane. The precipitate was washed with diethyl ether (3 x 15 mL) and pentane (2 x 10 mL). The precipitate was redissolved in 10 mL $CH_2Cl_2$and was filtered through dry celite to remove impurities (Yield: 0.29 g, 60 %).Dark purple X-ray quality crystals of **$[Ni_2\text{-}Fe_2]^{2+}$** were grown inCH_2Cl_2/pentane at -35 ^oCas BF_4^- salt. IR (CH_2Cl_2, cm^{-1}): ν(NO) 1805 (m), 1794 (s), 1749 (m), 1732 (s). ESI-MS^+: *m/z* 405.9737 (Calc. for $[M]^+$, 405.9731).

Synthesis of $[(NiN_2S_2)_2{\bullet}Fe(NO)_2][BF_4]$, $[Ni_2\text{-}Fe]^+$. In a manner similar to that of above **$[Ni_2\text{-}Fe]^+$** was synthesized by stirring reactants Ni(bme-daco) (0.56 g, 0.20 mmol) or Ni(bme-dach) (0.56 g, 0.20 mmol), $[Fe(CO)_3(NO)]^-Na^+(18\text{-}C\text{-}6)^3$ (0.47 g, 0.10 mmol) and $[NO]BF_4$ (0.23 g, 0.20 mmol) in 20 mL CH_2Cl_2 for 5 h under N_2. Recrystallization in CH_2Cl_2/hexane at -35 °C afforded dark brown X-ray quality crystals of **$[Ni_2\text{-}Fe]^+$** as BF_4^- salt. (Yield: 0.40 g, ~ 55 %). IR (CH_2Cl_2, cm^{-1}): ν(NO) 1790(m), 1736 (s) for complex having bme-dach ligand and ν(NO) 1789 (m), 1736 (s)for complex having bme-daco ligand. ESI-MS^+ (for complex having bme-dach ligand): *m/z*667.9484 (Calc. for $[M]^+$, 667.9839.

Calculation of Magnetic Susceptibility Using Evans' Method

The effective magnetic moment (μ_{eff}) of a compound is calculated according to following equation:[101]

$\mu_{eff} = \chi_p T = (1/8)[n(n+2)]$

χ_p = paramagnetic susceptibility

T = absolute temperature

n = number of unpaired electrons

The experimentally measured magnetic susceptibility (χ_{expt}) is the sum of χ_p and χ_D, where χ_D is the diamagnetic susceptibility. χ_D is independent of temperature with a negative magnitude, and is a property arising from all atoms in the compound.

$\chi_{expt} = \chi_p + \chi_D$

Thus, the diamagnetic susceptibility should be taken into account in order to calculate μ_{eff}.[101]

The ^{19}F NMR of **[Ni-Fe]$^+$** and **[Ni$_2$-Fe]$^+$** was measured in a 500 MHz NMR machine, using 9 mg and 12 mg of the compounds, respectively, with $C_6H_5CF_3$ as the standard, at 22.5 ^oC and 20.5 ^oC. A coaxial NMR tube was used for this purpose. The outer tube consisted of the Ni-Fe complex dissolved in 0.5 mL of CD_2Cl_2 and 1.245 μL of $C_6H_5CF_3$ while the inner tube contained only 0.5 mL of CD_2Cl_2 and 1.245 μL of $C_6H_5CF_3$. The ^{19}F NMR spectra of **[Ni-Fe]$^+$** and **[Ni$_2$-Fe]$^+$**are shown in Figure V-6 and 7, respectively.

The calculated χ_D of **[Ni-Fe]$^+$**and **[Ni$_2$-Fe]$^+$** were-0.0002393 and -0.0003881, respectively, which are close to [–(mol.wt.)/2]/1000000.[101]

Turnover Frequency Data for Chapter V

The turnover frequency data of complexes, **[Ni-Fe]**$^+$ and **[Fe-Fe]**$^+$, in various equivalents of $HBF_4.Et_2O$, are shown in Tables II-6 and 7, respectively.

Table II-6. Calculation of TOF for **[Ni-Fe]**$^+$ at various concentrations of $HBF_4.Et_2O$ in CH_2Cl_2 at scan rate of 0.2 V/s. The $[Fe(NO)_2]^{9/10}$ redox event at -0.73 V, i.e. the onset of the catalytic event, was considered for calculating i_p.

Acid (equiv.)	i_{cat} * 10^4 (A)	i_{cat}-i_{HBF4} (mA)	TOF (s^{-1})
0	0.000	---	0.000
24	1.689	1.633	17.08
26	1.811	1.755	19.72
28	1.858	1.802	20.79
31	1.903	1.847	21.84
37	2.145	2.089	27.94
41	2.337	2.281	33.31
49	2.458	2.402	36.94
61	2.485	2.429	37.77
70	2.529	2.473	39.16
79	2.545	2.489	39.66

Table II-7. Calculation of TOF for **[Fe-Fe]**$^{+}$ at various concentrations of $HBF_4.Et_2O$ in CH_2Cl_2 at scan rate of 0.2 V/s. The $[Fe(NO)_2]^{9/10}$ redox event at -0.78 V, *i.e.* the onset of the catalytic event, was considered for calculating i_p.

Acid (equiv.)	i_{cat} * 10^4 (A)	i_{cat}-i_{TFA} (mA)	TOF (s^{-1})
0	0	---	0.000
9	1.103	1.047	7.73
15	1.298	1.242	10.87
22	1.397	1.341	12.67
42	1.763	1.707	20.53
54	1.840	1.784	22.43
66	1.931	1.875	24.77
72	1.979	1.923	26.06
84	2.003	1.947	26.70

Experimental Details for Chapter VI

Synthesis of $[(IMes)Fe(NO)_2(bme\text{-}daco)Ni]_2[BF_4]_2$, Ni*-Fe'. To a solid mixture of 53 mg (0.1 mmol) of $[(IMes)Fe(NO)_3][BF_4]$ and 29 mg (0.1 mmol) of Ni(bme-daco) in a 50 mL Schlenk flask, 20 mL CH_2Cl_2 was added using a cannula and stirred for ten minutes. The formation of the product was monitored using IR spectroscopy. The reaction mixture was dried under vacuum and the solid product was washed with diethyl ether (20 mL x 3). It was redissolved in 10 mL of CH_2Cl_2 and was

filtered through celite. Recrystallization in CH_2Cl_2/hexane/ether at -28 ºC afforded dark purple X-ray quality crystals; IR (THF): ν(NO): 1789 (m), 1282 (s) cm^{-1}.

Synthesis of [(IMes)Fe(NO)$_2$(bme-daco)Co(NO)][BF$_4$], Co*-Fe'. In a manner similar to that of the above, complex **Co*-Fe'** was synthesized using 53 mg (0.1 mmol) of IMes[Fe(NO)$_3$][BF$_4$] and 32 mg (0.1 mmol) of (NO)Co(bme-daco) in 20 mL THF. Recrystallization in THF/hexane at -28 ºC afforded dark brown X-ray quality crystals; IR (THF): ν(NO): 1797 (m), 1735 (s), 1625 (m) cm^{-1}.

Synthesis of [(IMes)Fe(NO)$_2$(bme-daco)Fe(NO)][BF$_4$], Fe*-Fe'. In a manner similar to that of the above, complex **Fe*-Fe'** was synthesized using 53 mg (0.1 mmol) of IMes[Fe(NO)$_3$][BF$_4$] and 31 mg (0.1 mmol) of (NO)Fe(bme-daco) in 20 mL THF at 0 ºC. Recrystallization in THF/hexane/ether at -28 ºC afforded dark brown X-ray quality crystals; IR (THF): ν(NO): 1801 (m), 1742 (s), 1676 (m) cm^{-1}.

Synthesis of [(IMes)Fe(NO)$_2$(bme-dach)Ni][BF$_4$], Ni-Fe'. A 100 mL Schlenk flask was charged with a solid mixture of 53 mg (0.1 mmol) of IMes[Fe(NO)$_3$][BF$_4$] and 27 mg (0.1 mmol) of Ni(bme-dach). 25 mL of THF was added and stirred for ten minutes, the solvent was dried under vacuum and the solid product was washed with ether (20 mL x 3) followed by dissolving in 25 mL of THF. The THF solution was filtered through celite; IR (THF): ν(NO): 1792 (m), 1732 (s) cm^{-1}.

Synthesis of [(IMes)Fe(NO)$_2$(bme-dach)Co(NO)][BF$_4$], Co-Fe'. In a similar manner to that of the above, complex **Co-Fe''** was synthesized using 53 mg (0.1 mmol)

of IMes[Fe(NO)$_3$][BF$_4$] and 30 mg (0.1 mmol) of Co(NO)(bme-dach) in 25 mL THF. IR (THF): ν(NO): 1793 (m), 1736 (s), 1620 (m) cm^{-1}.

Reaction of Ni-Fe' with Ph$_3$PAuCl. A 50 mL Schlenk flask was charged with 49 mg (0.1 mmol) of Ph$_3$PAuCl and 78 mg (0.1 mmol) of **Ni-Fe'**. 20 mL of THF was added to the solid mixture and was stirred for ten minutes. The reaction was monitored by IR spectroscopy. The solvent was dried under vacuum and the solid product was washed with 20 mL of hexane. The product was redissolved in diethyl ether and was filtered through celite. The IR spectrum of the filtrate indicated formation of **(IMes)Fe(NO)$_2$Cl**; IR (THF): ν(NO): 1777 (m), 1713 (s) cm^{-1}. The solution was dried in vacuum and redissolved in THF. Recrystallization was done in THF/hexane at -28 ^{o}C to afford brown crystals of **(IMes)Fe(NO)$_2$Cl**. The residue was dissolved in 10 mL of CH_2Cl_2 and was filtered over a bed of celite. Recrystallization was done in CH_2Cl_2/hexane at -28 ^{o}C to yield reddish-brown blocks of **[Ni(bme-dach) AuPPh$_3$][BF$_4$]**.

Reaction of Co-Fe' with Ph$_3$PAuCl. In a similar manner to that of above 49 mg (0.1 mmol) of Ph$_3$PAuCl and 80 mg (0.1 mmol) of **Co-Fe'** were stirred in 20 mL of CH_2Cl_2. The solvent was dried under vacuum and the solid product was washed with 20 mL of hexane. The product was redissolved in diethyl ether and was filtered through celite. The IR spectrum of the filtrate indicated formation of **(IMes)Fe(NO)$_2$Cl**; IR (THF): ν(NO): 1777 (m), 1713 (s) cm^{-1}. The residue was redissolved in 20 mL of CH_2Cl_2 and was filtered over a bed of celite. Recrystallization was done in

CH_2Cl_2/hexane at -28 ºC. Two crystals of different morphology was observed **[(*cis*-(NO)CoN_2S_2)Au]$_2$** and **[(*trans*-(NO)CoN_2S_2)Au]$_2$**.

Synthesis of (IMes)Fe(NO)$_2$Br. Method 1. A 100 mL Schlenk flask was charged with a solid mixture of 17 mg (0.1 mmol) of benzyl bromide and 78 mg (0.1 mmol) of **Ni-Fe'**. 20 mL of THF was added and the reaction was stirred for 1 h. The solvent was dried under vacuum and the solid product was washed with hexane (20 mL x 3) followed by dissolving in 25 mL of diethyl ether. The ether solution was filtered through celite and dried under vacuum ad was redissolved in THF. Recrystallization was done in THF/hexane at -28 ºC; IR (THF): ν(NO): 1779 (m), 1718 (s) cm^{-1}. **Method 2.** A 100 mL Schlenk flask was charged with a solid mixture of 53 mg (0.1 mmol) of [(IMes)Fe(NO)$_3$][BF_4] and 10 mg (0.1 mmol) of NaBr. 20 mL of THF was added and the reaction was stirred for 15 min. The solvent was dried under vacuum and the solid product was washed with hexane (20 mL x 3) followed by dissolving in 25 mL of ether. The ether solution was filtered through celite and dried under vacuum and was redissolved in THF. Recrystallization was done in THF/hexane at -28 ºC; IR (THF): ν(NO): 1779 (m), 1718 (s) cm^{-1}

Synthesis of [Benzyl-Ni(bme-dach)][BF_4]. From the preparation technique of **(IMes)Fe(NO)$_2$Br** as described in method 1, the residue left in the Schlenk flask, after washing with ether, was dissolved in CH_3CN and filtered through celite. The solution was purged through a flash column with CH_2Cl_2/methanol. Recrystallization was done in CH_3CN/ ether at 5 ºC. Unfortunately X-ray quality crystals were not obtained from this reaction. ESI-MS^+: *m/z* 367.09 (Calc. for $[M]^+$, 367.08).

Synthesis of (IMes)Fe(NO)$_2$I. Method 1. A 100 mL Schlenk flask was charged with a solid mixture of 16 mg (0.1 mmol) of ethyl iodide and 78 mg (0.1 mmol) of **Ni-Fe'**. 20 mL of THF was added and the solution was heated to 40 ºC for 45 minutes. The completion of the reaction was monitored using IR spectroscopy. The solvent was dried under vacuum and the solid product was washed with hexane (20 mL x 3) followed by redissolving in 25 mL of diethyl ether. The ether solution was filtered through celite and was redissolved in THF. Recrystallization was done in THF/hexane at -28 ºC; IR (THF): ν(NO): 1780 (m), 1724 (s) cm^{-1}. **Method 2.** A 100 mL Schlenk flask was charged with a solid mixture of 53 mg (0.1 mmol) of [(IMes)Fe(NO)$_3$][BF$_4$] and 15 mg (0.1 mmol) of NaI. 20 mL of THF was added and the reaction was stirred for 15 min. The solvent was dried under vacuum and the solid product was washed with hexane (20 mL x 3) followed by dissolving in 25 mL of ether. The ether solution was filtered through celite and dried under vacuum ad was redissolved in THF. Recrystallization was done in THF/hexane at -28 ºC; IR (THF): ν(NO): 1780 (m), 1724 (s) cm^{-1}.

Synthesis of [Ethyl-Ni(bme-dach)][BF$_4$]. From the preparation technique of **(IMes)Fe(NO)$_2$I** as described in method 1, the residue left in the Schlenk flask, after washing with ether, was dissolved in CH_3CN and filtered through celite. The solution was purged through a flash column with CH_2Cl_2/methanol. Recrystallization was done in CH_3CN/ether at 5 ºC. ESI-MS$^+$: *m/z* 305.06 (Calc. for [M]$^+$, 305.07).

Reaction of Ni-Fe' with [Ph$_3$PAu(solv.)]$^+$. A 50 mL Schlenk flask, charged with a solid mixture of 49 mg (0.1 mmol) of Ph_3PAuCl and 19 mg (0.1 mmol) of $AgBF_4$, was dissolved in 20 mL CH_3CN and stirred for 20 minutes under dark. The mixture was

cooled down to -40 ºC and filtered through celite into a pre-cooled (-40 ºC) solution of 78 mg (0.1 mmol) of **Ni-Fe'** in 15 mL CH_3CN. The reaction was stirred for 15 min at -40 ºC. The solution was then filtered through celite. Recrystallization was done in CH_3CN/ether ; IR (CH_3CN) ν(NO) 1823 (m), 1756 (s) cm^{-1}.

Reaction of Co-Fe' with $[Ph_3PAu(solv.)]^+$ In a manner similar to above 80 mg (0.1 mmol) of **Co-Fe'** was used instead of of **Ni-Fe'**. Recrystallization was done in CH_3CN/ether ; IR (CH_3CN): ν(NO): 1823 (m), 1755 (s), 1672 (w), 1653 (w) cm^{-1}.

Reduction Reaction of Ni-Fe' with KEt_3BH. 78 mg (0.1 mmol) of **Ni-Fe'** was dissolved in 15 mL of THF. The solution was cooled to – 78 ºC. Using a degassed syringe 1 mL (0.1 mmol) of KEt_3BH (1 M in THF) was added to the pre-cooled solution. The color changed from reddish brown to green within a couple of minutes. The reaction was monitored with IR spectroscopy; IR (THF): ν(NO): 1664, 1620 cm^{-1}. Addition of 0.015 mL (0.1 mmol) of HBF_4•Et_2O to the same solution mixture formed reddish brown **Ni-Fe'**; IR (THF): ν(NO): 1792 (m), 1732 (s) cm^{-1}.

Experimental Details for Chapter VII

Synthesis 1 of $[(NO)Fe(N_2S_2)Fe(NO)_2][BF_4]$. A 100 mL Schlenk flask was loaded with 0.052 g (0.1 mmol) of $[Fe(bme\text{-}dame)]_2$ dimer and 0.107 g (0.2 mmol) of $[(IMes)Fe(NO)_3][BF_4]$ then dissolved with 25 mL of DCM. The reaction mixture was allowed to stir for 10 min then exposed to vacuum to obtain solids. The solids were washed with 15 mL (x 3) of diethyl ether then redissolved in CH_2Cl_2 to filter the product through a small column (1 x 4 cm) of celite. Isolated yield: 75%; IR (THF) ν(NO): 1809,

1779, 1743 cm^{-1}. The complex **[Fe-Fe*]**$^+$ was synthesized in a similar manner using 0.054 g (0.1 mmol) of $[Fe(bme\text{-}dach)]_2$ dimer and 0.107 g (0.2 mmol) of $[(IMes)Fe(NO)_3][BF_4]$. Isolated yield 80 %; IR (THF) ν(NO): 1796, 1761, 1742 cm^{-1}.

Synthesis 2 of [(NO)Fe(N_2S_2)Fe($NO)_2$][BF_4]. To a 100 mL Schlenk flask 0.052g (0.1 mmol) of $[Fe(bme\text{-}dame)]_2$ dimer, 0.092 g (0.2 mmol) of $[Fe(CO)_3NO][Na(18\text{-crown-}6)]$, and 0.047 g (0.4 mmol) of $[NO][BF_4]$ were loaded and dissolved with 25 mL freshly distilled dried THF. The reaction was allowed to stir for 8 hrs at room temperature and monitored through IR spectroscopy. The reaction mixture was dried under vacuum and washed with 15 mL (x 3) of ether. The solid product was redissolved with CH_2Cl_2 and filtered through a small column (1x4 cm) of celite. Isolated yield: 75 %; IR (THF) ν(NO): 1809, 1779, 1743 cm^{-1}. The CH_2Cl_2 solution of **[Fe'-Fe*]**$^+$ was layered with hexanes to yield dark brown X-ray quality crystals. The complex **[Fe-Fe*]**$^+$ was synthesized in a similar manner using 0.054 g (0.1 mmol) of $[Fe(bme\text{-}dach)]_2$ dimer, 0.092 g (0.2 mmol) of $[Fe(CO)_3NO][Na(18\text{-crown-}6)]$, and 0.047 g (0.4 mmol) of $[NO][BF_4]$. Isolated yield: 85 %; IR (THF) ν(NO): 1796, 1761, 1742 cm^{-1}.

Synthesis 3 of [(NO)Fe(N_2S_2)Fe($NO)_2$][BF_4]. A 50 mL Schlenk flask was charged with 0.052 g (0.1 mmol) of $[Fe(bme\text{-}dame)]_2$ dimer and excess NO_g. Stirring this solution mixture for 1 h results in the formation of a Roussin's Red Ester (RRE) as indicated by IR spectroscopy. To the solution of RRE, 0.023 g of $[NO][BF_4]$ was added under a high pressure of N_{2g} and allowed to stir for 2 h. The contents were evaporated to dryness under vacuum and washed with 15 mL (x 3) of ether. The product was then obtained by dissolving the solids with CH_2Cl_2 and filtering through a small packet (1 x 4

cm) of celite. Isolated yield: 80%. IR (THF) ν(NO): 1809, 1779, 1743 cm^{-1}. The complex **[Fe-Fe*]**$^{+}$ was synthesized in a similar manner using 0.054 g (0.1 mmol) of $[Fe(bme\text{-}dach)]_2$ dimer. Isolated yield: 85 %; IR (THF) ν(NO): 1796, 1761, 1742 cm^{-1}.

Synthesis 4 of [(NO)Fe(N_2S_2)Fe($NO)_2$][BF_4]. To a 50 mL Schlenk flask 0.029 g (0.1 mmol) of (NO)Fe(bme-dame), excess NO_g and moderate amount of O_{2g} was added. The solution mixture was dissolved with 25 mL of CH_2Cl_2 was added and stirred for 1 h. The mixture was evaporated to dryness and washed with 15 mL (x 3) of diethyl ether. The desired product was obtained by dissolving the solids with CH_2Cl_2 and filtering through a small packet (1 x 4 cm) of celite. Isolated yield: 36 %. IR (THF) ν(NO): 1809, 1779, 1743 cm^{-1}. The complex **[Fe-Fe*]**$^{+}$ was synthesized in a similar manner using 0.030 g (0.1 mmol) of (NO)Fe(bme-dach), and stirred for 4 h instead. Isolated yield: 35 %. IR (THF) ν(NO): 1796, 1761, 1742 cm^{-1}.

Synthesis 5 and 6 of [(NO)Fe(N_2S_2)Fe($NO)_2$][BF_4]. To a 50 mL Schlenk flask 0.029 g (0.1 mmol) of (NO)Fe(bme-dame) was added. For synthesis 5, 0.12 mL (0.1 mmol) of a 1.0 M reagent solution in CH_2Cl_2 of $[Et_3O][BF_4]$ was added with a syringe. For synthesis 6, 0.033 g (0.1 mmol) of $[Fc]^{+}[PF_6]^{-}$ was added under a high pressure of N_{2g}. From this point all post manipulations were the same for both. Starting materials were dissolved in 25 mL CH_2Cl_2 and stirred overnight. IR spectroscopy was used to verify completion of reaction. The contents were dried to solids by vacuum and washed with 15 mL (x 3). The products are then redissolved in CH_2Cl_2 and filtered through a small plug (1 x 4 cm) of celite. Synthesis 5's isolated yield: 18 %; synthesis 6's isolated yield: 12 %; IR (THF) ν(NO): 1809, 1779, 1743 cm^{-1}. The complex **[Fe-Fe*]**$^{+}$ was

synthesized in a similar manner using 0.030 g (0.1 mmol) of (NO)Fe(bme-dach) and 0.12 mL (0.1 mmol) of a 1.0 M reagent in CH_2Cl_2 of $[Et_3O][BF_4]$ or 0.033 g (0.1 mmol) of $[Fc]^+[PF_6]^-$ depending on the method used. Synthesis 5's isolated yield: 18 %; synthesis 6's isolated yield: 13 %; IR (THF) ν(NO): 1796, 1761, 1742 cm^{-1}.

Synthesis of (NO)Fe(bme-dame)•Fe(NO)$_2$, [Fe'-Fe*]^0. A 50 mL Schlenk flask was loaded with 0.050 g (0.1 mmol) of $[(NO)FeN_2S_2•Fe(NO)_2][BF_4]$ and dissolved with freshly distilled THF. The solution was cooled down to 0 ºC by placing the flask in an ice bath. 0.1 mL (0.1 mmol) of 1 M (THF) $KHBEt_3$ was added and stirred for 10 mins at 0 ºC. The reaction mixture turned green and was evaporated in vacuuo and washed with 15 ml (x 3) of cold diethyl ether. The solids were dissolved in cold CH_2Cl_2 and filtered through a small plug of celite (1 x 3 cm). Layering the CH_2Cl_2 solution of **[Fe'-Fe*]^0** with hexane yielded green X-ray quality crystals at -28 ºC; IR (THF) ν(NO): 1696, 1668, 1640 cm^{-1}.

Synthesis of [(NO)Fe(bme-dame)•Fe(NO)$_2$][K(18-crown-6)], [Fe'-Fe*]$^-$. The product **[Fe'-Fe*]$^-$** was synthesized in similar manner as **[Fe'-Fe*]^0** using 0.2 mL (0.2 mmol) of 1 M $KHBEt_3$ at -10 ºC instead of 0.1 mL and cold THF to filter through celite instead of CH_2Cl_2. Layering a THF solution of **[Fe'-Fe*]$^-$** with pentane produced dark-orange X-ray quality crystals at -28 ºC; IR (THF) ν(NO): 1667, 1637, 1607 cm^{-1}.

Experimental Details for Chapter VIII

Synthesis of (μ-pdt)[(CO)$_3$Fe^{I}Fe^I(CO)$_2$(NiN$_2$S$_2$)], 1a. A 100 mL long-necked Schlenk flask is charged with (μ-pdt)$[Fe_2(CO)_6]$ (0.153 g, 0.4 mmol) and NiN_2S_2 (0.110

g, 0.4 mmol). The Schlenk flask was then loaded to the glove box and Me_3NO (0.03 g, 0.4 mmol) was added to the flask. 15 mL of degassed THF was added and the solution was stirred for 1 h at 25 °C. The completion of the reaction was monitored with IR. The product was washed with hexane (3 x 15 mL) to remove unreacted starting materials. A fine powder of product was obtained by crashing it out using a mixture of hexane and dichloromethane (8:2). The product was redissolved in CH_2Cl_2. Layering a CH_2Cl_2 solution with hexane produced dark brown X-ray quality crystals at -28 ºC. IR (CH_2Cl_2) ν(CO): 2032, 1962, 1900 cm^{-1}.

Synthesis of (μ-dmpdt)[$(CO)_3Fe^IFe^I(CO)_2(NiN_2S_2)$], 1b. In a manner similar to **1a**, (μ-dmpdt)[$Fe_2(CO)_6$] (0.165 g, 0.4 mmol) and NiN_2S_2 (0.110 g, 0.4 mmol) were reacted in presence of Me_3NO (0.03 g, 0.4 mmol) for 1 h in THF. Layering a CH_2Cl_2 solution with hexane produced dark brown X-ray quality crystals at -28 ºC. IR (CH_2Cl_2) ν(CO): 2032, 1961, 1899 cm^{-1}.

Synthesis of (μ-NMe_3)[$(CO)_3Fe^IFe^I(CO)_2(NiN_2S_2)$], 1c. In a manner similar to **1a**, (μ-apdt)[$Fe_2(CO)_6$] (0.160 g, 0.4 mmol) and NiN_2S_2 (0.110 g, 0.4 mmol) were reacted in presence of Me_3NO (0.03 g, 0.4 mmol) for 1 h in THF. Layering a CH_2Cl_2 solution with hexane produced dark brown X-ray quality crystals at -28 ºC. IR (CH_2Cl_2) ν(CO): 2036, 1970, 1900 cm^{-1}.

Synthesis of (μ-pdt)[$(CO)_3Fe^I(Fe(NO))^{II}(IMe)(NiN_2S_2)]^+BF_4^-$, 2. A 100 mL long-necked Schlenk flask containing a magnetic stir bar is charged with (μ-pdt)[$Fe^I_2(CO)_5IMe$] (0.44 g, 0.97 mmol) and was dissolved in 10 mL CH_2Cl_2 and was

cooled to 0 ºC. A second Schlenk flask was loaded into the glove box and $[NO]BF_4$ (0.011 g, 0.1 mmol) and 18-Crown-6 (0.024g, 0.01 mmol) was added as solids. The mixture was dissolved in cold CH_2Cl_2 (10 ml). The temperature of the solution was also lowered to ~ 5 ºC in an ice-water bath. The second solution was stirred for 30 min and was transferred via a cannula under N_2 to the first solution and was stirred for an additional 30 min. The completion of the reaction was monitored with IR. The resulting dark-red solution was filtered over a bed of celite. The solution was dried under vacuuo and washed with hexane (3 x 10 mL) and diethyl ether (2 x 10 mL) to remove unreacted starting materials, under ice-cold conditions. The solution was dried under vacuuo to obtain a reddish-brown powder.[97] To the product, NiN_2S_2 (0.270 g, 0.1 mmol) was added as solid. 15 mL of CH_2Cl_2 was added to the solid mixture and was stirred for 20 min. The completion of the reaction was monitored with IR. The solution was dried under vacuuo and washed with hexane (3 x 10 mL) and diethyl ether (2 x 10 mL). A CH_2Cl_2 solution of the product was filtered over a bed of celite. Layering the CH_2Cl_2 solution with hexane produced dark brown X-ray quality crystals at -28 ºC. IR (CH_2Cl_2) ν(CO): 2056, 1990 cm^{-1}; ν(CO): 1740 cm^{-1}.

Synthesis of (μ-H)[(PMe$_3$)(CO)$_2$Fe^{II}Fe^{II}(CO)(PMe$_3$)(NiN$_2$S$_2$)]$^+$BArF$^-$, 3. A 100 mL long-necked Schlenk flask containing a magnetic stir bar is charged with (μ-pdt)[$Fe^{II}_2(CO)_4(PMe_3)_2]^+PF_6^-$ (0.0314 g, 0.05 mmol) and NiN_2S_2 (0.0138 g, 0.05 mmol). 15 mL of THF was added and the solution was stirred for 1 h at 25°C under white sun-lamp. The completion of the reaction was monitored with IR. The product was washed with hexane (3 x 10 mL) and diethyl ether (2 x 10 mL) to remove unreacted starting

materials. NaBarF (0.0443 g, 0.05 mmol) was added to a CH_2Cl_2 solution of the product and was stirred for 2 h. The solution was evaporated in vacuuo and was redissolved in THF. The THF solution was filtered over a bed of celite to remove insoluble $NaPF_6$. Layering the CH_2Cl_2 solution with hexane produced dark brown X-ray quality crystals at -28 ºC. IR (CH_2Cl_2) ν(CO): 2023, 1968, 1929.

Synthesis of (μ-H)[$(PMe_3)(CO)_2Fe^{II}Fe^{II}(CO)(PMe_3)(PPh_3)]^+PF_6^-$, 3-$PPh_3$. In a manner similar to **3**, (μ-pdt)[$Fe^{II}_2(CO)_4(PMe_3)_2]^+PF_6^-$ (0.0314 g, 0.05 mmol) and PPh_3 (0.0135 g, 0.05 mmol). 15 mL of THF was added and the solution was stirred for 30 min at 25°C under white sun-lamp. The anion exchange of PF_6^- with $BArF^-$ was not carried out for this synthesis. Layering the CH_2Cl_2 solution with hexane produced dark brown X-ray quality crystals at -28 ºC. IR (CH_2Cl_2) ν(CO): 2026, 1976, 1951 cm^{-1}.

CHAPTER III

HEMI-LABILE BRIDGING THIOLATES AS PROTON SHUTTLES IN BIO-INSPIRED H_2 PRODUCTION ELECTROCATALYSTS[#]

Introduction

Heterobimetallic molecular compositions utilizing thiolate-sulfurs as bridges are widespread in biology, especially in the active sites of metalloenzymes such as the [FeFe]- and [NiFe]-H_2ase and Acetyl CoA Synthase.[37, 72] That these biocatalysts facilitate organometallic-like transformations, using first- row/abundant transition metals, has inspired chemists to address the features that control their mechanisms of action through the synthetic-analogue approach.

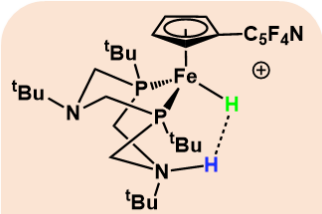

I

Figure III-1. P_2N_2 ligand supported (η^5-C_5H_4R)Fe^{II} showing H_2 activation in action.

[#]Major parts of this chapter were reproduced with permission from Ding, S.; Ghosh, P.; Lunsford, A. M.; Wang, N.; Bhuvanesh, N.; Hall, M. B.; Darensbourg, M. Y. *J. Am. Chem. Soc.*, **2016**, *138*, 12920-12927. Copyright **2016** American Chemical Society.
The theoretical calculations and their results described herein were computed by Dr. Shengda Ding and Prof. Michael B. Hall.
Dr. Allen M. Lunsford contributed equally in the electrochemical studies.

Synergy between synthesis and theory has developed by linking the mechanistic interpretation of assays, such as electrocatalytic proton reduction or hydrogen oxidation in the active sites of the hydrogenases, with those of the model complexes.[76] While the structures of individual components of the biocatalysts that are site-isolated by the protein are clear, functional reproductions in small molecule models have not been entirely successful. The role of a pendant amine base nearby an open site on iron was determined to be critical to the remarkable rates of hydrogen production in the [FeFe]-H_2ase[37] and has been successfully used to design H^+ reduction and H_2oxidation electrocatalysts in nickel-based complexes outfitted with the PNP- and P_2N_2-type ligands of Dubois, et al.[76, 102-106] Their team has also provided dramatic, *bona fide* examples of heterolytic H_2 cleavage products in $(\eta^5\text{-}C_5H_4R)Fe^{II}(P_2N_2)^+$ complexes, suggesting that the P_2N_2 ligand in Figure III-1, and its pendant base capabilities, might be considered as a surrogate for the $Ni(SR)_4$ metalloligand in the [NiFe]-H_2ase active site.[107-109] Thus, while the catalytic center of [NiFe]-H_2ase does not have a pendant amine as operative base, there is structural support from high resolution protein crystallography that a terminal cysteinyl thiolate on the nickel might serve in that capacity.[71, 110] Such a suggestion was made earlier in the mechanistic study of Niu and Hall.[111] Other persistent questions regarding the requirement of two metals in such active sites are as follows: Do they assist each other by dual electron storage? Does one tune the electronic character and redox potential of the other? Is a metallodithiolate biology's ultimate redox-active, non-innocent ligand?

There is an extensive class of bi- and polymetallic complexes derived from transition metals, largely Ni^{II}, in tetradentate $E_2S_2^{2-}$ (E = N, P, S) binding sites that use excess lone pairs on the cis thiolate sulfurs for binding in a bidentate manner to an additional metal, M'.[112-113] Analogous to the $(\eta^5\text{-}C_5H_4R)Fe^{II}(P_2N_2)^+$ complexes described above, myriad heterobimetallics have been reported in a developing area that uses η^5-cyclopentadienide ($\eta^5\text{-}C_5H_5$ or $\eta^5\text{-}C_5Me_5$, i.e., Cp and Cp*, respectively) or η^6-arenes bound to d^6 Fe^{II} or Ru^{II}, as M', which in combination with the bridging dithiolates from the NiN_2S_2 may offer a single open site for reactivity at M', Figure III-2.[112, 114-119]

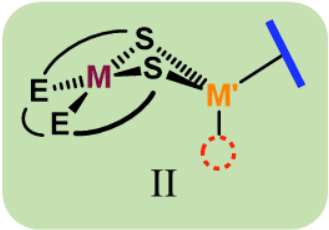

Figure III-2. $M(\mu\text{-}S)_2M'$ bimetallics displaying potential vacant site at M' for reactivity.

The tunability at the pi-ligand offers some control for oxidative addition in stoichiometric reactions, including both H_2 and O_2 activation.[120-123] Reports of proton reduction under electrochemical conditions by such $CpFe^{II}$ or $CpRu^{II}$ entities are scarce in the literature; however, there are examples of an S'_2NiS_2 (S' = thioether sulfur; S = thiolate sulfur) metalloligand bound to CpFe' and Cp*Fe' that demonstrated modest electrocatalysis and H_2 production.[115, 117] The MN_2S_2 platform offers opportunity to modify a metallodithiolate ligand by changing only the M, retaining consistency in steric features such that the S-donor and M'-acceptor effects might be deconvoluted. Thus, we have designed experimental and computational protocols to analyze the proton reduction

possibilities of the heterobimetallics represented in Figure III-2, with focus on the potential sites for electron and proton uptake, the order of their addition, and the requirements for hemi-lability and S-protonation of the MN_2S_2 metallodithiolate ligands at various redox levels.

Synthesis and Characterization

Figure III-3 displays the synthetic protocol used to prepare the bimetallic complexes, MN_2S_2•$CpFe(CO)^+BF_4^-$ (M=Fe(NO), Ni, the Fe in CpFe(CO) is Fe'), **Fe-Fe'**$^+$ and **Ni-Fe'**$^+$, in this work. The reaction of MN_2S_2 and $[CpFe(CO)_2(Solv)]^+$ or $[CpFe(CO)_2BF_4]$ prepared *in situ* from $CpFe(CO)_2I$ and $AgBF_4$ in CH_2Cl_2, at 22°C, formed an intermediate species MN_2S_2•$CpFe(CO)_2^+BF_4^-$, **Fe-Fe"**$^+$ and **Ni-Fe"**$^+$ (the Fe in $CpFe(CO)_2$ is Fe"). Subsequent photolysis released CO and permitted bidentate binding of the metallodithiolate ligands. While the intermediate species, **Fe-Fe"**$^+$ and **Ni-Fe"**$^+$, are light and air sensitive, the **Fe-Fe'**$^+$ and **Ni-Fe'**$^+$ complexes are isolated as intensely colored crystalline BF_4^-salts that are thermally and air stable in the solid form. Stringent conditions (CO pressure of 11 bar and 50°C) partially return the MFe'$^+$ to the MFe"$^+$. Figure III-4 shows the changes in the IR spectra for the conversion of **Ni-Fe'**$^+$ to **Ni-Fe"**$^+$.

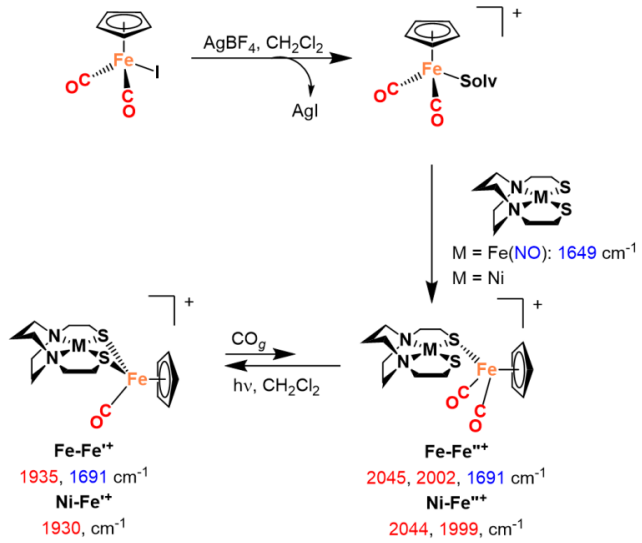

Figure III-3. The synthesis of **Fe-Fe'**$^{+}$ and **Ni-Fe'**$^{+}$ complexes as BF_4^- salts. The IR frequencies of CO and NO are in red and blue, respectively. The solvated species produced by addition of Ag^+ could also be a labile BF_4^- species.

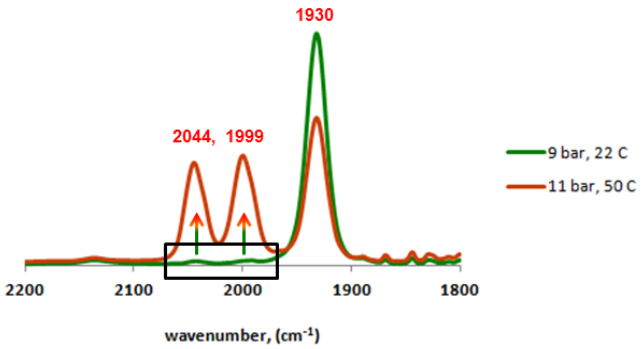

Figure III-4. IR spectra of a CH_2Cl_2 solution of **Ni-Fe'**$^{+}$ under a pressure of CO after heating for 19 hours. The peaks at 2044 cm^{-1} and 1999 cm^{-1} correspond to **Ni-Fe"**$^{+}$**.**

X-ray diffraction analysis of crystalline **Ni-Fe'**$^{+}$, **Fe-Fe'**$^{+}$, and **Ni-Fe"**$^{+}$ revealed molecular structures with typical piano-stool geometry about the $CpFe'(CO)^+$ unitand butterfly-like $[M(\mu\text{-}SR)_2Fe']$ cores in the **Ni-Fe'**$^{+}$ and **Fe-Fe'**$^{+}$ derivatives, Figure III-5.

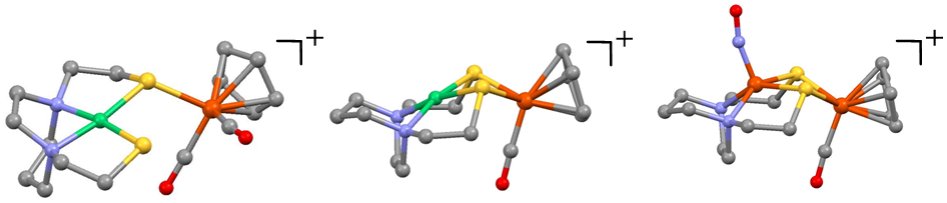

	Ni-Fe"+	Ni-Fe'+	Fe-Fe'+
M• • •Fe/Å	3.887 (2)	3.016 (1)	3.209 (1)
∠M-N-O/°	---	---	163.8 (3)
M-S/Å	2.172 (3)[a], 2.149 (3)[b]	2.152 (3)[c]	2.235 (1)[c]
Fe-S/Å	2.285 (3)[a], 3.999 (3)[b]	2.291 (3)[c]	2.285 (1)[c]
Hinge Angle/°	---	126.23	124.85

Figure III-5. Molecular structures of **Ni-Fe"**$^{+}$, **Fe-Fe'**$^{+}$, and **Ni-Fe'**$^{+}$ complexes. The BF_4^- ions are omitted for clarity; [a]bonded sulfur, [b]non-bonded sulfur, [c]average M-S distance.

Specifically, the bridging thiolate sulfur lone pairs impose a hinge angle (the intersection of the best N_2S_2 plane with the S_2Fe' plane) of ca. 125°. The mesocyclic diazacycloheptane framework in the MN_2S_2 portion of each provides similar N···N and S···S distances, and $\angle_{S-Fe'-S}$ of ca. 82°. In the **Fe-Fe'**$^{+}$ complex, the NO is transoid to the CO on the CpFe' unit; the$\angle_{Fe-N-O}$ angle is 163.8°. The M···Fe' distance in **Fe-Fe'**$^{+}$ and **Ni-Fe'**$^{+}$ are 3.203(1) and 3.016(1) Å, respectively. In contrast, the **Ni-Fe"**$^{+}$ dicarbonyl complex finds the NiN_2S_2 plane is shifted away from where it was in the **Ni-Fe'**$^{+}$, opening the Ni–S-Fe" bond angle to ca. 121.4(1)° from ca. 85.44(3)° in the **Ni-Fe'**$^{+}$, and yielding a Ni-Fe" distance some 0.7 to 0.9 Å greater than in the bidentate MN_2S_2-Fe' complex. The Fe"-S dative bond distance in **Ni-Fe"**$^{+}$ is 2.285(3) Å and the non-bonded thiolate S is at 3.999(3) Å from the Fe".

While the **Ni-Fe'**$^{+}$ complex is diamagnetic, the **Fe-Fe'**$^{+}$ has S = 1/2, consistent with the well-known $\{Fe(NO)\}^7$ electronic configuration.[77, 124] The 298 K, X-band EPR

spectrum, shows an isotropic triplet of *g* value = 2.04, with hyperfine coupling constant of 15.3 G, and only minor differences to the free metalloligand.[74] The low field Mössbauer spectra of the **M-Fe'**$^{+}$ complexes are presented in Figure III-6. The Mössbauer spectra were recorded by Dr. Codrina Popescu from Colgate University, USA.

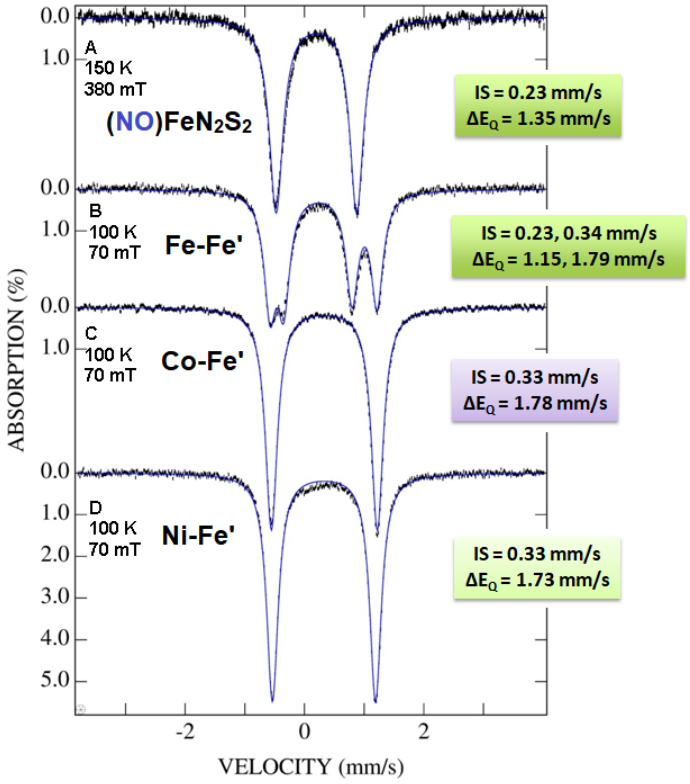

Figure III-6. Low field Mossbauer studies of (NO)FeN_2S_2, **Fe-Fe'**$^{+}$, **Co-Fe'**$^{+}$, and **Ni-Fe'**$^{+}$ complexes. Note: Details of the synthesis and characterizations of **Co-Fe'**$^{+}$ is shown in Chapter IV.

Electrochemistry

The same description of the electrochemical studies of complexes **Fe-Fe'**$^{+}$, and **Ni-Fe'**$^{+}$, is in the dissertation of Dr. Allen M. Lunsford. Cyclic voltammograms (CV) of

BF_4^- salts of **Fe-Fe'**$^+$, and **Ni-Fe'**$^+$, were recorded at 22° C under Ar. All scans are referenced to internal $Fc^{0/+}$ at $E_{1/2}$ = 0.0 V. Full scans of both complexes were initiated in the negative direction, Figure III-7. On initiating the electrochemical scan in the cathodic direction, two reduction events, and, upon reversal, two oxidation events were observed for both complexes within the CH_3CN solvent window. The initial reductive event, at -1.64 V in the case of the **Ni-Fe'**$^+$, is assigned to the $Ni^{II/I}$ couple; its irreversibility is addressed in the computational section below.

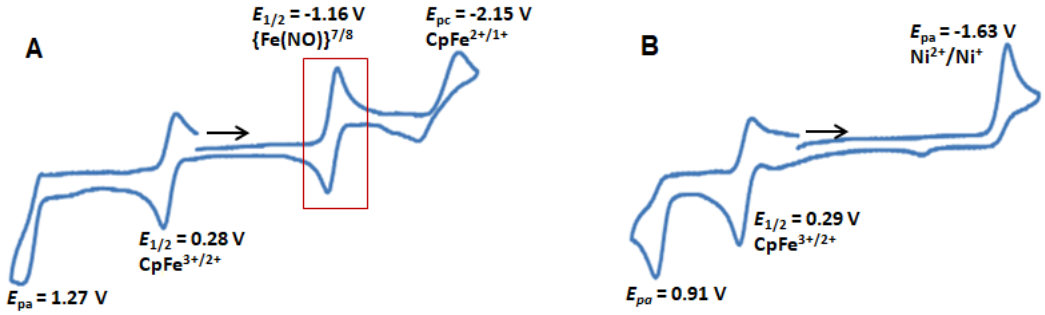

Figure III-7. Cyclic voltammograms of **Fe-Fe'**$^+$ (A) and **Ni-Fe'**$^+$ (B) recorded at 200mV/s in CH_2Cl_2 referenced vs $Fc^{0/+}$.

In contrast, for the **Fe-Fe'**$^+$ complex, the first reduction is quasi-reversible and at a more positive position, -1.19 V; it is assigned to the $\{Fe(NO)\}^{7/8}$ redox couple. In both cases, the first observed or more positive reduction event is anodically shifted compared to the MN_2S_2 (free metalloligand) precursors, thus illustrating the electron-withdrawing nature of the $[CpFe'(CO)]^+$ unit and its ability to modulate redox events on the MN_2S_2 unit.[77, 125] The second, more negative, irreversible reduction event in the **Fe-Fe'**$^+$ complex is assigned to the $Fe'^{II/I}$ couple in the $[CpFe'(CO)]^+$ unit. For the **Ni-Fe'**$^+$ complex, assignment of the more negative event is not straight-forward due to the

irreversibility of the previous redox event; computational studies, *vide infra*, indicate an intramolecular Ni^{I} to Fe^{II} electron transfer concomitant with structural rearrangement accounts for this irreversible behavior.

Addition of trifluoroacetic acid (TFA) to the electrochemical cell containing **Ni-Fe'**$^{+}$or **Fe-Fe'**$^{+}$ increases the current of the initial reduction events described above. [Methanesulfonic acid gave similar results as TFA, however considerable fouling of the electrode surface discouraged extensive studies with this acid.]

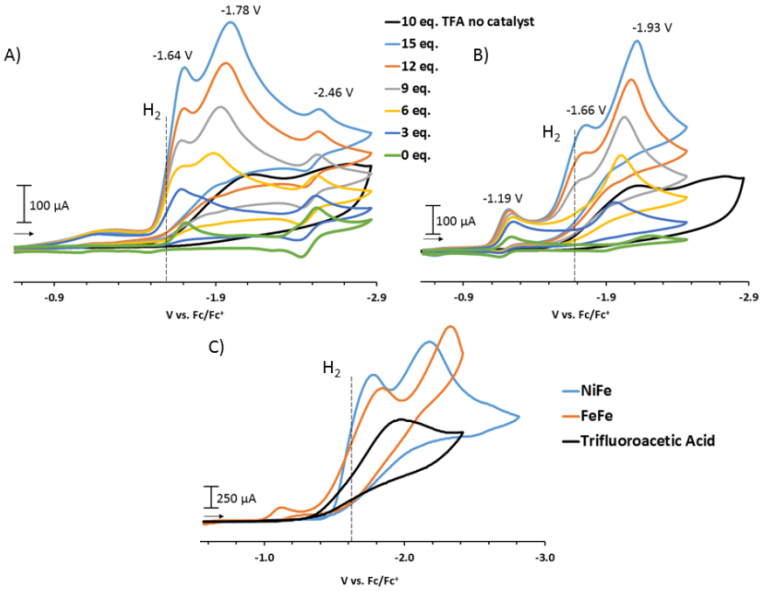

Figure III-8. CV of 2 mM A) **Ni-Fe'**$^{+}$ and B) **Fe-Fe'**$^{+}$ under Ar in CH_3CN solutions containing 0.1 M [$^{t}Bu_4N$][PF_6] as supporting electrolyte with addition of equivalents of trifluoroacetic acid. C) An overlay of **Ni-Fe'**$^{+}$and **Fe-Fe'**$^{+}$ in the presence of 50 equivalents of TFA as well as 50 equivalents of TFA in the absence of either catalyst. The dotted line denotes the potential applied during bulk electrolysis, -1.56 V.

For the **Ni-Fe'**$^{+}$ complex, this current continues to increase with additional equivalents of TFA, Figure III-8A, while for the **Fe-Fe'**$^{+}$ complex the initial reduction event's current is saturated after addition of 12 equiv. of TFA, Figure III-8B. With

greater than 6 equiv. of TFA, a new peak at -1.66 V appears for the **Fe-Fe'**$^{+}$ complex and its intensity increases with additional equiv. of TFA. An overlay of both complexes after addition of 50 equiv. of TFA as well as TFA in the absence of either catalyst is displayed in Figure III-8C. The large current enhancement was attributed to the catalytic production of H_2, which was quantified by bulk electrolysis studies described below.

From the CV experiments, turnover frequencies (TOFs) of 69 s^{-1} and 52 s^{-1} (experimental barriers: 14.9 and 15.1 kcal/mol at 298.15 K by Eyring equation) and overpotentials of 938 mV and 942 mV for the **Fe-Fe'**$^{+}$ and **Ni-Fe'**$^{+}$ complexes respectively, were obtained.[98, 100, 126] The calculation of TOFs and overpotentials follows the approach described by Helm, Appel, and Wiese, see the Table II-1 and 2 for specifics.[98-99] It is noteworthy to mention the observed barrier is a comprehensive parameter reflecting the activation of electron transfer, proton transfer and intra-/inter-molecular processes throughout the catalytic cycle. It is often higher than the calculated barriers of intramolecular processes, *vide infra*. The H/D kinetic isotope effects on **Fe-Fe'**$^{+}$ and **Ni-Fe'**$^{+}$ turnover frequencies (k_H/k_D) were determined to be 1.46 and 1.56, respectively, Table II-1 and 2. While k_H/k_D isotope effects are known to vary widely, these relatively low ratios are consistent with the likely involvement of metal-hydride species in the catalytic cycles.[127-128]

Electrocatalytic H_2 Production

The headspace of the bulk electrolysis setup was analyzed for H_2 using gas chromatography after applying a constant potential at -1.56 V (dotted line, Figure III-8)

in the presence of catalyst and 50 equivalents of TFA. Due to the overlap of the background TFA peak and the catalytic peaks, the H_2 evolving from the acid itself must be deducted, Figure III-8 and Tables II-1 and 2. All values obtained are an average of three separate bulk electrolysis experiments. After 30 min of electrolysis with the **Ni-Fe'**$^+$ catalyst, 0.98 ± 0.04 Coulombs (after acid subtraction) was passed through the solution resulting in a turn-over-number (TON) of 0.26 ± 0.01 with a Faradaic efficiency of 96.0 ± 2.9 % for H_2 production. Similarly in the presence of the **Fe-Fe'**$^+$ catalyst, passage of 1.29 ± 0.06 Coulombs through the solution gave a TON of 0.33 ± 0.02 with a Faradaic efficiency of 77.2 ± 7.9 % for H_2. The specifics for the calculation of TON are in the supporting information (SI) of Ding, *et al*., *J. Am. Chem. Soc*., **2016**, *138*, 12920−12927. These results confirm that the current enhancement in the cyclic voltammogram is in fact due to the reduction of protons to H_2 by the **Ni-Fe'**$^+$ and **Fe-Fe'**$^+$ catalysts in the presence of TFA.

Computational Investigation (Dr. Shengda Ding and Prof. Michael B. Hall)

From computational studies described in the Ding, *et al*., *J. Am. Chem. Soc*., **2016**, *138*, 12920−12927 paper and also in the dissertation of Dr. Shengda Ding, full mechanistic pathways were determined. These are summarized in Figures III-9 and 10 and in the write-up that follows. The intricacies of the cyclic voltammograms, in the presence of added trifluoroacetic acid, of the **Ni-Fe'**$^+$ or **Fe-Fe'**$^+$ complexes, indicate the existence of protonated and/or rearranged species. Computational studies were done to correlate events in electrocatalysis with E of a redox process and pK_a of the added acid. A minimum of two chemical steps (C steps, *i.e.*, protonation) and two electrochemical

steps (E steps, *i.e.*, reduction) is required to produce H_2 from protons and electrons; they often take place in an alternating order to prevent the accumulation of charges.[58, 129-130] To computationally predict the E and C steps in the catalytic process, the redox potentials (E^0 vs. $Fc^{+/0}$) and relative acidities ($\Delta pK_a = pK_a(CatH) - pK_a(CF_3COOH)$) of components were predicted by calculations. Detailed methodology information and optimized geometries (*xyz* files) are deposited in the SI of Ding, *et al.*, *J. Am. Chem. Soc.*, **2016**, *138*, 12920−12927.

The bimetallic constitution of **Fe-Fe'**$^+$ and **Ni-Fe'**$^+$ complexes, enables them to buffer electrons, which can be additionally stabilized by the non-innocent ligands, particularly NO in the case of **Fe-Fe'**$^+$.[74] Typically after reduction(s), a complex should accept a proton, convert it into a hydride bound to the metal, followed by reaction with an additional proton, located on some basic site, to yield H_2. Our model complexes, however, lack a built-in pendant base or terminal thiolates to serve as a proton reservoir, as found in the bridgehead amine and a terminal thiolate in active sites of [FeFe]-[37, 130-133] and [NiFe]-H_2ase,[37, 71, 110] respectively. Instead, one of the two Fe'-S bonds in **Fe-Fe'**$^+$ and **Ni-Fe'**$^+$ may dissociate, showing features of hemi-lability; the isolation of such a mono-dentate thiolate bound species, **Ni-Fe"**$^+$, supports this argument, Figure III-3. Such a bond-cleavage generates reactive sites on S and Fe'; *i.e.*, a Lewis acid-base pair is created for proton and hydride binding, respectively. The possibility of converting a bridging thiolate into a proton-capturing base was inspired by early theoretical studies of the [FeFe]-H_2ase.[58, 134]

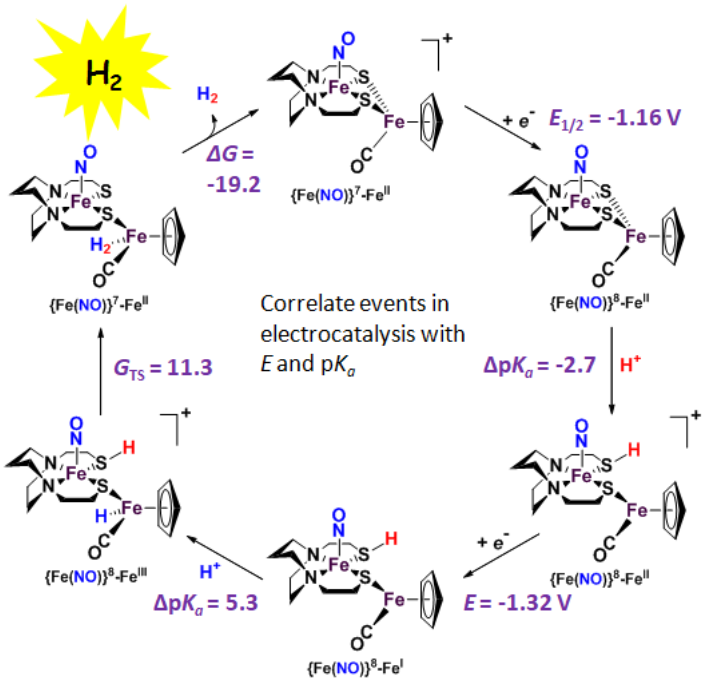

Figure III-9. The simplified calculated electrocatalytic cycle for H_2 production on **Fe-Fe'**$^+$ in the presence of TFA. The relative Gibbs free energies are provided in kcal/mol and the reference point (G = 0) resets after every reduction or protonation. The redox potentials (E) are reported in V with reference to the standard redox couple $Fc^{+/0}$ and the relative acidities (ΔpK_a) are reported with reference to TFA. Note: The two electron catalytic cycle is shown here. For a detailed mechanistic cycle please refer Ding, *et al.*, *J. Am. Chem. Soc.*, **2016**, *138*, 12920−12927.

The advent of semi-synthetic approaches to biohybrids in recent years, [FeFe]-H_2ase has established the pivotal role of this pendant base in proton transfer, thus negating the requirement for Fe-S bond cleavage in such functionalized dithiolates.[135-138]

The calculated electrocatalytic cycles with **Fe-Fe'**$^+$ and **Ni-Fe'**$^+$, for H_2 production, are shown in Figures III-9 and 10, respectively. The cyclic voltammogram of **Fe-Fe'**$^+$ in absence of added acid, shows two reduction events. A reversible redox couple at -1.19 V (calcd. -1.11 V) is assigned for $\{Fe(NO)\}^{7/8}$-Fe'^{II}. The neutral **Fe-Fe'**, formed

after 1 e^- reduction, has a linear triplet $\{Fe(NO)\}^8$ moiety, formed by antiferromagnetic coupling of high spin Fe^{II} with high-spin NO^-.[74, 139] Further irreversible reduction, calculated at - 1.99 V (exp. - 2.07 V), to **Fe-Fe'**$^-$, leads to one S-Fe' bond dissociation. The added electron is accommodated by the Fe' with a final redox level of $\{Fe(NO)\}^8$-Fe'^I.

Sequential addition of TFA showed a slight increase in the cathodic current at the first reduction event at -1.19 V without shifting position; this response was saturated after ~12 equivalents of TFA. This phenomenon can be explained by the reaction of TFA with the one e^- reduced **Fe-Fe'** state and its depletion, thus enhancing diffusion of **Fe-Fe'**$^+$ into the double layer at the electrode. Calculations suggested possible H^+ binding sites to the the S and the N of Fe(NO). Protonation at Fe(NO) would result in HNO formation that would be thermodynamically non-productive for H_2 production. Hence according to calculations S was the thermodynamically favorable protonation site in a productive catalytic cycle. Protonation on the latter, leads to an immediate Fe'-S bond cleavage, that stabilizes the system by 3.7 kcal/mol. Although the ΔpK_a (vs. TFA) is negative, indicating slightly unfavorable thermodynamic processes, the excess acid drives the protonation of **Fe-Fe'**. This phenomenon can be observed by the saturation of current enhancement at -1.19 V after addition of multiple equivalents (> 12 equiv.) of acid. The possibility of second protonation can also be ruled out based on this observation. Despite the initial increase in current response, this is not catalytic as at this reduction potential, the system is not suffucuently basic to bind a second proton.

The appearance of a second current enhancement at -1.66 V, suggests formation of a new species, **Fe-Fe'-S^{UP}H$^+$**, generated by protonation. As formation of this species is energetically unfavorable, the reduction event of **Fe-Fe'-S^{UP}H$^+$**, is only observed with the presence of more than 6 equiv. of TFA. The calculated reduction potential of **Fe-Fe'-S^{UP}H$^+$** is -1.32 V, converting the Fe^{II} of Fe' to Fe^{I}. Calculations suggest the reduced product, **Fe-Fe'-S^{UP}H** (G = 1.4 kcal/mol) may transform into a hydride-bearing species **Fe-Fe'H** (G = 1.7 kcal/mol) via the S-H inversion species **Fe-Fe'-S^{DN}H** (G = 0 kcal/mol) passing through two low-lying transition states (G = 4.2 and 7.6 kcal/mol). The **Fe-Fe'H** species shows a {Fe(NO)}^{8}-Fe'^{III} redox level, as the electrons are transferred from the reduced iron forming the iron-hydride.

The second proton addition follows two pathways shown in Figure III-9. The protonation step, either on S of **Fe-Fe'H** or on Fe' of **Fe-Fe'-S^{DN}H**, produces the same thiol-hydride, **Fe-Fe'H-S^{DN}H$^+$**. Both protonations are thermodynamically favored, with ΔpK_a values of 6.6 or 5.3 kcal/mol, respectively. The hydride-proton spatial positioning on **Fe-Fe'H-S^{DN}H$^+$** allows coupling of the two over a barrier of G = 11.6 kcal/mol. The resulting H_2 σ-complex **Fe-Fe'H$_2^+$** traverses another barrier of G = 12.0 kcal/mol to dissociate H_2 and regenerate the catalyst **Fe-Fe'$^+$**. Thus, this catalytic cycle that uses sulfur as proton relay, closes with an [ECEC] mechanism.

According to calculations, the possibility that TFA may directly provide H^+ to the hydride of **Fe-FeH'** via an intermolecular pathway to generate **Fe-FeH$_2^+$**, is not possible as a relatively high barrier of 16.2 kcal/mol is required to accomplish this step. Interestingly, delivery of proton from the sulfur requires a negligible barrier.

Addition of a third e^- to **Fe-Fe'H-S^{DN}H$^+$**, at a redox potential of - 1.27 V lowers the barrier for H_2 formation significantly to 4.9 kcal/mol (refer Ding, *et al.*, *J. Am. Chem. Soc.*, **2016**, *138*, 12920−12927 for full computational analysis). In this case the catalytic cycle closes as an E[CECE] regenerating the reduced **Fe-Fe'**, instead of **Fe-Fe'$^+$**. In this catalytic cycle the first reduction event essentially serves as an activation step. According to the calculations, the current enhancement associated with the second reduction event at -1.32 V (calcd; observed at -1.66 V) is considered to be catalytic and productive in either the slow or fast catalytic cycle as subsequent reduction events are all calculated to be less negative than -1.32 V.

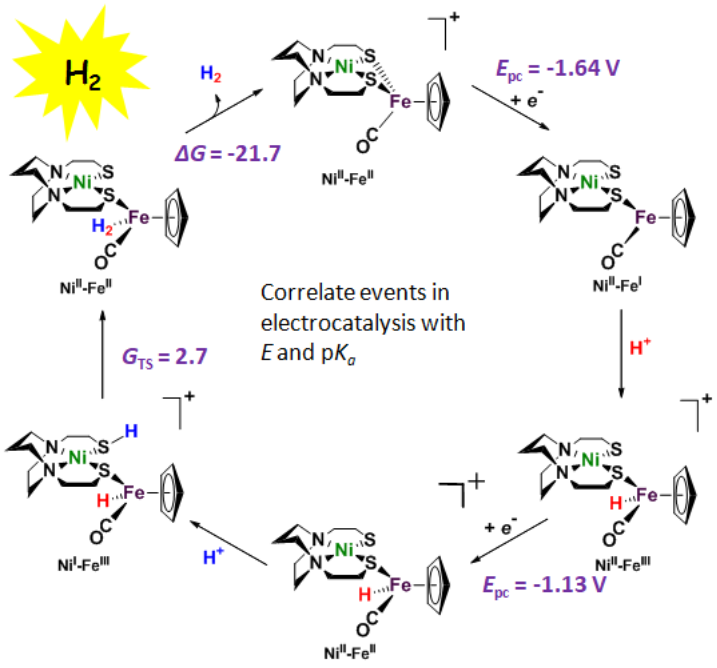

Figure III-10. The simplified two electron calculated electrocatalytic cycle for H_2 production on **Ni-Fe'$^+$** in the presence of TFA. For a detailed mechanistic cycle please refer Ding, *et al.*, *J. Am. Chem. Soc.*, **2016**, *138*, 12920−12927.

The catalytic cycle of **Ni-Fe'**$^{+}$ shows similar mechanistic features to that of **Fe-Fe'**$^{+}$ with a few exceptions, Figure III-10 (refer Ding, *et al.*, *J. Am. Chem. Soc.*, **2016**, *138*, 12920−12927 for full computational analysis). The first e^- is added on the NiN_2S_2 moiety of the **Ni-Fe'**$^{+}$ complex similar to that of **Fe-Fe'**. As the four-coordinate nickel in NiN_2S_2 lacks electronic buffering capability, unlike (NO)Fe in **Fe-Fe'**, the added electron resides on the antibonding d_{x2-y2} orbital of nickel as it is reduced to Ni^{I}-Fe'^{II} in **Ni-Fe'***. Hence, the calculated redox potential is significantly high -2.00 V (exp. -1.64 V). This leads to the opening of the $Ni(\mu\text{-}SR)_2Fe'$ core via Fe'-S bond dissocition. The destabilized e^- on Ni^{I} is readily transferred to the unsaturated (16-e^-) Fe' resulting in electron counts to a 16-e^- Ni^{II} and a 17-e^- Fe'^{I}. This configurational rearrangement stabilizes the monodentate species, **Ni-Fe'**, by 1.0 kcal/mol, accounting for the observed electrochemical irreversibility. Experimentally an IR shift of -157 cm^{-1}, upon the reduction of **Ni-Fe'**$^{+}$, confirms **Ni-Fe'** (calc'd shift: -127 cm^{-1}) to be the reduced product, see supporting information (SI) of Ding, *et al.*, *J. Am. Chem. Soc.*, **2016**, *138*, 12920−12927.

In the absence of acid, the second reduction on **Ni-Fe'** places the electron again undergoes a $Ni^{II/I}$ reduction. According to calculations the first redox potential is more negative compared to any subsequent steps in the catalytic cycles in the presence of TFA. The CV current enhancement at -1.64 V is thus catalytic, Figure III-10. The protonation on **Ni-Fe'** goes directly to the reduced Fe' to form a Fe^{III}-hydride, as the Fe'^{I} has sufficient electron density compared to the free thiolate. The following mechanistic steps are similar to those of **Fe-Fe'**$^{+}$, Figure III-9. The **Ni-Fe'**$^{+}$ may also have two

working catalytic cycles, either [ECEC] or E[CECE] depending on the requirement of a third electron addition step, which might be non-mandatory. The homoconjugation of TFA was taken into consideration by calculations.[140-141]

In case of the monodentate **Ni-Fe"**$^{+}$, reduction should break its single Fe-S bond, following similar mechanistic steps as that of **Ni-Fe'**$^{+}$. This phenomenon is experimentally observed. The cleaved fragment is a •$FeCp(CO)_2$ radical, that also shows catalytic H_2 production, before fast dimerization and subsequent deactivation.[142]

Discussion

An extensive discussion (see ref. Ding, *et al.*, *J. Am. Chem. Soc.*, **2016**, *138*, 12920−12927 for details) of the analysis of electrochemical events, with pK_a and electrode potential (E) is summarized. Salient features regarding the mechanistic analysis of the two $[MN_2S_2•CpFe(CO)]^+$ electrocatalysts are as follows:

The initial electron uptake takes place at the M in the MN_2S_2 of the bimetallic complex, rather than the $CpFe'(CO)^+$. In case of the $[(NO)FeN_2S_2•CpFe(CO)]^+$ complex, the $\{Fe(NO)\}^7$ provides a rather soft delocalized site for the added electron, preventing a subsequent Fe-H formation, as the iron is not sufficiently basic. The added electron is seemingly held at the $\{Fe(NO)\}^8$ unit, within the $(NO)FeN_2S_2$ metalloligand. This is observed throughout the catalytic cycle making it a rather "redox-active, spectator ligand"[143] compared to the CpFe(CO) unit, the reactive center, in the preferred E[CECE] path. While in $[NiN_2S_2•CpFe(CO)]^+$ complex, the initially reduced $Ni^{I}N_2S_2$ transfers its electron readily to the CpFe(CO) unit, with a concomitant Ni^{II}-(μ-SR)$_2$-Fe'^{I} ring opening

or Fe'-S bond cleavage, prior to protonation. Thus, the Ni^{II} in the NiN_2S_2 metalloligand of the monodentate bimetallic cannot bind a proton to form a Ni-H bond. This is in contrary to the recent NMR characterized Ni-bound hydride by Artero *et al.*,[144] that contained a non-innocent Ni bound bipyridyl (bipy) ligand to delocalize the added electron.[144] Moreover, the Fe in $(NO)FeN_2S_2$, is also shielded from protonation by the relatively basic sites on S and reduced Fe'.

The optimal orientation of the hydride and protonated thiolate provides guidance for the importance of the doubly reduced or triply reduced species in the catalytic cycle. Thus the H^+---H^- distances in our calculated diprotonated intermediates can be compared with the experimental data from the doubly protonated $P_2N_2FeCpR(CO)$ complex of Liu, *et al.*,[107] Figures III-1 and 11. The H^+---H^- distance in the **Fe-Fe'H-S^{DN}H** form is calculated to be 1.486 Å, which is surprisingly similar to that found in the amine pendant base $P_2N_2FeCpR(CO)$ complex (1.489 Å). The third reduction of **Fe-Fe'H-S^{DN}H$^+$** shortens the H^+---H^- distance from 2.634 Å to 1.486 Å via structural shifts in the $Fe(NO)N_2S(SH)$ metalloligand, involving both a rotation around the Fe'-S bond as well as a small change in the τ parameter[145]. These changes orient the proton-hydride pair into a close proximity, creating an early transition state according to Hammond's postulate,[146] amenable for H_2 elimination via the E[CECE], low barrier path. Note that the H^+---H^- coupling distance in the Fan and Hall calculated mechanism for proton reduction in the [FeFe]-H_2ase active site is 1.472 Å, remarkably consistent with the experimental value from Figure III-1.[128] In contrast the doubly reduced species holds the H^+---H^- distance at 2.634 Å, followed by H^+/H^- coupling, surmounting a high barrier, following the [ECEC]

mechanistic path. Interestingly, the proton/hydride pair, recently characterized in the ultra-high resolution crystal structure of Ni-R state in the [NiFe]-H_2ase catalytic cycle active site shows a H^+---H^- distance of 2.45 Å,[71] a distance related to the two e^- reduced intermediate in our slow route for H_2 production.

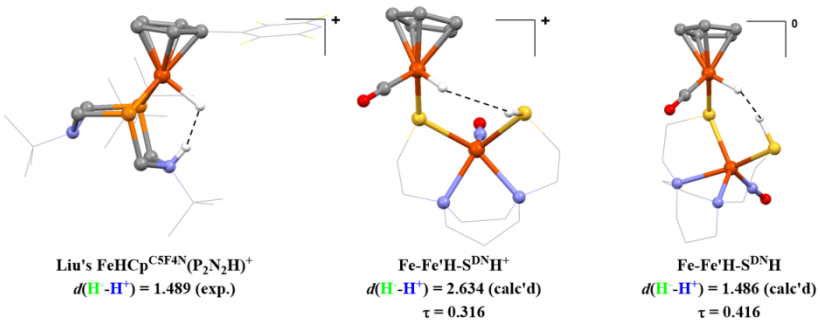

Figure III-11. Species featuring proximate proton-hydride pairs and the comparisons of H^+-H^- distances. The τ value, a measure of square pyramid ($\tau = 0$) vs. trigonal bipyramid ($\tau = 1$) geometry in the $Fe(NO)N_2S_2$ unit.

Conclusion

The well-studied P_2N_2 ligand of Dubois, *et al.*[102] has control of optimal proton placement via the chair/boat interconversion of the six-membered FeP_2C_2N cyclohexane-like ring described in Figure III-1,[107] a feature that was exploited in the design and development of further generations of the $Ni(P_2N_2)_2$ catalyst(s) and presaged by Nature's azadithiolate bidentate bridging ligand in the [FeFe]-H_2ase active site.[37] The heterobimetallics explored herein demonstrate the possibility for very stable bidentate ligands based on metallodithiolates (a metal-tamed S-donor or nature's version of a phosphine P-donor) that respond to an electrochemical event by switching a coordinate

covalent bond into a Lewis acid-base pair and concomitantly placing a proton and hydride within an optimal coupling distance. Easily accessible molecular motions and coordination sphere distortions are available to render the tethered thiolate into a pendant base of greater activity for proton delivery to the metal-hydride. The opportunities for tuning catalysts according to this approach lie both on the metal responsible for the hydride activity and, as we have also shown, the metal that holds and orients the pendant base. Our future plans are to optimize the catalysts via the bidentate S-M-S angle and to pursue experimental evidence for the thiol-hydride pair.

CHAPTER IV

COMPLEXES OF MN_2S_2•Fe(η^5-C_5R_5)(CO) AS PLATFORM FOR EXPLORING COOPERATIVE HETEROBIMETALLIC EFFECTS IN HER ELECTROCATALYSIS[#]

Introduction

Synthetic approaches to small molecule models of the active sites [FeFe]-, [NiFe]-hydrogenases[37] and Acetyl CoA synthase (ACS)[72-73] and potential heterobimetallic catalysts have exploited the mono/bidentate binding possibilities of metallodithiolates, particularly MN_2S_2, in development of a number of structural and functional analogues.[56, 144, 147-149] In particular, the π^* interaction resulting from filled Ni_d-S_p orbital contacts in square planar NiN_2S_2 or NiS'_2S_2 (S' = thioether) complexes, promote the nucleophilic reactivity of cis-dithiolate sulfurs including specific metal aggregation via mono-dentate or bidentate binding.[113, 150] The ability of the N_2S_2 tetradentate ligand to securely bind a variety of metals, including the redox active $\{Fe(NO)\}^{7/8}$ and $\{Co(NO)\}^{8/9}$ units (Enemark Feltham notation[151]), encourages explorations of redox cooperativity between MN_2S_2 donors and receivers. Various receiver units such as $\{Fe(NO)_2\}^{9/10}$, as well as Fe^{II} or Ru^{II} bound to η^5-C_5R_5 (where R = H, CH_3) or η^6-arenes have been used in this rapidly growing area of bioinspired heterobimetallics.[114-119, 122, 152-156]

[#]Reproduced by permission of The Royal Society of Chemistry from Ghosh, P.; Quiroz, M.; Wang, N.; Bhuvanesh, N.; Darensbourg, M. Y., *Dalton Trans.* 2017, ***46***, 5617-5624.

Especially notable are the NiN_2S_2 derivatives of $(\eta^6\text{-arene})Ru^{II}$ or $[P(OR)_3]_3Fe^{II}$ from the Ogo group which demonstrated impressive heterolytic splitting of H_2 in aqueous or methanol media, generating a bridging hydride.[112, 157] Replacement of the neutral methyl-substituted arenes on such Ni-Ru/Fe complexes with anionic $\eta^5\text{-}C_5Me_5$, Cp*, showed oxidative addition of O_2, resulting in $\eta^2\text{-}O_2^{2-}$ derivatives of Ru^{IV}/Fe^{IV} complexes that were isolated and characterized.[121, 123, 153, 158-159] Thus subtle modulations in the electronic features of the model complexes lead to unique organometallic chemistry that exploits a wide range of electrochemical potentials.

Recent studies from our laboratory of MN_2S_2 (M = Ni^{2+}, $[Fe(NO)]^{2+}$) bound to $[(\eta^5\text{-}C_5H_5)Fe'(CO)]^+$, demonstrated electrocatalytic HER (hydrogen evolution reactivity) in the presence of trifluoroacetic acid (TFA). A computation-based approach for

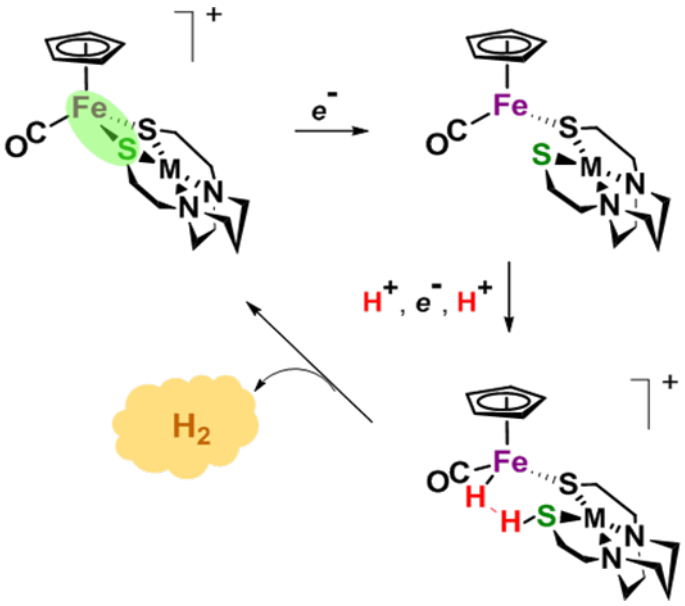

Figure IV-1. Salient features in the computationally proposed mechanistic path for electrocatalytic H_2 production catalyzed by MN_2S_2•$[Fe(\eta^5\text{-}C_5H_5)(CO)]^+$ as catalyst.[160]

assignment of the electrochemical events suggested that reduction-induced, iron-sulfur bond cleavage, *i.e.*, the hemi-lability of the N_2S_2 metalloligand,[161] should be a key step in the HER mechanism.[160] *That is, in such complexes that do not have an open site on the metal envisioned as an electron/proton landing site for conversion to a hydride, nor a pendant base for positioning a proton, the hemi-lability of a metallodithiolate may be invoked to provide both needed components for the heterolytic H^-/H^+ coupling coupling to make dihydrogen,* Figure IV-1. The consequence of exchange of η^5-C_5H_5 with the electron rich η^5-C_5Me_5 unit, generating the $(\eta^5$-$C_5Me_5)Fe(CO)^+$ receiver group for the bidentate metallodithiolate ligand, might be anticipated as follows: Expected for hemi-lability, the $M(\mu$-$SR)_2Fe$' ring opening should be enhanced by the additional electron richness, thus more easily generating the open sites on sulfur and on Fe'. The proton affinity of the available thiolate sulfur could be enhanced, although likely not by much. Most debatable is the reduction potential of the Fe', which in the $(\eta^5$-$C_5Me_5)$ derivative is expected to be more negative and hence increase the overpotential for the overall reaction. However the enhanced proton affinity at the Fe', coupled with the proximal thiolate S-H orientation that yields the optimal H^+/H^- coupling distance might compensate for the overpotential. These are questions to be addressed, beginning with the synthesis of complexes with MN_2S_2 metallodithiolate ligands bound to $[(\eta^5$-$C_5R_5)Fe(CO)]^+$ (R = H, CH_3; Cp and Cp*, respectively). Herein we report the synthesis and characterization of a set of such bimetallics, emphasizing their structural and electronic properties for assessing features of significance to electrocatalysis of the hydrogen evolution reaction.

Synthesis and Characterization

Similar to published reports,[115, 117, 144, 160] the preparation of heterobimetallic complexes, $[MN_2S_2•FeCp(CO)]^+[BF_4]^-$ and $[MN_2S_2•FeCp^*(CO)]^+[PF_6]^-$, (M = Ni, [Co(NO)]) is readily accomplished by thermal and photochemical displacement of CO as shown in Figure[118-119] 1V-2.

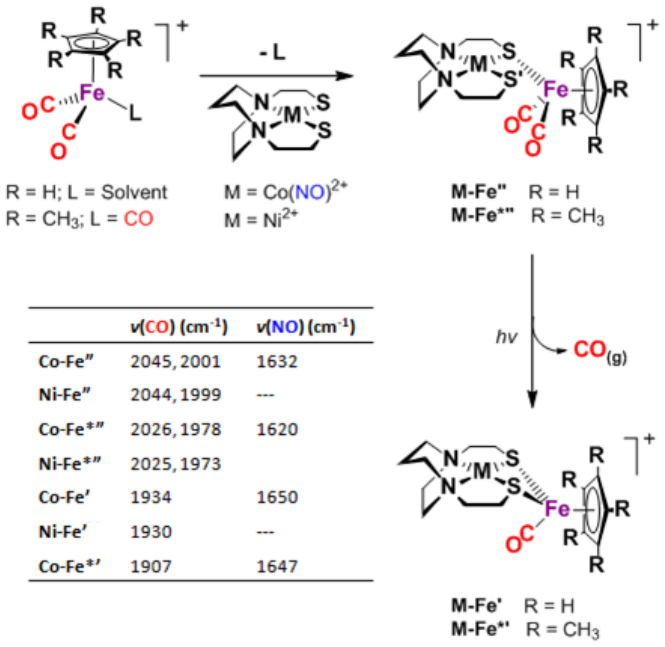

	ν(CO) (cm⁻¹)	ν(NO) (cm⁻¹)
Co-Fe"	2045, 2001	1632
Ni-Fe"	2044, 1999	---
Co-Fe*"	2026, 1978	1620
Ni-Fe*"	2025, 1973	
Co-Fe'	1934	1650
Ni-Fe'	1930	---
Co-Fe*'	1907	1647

Figure IV-2. Synthesis of **Co-Fe"** and **Co-Fe'** as BF_4^- salts and **Co-Fe*'** and **Ni-Fe*'** as PF_6^- salts. The IR frequencies of the complexes in CH_2Cl_2 are shown in the table.

The receiver units for the bidentate products, FeCp(CO) and FeCp*(CO), are hereafter abbreviated as **Fe'** and **Fe*'**, respectively; while the monodentate products, $FeCp(CO)_2$ and $FeCp^*(CO)_2$ are abbreviated as **Fe"** and **Fe*"**, respectively. Overall, the room temperature reaction of $[CpFe(CO)_2BF_4]$ or $[CpFe(CO)_2(Solv)]^+[BF_4]^-$ or

$[Cp^*Fe(CO)_3]^+[PF_6]^-$ with MN_2S_2 in CH_2Cl_2 forms the monodentate complexes, $[\kappa^1$-MN_2S_2•$FeCp(CO)_2]^+[BF_4]^-$ (**Co-Fe"**) and $[\kappa^1$-MN_2S_2•$FeCp^*(CO)_2]^+[PF_6]^-$ (**Ni-Fe*"** and **Co-Fe*"**). Although **Co-Fe"** can be synthesized and isolated as a pure purple solid, the **Ni-Fe*"** and **Co-Fe*"** are present as a mixture with the starting material. Positive-ion ESI mass spectrum of **Ni-Fe*"** and **Co-Fe*"** displayed prominent signals at the molecular ion masses, *m/z* 523.05 and *m/z* 554.05, respectively, with characteristic isotopic distribution patterns which closely matched the calculated bundle, Figure IV-3.

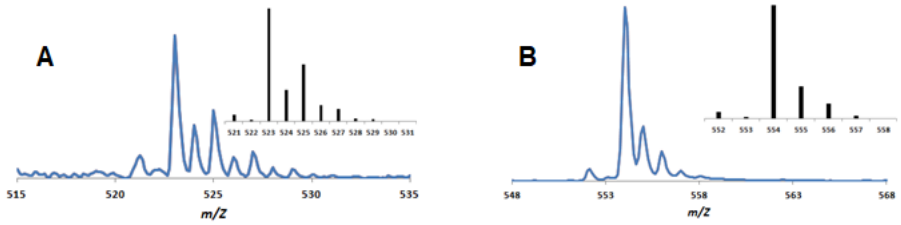

Figure IV-3. Positive-ion ESI mass spectra of A) **Ni-Fe*" (PF_6)** and B) **Co-Fe*" (PF_6)** in CH_3CN; inset: Calculated isotopic distribution for complex **Ni-Fe*"** and **Co-Fe*"**, respectively.

Photolysis of the monodentate (**M-Fe"** or **M-Fe*"**) complexes resulted in loss of one CO to form air-stable, bidentate complexes, **Co-Fe'** as the BF_4^- salt, and **Ni-Fe*'** and **Co-Fe*'** as PF_6^- salts. Additional photolysis of the bidentate complexes led to decomposition. The ν(CO) stretching frequency is an important reporter unit for the electron density at the **Fe'** or **Fe*'** centers in accordance with the conventional σ-donor/π-back-bonding arguments. Due to the greater electron donor ability of the η^5-C_5Me_5, the ν(CO) stretching frequency of **Ni-Fe*'**and **Co-Fe*'**, (1905 and 1907 cm^{-1} respectively), showed a bathochromic shift of ca. 25 cm^{-1} compared to the $[NiN_2S_2$•$FeCp(CO)]^+[BF_4]^-$ and **Co-Fe'** congeners, Figure IV-4.[160] The effect on the

ν(NO) stretching frequency was less prominent with an overall lowering of ν(NO) by 3 cm^{-1} for **Co-Fe*'**.

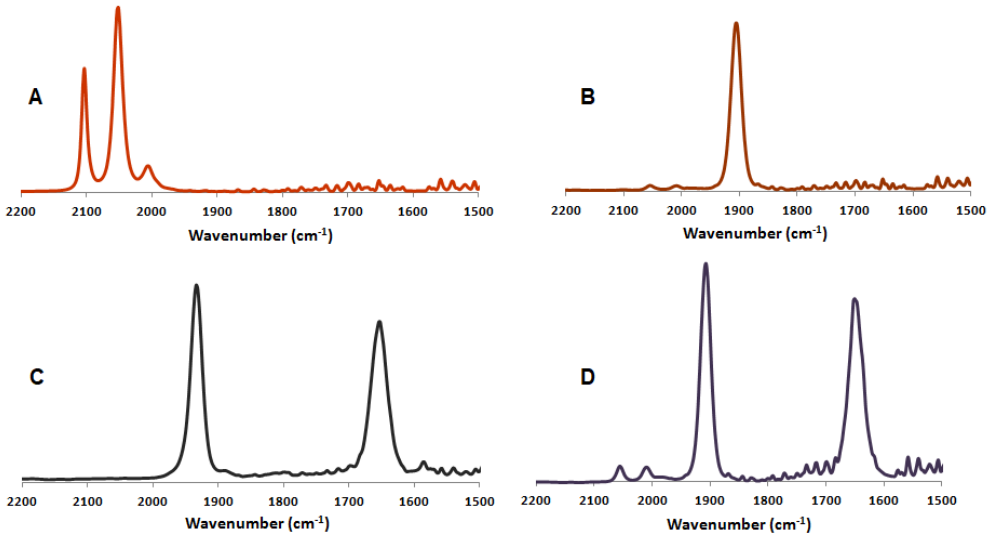

Figure IV-4. IR spectra of A) $[(\eta^5\text{-}C_5Me_5)Fe(CO)_3]^+$ $[PF_6]^-$ in CH_3CN, B) **Ni-Fe*'** in CH_2Cl_2, C) **Co-Fe'** in CH_2Cl_2, D) **Co-Fe*'** in CH_2Cl_2.

Slightly lower ν(CO) stretching frequencies of **Ni-Fe*'**, compared to **Co-Fe*'**, has precedence from previous studies with $(\eta^5\text{-}C_5H_5)Fe(CO)$ or $W(CO)_4$ reporter units, showcasing the higher electron donor ability of NiN_2S_2 over $(NO)CoN_2S_2$ metalloligands.[78, 160] The monodentate complex, **Co-Fe"**, showed two ν(CO) stretching frequencies at 2045 and 2002 cm^{-1} and a ν(NO) at 1630 cm^{-1}. All the newly synthesized complexes are diamagnetic and were characterized by ^1H and ^{13}C NMR spectroscopies, see SI of Ghosh *et al*. *Dalton Trans*. **2017**, *46*, 5617-5624. The ^{13}C NMR spectra of **Co-Fe"** and **Co-Fe'**, at 23.2 °C using a 500 MHz NMR under N_2 referenced to residual CH_2Cl_2, are shown in Figure IV-5 and 6, respectively.

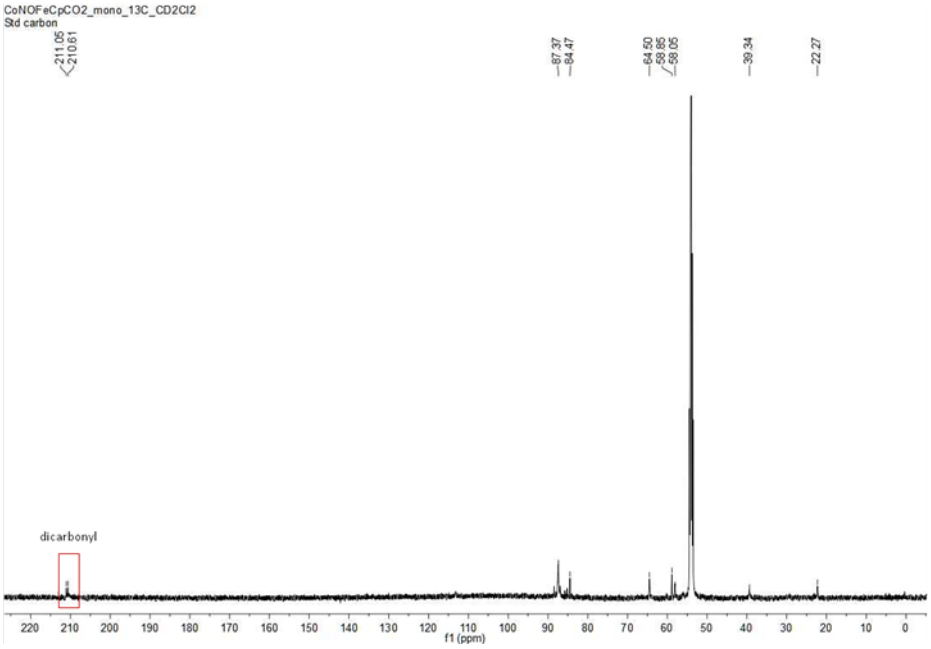

Figure IV-5. ^{13}C NMR Spectrum of **Co-Fe"** at 23.2 ºC using a 500 MHz NMR under N_2 referenced to residual CH_2Cl_2.

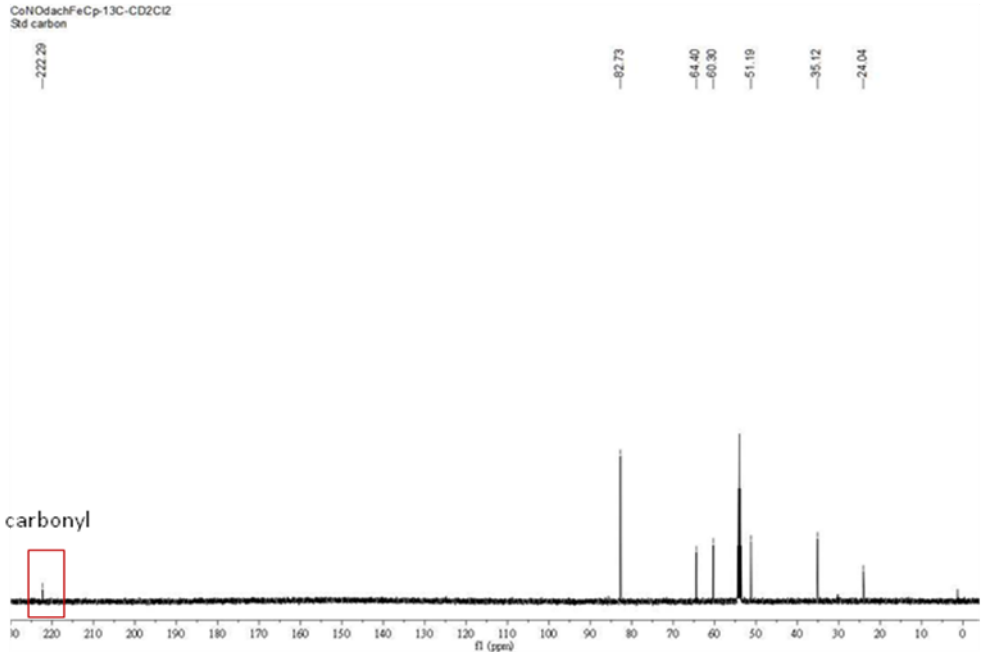

Figure IV-6. ^{13}C NMR Spectrum of **Co-Fe'** at 23.2 ºC using a 500 MHz NMR under N_2 referenced to residual CH_2Cl_2.

X-ray Diffraction Analyses

X-ray quality crystals were obtained by layering a concentrated solution of the complexes in CH_2Cl_2 with hexanes at -28 ºC. While the monodentate **Co-Fe"** was obtained as dark needles, the **Co-Fe'** and **Co-Fe*'** presented as dark violet blocks, and the **Ni-Fe*'** complex crystallized as brown blocks. The molecular structures of the complexes **Co-Fe"**, **Co-Fe'**, **Ni-Fe*'** and **Co-Fe*'** are shown in Figure IV-7, as ball and stick renditions. Full structural reports are deposited in the Cambridge Crystallographic Data Centre. The structures feature typical piano-stool coordination geometries about the iron in $FeCp(CO)^+$ and $FeCp^*(CO)^+$ units.

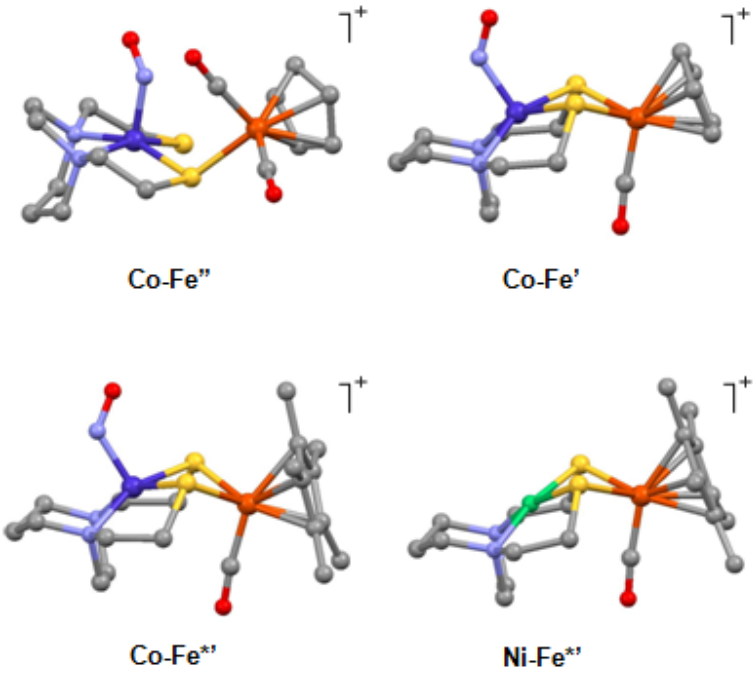

Figure IV-7. Molecular structures of **Co-Fe"**, **Co-Fe'**, **Co-Fe*'** and **Ni-Fe*'**. The BF_4^- counter anions of **Co-Fe"** and **Co-Fe'** and the PF_6^- counter anions of **Co-Fe*'** and **Ni-Fe*'** are omitted for clarity.

In **Co-Fe'**, **Ni-Fe*'** and **Co-Fe*'** the convergent lone pairs on the bridging thiolates enforce bidentate binding at the iron (**Fe'** or **Fe"**) center leading to a butterfly-

like [M(μ-SR)$_2$Fe] core, constraining the ∠**S-M-S** by ca. 7-9° compared to the free metallodithiolate ligands.[162] The hinge angle (the intersection of the N_2S_2 best plane with the S_2Fe' or S_2Fe*' best plane) is ca. 126° for **Co-Fe'** which constricts by ca. 4° in **Ni-Fe*'** and **Co-Fe*'**. This might be related to the added electron density and steric encumbrance in the **Ni-Fe*'** and **Co-Fe*'** due to the (η^5-C_5Me_5) compared to the (η^5-C_5H_5). The **Co-Fe'** and **Co-Fe*'** derivatives find the NO positioned transoid to the CO on the FeCp and FeCp* units.

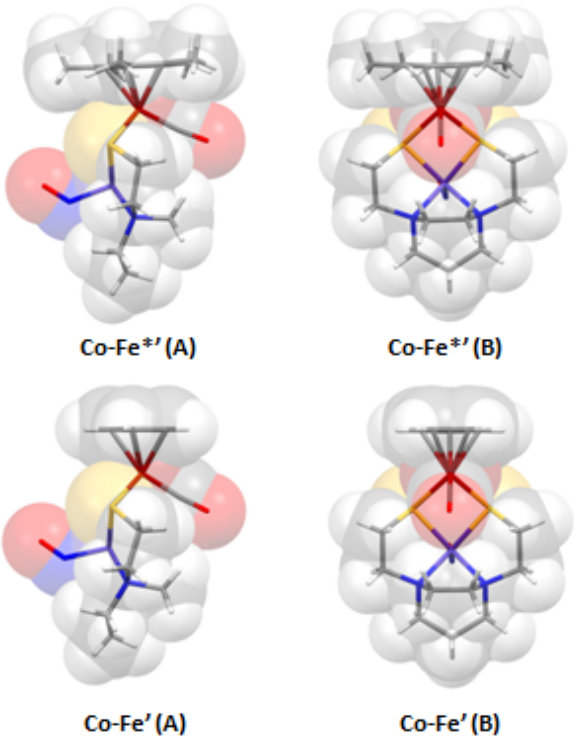

Figure IV-8. Space filling models of, **Co-Fe*'** and **Co-Fe'** shown in two orientations; (B) is rotated by 90° from (A).

Furthermore, in the bidentate complexes, **Co-Fe'** and **Co-Fe*'**, the NO is on the side of the N_2S_2 ligand that has the 3-carbon chain between the two N atoms, whereas in

the monodentate complex, **Co-Fe"**, the NO resides on the side of the 2-carbon chain. In all three bidentate complexes, the N to S linkers are eclipsed and the bridging dithiolate hinge positions the downward oriented methylene groups, α to S, so as to cradle the Fe-CO moiety, resulting in C_{CO} to $H_{\alpha\text{-}CH2}$ distances of ca. 2.7-2.8 Å. Space-filling models highlight the close encounter of the hydrocarbon linkers on the CO, Figure IV-8, and the minimal space taken up by the folded structure. Nevertheless, the M•••Fe' and M•••Fe*' distances of 3.0 – 3.2 Å in our complexes are too long to implicate a bonding interaction. The report of Kure, Tanase, *et al*., of analogous MP_2S_2•M'Cp* structures (M = Ni^{II}, Pd^{II}, Pt^{II}; M' = Rh^{III}, Ir^{III}) that find a μ-H between M and M' describe this pocket as a nest, and the bridging hydride as a "nesting" hydride.[122]

The bridging thiolate (μ-SR) of the monodentate complex, uses one of its divergent lone pairs to bind $FeCp(CO)_2^+$, allowing the latter to be oriented away from the free thiolate. The Co-S-Fe' opens up by ca. 30° compared to the bidentate complexes. A similar phenomenon was observed for $[\kappa^1\text{-}NiN_2S_2\text{•}FeCp(CO)_2]^+[BF_4]^-$.[160] Selected metric parameters of the four complexes are tabulated in Table IV-1.

Table IV-1. Selected metric parameters of **Co-Fe"**, **Co-Fe'**, **Co-Fe*'** and **Ni-Fe*'**.

	Co-Fe"	**Co-Fe'**	**Co-Fe*'**	**Ni-Fe*'**
M···Fe' / Å	3.913 (1)	3.153 (1)	3.136 (2)	3.005 (1)
M···C_{CO} / Å	4.559 (2)[a]	3.386 (4)	3.370 (4)	3.096 (5)
S···S / Å	3.321 (1)	2.994 (2)	2.977 (1)	2.954 (2)
N···N / Å	2.545 (3)	2.598 (5)	2.585 (4)	2.571 (9)
∠M-N-O / °	124.7 (9)	131.4 (4)	126.6 (3)	---
∠S-Fe-S / °	---	81.9 (2)	80.8 (3)	79.6 (6)
∠S-M-S / °	95.9 (3)	85.8 (5)	85.2 (4)	87.1 (7)
∠N-M-N / °	80.4 (9)	81.7 (1)	81.7 (1)	83.7 (3)
Hinge Angle[b] / °	118.3 (3)[c]	126.2	121.9	121.5
M-N_2S_2 disp.[d] / Å	0.361	0.432	0.429	0.205

[a] Average value.
[b] The angle between N_2S_2 and S_2Fe' best planes.
[c] The ∠Co-S-Fe is given in lieu of the hinge angle.
[d] Displacement of M from N_2S_2 best plane.

Electrochemistry

Cyclic voltammograms (CV) of **Co-Fe'** as BF_4^- salt and **Co-Fe*'** and **Ni-Fe*'** as PF_6^- salts were recorded at room temperature under argon in CH_3CN solutions containing 0.1 M [$^tBu_4N$][PF_6] as supporting electrolyte using a glassy carbon working electrode. The scans at 200 mV/sec are shown in Figure IV-9, with assignments listed therein. Scan rate overlays to determine reversibility or quasi-reversibility are given in the SI of Ghosh *et al*. *Dalton Trans*. **2017**, *46*, 5617-5624.

The complexes in general showed two distinct redox events. The quasi-reversible event at slightly positive potential was assigned to the $Fe'^{II/III}$ or $Fe^{*II/III}$ redox couple,

and the one at negative potential was assigned to the $M^{II/I}N_2S_2$ reduction. The oxidation event at 0.32 V assigned to the $Fe'^{II/III}$ couple for the **Co-Fe'** complex showed a positive shift of ca. 200 mV with respect to the $Fe^{*'II/III}$ couple of **Co-Fe*'** implying a greater ease of oxidation at the Fe center electron-enriched by the η^5-C_5Me_5 unit. Consistently, the $\{Co(NO)\}^{8/9}$ reduction event of **Co-Fe*'** at -1.19 V differs by 70 mV as compared to the **Co-Fe'** indicating the greater stabilization of the oxidized $\{Co(NO)\}^8$ state in the **Co-Fe*'** complex. The $Fe^{*'II/III}$ couple of the **Ni-Fe*'** complex showed a quasi-reversible oxidation event at 0.07 V, which is ca. 220 mV less positive than the $Fe'^{II/III}$ couple of the $[NiN_2S_2•FeCp(CO)]^+[BF_4]^-$ complex, for similar reasons.[160]

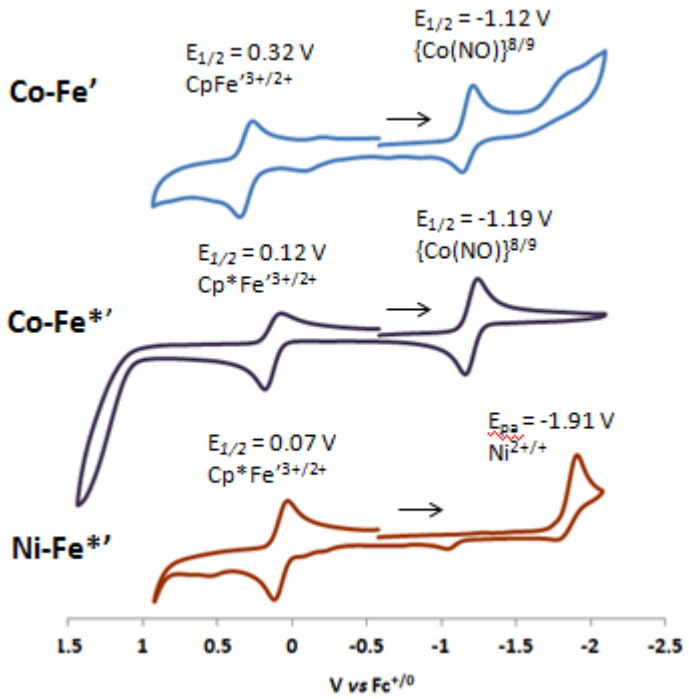

Figure IV-9. Cyclic voltammograms of **Co-Fe'**, **Co-Fe*'** and **Ni-Fe*'** as 2 mM CH_3CN solutions containing 0.1 M $[^tBu_4N][PF_6]$.

Likewise a negative shift of the $Ni^{II/I}$ couple by 280 mV was observed for the **Ni-Fe*'** complex relative to the $[NiN_2S_2•FeCp(CO)]^+[BF_4]^-$ complex.[160] All complexes showed an irreversible oxidation event at greater than 1.00 V, possibly due to dithiolate-based oxidation. Overall, the effect of greater electron donor ability of η^5-C_5Me_5 over the η^5-C_5H_5 unit was manifested in a more energetically demanding reduction couple and, consistently, more facile oxidation events.

Electrocatalysis

Electrochemical studies of **Co-Fe'**, **Co-Fe*'** and **Ni-Fe*'** were carried out in the presence of trifluoroacetic acid (TFA) and are shown in Figure IV-10. The increase in the cathodic current that was observed at the $\{Co(NO)\}^{8/9}$ reduction event for **Co-Fe*'** (-1.19 V) and **Co-Fe'** (-1.12 V), was saturated after addition of 8 equivalents of TFA. An additional event at -1.75 V appeared for the **Co-Fe*'** on addition of first equivalent of acid and further acid additions showed a steady increase in this current response. A new major current event appeared at -1.56 V, for complex **Co-Fe'**, with TFA > 6 equivalents.

A similar pre-peak phenomenon was observed for $[(NO)FeN_2S_2•FeCp(CO)]^+[BF_4]^-$ complex at -1.66 V.[160] Similarly, addition of TFA to the **Ni-Fe*'** complex showed the formation of a pre-peak at -1.74 V that increased in current intensity along with the major $Ni^{II/I}$ reduction event at -1.91 V.

The attribution of the reduction-induced cathodic current enhancement upon addition of TFA to electrocatalytic H_2 production was verified by gas chromatography and quantified by an average of two consistent bulk electrolysis experiments. A constant

potential at -1.80 V (dotted line in Figure IV-10), for 30 min, was applied in a CH_3CN solution containing 2 mM of catalyst and 50 equivalents of TFA.

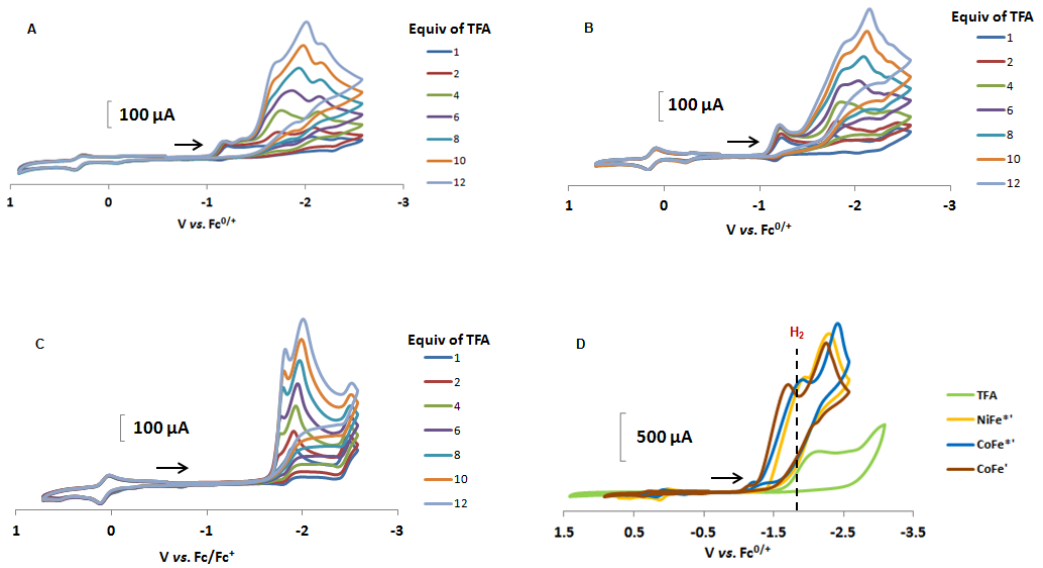

Figure IV-10. Cyclic voltammograms of (A) **Co-Fe'**, (B) **Co-Fe*'** and (C) **Ni-Fe*'** as 2 mM CH_3CN solutions containing 0.1 M [^{t}Bu$_4$N][PF_6] as supporting electrolyte with added equivalents of TFA. (D) Overlay of catalytic current responses of **Co-Fe'**, **Co-Fe*'** and **Ni-Fe*'** in presence of 50 equivalents of TFA and 50 equivalents of TFA in absence of catalyst. The dotted line indicates the constant potential applied for bulk electrolysis, -1.80 V.

Since the background H_2 evolved from TFA itself at this potential overlaps the response from the electrocatalyst, the former was subtracted to obtain corrected values of the catalytic response, *vide* SI of Ghosh *et al*., *Dalton Trans*. **2017**, *46*, 5617-5624. The turnover numbers (TON) for **Ni-Fe*'**, **Co-Fe*'** and **Co-Fe'** were found to be 0.32 ± 0.05, 0.15 ± 0.01 and 0.35 ± 0.05, respectively, with Faradaic efficiencies of 88 ± 4 %, 99 ± 0.2 % and 92 ± 1 %, respectively, for H_2 production. Following the approach of

Wiese[99] and Helm and Appel,[98] turnover frequencies (TOF), derived from the cyclic voltammetry studies, were determined to be 32 s^{-1}, 65 s^{-1}, 79 s^{-1} for **Ni-Fe*'**, **Co-Fe*'** and **Co-Fe'**, respectively. The high overpotentials for **Ni-Fe*'** and **Co-Fe*'** complexes, 1.31 V and 1.27 V, respectively, are consistent with the electron rich η^5-C_5Me_5 unit present in these complexes while the moderately lower overpotential for **Co-Fe'**, 1.06 V, with the η^5-C_5H_5 unit, is comparable to those reported for the $[(NO)FeN_2S_2•FeCp(CO)]^+[BF_4]^-$ and $[NiN_2S_2•FeCp(CO)]^+[BF_4]^-$ complexes.[160]

Table IV-2. Overpotential, turnover number (TON) and turnover frequency (TOF) of **Ni-Fe*'**, **Co-Fe*'**, **Ni-Fe'**,[160] **Fe-Fe'**[160] and **Co-Fe'**.

	Overpotential (V)	Turnover Number (TON)	Turnover Freq. (TOF) (s^{-1})
Ni-Fe*'	1.31	0.32 ± 0.05	32
Co-Fe*'	1.27	0.15 ± 0.01	65
Ni-Fe'[30]	0.94	0.26 ± 0.01	52
Fe-Fe'[30]	0.94	0.33 ± 0.02	69
Co-Fe'	1.06	0.35 ± 0.05	79

Table IV-2 shows a comparative listing of overpotential, turnover number (TON) and turnover frequency (TOF) of the different complexes used in this study. The data obtained for calculating such values, *vide* SI of Ghosh *et al*., *Dalton Trans*. **2017**, *46*, 5617-5624. The complexes, $[(NO)FeN_2S_2•FeCp(CO)]^+[BF_4]^-$ and $[NiN_2S_2•FeCp(CO)]^+[BF_4]^-$, showed H/D kinetic isotope effects on TOF and the (k_H/k_D) were determined to be ca. 1.5.[160] The consistency in the TOF values for **M-Fe*'** and **M-**

Fe' complexes leads to the overall assumption that the reaction path for the catalytic process is similar and involves a metal-hydride species as an intermediate in the catalytic cycle.

Conclusion

In summary, the proficiencies of three MN_2S_2•$Fe(\eta^5\text{-}C_5R_5)(CO)^+$ complexes (R = H or CH_3) for catalysis of the HER were determined by standard electrochemical analyses and structure/function comparisons are made. The **Co-Fe'** complex relates to **M-Fe'** complexes, M = Ni^{2+} and $[Fe(NO)]^{2+}$ reported earlier.[160] Its properties are by and large precise analogues of the Fe(NO) derivative, **Fe-Fe'**, and can be used as a reference to connect the two studies. The CO and NO ligands that report via vibrational spectroscopy on electronic results from aggregating the individual components of the bimetallics are entirely consistent with the shifts in redox potentials of the **Fe'** and **Fe*'** units and the metallodithiolate ligands.

The overall conclusion must be that the Cp* enriches the electron density mainly at the Fe center, and has an effect, however less prominent, at the metallodithiolate ligand. At this point, we have not attempted an extensive computational study of the mechanism as was done for the prior study.[160] We assume that the reaction path is similar (or identical) and the energy requirement for the ring opening process that creates the needed Lewis pair for H^+•••H^- coupling is a dominant factor for determining overpotential but has less significance for other electrochemical features such as turnover number and turnover frequency. Our working hypothesis continues to focus on

the bimetallic mechanism, assuming that the bimetallic remains intact via a single thiolate bridge. Clearly it would be reassuring to obtain experimental evidence for the presumed iron-hydride/protonated thiolate sulfur intermediate.[160] At this point we still search for these illusive species, and other mechanistic possibilities cannot be ruled out. Concomitant with the more negative reduction event is a more accessible, reversible oxidation event. Hence the catalytic propensities of these Cp* complexes might be more advantageously applied to oxidation catalysis.[121, 123]

CHAPTER V

A MATRIX OF HETEROBIMETALLIC COMPLEXES FOR INTERROGATION OF HYDROGEN EVOLUTION REACTION ELECTROCATALYSTS[#]

Introduction

From protein crystallography the bimetallic active site structures in enzymes such as [NiFe]-, [FeFe]-hydrogenases (H_2ase), CO-dehydrogenases and acetyl coA synthase (ACS) have been convincingly interpreted in terms of characteristics needed for their organometallic-like functions.[37, 72-73] Whereas most major homogeneous catalytic applications involving redox processes use precious metals that can operate as single site catalysts, the intricate molecular arrangements in nature's biocatalysts harness combinations of at least two first row transition metals, connected by sulfides or thiolates, along with Lewis acid/base sites.[163] Over the past two decades a rich area in synthetic chemistry inspired by such natural products has developed, yielding biomimetics for insight into enzyme mechanisms.

[#]Reproduced by permission of The Royal Society of Chemistry from Ghosh, P.; Ding. S.; Chupik, R. B.; Hsieh, C. –H.; Quiroz, M.; Bhuvanesh, N.; Hall, M. B.; Darensbourg, M. Y. *Chem. Sci.* **2017** (DOI: 10.1039/C7SC03378H).
The theoretical calculations and their results described herein were computed by Dr. Shengda Ding and Prof. Michael B. Hall.

In addition the link between the [NiFe]- and [FeFe]-H_2ase active sites and base metal, sustainable catalysts for the Hydrogen Evolution Reaction (HER), holds promise for the production of H_2 from "solar" (photovoltaic) electrons via electrocatalysis.[76] Specific efforts have been directed towards the use of metallodithiolates from MN_2S_2 complexes as bidentate donor ligands (readily deduced from the structure of the ACS enzyme active site), that bind to receiver metal units via bridging dithiolates.[56, 74, 112, 114-116, 118-121, 123, 144, 155-157, 160, 162] The electronic requirements of the thiolate sulfurs have a steric consequence in the butterfly $M(\mu\text{-}SR)_2M'$ cores that are seen in the H_2ase active sites, placing M and M' within close proximity.[162, 164]

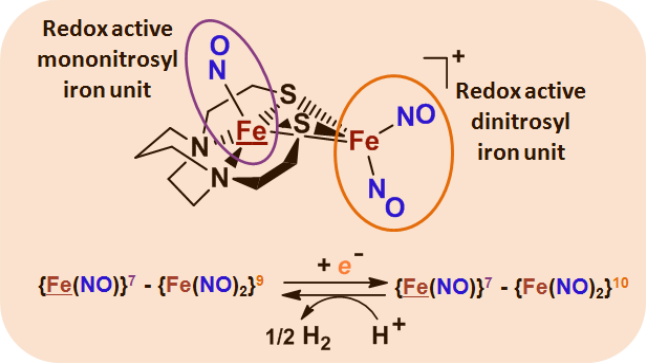

Figure V-1. Structure and redox activity of $[(NO)\underline{Fe}N_2S_2\bullet Fe(NO)_2]^+$, **[<u>Fe</u>-Fe]**$^+$; protonation of the one-electron reduced diiron complex yields H_2.[74]

The advancement of chemistry via structure/function analysis of sets of compounds with well-known differences in composition and structure is a challenge in the complicated area of HER electrocatalysis. Nonetheless the metallodithiolate-as-synthon approach, inspired from the ACS active site, permits modular design that includes some features of the bimetallic [NiFe]- and [FeFe]-H_2ase active sites beyond the obvious dithiolate core structures. An initial foray explored the properties of the

diiron, trinitrosyl complex shown in Figure V-1.[74, 96] With it we intended to exploit the redox-activity of $\{\underline{Fe}(NO)\}^{7/8}$ in the $(NO)\underline{Fe}N_2S_2$metalloligand bound to a redox-active $\{Fe(NO)_2\}^{9/10}$, iron dinitrosyl unit. Electrochemical studies of $[(NO)\underline{Fe}N_2S_2{\bullet}Fe(NO)_2]^+$, **[<u>Fe</u>-Fe]$^+$**, Figure V-1, found two single-electron, reversible reduction events, -0.78 V and -1.33 V, assigned to $\{Fe(NO)_2\}^{9/10}$ and $\{\underline{Fe}(NO)\}^{7/8}$ couples, respectively.[74] The Fe of the $(NO)\underline{Fe}N_2S_2$ metalloligand is herein distinguished as <u>Fe</u>; the electron count of the iron nitrosyl units uses the Enemark–Feltham approach.[151] Consistent with the stoichiometric reaction shown in Figure V-1, the $\{Fe(NO)_2\}^{9/10}$ couple, at -0.78 V, was the catalytically active center for electrochemical proton reduction in the presence of strong acid, $HBF_4{\bullet}Et_2O$. Although modest in overpotential and TOF, electrocatalysis for H_2 production was observed at this potential; preliminary computational studies indicated that a hydride-bound $\{Fe(NO)_2\}^8$ could likely be a transient intermediate, however the overall H_2 releasing mechanism was at that stage incomplete.[74] Interestingly, the second reduction process, related to the more negative $\{\underline{Fe}(NO)\}^{7/8}$ couple, showed a current response to added weak acid, however H_2 was not detected. Computational study attributed this to a non-productive reduction event with protonation on the nitrosyl, which terminates the catalytic cycle.[74]

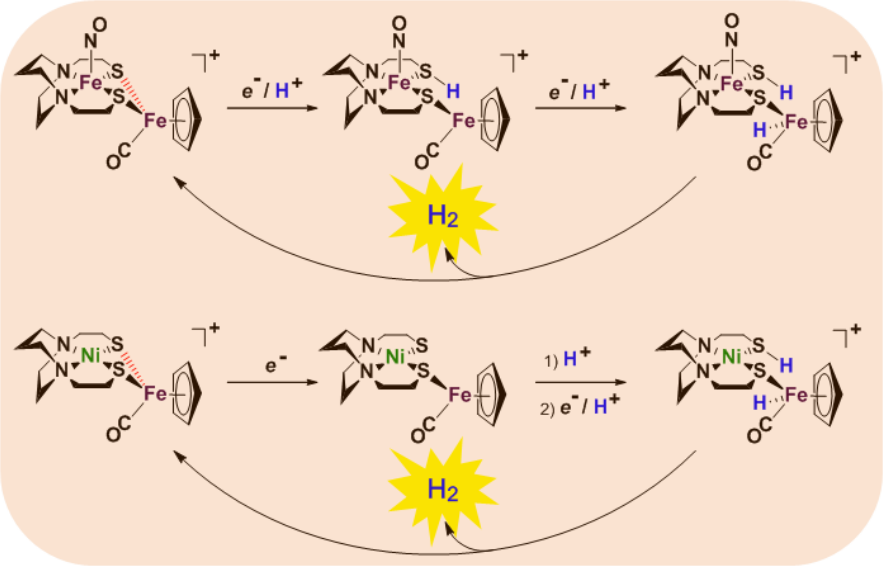

Figure V-2. Abbreviated computational mechanisms for electrocatalysis of H_2 production by the [Fe-Fe']$^+$ and [Ni-Fe']$^+$ electrocatalysts.[160] Shown in red is the Fe – S bond that undergoes reductive bond cleavage.

We have made analogues of the diiriontrinitrosyl complex making use of NiN_2S_2 and (NO)FeN_2S_2 metallodithiolates in combination with η^5-C_5R_5 derivatives (R = H, CH_3),[160, 165] of Fe^{II} shown in Figure V-2. The large differences in reduction potential of the MN_2S_2 ligands, with the d^8-Ni^{II} being more negative because of a more rigid, less polarizable electronic structure as compared to the delocalized {Fe(NO)}^{7} unit, of greater electronic flexibility, inspired the labels of "hard" for the former MN_2S_2 unit, and "soft" S-donor unit for the latter. The Fe-receivers also differ in electronic flexibility and their ease of electron uptake, the term "soft" describing the highly delocalized {$Fe(NO)_2$}^{9} unit, and the indefinite oxidation state of the iron, as compared to the definite Fe^{II} of the η^5-C_5R_5, "hard" receiver derivatives.[160, 165] The hard receiver unit, (η^5-C_5H_5)Fe(CO)$^+$, is herein distinguished from the soft $Fe(NO)_2$ unit by Fe' and Fe, respectively.

Notable from the computational approach that guided the interpretation of electrochemical events of the **[Ni-Fe']**$^{+}$ and **[<u>Fe</u>-Fe']**$^{+}$ complexes in the presence of acid was the indication of a reductive iron-sulfur bond cleavage (shown in red, Figure V-2,) that converted the bidentate dithiolate into a monodentate S-donor, thus creating a transient frustrated Lewis pair, *i.e.*, yielding reactive sites for proton and electron uptake on the free thiolate and the open site on iron, respectively, see Figure V-2.[160] *In this way, complexes that do not have a built-in amine pendant base for proton uptake and storage, or open sites on iron that are stabilized by the protein super structure as in the [FeFe]-H_2ase active site,*[135-138, 1663] *may electrochemically generate a place to park the proton via concomitant or coupled electron/proton uptake.* While the mild potential for the first EC process for the **[<u>Fe</u>-Fe']**$^{+}$ complex required both proton/electron uptake for genesis of the pendant base, the more negative potential that reduces the **[Ni-Fe']**$^{+}$ labilizes the sulfur and creates an Fe^{III}-H^{-} at the first reduction, Figure V-2.[74, 160]

In this report we provide a more complete matrix of MN_2S_2-Fe complexes of electrocatalytic potential for experimental and computational analysis, in particular to incorporate a redox innocent ("hard") metalloligand, NiN_2S_2, of more negative reduction potential, instead of (NO)<u>Fe</u>N_2S_2, and generate the missing $[Ni^{II}N_2S_2{\bullet}Fe(NO)_2]^{0/+}$ "hard"/"soft" complex for comparison to the other members of the matrix. The solid state structures of $[Ni^{II}N_2S_2{\bullet}Fe(NO)_2]^{0/+}$ in two redox levels and its characteristics as an electrocatalyst (robustness, turnover frequency, turnover number) for proton reduction are also described. Computational study, with mechanisms clarifying the order of reductions and protonations, and revealing the intricacies of hemi-lability of the bridging

thiolates in forming a pendant base, *point to a unifying principle for the build-up effect of redox-active, non-innocent NO ligands*.

Results and Discussion

Shown in Figure V-3 are the synthetic routes to NiN_2S_2•$Fe(NO)_2$, **[Ni-Fe]^0**, and its one-electron oxidized analogue, **[Ni-Fe]$^+$**, isolated and crystallographically characterized as a dimer, $[NiN_2S_2$•$Fe(NO)_2]_2^{2+}$ or **[Ni$_2$-Fe$_2$]$^{2+}$**, (N_2S_2 = *N*,*N*-bis(2-mercaptoethyl)-1,5-diazacyclooctane or bme-daco). Infrared values listed for the diatomic ligands were recorded in CH_2Cl_2 or THF solution. Freshly prepared $Fe(CO)_2(NO)_2$ in THF readily reacts with NiN_2S_2 at 22 °C, with replacement of one CO, releasing the second CO under photolysis, or within 20 min at 40 °C, thus converting the NiN_2S_2 from mono- to bidentate ligand.[167-170]

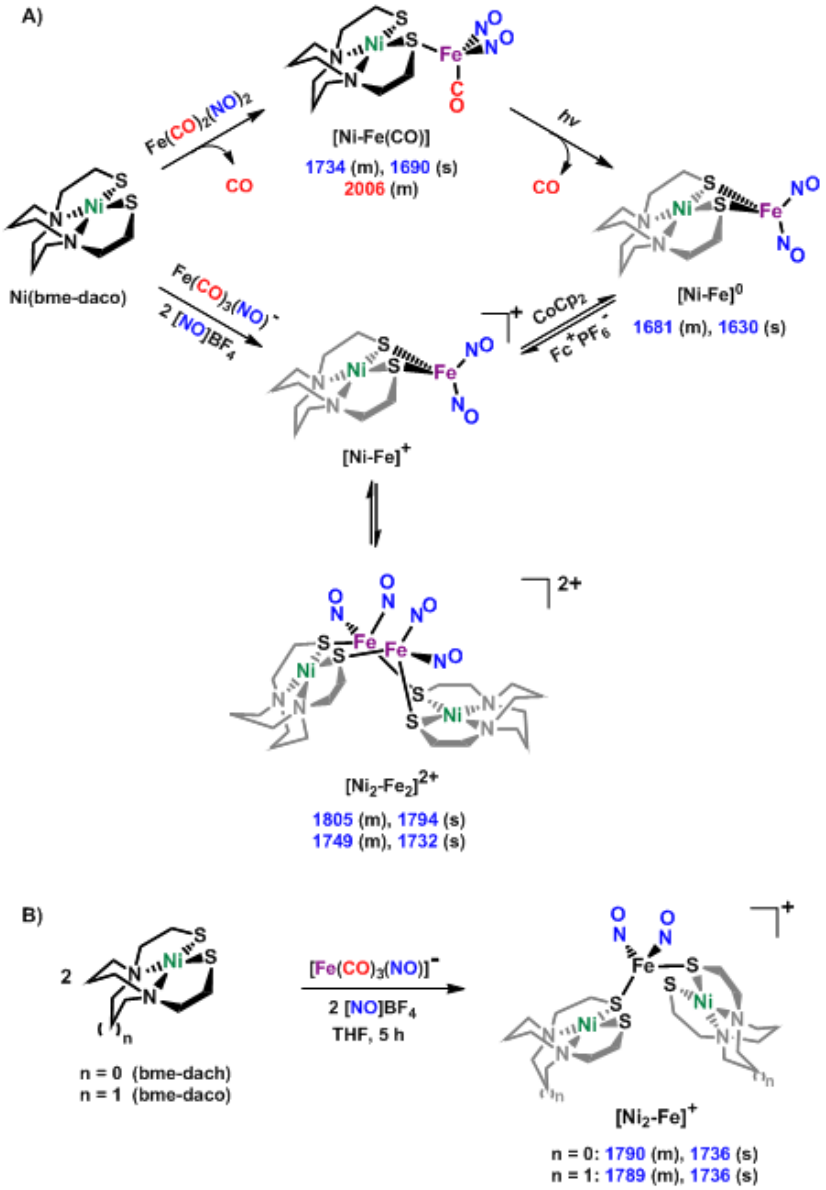

Figure V-3. A) The syntheses of **[Ni-Fe]^0** and **[NiFe(CO)]^0** as neutral complexes, and **[Ni$_2$-Fe$_2$]$^{2+}$** and B) **[Ni$_2$-Fe]$^+$** as BF_4^- salt. The IR values (in cm^{-1}) of CO and NO are in red and blue, respectively.

From this approach the **[Ni-Fe]^0** complex was isolated as a brown solid that is stable at ambient temperature under Ar. Oxidation of **[Ni-Fe]^0** by $Fc^+PF_6^-$ at 0 °C

resulted in a color change of the THF solution from brown to dark purple with concomitant shifts of the ν(NO) values by an average of ca. 110 cm^{-1} to higher wave numbers. The reversibility of this oxidation was confirmed by reaction with cobaltocene and return to the reduced **[Ni-Fe]^0**. The ν(NO) bands listed under **[Ni$_2$-Fe$_2$]$^{2+}$**, Figure V-3, reflect the presence of overlapping components which were resolved into two sets of absorbances, interpreted as a likely mixture of monomeric cation and dicationic dimer, with the set at lower values slightly less in intensity, Figure V-4.

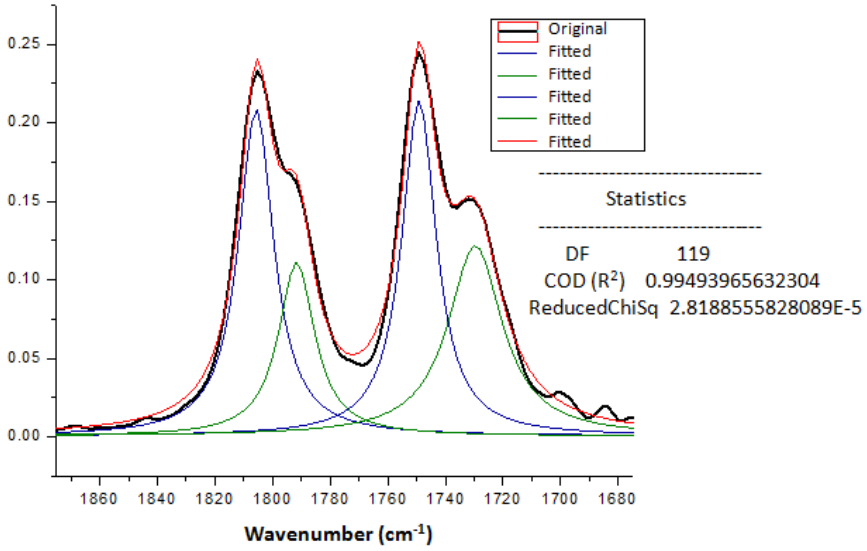

Figure V-4. Deconvoluted IR spectra of **[Ni$_2$-Fe$_2$]$^{2+}$** or **[Ni-Fe]$^+$** in CH_2Cl_2 solution using Lorentzian curve fitting. Fitting parameters are shown on the right. OriginPro8 software was used for fitting.

As other experimental data, *vide infra*, as well as computational studies, indicate the predominance of monomeric **[Ni-Fe]$^+$**, we postulate that the set of absorbances at slightly lower wavenumbers (as shoulders on the major bands) are due to the dimeric **[Ni$_2$-Fe$_2$]$^{2+}$**. We note that the electron-spray ionization mass spectrum of **[Ni-Fe]$^+$** has a

parent ion with isotopic bundle distribution at *m/z* that is consistent with a monomeric **[Ni-Fe]**$^{+}$ rather than a dimeric **[Ni$_2$-Fe$_2$]**$^{2+}$, Figure V-5. The difference between two consecutive isotopic mass units is ~1, rather than 0.5, which indicates the predominance of the monomer, **[Ni-Fe]**$^{+}$, in the polar solvents in which they are soluble.

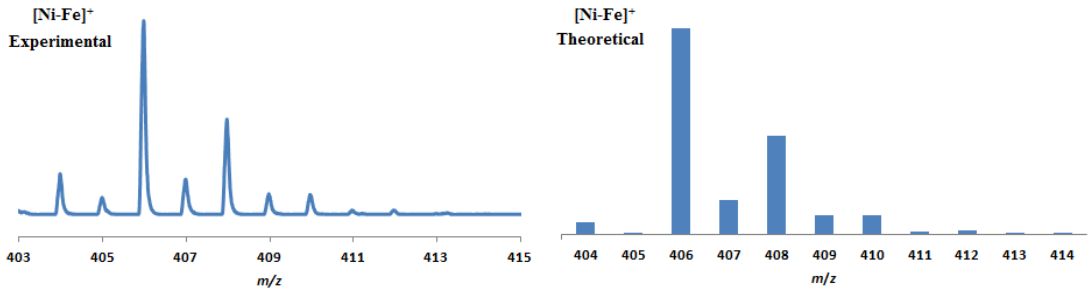

Figure V-5. Positive-ion ESI mass spectrum of **[Ni-Fe]**$^{+}$ in CH_2Cl_2.

The magnetic moments of **[Ni-Fe]**$^{+}$ and **[Ni$_2$-Fe]**$^{+}$ are 1.54 B.M. and 1.76 B.M., respectively, measured by Evans' method at room temperature in CD_2Cl_2.[100] This is consistent with the presence of a single unpaired electron. The ^{19}F NMR spectra of **[Ni-Fe]**$^{+}$ and **[Ni$_2$-Fe]**$^{+}$ are shown in Figures V-6 and 7, respectively. The EPR spectra for both complexes display the isotropic g = 2.03 signal that is prototypical of the $\{Fe(NO)_2\}^9$ unit, Figures V-8A and B, respectively. The 77 K EPR spectrum of the **[Ni-Fe]**$^{+}$ displayed fine structure requiring two signals for simulation: A major isotropic signal of g = 2.035 showed coupling with nitrogen of $A(^{14}N)$ = 32.74 MHz and a minor anisotropic signal had parameters of g_{xyz} = 2.183, 2.012, 1.908 and no observable hyperfine coupling, Figure V-8A.

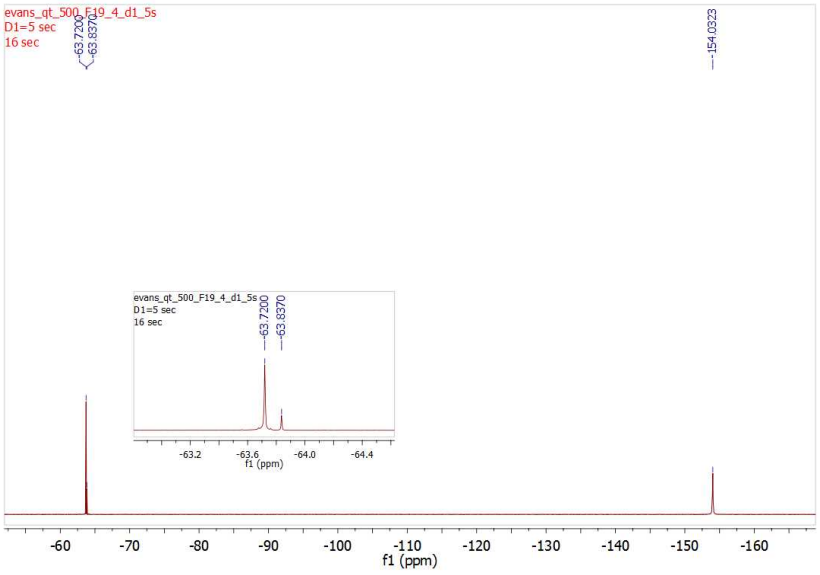

Figure V-6: ^{19}F NMR Spectrum of **[Ni-Fe]**$^{+}$at 22.5 ºCusing a 500 MHz NMR under Ar referenced to $C_6H_5CF_3$ at -63.7200 ppm.

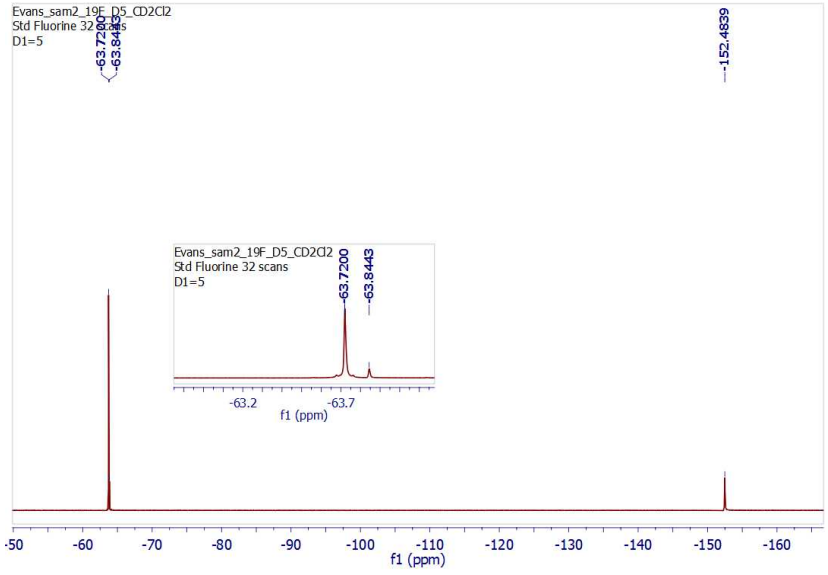

FigureV-7: ^{19}F NMR Spectrum of **[Ni$_2$-Fe]**$^{+}$ at 20.5 ºC using a 500 MHz NMR under Ar referenced to $C_6H_5CF_3$ at -63.7200 ppm.

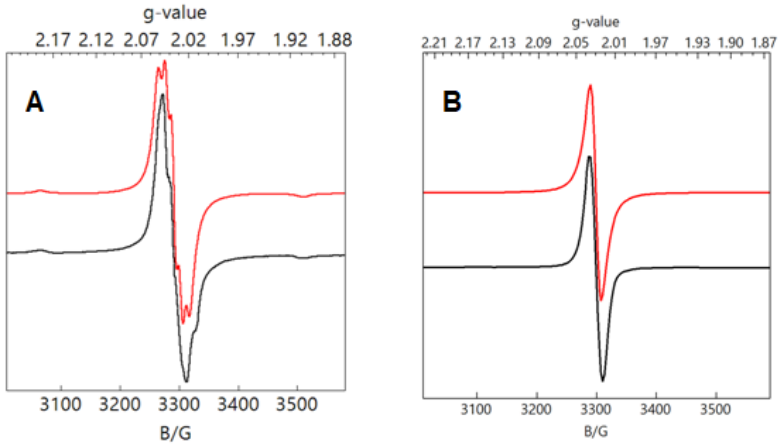

Figure V-8. Frozen solution EPR spectra of a CH_2Cl_2 solution of A) **[Ni-Fe]**$^+$ and B) **[Ni$_2$-Fe]**$^+$ at 77 K, respectively.

X-ray diffraction quality crystals of the oxidized Ni-Fe compound were obtained from the one-pot reaction of equimolar NiN_2S_2 and (putative) $[Fe(CO)_2(NO)_2]^+$ (prepared *in situ* by reacting $[Fe(CO)_3(NO)]^-$ with two equivalents of $[NO]BF_4$)[171] in CH_2Cl_2 at ambient temperature, Figure V-3A. A third Ni-Fe complex, [**Ni$_2$-Fe**]$^+$, was obtained on combining NiN_2S_2 with $[Fe(CO)_2(NO)_2]^+$ in 2:1 ratio in THF solution, Figure V-3B. X-ray quality crystals of this trimetallic as its BF_4^- salt were obtained from hexane/THF layering at -28 °C. Its ν(NO) IR spectral features are typical of monomeric DNICs in the $\{Fe(NO)_2\}^9$ redox level. The EPR spectra are shown above, Figure V-8.

X-ray Diffraction Studies

The molecular structures of the heterometallic complexes **[Ni-Fe]^0**, **[Ni$_2$-Fe$_2$]$^{2+}$** and **[Ni$_2$-Fe]**$^+$ are shown in Figure V-9.

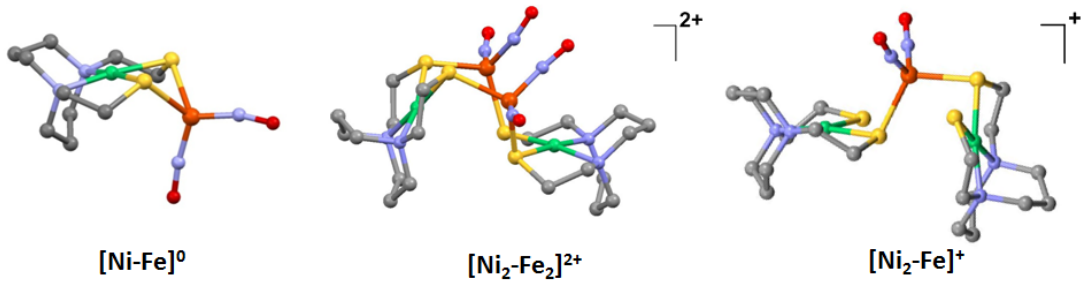

Figure V-9. Molecular structures of a) **[Ni-Fe]^0**, b) **[Ni$_2$-Fe$_2$]$^{2+}$** and c) **[Ni$_2$-Fe]$^+$** from X-ray diffraction. The BF_4^- counter ions of **[Ni$_2$-Fe$_2$]$^{2+}$** and **[Ni$_2$-Fe]$^+$** are omitted for clarity.

The bimetallic complex **[Ni-Fe]^0**, exhibits an overall butterfly-like Ni(μ-SR)$_2$Fe core, analogous to the report of Pohl *et al*., where an open chain N_2S_2 ligand chelated the Ni^{II}.[169] The converging lone pairs (see below) on the cis-dithiolates engage in bidentate binding and impose a hinge angle (the intersection of the best N_2S_2 plane with the S_2Feplane) of ca. 117 °, vis-à-vis constricting the ∠S−Ni−S angle by ca. 4° compared to the free metalloligand.[92] The two nitrosyl units bound to the pseudo tetrahedral iron center are slightly bent towards each other, in an "attracto" orientation;[172] the average ∠Fe−N−O angle is ~ 163.8 °. The Ni•••Fe distance of 3.001 (2) Å, is slightly longer (by 0.022 Å) than that obtained in the Pohl *et al*. structure.[169]

The oxidized NiFe complex crystallizes as dimeric **[Ni$_2$-Fe$_2$]$^{2+}$** with two BF_4^- anions; two dinitrosyl iron units are bridged by two NiN_2S_2 metalloligands. The tetrahedral geometry about each Fe(NO)$_2$ unit is thus completed by two thiolates from

different NiN_2S_2 metalloligands, thus generating an abbreviated paddlewheel, or propeller type, complex seen in examples of nickel-gold tetrametallic complexes.[173]

Likewise, the molecular structure of **[Ni$_2$-Fe]$^+$** demonstrates that one $Fe(NO)_2$ unit bridges two NiN_2S_2 metalloligands, each acting as a monodentate ligand. As shown in the **[Ni$_2$-Fe]$^+$** structure, Figure V-9, the free unbound thiolates of two NiN_2S_2 units are transoid to each other. The addition of a second $Fe(NO)_2^+$ unit to generate the dication, **[Ni$_2$-Fe$_2$]$^{2+}$**, would require rotation about one Fe-S bond in order to align the two metalloligands.

The average Ni•••Fe distances in **[Ni$_2$-Fe$_2$]$^{2+}$** and **[Ni$_2$-Fe]$^+$**, are 3.680 (2) Å and 3.521 (2) Å, respectively, and are longer than in the **[Ni-Fe]^0** reduced complex by ca. 0.5 Å. The Ni^{II} maintains a square planar geometry in the reduced and oxidized complexes with a displacement of no more than 0.1 Å from the N_2S_2 best plane. Overall these structures demonstrate the impressive adaptability of the NiN_2S_2 metalloligands, and their potential to template clusters through S-based aggregation.[162]

Computational Structural Study (Dr. Shengda Ding and Prof. Michael B. Hall)

This computational section uses density functional theory (DFT) analysis to address the structural question in particular that was raised by the x-ray diffraction report: Is there an electronic factor that governs the different μ_2-SR binding modes found in the three forms of NiFe heterometallic aggregates? TPSS/6-311++G(d,p) and natural bond orbital (NBO) analysis were applied to computational structural modeling of the free metalloligand NiN_2S_2 and its derivatives **[Ni-Fe]^0**, [**Ni$_2$-Fe$_2$]$^{2+}$**.

The Divergent or Convergent Orientation of S Lone Pairs of NiN_2S_2 Metalloligand and Influences on Structures of NiN_2S_2•M' Heterobimetallics

Traditional bidentate ligands such as diphosphines, diamines and bipyridyls have a single lone pair on each donor site. These lone pairs are positioned on orbitals originating from sp^x-hybridization and are highly directional.[174] They provide fixed binding orientations that match the coordination preference of traditional metal receivers. In contrast, the binding between the sulfurs of the metallothiolate NiN_2S_2 and an exogeneous metal are more geometrically flexible because of the multiple S lone pairs. From NBO bonding analysis, sulfur in the NiN_2S_2 metalloligand is found to use mainly *p* orbitals for bonding to Ni and C.[175-176] For example, in a free NiN_2S_2, *p* character makes up 83% and 86% of the S contributions in the S-Ni bonds and S-C_α bonds (C_α and C_β refer to the C_2H_4 linker connecting S and N where C_α is directly bound to S, Figure V-10), which leaves one lone pair in a *p* orbital and another in an *s*-dominated orbital on each S. Because a receiver group, *i.e.*, a $Fe(NO)_2$ unit in our case, may bind to either lobe of the *p* lone pair(s), whose orientation is determined by the Ni-S-C_α torsion angle, a diversity of structures results.[162, 164]

The orientation of this remaining *p* lone pair in the NiN_2S_2 metalloligand is determined by the NiN_2S_2 metalloligand's Ni-S-C_α-C_β-N five-membered rings that adopt a non-planar envelope conformation like cyclopentane. The C_α carbon, the "flap" of the envelope conformation, puckers towards one side or the other of the N_2S_2 plane, Figure V-9. Figure V-10 shows how this puckering tilts the remaining *3p*-lone pair on each sulfur from the normal to the N_2S_2 plane. This tilt causes two *p*-orbital lobes (green

lobes) to **converge** on the side to which the flap puckers, while the red lobes **diverge** on the opposite side. The orientation of the added $Fe(NO)_2$ receiver unit(s), will be thus determined by such directional property of the donor *p* lone pairs. The structure of the reduced monomer **[Ni-Fe]^0** shows the $Fe(NO)_2$ fragment is on the same side as the flap; while in the oxidized dimer **[Ni$_2$-Fe$_2$]$^{2+}$** the flap and the $Fe(NO)_2$ fragment(s) appear on different sides of each N_2S_2 plane, thus, binding to the other end of the *p* lone pair. Based on the analysis above, the converging lobes of the *p* donor lone pairs maximize contact to the $Fe(NO)_2$ unit in the monomer **[Ni-Fe]^0**, while the diverging lobes are preferred by two bridging $Fe(NO)_2$ units between two metalloligands in the dimer **[Ni$_2$-Fe$_2$]$^{2+}$**. The utilization of the divergent lobes apparently lessens the steric repulsion between $Fe(NO)_2$ units. In summary, the binding position of the $Fe(NO)_2$ unit with respect to the flap in the Ni-S-C_α-C_β-N five-membered rings are correlated by the competition between chemical bond directionality of the binding sulfurs and steric repulsion of the receiver units, Figure V-10.

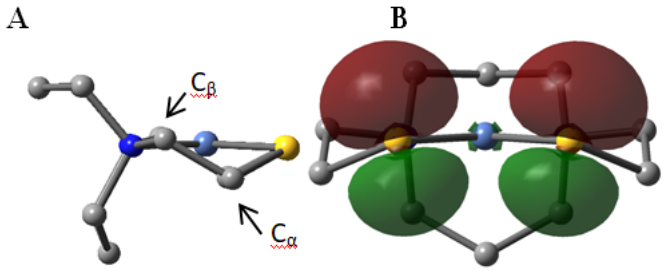

Figure V-10. A) The geometry of a free metalloligand NiN_2S_2 and **B**) its two 3*p* lone pairs presented one on each sulfur (contour plots at isovalue = 0.05 a.u. by NBO analysis). Note the relative positions of the S-C_α / S-Ni bonds and the 3*p*-lone pair.

Electrochemistry

The cyclic voltammograms of **[Ni-Fe]$^+$** (in CH_2Cl_2), **[Ni$_2$-Fe]$^+$** (in CH_3CN), as BF_4^- salts, and **[Ni-Fe]^0** (in CH_2Cl_2), were recorded under Ar at 22 ºC, and referenced to $Fc^{0/+}$ ($E_{1/2}$ = 0.0 V) as an internal standard, Figure V-11. Both the neutral complex **[Ni-Fe]^0** and the cationic analogue, **[Ni-Fe]$^+$**, used in the CV studies as its BF_4^- salt, displayed reversible reduction events at ca. -0.73 V (CH_2Cl_2), assigned to the $\{Fe(NO)_2\}^{9/10}$ couple. The NiFe complexes also present two irreversible oxidation events at ca. -0.10 V and ca. +0.45 V, differing somewhat in intensities according to the neutral or cationic sources. Both of these events are assumed to be S-based.

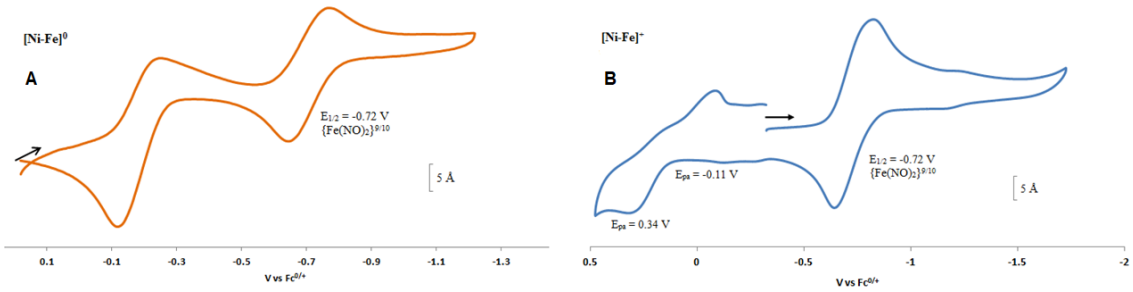

Figure V-11. Cyclic voltammograms of 2.0 mM **A) [Ni-Fe]^0** and **B) [Ni-Fe]$^+$** in CH_2Cl_2, vs $Fc^{0/+}$. The arrow indicates the initial point and direction of scan.

In CH_3CN, the trimetallic complex **[Ni$_2$-Fe]$^+$**, showed a reversible event at, $E_{1/2}$ = -0.75 V, assigned to the $\{Fe(NO)_2\}^{9/10}$ couple and an irreversible oxidation event at E_{pa} = -0.05 V, Figure V-12**.** The $E_{1/2}$ value for the $\{Fe(NO)_2\}^{9/10}$ couple, is anodically shifted by ca. 30 mV relative to the 1:1, NiFe complexes, resulting from the greater electron donation of two NiN_2S_2 centers to the $Fe(NO)_2$ redox marker. The scan rate dependences

of the $\{Fe(NO)_2\}^{9/10}$ couple for all three complexes support the assignments to reversible or quasi-reversible.

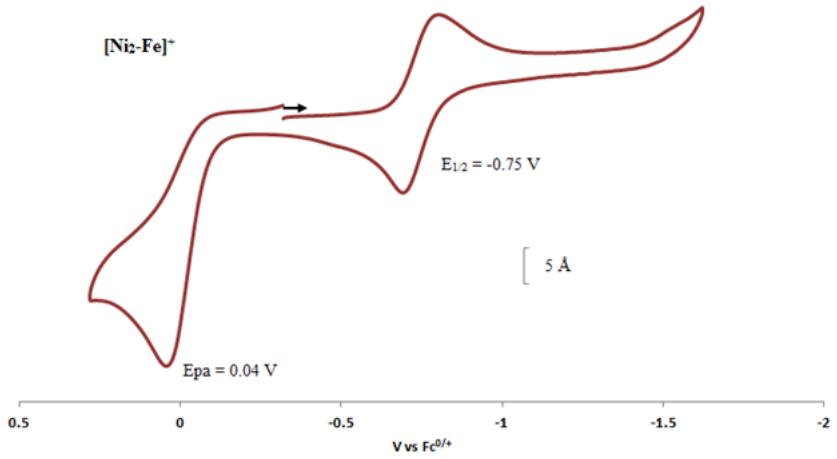

Figure V-12. Cyclic voltammogram of 2.0 mM **[Ni$_2$-Fe]$^{2+}$** in CH_2Cl_2, vs $Fc^{0/+}$. The arrow indicates the initial point and direction of scan.

Cyclic Voltammetry and Response to Added Acid.

Electrochemical studies of **[Ni-Fe]$^+$** and **[Ni$_2$-Fe]$^+$** were carried out in presence of HBF_4•Et_2O under a N_2/Ar atmosphere. For comparison the **[<u>Fe</u>-Fe]$^+$** complex was examined under similar experimental conditions. Sequential addition of HBF_4•Et_2O to a CH_2Cl_2 solution of **[Ni-Fe]$^+$** (2 mM **[Ni$_2$-Fe$_2$]$^{2+}$**) showed an increase in the cathodic current at the $\{Fe(NO)_2\}^{9/10}$ redox event at -0.73 V. The initial cathodic current response saturates with ~20 equivalents of the acid, Figure V-13 (inset). A second rise in cathodic current at -1.10 V, is observed upon addition of > 12 equivalents of the acid, which continues to rise as the catalytic current response, Figure V-13.

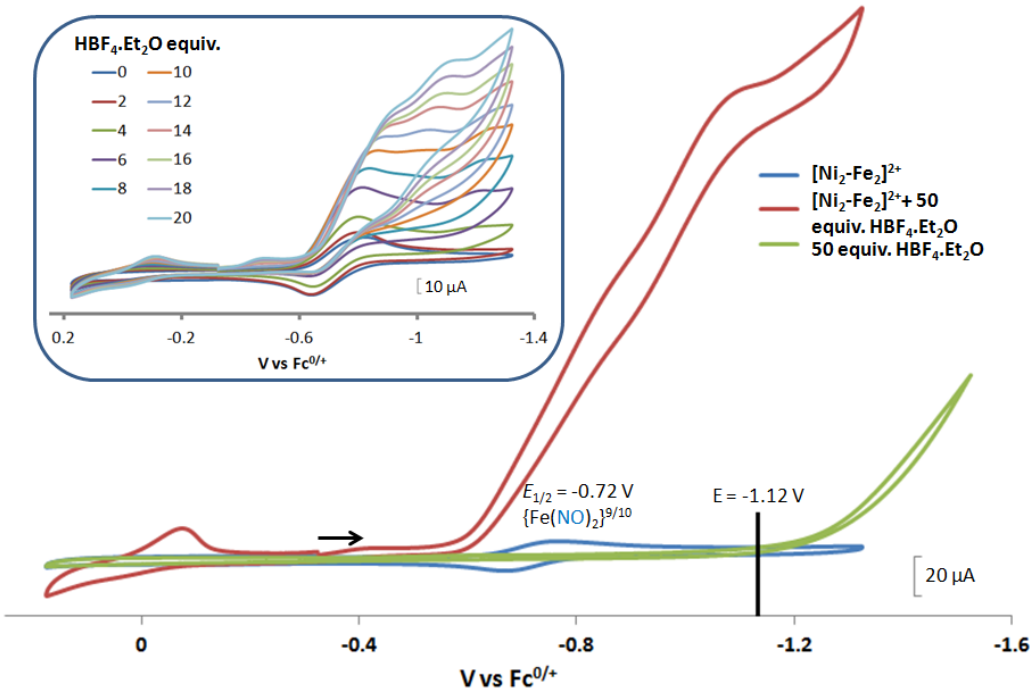

Figure V-13. Cyclic voltammograms of 2.0 mM CH_2Cl_2 solutions of $[\mathbf{Ni_2\text{-}Fe_2}]^{2+}$(or $[\mathbf{Ni\text{-}Fe}]^{+}$(blue)); with 50 equiv. (0.1 M) of added HBF_4•Et_2O (red); and, for reference, 50 equiv. (0.1 M) of HBF_4•Et_2O (green). The black line indicates the constant potential applied for bulk electrolysis, -1.12 V. Inset: Cyclic voltammograms of $[\mathbf{Ni_2\text{-}Fe_2}]^{2+}$ (or $[\mathbf{Ni\text{-}Fe}]^{+}$) with 2 to 20 equiv. aliquots of HBF_4•Et_2O. Crystalline $[\mathbf{Ni_2\text{-}Fe_2}]^{2+}$ was dissolved as its BF_4^- salt, in 0.1 M $^tBu_4NPF_6$ as supporting electrolyte, with a glassy carbon electrode at scan rate of 200 mV/s. Note: equivalents of HBF_4•Et_2O was calculated with respect to the dimeric $[\mathbf{Ni_2\text{-}Fe_2}]^{2+}$.

The phenomenon can be explained as follows: The increase in the cathodic current at -0.72 V is due to the build-up of the $\{Fe(NO)_2\}^{10}$-H^+ or $\{Fe(NO)_2\}^{8}$-H^- which is formed after the first reduction and protonation step, Figure V-15B. This H-bound species adds a second electron at -1.10 V, which results in a Fe-S bond cleavage and protonation at the free thiolate to form a thiol, Figure V-15B. The hydride on the Ni and the proton on the thiolate couples to form dihydrogen. This leads to the increase in the cathodic current at -1.10 V which is catalytic. The equivalents of HBF_4•Et_2O was

calculated with respect to the dimeric **[Ni$_2$-Fe$_2$]$^{2+}$**. Overlays of this response of the NiFe complex in presence of 50 equivalents of HBF_4•Et_2O (0.1 M), as well as the CV of the free acid, are shown in Figure V-13. The catalytic H_2 produced was confirmed by applying a constant potential at -1.12 V for 60 min (black bold line in Figure V-13), and analysis of the headspace by gas chromatography. The H_2 was quantified by an average of two consistent constant potential coulometry experiments with subtraction of the H_2 produced from the free acid. The turnover numbers (TON) for **[Ni-Fe]**$^+$ and **[<u>Fe</u>-Fe]**$^+$ were found to be 0.033 ± 0.004 and 0.042 ± 0.004, respectively, with Faradaic efficiencies of 67.6 ± 2.1% and 58.5 ± 1.3%, respectively, for H_2 production.

Following the approach of Helm and Appel,[98] and Wiese,[99] the turnover frequency (TOF) as calculated from the CV experiment for **[Ni-Fe]**$^+$, was 39.7 s^{-1}, which is slightly better than the **[<u>Fe</u>-Fe]**$^+$ complex, 26.7 s^{-1}, calculated under similar experimental conditions. The **[Ni-Fe]**$^+$ shows a saturation of the more negative catalytic current upon addition of 80 equivalents of HBF_4•Et_2O, i.e., ~0.16 M CH_2Cl_2 solution. Notably, the behavior of the **[<u>Fe</u>-Fe]**$^+$ complex is similar, and further addition of acid leads to decomposition of both catalysts. The precise calculation of overpotential is indeterminable as the thermodynamic potential ($E_{HBF4/H2,BF4-}$) of 0.1 M HBF_4•Et_2O in CH_2Cl_2 is unavailable.[126] Using the thermodynamic potential of HBF_4•Et_2O in acetonitrile (-0.26 V),[100, 177] an estimate of the overpotential of **[Ni-Fe]**$^+$ and **[<u>Fe</u>-Fe]**$^+$ were 711 mV and 660 mV, respectively, which are better relative to the **[Ni-Fe']**$^+$ and **[<u>Fe</u>-Fe']**$^+$ electrocatalysts by over 220 mV.

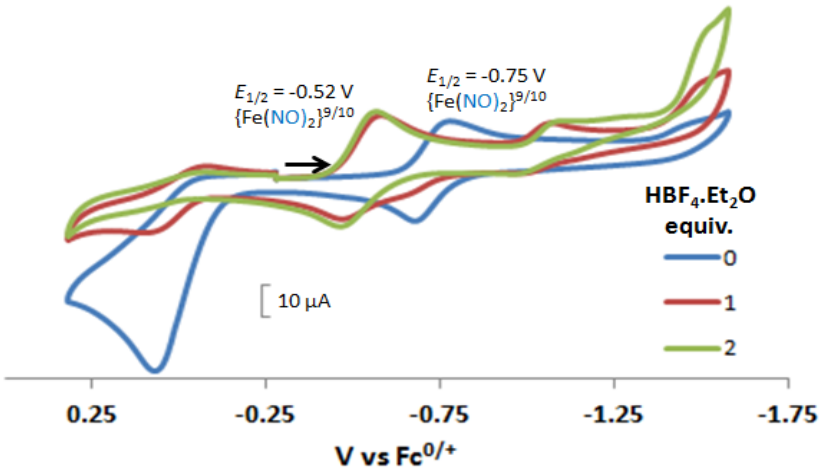

Figure V-14. Cyclic voltammograms of 2.0 mM CH_3CN solution of **[Ni$_2$-Fe]**$^+$ (blue), with 1 and 2 equiv. of added HBF_4•Et_2O (red and green, respectively).

In contrast to the NiFe complexes, addition of HBF_4•Et_2O to a 2.0 mM CH_3CN solution of [**Ni$_2$-Fe**]$^+$, did <u>not</u> show an increase in the cathodic current at -0.75 V, the reversible {Fe(NO)$_2$}$^{9/10}$ redox event. Instead, a new reversible redox event at $E_{1/2}$ = -0.52 V, appeared upon addition of two equivalents of HBF_4•Et_2O with a concomitant disappearance of the original redox process, Figure V-14. Further addition of acid resulted in electrode fouling. A possible explanation, from computational chemistry, *vide infra*, for the positive 230 mV shift is that **[Ni$_2$-Fe]**$^+$ can be protonated on its exposed thiolate sulfur by HBF_4•Et_2O, *vide infra*. Such would account for the greater ease of reduction for the {Fe(NO)$_2$}$^{9/10}$ couple, compared to the **[Ni$_2$-Fe]**$^+$ complex. Supporting this conclusion is that addition of 1 equivalent of HBF_4•Et_2O to a CH_3CN solution of **[Ni$_2$-Fe]**$^+$ produced a small but definite shift of the ν(NO) in the IR spectrum from 1787 and 1734 cm^{-1} to 1793 and 1737 cm^{-1}. In addition, the irreversible oxidation event at 0.07 V, which is assumed to be sulfur-based oxidation, shows a decrease in the anodic

current upon addition of acid, indicating disulfide formation is inhibited under acidic conditions.

Computational Mechanistic Study (Dr. Shengda Ding and Prof. Michael B. Hall)

The electrochemical study points to additional questions for computational study: A) How do the calculated electrocatalytic mechanisms compare for the hard-soft vs. soft-soft donor/receiver adducts? B) Can computational analysis clarify those cases of non-catalytic electrochemical responses to added protons? Modeling is extended to **[Ni$_2$-Fe]$^+$**, along with **[Ni-Fe]^0**, [**Ni-Fe**]$^+$, in various oxidation states and with multiple added protons to answer these questions.

Mechanistic Perspectives of the Proton Reduction Electrocatalysis by [Ni-Fe]$^+$/[Ni-Fe]^0 and Comparison to [Fe-Fe]$^+$

An earlier computational analysis of a HER electrocatalysis mechanism proposed for the **[Fe-Fe]$^+$** complex, Figure V-1, focused on the first reduction event with a strong acid proton source.[74] The successive reduction event ultimately allowed for double proton addition to the $Fe(NO)_2$ unit and formation of a dihydride, Figure V-15A.[74, 178] Making use of electron transfer from the reduced $\{Fe(NO)\}^8$, reductive elimination from the $\{Fe(NO)\}^6$-$\{Fe(NO)_2\}^8$ morphed into an η^2-H_2–$Fe(NO)_2$, restoring $\{Fe(NO)\}^7$-$\{Fe(NO)\}^9$, with H_2 formation and loss. Note that no hemi-lability of the metallodithiolate ligand is necessary here as the mechanism does not entail hydride/proton coupling to H_2, but rather reductive elimination from two hydrides.[178]

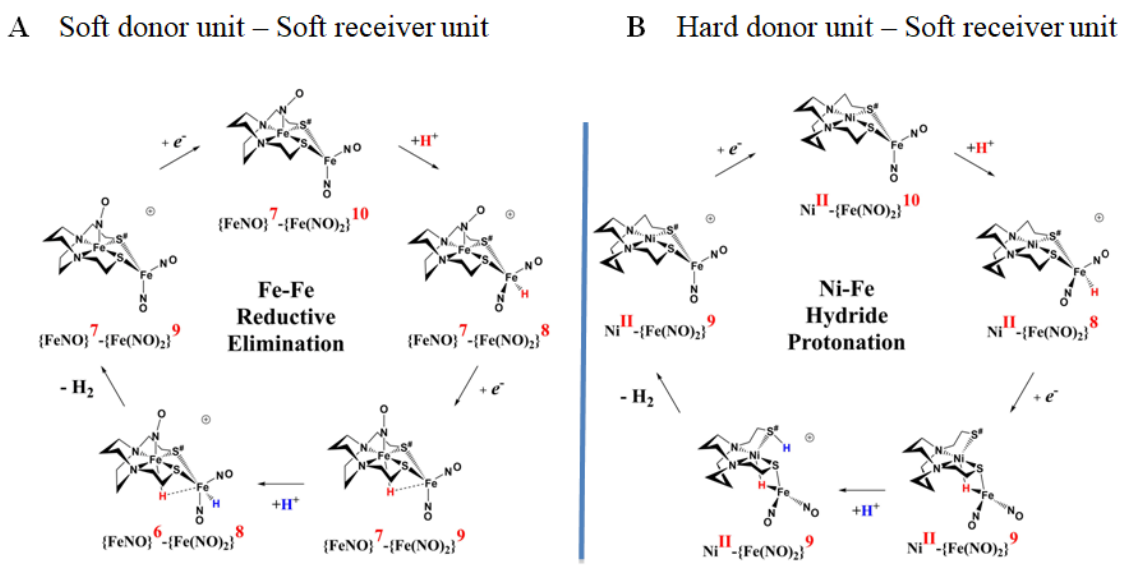

Figure V-15. Comparative catalytic cycles for H_2 production catalyzed by **[Fe-Fe]**$^+$ and **[Ni-Fe]**$^+$**.** All p*K*a, thermodynamic,and metric data for the two mechanisms are available in a separate report.[50]

The **[Ni-Fe]**$^+$ and its reduced counterpart **[Ni-Fe]**^{0} are determined to be electrocatalysts at -0.73 V for H_2 production with HBF_4•Et_2O, Figure V-13. [Note: The computational study finds that the **[Ni$_2$-Fe$_2$]**$^{2+}$, whose dimeric structure was established in the solid state by crystallography, finds greater stability in solution as the monomeric form, **[Ni-Fe]**$^+$. Experimental evidences including ESI-MS and determination of μ_{eff} support this thesis, *vide supra*.] The catalytic cycle is thus initiated with the monomer **[Ni-Fe]**$^+$ (Figure V-15B). As indicated in Figure V-15B, the $\{Fe(NO)_2\}^9$ in the **[Ni-Fe]**$^+$ unit accepts the first incoming electron, followed by the first proton, to create a hydride on the now $\{Fe(NO)_2\}^8$ unit. Addition of a second electron activates the hemi-lability of the bridging thiolate to break one S-Fe bond, while the terminal hydride becomes bridging between Fe and Ni. The cleavage of the S-Fe dative bond essentially releases

one *p* lone pair of the thiolate so that S can act as a pendant base to accept the second proton and guide it to a coupling position with the hydride and produce H_2. Details of the full catalytic cycle with energetics and analysis of electronic structure evolution for both **[Fe-Fe]**$^+$ and **[Ni-Fe]**$^+$ are presented in a separate report.[178]

Explanation for the Absence of Catalytic Activity of [Ni$_2$-Fe]$^+$.

While one might have expected the dangling thiolates in the 2:1 complex **[Ni$_2$-Fe]**$^+$ to act as a pendant base, in fact this complex does not show any catalytic activity in the presence of strong acid, HBF_4•Et_2O, within the solvent potential window. A computational study, summarized in Figure V-16, reveals that while reduction still occurs on the $Fe(NO)_2$ unit, the protonation process is diverted from the $Fe(NO)_2$ unit. In this 2:1 complex, the computations show that only one thiolate from each NiN_2S_2 binds to $Fe(NO)_2$, while the other thiolate, is "free" to interact with other electron acceptors; thus it may also be protonated, even before the reduction of the $\{Fe(NO)_2\}^9$ unit occurs, which is supported by experiment, *vide supra*.

According to the computations, in the reduced **[Ni$_2$-Fe]^0** the "free" thiolate competes with the reduced $\{Fe(NO)_2\}^{10}$ unit for the incoming proton (Figure V-16A); in addition, by rotation around an Fe-S bond, the two NiN_2S_2 ligands may orient their "free" thiolate sulfurs to pinch the proton, *i.e.*, consequently forming a strong hydrogen bond, Figure V-16 A and B. Spectroscopic evidence supports protonation on S even before reduction, i.e., in **[Ni$_2$-Fe]**$^+$. Two geometries of the pinched proton by two "free" thiolates, **[Ni$_2$-Fe-SHS-1]**$^+$ and **[Ni$_2$-Fe-SHS-2]**$^+$ can be achieved by either translating or

rotating one NiN_2S_2 unit of **[Ni$_2$-Fe]**, respectively. Precedent in Dubois' $Ni(P_2N_2)_2$ catalysts,[102] a proton pinched between two amine N bases is relatively stable; in our case, the pinched proton is even more stable than a hydride on $Fe(NO)_2$ (Figure V-16A). However, the mechanistic clue from the **[Ni-Fe]** complex[178] indicates the requirement for a proton to be reduced into a hydride, by $\{Fe(NO)_2\}^{10}$, before the H_2 can be produced by the proton-hydride coupling mechanism. Therefore, the formation of a stable pinched proton likely prevents the generation of the hydride and cuts off the catalytic cycle. The thiolate already bound to $Fe(NO)_2$ also helps stabilize the proton on a "free" thiolate, to a smaller extent, with the example of **[Ni$_2$-Fe-SHS-3]**$^+$ (Figure V-16A).

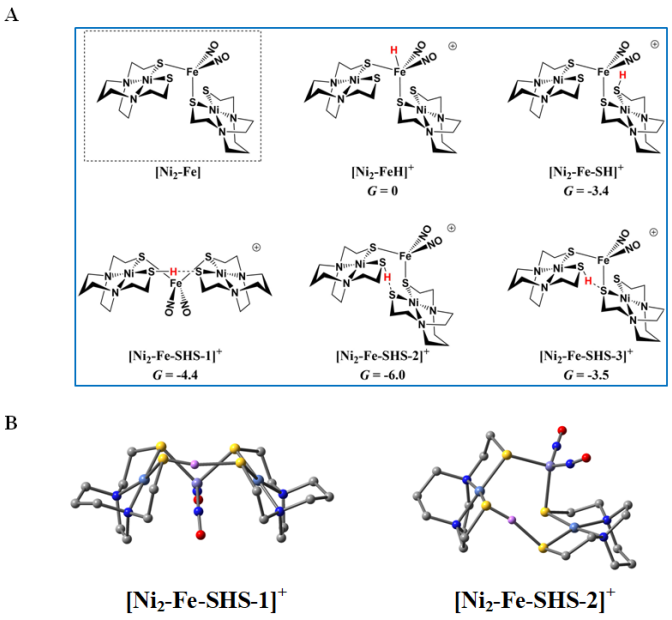

Figure V-16. The protonation of **[Ni$_2$-Fe]**, the reduced form of **[Ni$_2$-Fe]**$^+$ and **A**) possible protonated products with **B**) 3D geometric presentations of selected species featuring the pinched proton. The computationally derived structures are rendered so as to show the NiN_2S_2 metalloligand without altering the rigidity of the N_2S_2 planar structure. All hydrogens except the one pinched between two sulfurs are omitted.

Conclusion

Our collection of hydrogen evolution reaction catalysts is summarized in Figure V-17. While the small differences in donor units and acceptor units do not influence the overall structures of the S-bridged bimetallics; all have butterfly-like [M(μ-SR)$_2$Fe] core and the potential for opening up sites for proton addition via the hemi-lability of the metallothiolate donors. Nevertheless demonstrable and explicable differences are seen in their catalytic performances as indicated by catalytic potential, required acid strength, TOF and TON.

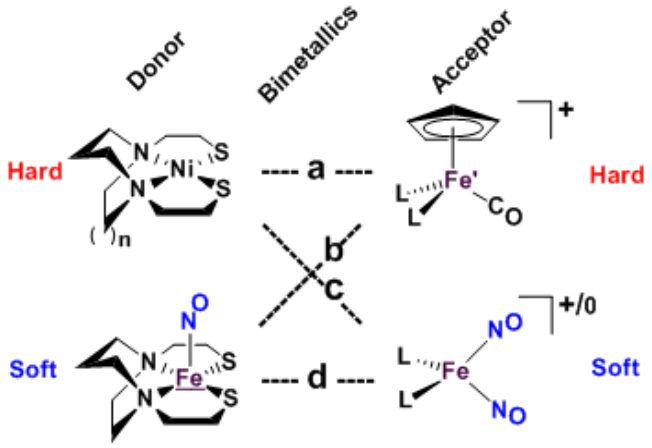

Bimetallics			E (V)	TOF (s^{-1})	TON
[Ni-Fe']$^+$	(a)	hard - hard	-1.64	52 (TFA)	0.26
[Fe-Fe']$^+$	(b)	soft - hard	-1.19	69 (TFA)	0.33
[Ni-Fe]$^+$	(c)	hard - soft	-0.73	39 ($HBF_4.Et_2O$)	0.033
[Fe-Fe]$^+$	(d)	soft - soft	-0.78	26 ($HBF_4.Et_2O$)	0.042

Figure V-17. A comparative schematic for a matrix of bimetallic electrocatalysts containing hard/soft donor/acceptor units.

Analogous to the HSAB (Hard and Soft (Lewis) acids and bases) concept, we offer an electronic parallel, "soft *vs.* hard donor/receiver units", in this case directed

towards the number of NO ligands in the bimetallics ranging from 0 to 3, with increasing flexibility (*i.e*. softness) of electronic structure within each unit. The non-innocence of the NO ligand confers electron uptake at milder potentials, which we have seen in both the donor units and acceptor units. Thus the incorporation of NO ligands on the acceptor units, the 'hard-soft' and 'soft-soft' electrocatalysts lead to energetically more accessible catalytic current, however, at the cost of a stronger acid and a lower TOF in comparison to the bimetallics with hard acceptor units.

While these electrocatalysts are only moderately efficient for H_2 production, they are well-behaved and have demonstrated reproducibility. Two of the catalysts, **c** and **d**, with soft receivers, are isolated and crystallized in both oxidized and reduced forms at ambient conditions lending confidence to the presumed catalytic cycle.

Features in the electrochemical scans may be reasonably ascribed to protonation products whose identities are further described by computational chemistry. The resulting computational mechanisms identify key features that may guide future synthetic targets. For example, the hemi-lability of the S-donors may be optimized by steric constraints; the usefulness of the $Fe(NO)_2$ unit as electron depot and protonation site with low redox potential, should encourage explorations with other redox-active, soft acceptors. The computations also suggest a mechanistic paradigm of heterolytic H^-/H^+, hydride-proton, coupling for bimetallics **a**, **b** and **c** from the chart, and reductive elimination from **d** arising in the soft-soft construct. Such a supposition derives from extreme electron delocalization in the trinitrosylated **[Fe-Fe]**$^+$ complex and argues that

suitably constructed first row, bimetallic complexes may take on two-electron processes that emulate noble metals.

CHAPTER VI

DEVELOPMENT OF HETEROBIMETALLICS FOR REACTIVITY STUDIES OF TERMINAL THIOLATES

Introduction

The compositions of enzyme active sites (EAS) that mediate transformations suggestive of classical organometallic chemistry, such as the C - C coupling of CH_3 and CO in Acetyl coA synthase (ACS),[72-73] or the assembly/disassembly of dihydrogen via H^+-H^- processes in the hydrogenases (H_2ase),[37] have encouraged synthetic analogue design within a new area of multi-metallic chemistry.[56, 179] As in organic natural product synthesis, the development of methods to access complex heterobi- and heteropolymetallic models of metallo-EAS's is a worthy challenge, with fundamental discoveries and potential applications beyond that of reproducing properties immediately associated with the molecular structure of a particular inorganic natural product. In each of the examples cited above, *i.e.*, ACS,[72-73] [FeFe]- and [NiFe]-H_2ase,[37] the presence of thiolates that act as sulfur bridges between two metals stand out as a core feature. Furthermore, and of importance to this report, in the [NiFe]-H_2ase a terminal cysteinyl thiolate sulfur is well positioned to act as an internal pendant base, participating in Lewis pairs of H^- and H^+ required in the catalysis.[37, 71] We, and others, have demonstrated that metallothiolates within a class of MN_2S_2 complexes may act as S-donor ligands to a selection of iron receivers, such as $[(\eta^5\text{-}C_5R_5)Fe(CO)]^+$ (R = H, CH_3; Cp and Cp*,

respectively) and the iron dinitrosyl unit, $Fe(NO)_2$.[160, 162, 164-165] Whereas most bimetallic products enlisting the MN_2S_2 complexes as metalloligands demonstrate bidentate binding with butterfly-like $M(\mu\text{-}SR)_2M'$ core structures,[162, 164] the monodentate $(RS)M(\mu\text{-}SR)M'$ derivative is accessible in some cases;[162] both the monodentate $[\kappa^1\text{-}MN_2S_2\bullet Fe(CO)_2]^+[BF_4]^-$ and the bidentate $[\kappa^2\text{-}MN_2S_2\bullet FeCp(CO)]^+[BF_4]^-$ were isolated and characterized in the development of the mechanism of electrocatalytic proton reduction.[117, 160, 165] The bidentate complexes, in particular, delineated reduction-induced hemi-lability of the cis-dithiolates to generate terminal-thiolate, competent to bind a proton, as an intermediate for $H^-\bullet\bullet\bullet H^+$ coupling for dihydrogen production in the catalytic cycle, under electrochemical conditions.[160, 178]

In an earlier study we showed the non-innocence of the $Fe(NO)_2$ unit, as a receiver group, bound to redox-active $(NO)FeN_2S_2$ metalloligand, that in general served as an electrocatalyst for proton reduction.[74] The $Fe(NO)_2$ unit, which arguably may serve as surrogate for the $Fe(CO)(CN)_2$ portion of the [NiFe]-H_2ase active site,[74] has an added property of redox activity typically indicated by the Enemark/Feltham notation,[151] $\{Fe(NO)_2\}^{9,10}$. Herein, we describe the synthesis, characterization and reactivity study of a class of model complexes bearing N-heterocyclic carbene (NHC) stabilized $Fe(NO)_2$ unit with MN_2S_2metalloligands in monodentate binding mode, $[\kappa^1\text{-}MN_2S_2\bullet Fe(NO)_2(IMes)]^+[BF_4]^-$, (where M = Fe(NO), Co(NO), Ni).[180] In accordance with the concept of the cysteinyl-S as a potential protonation site in [Ni-R] state of the [NiFe]-H_2ase enzyme catalytic cycle,[71] the free thiolate in the model complexes emulates the former in the same capacity. The NHC-stabilized trinitrosyl iron unit,

$[(IMes)Fe(NO)_3]^+$,[96] show-cases its efficiency as an inorganic synthon for generating a series heterobimetallic model complexes.

Results and Discussion

Figure VI-1 displays the building blocks leading to a series of $Fe(NO)_2$ complexes in which MN_2S_2 metallodithiolates serve as monodentate donor ligands,[180] while holding a second thiolate nearby as potential pendant base. The MN_2S_2 metalloligands (where N_2S_2 is bismercaptoethanediazacyclooctane or bme-daco and M = Fe(NO), Co(NO), Ni) are hereafter abbreviated as **Fe***, **Co***, **Ni***, respectively, the $(IMes)Fe(NO)_2$ unit as **Fe'**, and the resulting three bimetallic complexes are referred to as**Fe*-Fe'**, **Co*-Fe'** and **Ni*-Fe'**.

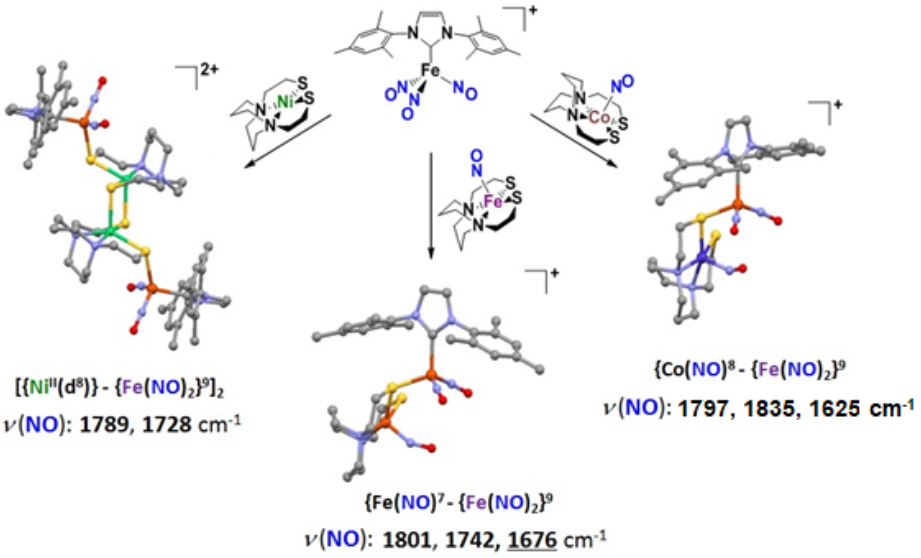

Figure VI-1. Synthesis of bimetallics derived from the TNIC[96] synthon. The BF_4^- counter anion was omitted for clarity. The THF solution ν(NO) values are listed below each structure. The ν(NO) for $(NO)MN_2S_2$ metalloligands are underlined.

The homolog of bme-daco, bismercaptoethanediazacyclohepane or bme-dach, was also used in certain cases for comparison, and such MN_2S_2's are abbreviated as **M**, where M = (NO)Co,[180] (NO)Fe and Ni, and the resulting heterobimetallics are referred as **Co-Fe'**[181] and **Ni-Fe'**. The lability of a single NO ligand in the $(IMes)Fe(NO)_3^+$ synthon, and the evident stability of the subsequently produced $Fe(NO)_2$ unit, is the basis of the success of this approach.[96]

The reactants are mixed together as solids and the bimetallic products immediately form in near quantitative yields as solvent is added demonstrating the prominent reactivity/electrophilicity of the $(IMes)Fe(NO)_3^+$ synthon. Isolated as crystalline solids, the molecular structures of the products are presented in Figure VI-1, and described in detail below. The *v*(NO) IR spectral monitor indicates completeness of reaction; further, the shifts of *v*(NO) are readily interpreted according to the drain of electron density from the metallodithiolate ligand, and enhancement of electron density at the $Fe(NO)_2$ acceptor. Note that the composition of complex, **Ni*-Fe'**, results from dimerization, producing the Ni_2S_2 core with pentacoordinate Ni^{II} centers. Whether this structure persists in solution or dissociates to the monomeric complex, analogous to the **Fe*-Fe'** and **Co*-Fe'**, is not known with certainty. Nevertheless, pentacordinate nickel complexes are not common. Structural overlays of **Ni*-Fe'** (in gold) with similar core structures found in A) **[Fe(bme-daco)]$_2$** and B) **[Zn(bme-daco)]$_2$** (in grey), shown in Figure VI-2, display the consistency of the Ni_2S_2 core in these complexes.

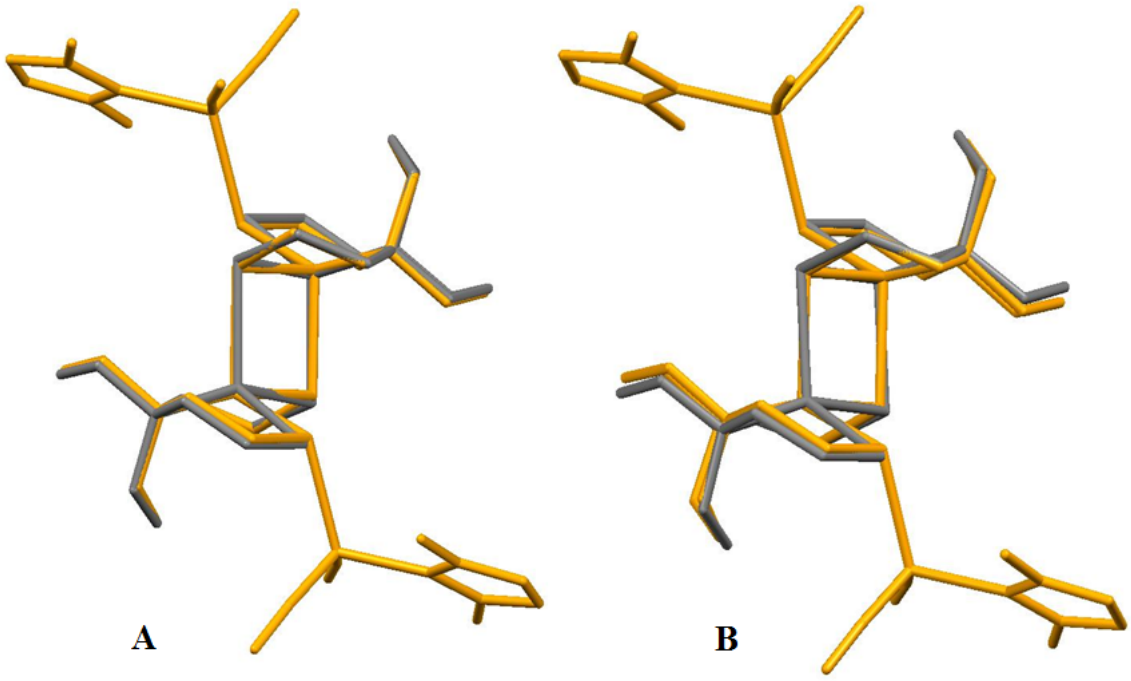

Figure VI-2. Structural overlays of **Ni*-Fe'** in gold with A) $[Fe(bme\text{-}daco)]_2$ and B) $[Zn(bme\text{-}daco)]_2$ in grey. Hydrogen atoms and the mesityl groups of the NHC are omitted for clarity.

Notably, the **Ni-Fe'** derivative, in which the nickel is in the bme-dach ligand framework, shows a two-line *ν*(NO) IR spectral pattern, typical of DNICs. In contrast, the solution spectrum of **Ni*-Fe'** invariably shows shoulders on each absorption, which might be an indication of two species in solution. The dimerization of the **Ni*-Fe'** complex can be somewhat explained as follows: the drain of electron density from the NiN_2S_2 metallodithiolate ligand upon binding to the electrophilic $(IMes)Fe(NO)_2^+$ unit leads to an apparent dearth of electron density at the Ni^{II} center, compensating by a needed stabilization from an adjacent thiolate of a second NiN_2S_2 unit. The Ni^{II} center is displaced from the mean N_2S_2 plane by about 0.4 Å in the process. The flexibility of the

bme-daco ligand over bme-dach ligand allows such distortion in the NiN_2S_2 plane with a τ parameter of 0.33 for **Ni*-Fe'** complex. This apparent puckering of the N_2S_2 plane is reflected in its evident stability in the solid state as a dimer. It may account for the failure to grow X-ray quality crystal of **Ni-Fe'** with the less flexible bme-dach ligand.

The bimetallic products **Ni*-Fe'**, **Co*-Fe'** and **Fe*-Fe'** somewhat vary in stability. The diiron complex **Fe*-Fe'** readily releases its NHC ligand, IMes, with monodentate-bidentate conversion yielding the diamagnetic $\{Fe(NO)\}^7$•$\{Fe(NO)_2\}^9$ cation, $[(\kappa^2\text{-}Fe(NO)N_2S_2)Fe(NO)_2]^+$,[74] Figure VI-3, earlier studied extensively (with bme-dach, n = 1) for its ability as an electrocatalyst for proton reduction.[74] In contrast, the nickel and cobalt derivatives are stable in the monodentate form. The $\{Co(NO)\}^8$•$\{Fe(NO)_2\}^9$ cation, **Co*-Fe'**, structurally identical to the diiron species, **Fe*-Fe'**, is also stable as formulated in Figure VI-1. That is, the κ^1-$Co(NO)N_2S_2$ or the κ^1-NiN_2S_2 metalloligands do not ring-close and form the analogue of its iron congener,[74] even under thermal stress. As indicated in Figure VI-1, the structure remains intact, retaining the NHC ligand. Addition of a second equivalent of NiN_2S_2 to **Ni-Fe'**, however, leads to a loss of NHC ligand and a trimetallic complex $[(\kappa^1\text{-}NiN_2S_2)_2Fe(NO)_2]^+$is obtained, Figure VI-3. Similar displacement of NHC ligand in **Co-Fe'** by excess $(NO)CoN_2S_2$ was not observed. The loss of NHC ligand in case of the **Fe*-Fe'** complex to form the bidentate compound can be explained as that of spin-pairing of the individual paramagnetic $\{Fe(NO)\}^7$ and $\{Fe(NO)_2\}^9$ diiron centers and resulting diamagnetism, the Fe-Fe distance being ~2.7 Å.[74] The higher donor ability of

NiN_2S_2 over $(NO)CoN_2S_2$ might be a plausible reason for the displacement of the NHC in case of the former.[124]

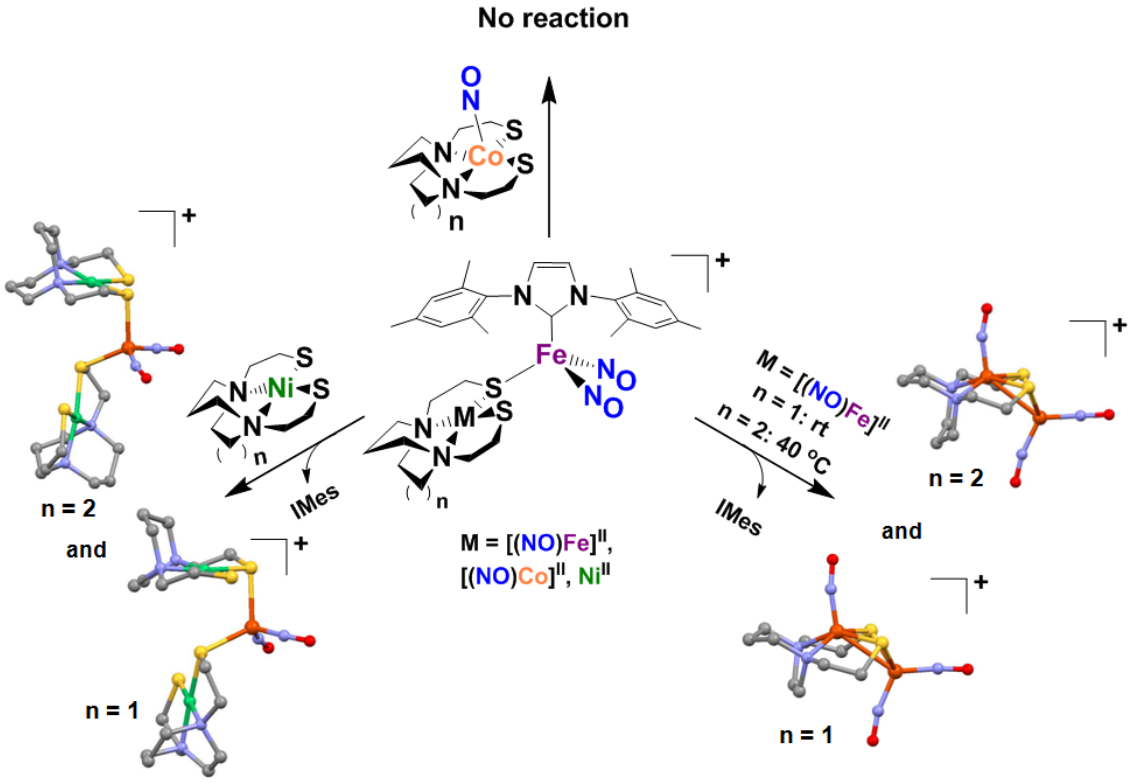

Figure VI-3. Reactivity and stability studies of $[IMes(\kappa^1\text{-}MN_2S_2)Fe(NO)_2]^+$ showing displacement of the carbene, IMes, ligand. The molecular structures of $[(\kappa^2\text{-}Fe(NO)N_2S_2)Fe(NO)_2]^+$ with the bme-dach ligand (n = 1) and $[(\kappa^1\text{-}NiN_2S_2)_2Fe(NO)_2]^+$ with bme-daco ligand (n = 2) were previously reported. The BF_4^- anions are omitted for clarity.

Molecular Structures

As indicated in Figure VI-1, and confirmed by the metric parameters provided in the Table VI-1, the structures of the metallodithiolate components and the $(IMes)Fe(NO)_2$ moiety within the bimetallics are by and large identical to their isolated

forms. The overall M•••Fe' distance, *ca*. 3.9 Å, disproves any metal-metal bonding interaction in the bimetallic complexes, and allows for along S_{nb}•••Fe' distance of *ca*. 4.1 Å. The $[\kappa^1\text{-}MN_2S_2\bullet FeCp(CO)_2]^+$ complexes, where M is Ni and (NO)Co, reported similar M•••Fe distances with S_{nb}•••Fe' distance ranging from *ca*. 4 to 4.5 Å.[160, 165] The utilization of the diverging lobe of one of the lone pair of electrons on the bridging thiolate, which is nearly co-linear/parallel with that of the S-C_α bond, permits this conformation of the metallodithiolate construct with the free thiolate slightly oriented away from the $Fe(NO)_2$ unit.[160, 165] This orientational effect of the bridging thiolate lone pairs were hypothesed in the '*gedanken*' experiment to strategically create a frustrated Lewis pair (FLP), involving the unbound, basic thiolate and the redox-active $Fe(NO)_2$ unit, that might promote proton-hydride binding/coupling, at respective centers.

A pseudo tetrahedral geometry is observed at the Fe' center with C-Fe'-S_b angle being *ca*. 110° and the N-Fe'-N angle ranges from 115° to 121°. The dinitrosyl iron units display a typical bent nitrosyl-iron bond angle, having an 'attracto' orientation,[172] with an average Fe'-N-O angle of *ca*. 169° typical of oxidized $\{Fe(NO)_2\}^9$ units. The metallodithiolate unit displays interesting changes in their metric parameters upon binding to the dinitrosyl iron unit. The M-N-O angle in the **Fe*-Fe'** complex are slightly more linear, by 2°, than the free metalloligand while the M-N-O angle in **Co*-Fe'** complex displays sufficient linearity by around 8°. The S-M-S angle remains almost constant for **Fe*-Fe'** complex with a slight constriction for the **Co*-Fe'** by 2°, while in **Ni*-Fe'**, it shows a remarkably opposite trend where S-M-S angle opens up by 5°, a feature which is unprecedented.[162] Similar features were observed in the previously

reported monodentate (κ^1-MN_2S_2)M' complexes.[160, 165] Metric parameters of significance to the three [(NHC)(κ^1-MN_2S_2)Fe$(NO)_2$]$^+$ complexes are given in Table VI-1.

Table VI-1. Selected metric parameters of **Ni*-Fe'**, **Co*-Fe'**, **and Fe*-Fe'**.

	Ni*-Fe'	**Co*-Fe'**	**Fe*-Fe'**
M···Fe' / Å	3.838 (8)[a]	3.873 (1)	3.925 (1)
S_b-Fe' / Å	2.272 (1)[a]	2.296 (1)	2.257 (1)
S_{nb}···Fe' / Å	4.192 (1)[a]	4.278 (1)	4.098 (2)
Fe'-C / Å	2.025 (4)[a]	2.039 (5)	2.046 (3)
S_b-M / Å	2.367 (1)[a]	2.262 (1)	2.242 (1)
S_{nb}-M / Å	2.336 (1)[a]	2.220 (2)	2.215 (1)
∠C-Fe'-S_b / °	111.4 (1)	111.0 (2)	109.5 (1)
∠S-M-S / °	94.7 (4)[a] *89.4 (1)*[b]	86.7 (5) *88.6 (6)*[b]	88.5 (4) *88.1 (9)*[b]
∠M-S-Fe' / °	111.6 (4)[a]	116.4 (6)	121.5 (4)
∠M-N-O / °	---	143.9 (1) 137 *129.1 (6)*[b]	153.1 (3) *151.3 (6)*[b]
∠Fe'-N-O / °	170.2 (3)[a]	169.2 (4)[a]	168.1 (3)[a]
∠N-Fe'-N / °	117.6 (2)[a]	121.1 (2)	115.2 (2)
∠O-Fe'-O / °	109.7 (1)[a]	115.3 (1)	105.5 (9)
M-N_2S_2disp.[c] **/ Å**	0.396[a] *0.000*[b]	0.368 *0.372*[b]	0.478 *0.480*[b]

[a]Average value.
[b]Represents corresponding metric data of the free metalloligand, M(bme-daco)
[c]Displacement of M from N_2S_2 best plane.

Electrochemical Studies

Due to the similarity in the electron donor abilities of the (bme-daco)M and the (bme-dach)M metalloligands,[162] the heterobimetallic complexes with the metalloligands bearing the bme-dach ligand framework was primarily chosen for study. Cyclic voltammogram (CV) of **Ni-Fe'** as BF_4^- salt, was recorded at room temperature under argon in CH_3CN solutions containing 0.1 M [^{t}Bu$_4$N][PF_6] as supporting electrolyte using

a glassy carbon working electrode. The CV scans at 200mV/sec are shown in Figure VI-4 with assignments listed therein.

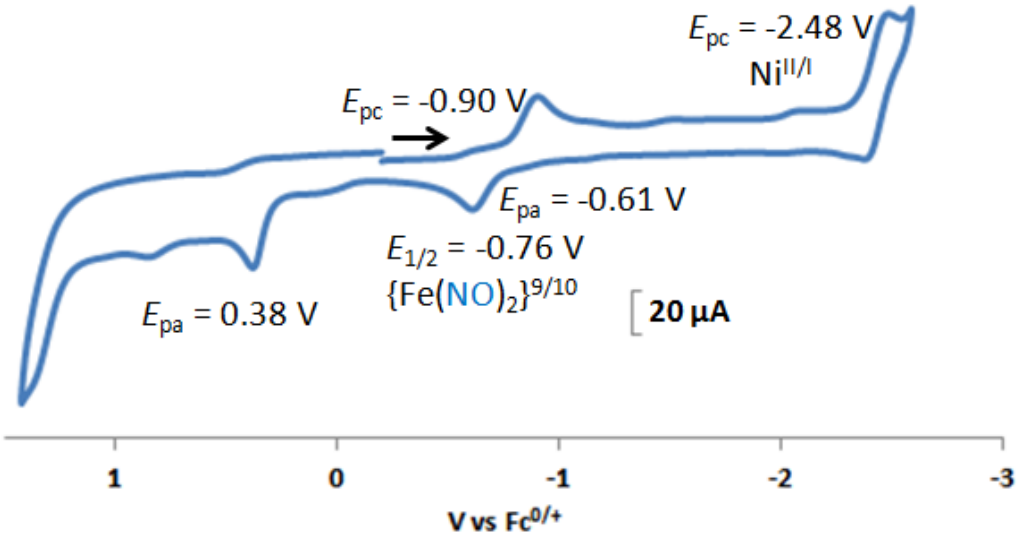

Figure VI-4. Cyclic voltammogram of **Ni-Fe'** as its BF_4 salt in CH_3CN at 200 mV/s.

The **Ni-Fe'** complex showed a reduction event at -0.90 V and a concomitant oxidation event at -0.61 V that are assigned for the $\{Fe(NO)_2\}^{9/10}$ redox events. Since the ΔE for these two redox processes is 290 mV we tentatively call these events chemically quasi-reversible (with an apparent $E_{1/2}$ of -0.76 V); the scan rate studies are shown in Figure VI-5. The irreversible cathodic event at -2.48 V was assigned to the $Ni^{II/I}$ reduction event as it shows an almost negligible shift in the redox potential compared to the free metalloligand (NiN_2S_2); a feature that has precedence in literature and can be explained by the fact that an initial addition of electron to the $Fe(NO)_2$ unit calls for higher energy $Ni^{II/I}$ reduction.[181] Consistency of the repeated scans, with minor

deposition on the working electrode, argues for stability of the complex. An irreversible oxidation event at 0.38 V was assigned to S- based oxidation.

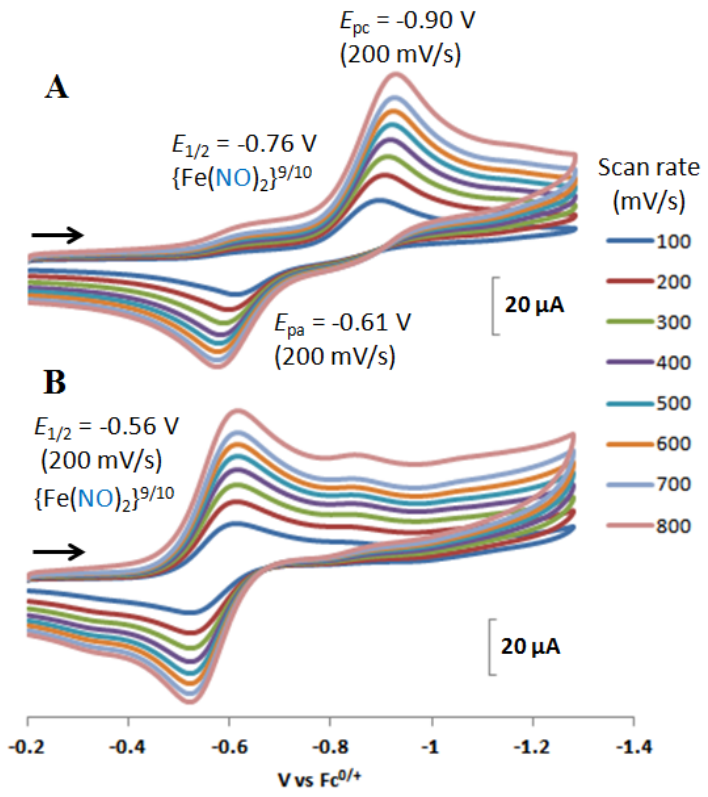

Figure VI-5. Stacked cyclic voltammograms of A) **Ni-Fe'**and B) **Ni-Fe'** in presence of 1 equivalent of $HBF_4.Et_2O$ as a function of their scan rates in CH_3CN.

Cyclic voltammograms of **Ni-Fe'** in presence of one equivalent of HBF_4•Et_2O showed a significant positive shift in the $\{Fe(NO)_2\}^{9/10}$ cathodic reduction event by ~300 mV while a small positive shift was noticeable for the anodic oxidation event, by 90 mV, Figure VI-5. The ΔE for the new redox events is 60 mV, which is within the limits for the features of a Nernstian reversibility (i_{pa}/i_{pc} = 0.95). Further addition of acid, however, did not show an increase in cathodic current as expected for catalytic H^+ reduction.

Instead, the reversible features were maintained till 2.5 equivalents of acid. This apparent shift in the redox potentials bears semblance to previous studies involving $[(NiN_2S_2)_2(Fe(NO)_2]^+$ complexes, as discussed in Chapter V.[182] It was postulated that a proton was bound to the unbound thiolate which was further stabilized by hydrogen bonding to the nearby free thiolate.[182] However, in the present case, stabilization via H-bond is unrealistic; one might argue about the redox state of the new species formed upon protonation of the **Ni-Fe'** under electrochemical conditions, *i.e.*, the **Ni-Fe'** complex gets reduced to $\{Fe(NO)_2\}^{10}$ prior to protonation or does the unbound thiolate have a sufficiently high pKa to effect protonation prior to reduction. Such questions from the CVs compelled us to check the nucleophilicity/basicity of the unbound thiolate with suitable electrophiles.

Reactivity Studies

Reactivity studies of the terminal thiolate in $[(NHC)(\kappa^1\text{-}MN_2S_2)Fe(NO)_2]^+$ complexes with electrophiles are summarized for **Ni-Fe'** in Figure VI-6. With alkyl halides, IR spectral changes were associated with cleavage of the Fe-S bond, capture of the $[(IMes)Fe(NO)_2]^+$ unit by the halide, and a concomitant formation of the S-alkylated $NiN_2S_2{\bullet}R^+$ complexes. The products in these reactions were isolated and characterized. The $NiN_2S_2{\bullet}R^+$ (where R = C_2H_5 and $C_6H_5CH_2$) were isolated and characterized using ^1H, ^{13}C and ESI-MS studies. The molecular structure with X = Br was obtained in this study; that of the $(IMes)Fe(NO)_2I$,[183] derived via an alternate synthetic procedure, is in the literature.

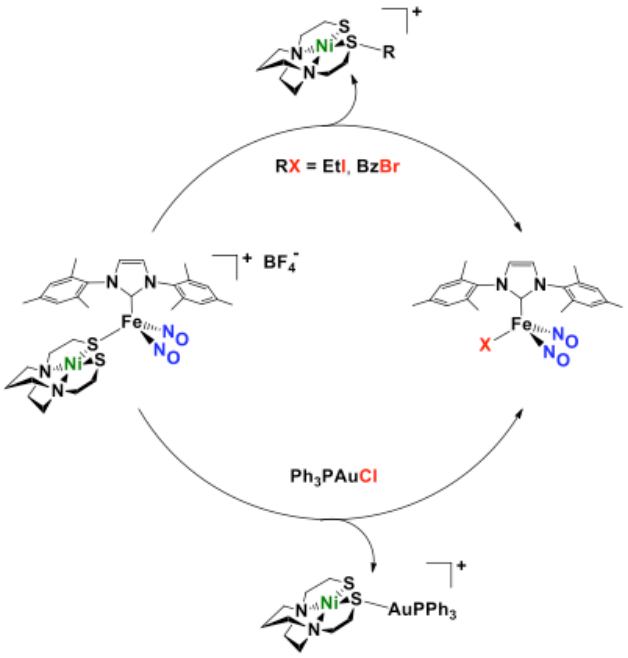

Figure VI-6. Reaction of **Ni-Fe'** with alkyl halides and Ph_3PAuCl in THF solvent.

Likewise, with the Ph_3PAuCl reagent, a rapid reaction ensues with products that find displacement of the NiN_2S_2 metalloligand in the DNIC while the Ph_3PAu^+ electrophile, introduced as a surrogate for a proton addition, *vide infra*, completes the metathesis by attaching itself to a thiolate sulfur. The products, $[NiN_2S_2{\bullet}AuPPh_3]^+[BF_4]^-$ and $(IMes)Fe(NO)_2Cl$, co-crystallized from the same solution. $AuPPh_3^+$ bound Ni(bme-daco) and CH_3 bound Ni(bme-dach) were reported earlier,[81, 173] synthesized from different synthetic routes. The molecular structures of $(IMes)Fe(NO)_2X$ (where X = Cl, Br, I) are shown in Figure VI-7 and their metric parameters are summarized in Table VI-2.

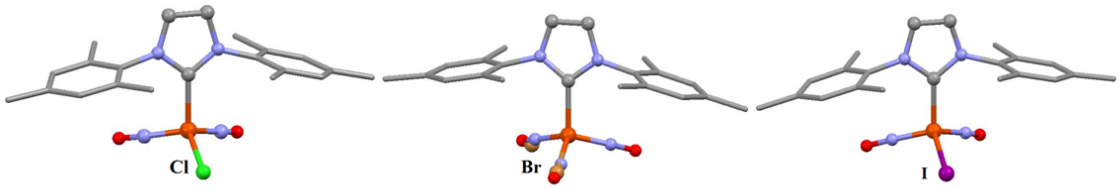

(IMes)Fe(NO)$_2$Cl **(IMes)Fe(NO)$_2$Br** **(IMes)Fe(NO)$_2$I**

Figure VI-7. Molecular structures of **(IMes)Fe(NO)$_2$X** (where X = Cl, Br, I[184]) as ball and stick renditions.

Table VI-2. Selected metric parameters of **(IMes)Fe(NO)$_2$X** (where X = Cl, Br, I[184])

	(IMes)Fe(NO)$_2$Cl	**(IMes)Fe(NO)$_2$Br**	**(IMes)Fe(NO)$_2$I**[184]
Fe-X / Å	2.247 (2)	2.362 (5)[a]	2.574 (1)
Fe'-C$_{NHC}$ / Å	2.049 (6)	2.046 (3)	2.041 (3)
∠O-Fe'-O / °	96.0 (1)	-disorder-	99.7 (7)
∠Fe-N-O / °	163.2 (5)[a]	165.8 (3)	164.8 (3)[a]
∠N-Fe-N / °	109.6 (3)	-disorder-	111.9 (1)

[a]Average values.

The Fe'-X bond distance gradually increases with the increase in the covalent radii of the halide, while limiting the Fe'-C$_{NHC}$ around 2.04 Å. The Fe center maintains a pseudo tetrahedral geometry with slight broadening of ∠O-Fe'-O from chloride to iodide. Disorder in the position of Br in (IMes)Fe(NO)$_2$Br prevents precise metric comparisons. The ∠Fe-N-O angle is bent, ca 164°, and maintains an 'attracto' orientation.[172] The ∠N-Ni-N and ∠S-Ni-S in NiN$_2$S$_2$•R$^+$, show negligible distortions compared to the free metallodithiolates, NiN$_2$S$_2$s, as can be comprehended by the use of the divergent lobe of the *p*-type lone pair[183] of the thiolates for adduct formation.

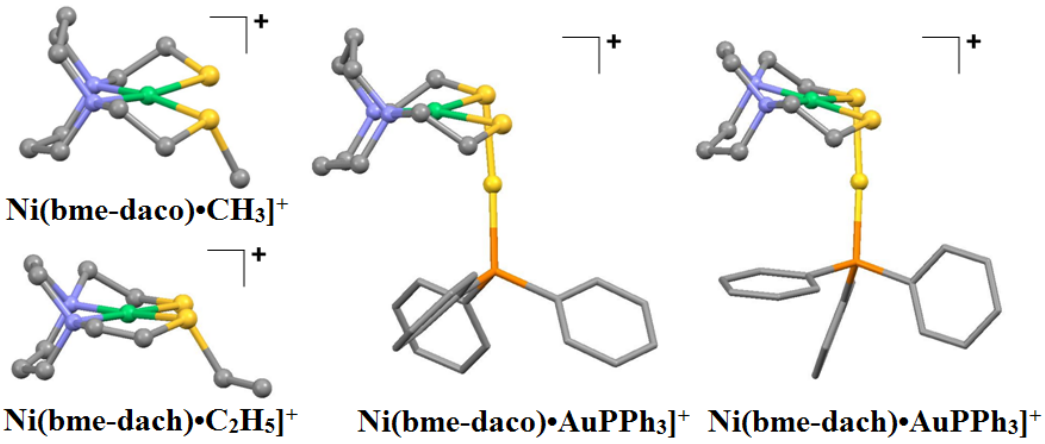

Figure VI-8. Molecular structures of $NiN_2S_2•R^+$ as $[Ni(bme\text{-}daco)•CH_3]^+I^-$,[81] $[Ni(bme\text{-}dach)•C_2H_5]^+[PF_6]^-$, $[Ni(bme\text{-}daco)•AuPPh_3]^+Cl^-$,[173] $[Ni(bme\text{-}dach)•AuPPh_3]^+[BF_4^-]$.

In contrast, the '*p*' character of the thiolate lone pair, changes its magnitude severely upon binding Au^+ over alkyls, as can be seen from the constriction of ∠Ni-S-Xs, (where X = alkyl, Au^+). The lone pair of the thiolate is expected to show higher sp^3 hybrid character with alkyls (107°) and is almost pure '*p*' type with Au^+ cations (82 - 85°). The molecular structures of $NiN_2S_2•R^+$ (where R = C_2H_5, $CH_3$and Ph_3PAu^+) and their metric parameters are shown in Figure VI-8 and Table VI-3, respectively.

Table VI-3. Selected metric parameters of $NiN_2S_2•R^+$ as $[Ni(bme\text{-}daco)•CH_3]^+I^-$,[81] $[Ni(bme\text{-}dach)•C_2H_5]^+[PF_6]^-$, $[Ni(bme\text{-}daco)•AuPPh_3]^+Cl^-$,[173] $[Ni(bme\text{-}dach)•AuPPh_3]^+[BF_4^-]$.

	$[Ni(bme\text{-}daco)•CH_3]^+$	**$[Ni(bme\text{-}dach)•C_2H_5]^+$**	**$[Ni(bme\text{-}daco)•AuPPh_3]^+$**	**$[Ni(bme\text{-}dach)•AuPPh_3]^+$**
∠N-Ni-N / °	90.6 (2)	82.4 (1)	90.7 (9)	83.2 (4)
∠S-Ni-S / °	89.4 (7)	94.4 (1)	89.1 (3)	94.3 (4)
∠Ni-S-R / °[a]	107.9 (2)	107.9 (1)	81.6 (2)	85.3 (4)

[a]R = alkyls, Au^+

The ν(NO) stretching frequencies of IMesFe(NO)$_2$X showed a distinct trend in accordance with the halide donor abilities which was also reflected in their irreversible {Fe(NO)$_2$}$^{9/10}$ reduction event from electrochemical studies, Figure VI-9. A comparison of their ν(NO) stretching frequencies in THF and E_{pc} values, {Fe(NO)$_2$}$^{9/10}$, in CH_3CN, are summarized in Table VI-4.

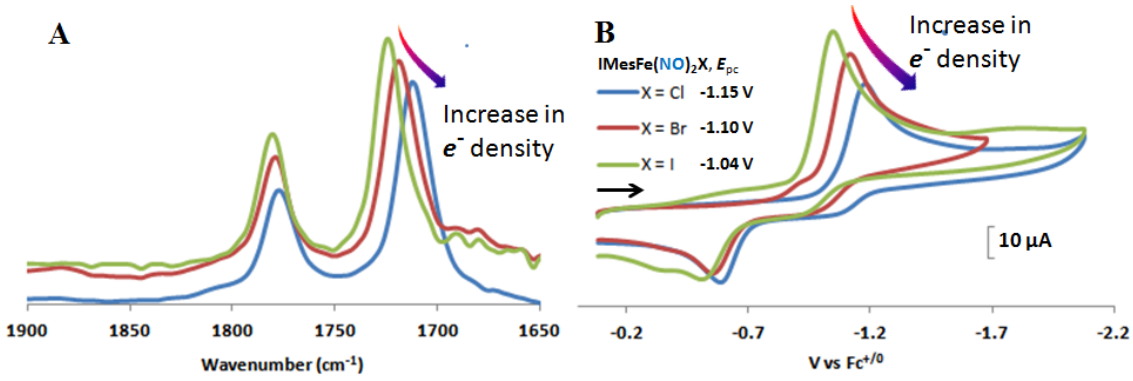

Figure VI-9. A) Normalized and stacked IR plots of **IMesFe(NO)$_2$X** (X = Cl, Br, I) in THF. B) Overlay of cyclic voltammograms of ~2 mM **IMesFe(NO)$_2$X** (X = Cl, Br, I) under Ar in CH_3CN at 200 mV/s.

Table VI-4. A comparison of ν(NO) stretching frequencies in THF and E_{pc} values, {Fe(NO)$_2$}$^{9/10}$, in CH_3CN, of **IMesFe(NO)$_2$X** (X = Cl, Br, I).

Complexes	**ν(NO) (cm^{-1})**	**E_{pc} (V) {Fe(NO)$_2$}$^{9/10}$**
IMesFe(NO)$_2$Cl	1777, 1713	- 1.15
IMesFe(NO)$_2$Br	1779, 1718	-1.10
IMesFe(NO)$_2$I	1780, 1724	-1.04

In an attempt to isolate what might be expected as the first-formed product in the Ph_3PAuCl reaction, *i.e.*, to limit the halide displacement of the MN_2S_2 on the DNIC in

reactions of the Ph_3PAu^+ reagent, the halide was removed using $AgBF_4$. The use of a non-coordinating anion, BF_4^-, with Au^+, should in principle parallel $H^+BF_4^-$ addition.**Ni-Fe'** and **Co-Fe'** were reacted with $[Ph_3PAu(Solv)]^+[BF_4^-]$ at -40 ºC.

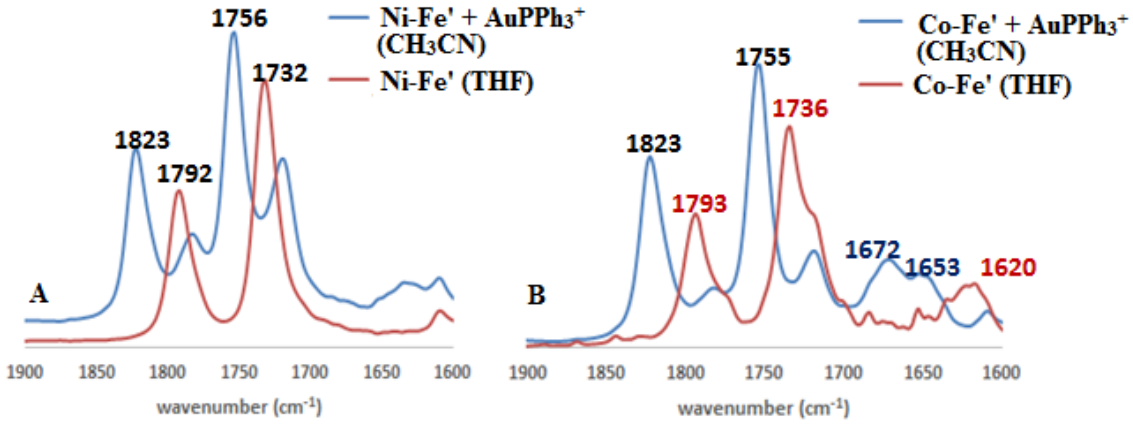

Figure VI-10. Normalized and stacked IR plots of A) **Ni-Fe'** (blue) and **Ni-Fe'** and $AuPPh_3^+$and B) **Co-Fe'** (blue) and **Co-Fe'** and $AuPPh_3^+$ at -40 ºC.

The solution IR spectra for both the reactions showed a shift in the *v*(NO) stretching frequencies ($Fe(NO)_2$moeity) to higher wavenumbers, by ca. 30 cm^{-1}, indicating attachment of Ph_3PAu^+ to the free thiolate of the **Ni-Fe'** and **Co-Fe'**to form dicatioinc species, Figure VI-10. The *v*(NO) stretching frequencies of the $(NO)CoN_2S_2$ showed the formation of two *v*(NO) peaks at 1652 and 1673 cm^{-1} upon $AuPPh_3^+$ addition from 1620 cm^{-1}. Analogous studies involving addition of $HBF_4.Et_2O$ to **Ni*-Fe'** showed a similar *v*(NO) bathochromic shift. However, the instability of the dicationic species at room temperature led to tetrametallic-digold complexes as thermodynamically stable products. The digold bound crystalline material obtained with **Ni-Fe'**, as [*trans*-NiN_2S_2-$Au]_2^{2+}$, is reported in literature, albeit synthesized from a different route. The cobalt

congener showed two isomers; one in which two $(NO)CoN_2S_2$ are *cisoid* while the other was oriented in a *transoid* disposition, Figure VI-11. In both the isomers the nitrosyls are oriented away from each other.

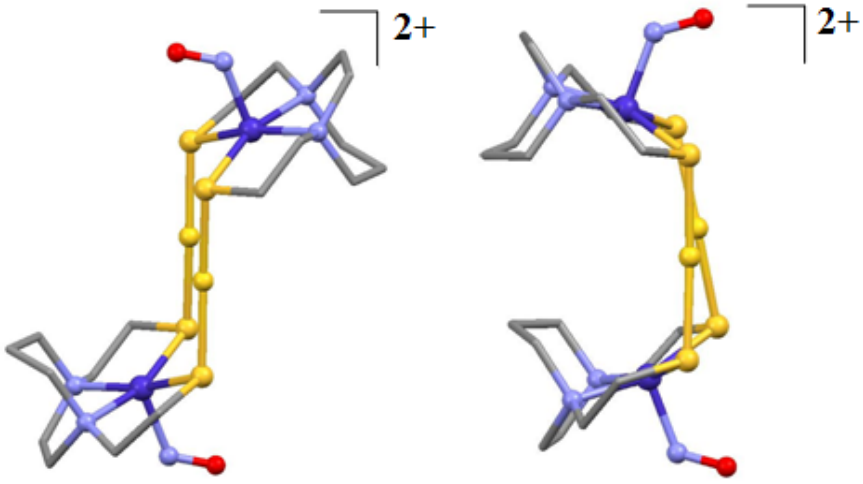

	[{*trans*-(NO)CoN_2S_2}Au]$_2^{2+}$	[{*cis*-(NO)CoN_2S_2}Au]$_2^{2+}$
Au···Au / Å	3.058 (1)	3.035 (7)
∠S-M-S_{avg} / °	95.9 (1)	97.9 (1)
∠Co-N-O_{avg} / °	124.3 (2)	123.8 (1)

Figure VI-11. Molecular structures of [{trans-(NO)CoN_2S_2}Au]$_2^{2+}$ and [{*cis*-(NO)CoN_2S_2}Au]$_2^{2+}$ as BF_4^- salts. Selected metric parameters are listed below.

Reduction Reactions

The reduction of **Ni-Fe'** was carried out in presence of KEt_3BH in THF at -78 °C. The reaction was monitored using IR spectroscopy with respect to ν(NO) stretching frequencies. Addition of ~0.5 equivalents of KEt_3BH showed the formation of an intermediate with a slight shift of the original ν(NO) stretching frequencies, 1791, 1732 cm^{-1}, to 1784, 1716 cm^{-1} along with the formation of new ν(NO) bands at 1678, 1616

cm^{-1}, Figure VI-12. This new species formed can be postulated to be the formation of BEt_3 adduct of the reduced compound. Addition of 1 equivalent of KEt_3BH showed a change in color from reddish brown to green with the formation of new ν(NO) bands at 1664, 1620 cm^{-1}, as the totally reduced compound. The Δν(NO) for this reduction reaction is ~110 cm^{-1}, consistent with similar $\{Fe(NO)_2\}^{9/10}$ redox systems.[74, 182] Addition of excess KEt_3BH (> 2.2 equivalents) showed no change in the ν(NO) stretching frequencies.

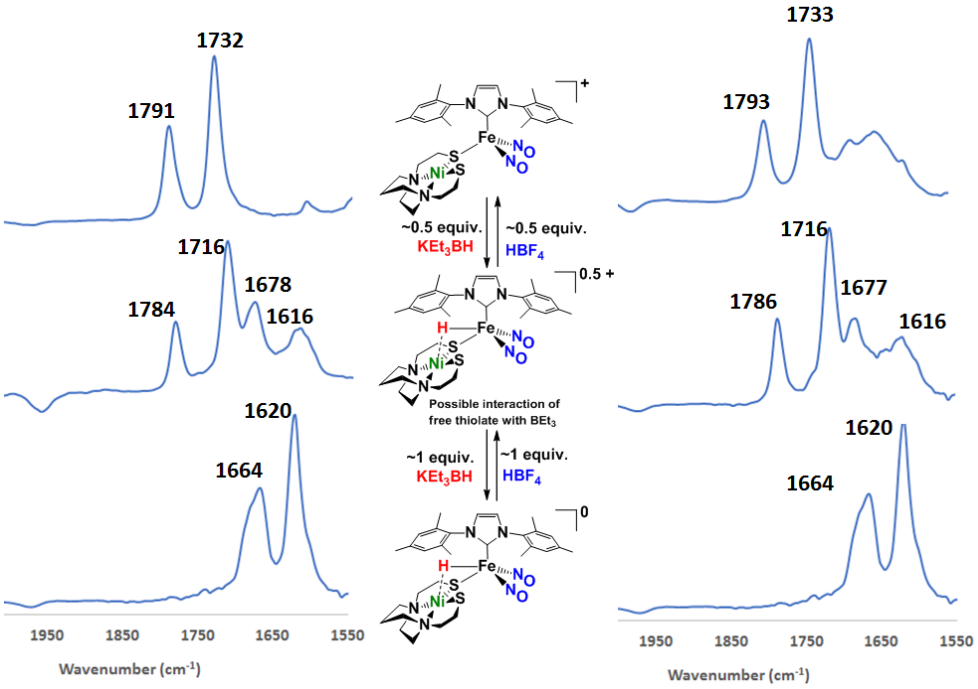

Figure VI-12. ν(NO) monitor for the reduction reactions of **Ni-Fe'** at -78 ºC with sequential addition of KEt_3BH (left) followed by oxidation with $HBF_4.Et_2O$ to regenerate **Ni-Fe'**.

The reversibility of the reaction was tested by the addition of $HBF_4.Et_2O$ in the reaction mixture maintained at -78 ºC. Addition of 1 equivalent of $HBF_4.Et_2O$ showed

the formation of the similar intermediate with ν(NO) stretching frequencies at 1786, 1716 cm^{-1}, as the intense bands along with smaller bands at 1677, 1616 cm^{-1}. Further addition of 0.5 equivalent of $HBF_4.Et_2O$ showed a complete change in color to dark reddish brown with the formation of new ν(NO) bands at 1793, 1733 cm^{-1}, producing the **Ni-Fe'**, Figure VI-12.

Conclusion

The versatility of the TNIC, $[(IMes)Fe(NO)_3]^+$, as an efficient synthon was shown in its reaction capabilities with various nucleophiles, ranging from metallodithiolates to halides. The homo/heterobimetallic complexes synthesized from this approach showed unique geometry such that the free thiolate could potentially act as a pendant base for binding exogenously added electrophiles. Proton addition at the unbound thiolate was supported through IR spectroscopy and electrochemical studies. Similar reactivity with Au^+ as an isolobal surrogate for proton supports the thesis. Although structural characterizations of H^+/Au^+ bound species eluded the research endeavors, systematic analysis of the proposed reactivity was demonstrated with electrophiles having nucleophilic counter anions. Nucleophilic halides competed with the thiolates for their reactivity at the iron center of the DNIU and resulted in metallodithiolate displacement. The free metallodithiolate in turn showed efficient binding with the existing electrophiles present in the reaction medium. All the products of the reactions were isolated and structurally characterized.

CHAPTER VII

TRIPLET, HIGH-SPIN, LINEAR $\{Fe(NO)\}^8$: REDOX FEATURE OF A STABLE DIIRON TRINITROSYL COMPLEX

Introduction

Nitric oxide ($NO^{\bullet}$), a popular small molecule among chemists and biologists with regards to its physiological applications,[184-185] shows abstruse electronic interplay in metal-nitrosyl bonds with one electron reduced (NO^-), neutral ($^{\bullet}NO$) and one electron oxidized (NO^+) forms that calls for thorough structural and bonding investigation.[151, 186] The immediate chemical relevance of NO in biology stems from the various $\{Fe(NO)\}^{6/7/8}$ species that provide signature IR and EPR spectral features and select solid state metric parameters.[19, 187]

Although heme based $\{Fe(NO)\}^7$ are quite well-known in the literature, studies on $\{Fe(NO)\}^8$ species fail to punctuate the scientific library in that capacity.[188] This may be related to their inherent instability and high reactivity.[188] Fundamental spectroscopic studies on $\{Fe(NO)\}^8$ by Kadish [189] and Ryan,[190-191] followed by its isolation in the solid state by Doctorovich,[192] were important developments in this field of research.

The theoretical calculations and their results described herein were computed by Dr. Shengda Ding and Prof. Michael B. Hall.

The first breakthrough came from studies of Hu and Li[193] and later on by Ryan[194] when they independently obtained single crystals of heme based $\{Fe(NO)\}^8$. The general strategy for stabilizing the electron-rich NO^- was by the extensive use of electron-withdrawing groups on the porphyrins that led to an overall low spin (LS) iron center.[188, 193] Likewise, studies by Wieghardt[195-196] and Lehnert[197-198] showed the efficient interplay of the $\{Fe(NO)\}^{6/7/8}$ in non-heme cyclam based macrocycles. Although single crystals of non-heme $\{Fe(NO)\}^8$ eluded the scientific community, recent studies by Meyers *et al*., delineated the X-ray crystal structures of the iron-mononitrosyl in three redox states $\{Fe(NO)\}^{6/7/8}$ in a tetracarbene scaffold.[188] The Fe-N-O angles reported by Hu and Li,[193] and Ryan,[194] where the iron resides in a square pyramidal geometry, are sufficiently bent, 122° and 127°, respectively, suggesting Fe^{II}-NO^- bonding. The $\{Fe(NO)\}^8$ complex isolated by Meyers, however, showed the Fe-N-O as 169°.[188] In general, the isolated $\{Fe(NO)\}^8$ iron-mononitrosyl complexes (heme and non-heme) showed the presence of low spin (LS) species.[188] More recently, high-spin (HS) $\{Fe(NO)\}^8$ complexes, characterized spectroscopically by Goldberg and Lehnert, showed interesting N_2O chemistry.[199-200]

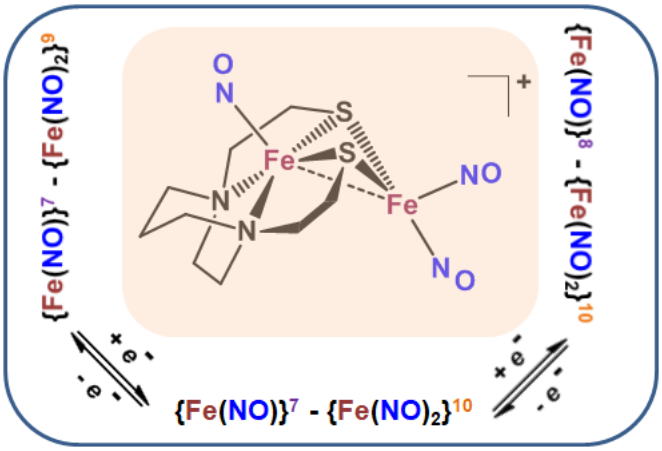

Figure VII-1. The three redox levels delineated by the diirontrinitrosyl complex isolated in the oxidized state.[74]

The tetradentate N_2S_2 ligands extensively used by the Darensbourg group over two decades have shown efficient and versatile chelating properties.[162] Metal-nitrosyl redox non-innocence was observed for $(NO)FeN_2S_2$ and $(NO)CoN_2S_2$ complexes that deftly showed reversible $\{Fe(NO)\}^{7/8}$ and $\{Co(NO)\}^{8/9}$ electrochemical events in such non-heme environments.[77-78] The $(NO)FeN_2S_2$, with S = 1/2, has been exploited as a metalloligand to bind numerous receiver units, like redox innocent $[(\eta^5\text{-}C_5R_5)Fe'(CO)]^+$,[160, 165] $W(CO)_4$ units,[78] and redox non-innocent $\{Fe(NO)_2\}^{9/10}$ units.[74] The latter, diirontrinitrosyl complex, synthesized in the oxidized form, $\{Fe(NO)\}^7$-$\{Fe(NO)_2\}^9$, studied extensively as moderate electrocatalysts for H^+ reduction, showed two distinct single electron reversible events at -0.78 V and -1.33 V, under electrochemical conditions in CH_2Cl_2. These events were assigned for the existence of three redox states, viz., $\{Fe(NO)\}^7$-$\{Fe(NO)_2\}^9$, $\{Fe(NO)\}^7$-$\{Fe(NO)_2\}^{10}$, $\{Fe(NO)\}^8$-$\{Fe(NO)_2\}^{10}$, Figure VII-1.[74] The N_2S_2 ligand, bme-dach

(bismercaptoethyldiazacycloheptane), was employed as the tetradentate ligand to obtain molecular structures for the first redox couple, $\{Fe(NO)\}^7$-$\{Fe(NO)_2\}^9$, $\{Fe(NO)\}^7$-$\{Fe(NO)_2\}^{10}$. The one electron reduced neutral compound showed impressive structural similarity with its oxidized cationic congener, with regards to the overall butterfly structure. Addition of a second electron, however, did not lead to the isolation of the $\{Fe(NO)\}^8$-$\{Fe(NO)_2\}^{10}$ species.[74]

In this report we have shown the impressive thermodynamic stability of the cationic diirontrinitrosyl complex, $\{Fe(NO)\}^7$-$\{Fe(NO)_2\}^9$, by its isolation from six synthetic routes using the moderately flexible, open-chain, bme-dame[85] (bismercaptoethyldiazamethylethane) and the relatively rigid, mesocyclic, bme-dach,[79] tetradentate N_2S_2 ligands. Stable, bimetallic, redox non-innocent molecules as thermodynamic sinks are of imminent interest among synthetic chemists as noteworthy electrochemical benchmarks with distinct reversible redox features. The extent of metal-metal interaction, buffered by soft nitrosyl ligands as moderators for electronic charge distribution, draws significance to the insightful concept of metal-nitrosyl non-innocence.

The oxidized complex was systematically reduced to its neutral and anionic forms by sequential addition of 1 and 2 equivalents of KEt_3BH, respectively.[74] The molecular structures of the oxidized $\{Fe(NO)\}^7$-$\{Fe(NO)_2\}^9$, and the singly reduced $\{Fe(NO)\}^7$-$\{Fe(NO)_2\}^{10}$ complexes were reported earlier with the bme-dach N_2S_2 backbone.[74] Herein we report the isolated molecular structures of $\{Fe(NO)\}^7$-$\{Fe(NO)_2\}^9$, singly reduced $\{Fe(NO)\}^7$-$\{Fe(NO)_2\}^{10}$ and doubly reduced $\{Fe(NO)\}^8$-

$\{Fe(NO)_2\}^{10}$ complexes using the moderately flexible bme-dame N_2S_2 ligands. The mononitrosyl-iron unit in the anionic $\{Fe(NO)\}^8$-$\{Fe(NO)_2\}^{10}$ complex showed marked linearity in the Fe-N-O angle which is a *de-novo* example of a non-heme, linear $\{Fe(NO)\}^8$ species. Computational studies support the experimental results showing a triplet, high spin (HS) $\{Fe(NO)\}^8$ that undergoes an impressive spin-polarization to achieve linearity.

Results and Discussion

Ligand flexibility in the N_2S_2 core was implemented using an open chain N_2S_2 ligand, bismercaptoethyldiazamethylethane, (bme-dame). This ligand was first reported by Karlin and Lippard in 1973 and was later shown for its impressive chelating properties by binding a host of metal ions, particularly the (NO)Fe(bme-dame)[84] complex. The oxidized complex, $\{Fe(NO)\}^7$-$\{Fe(NO)_2\}^9$, was synthesized from six synthetic routes using both the bme-dach and bme-dame ligands, Figure VII-2. The (NO)FeN_2S_2s are hereafter designated as **Fe** and **Fe'**, with respect to the bme-dach and bme-dame ligands, respectively, the $Fe(NO)_2$ unit as **Fe***, and likewise, the overall oxidized complexes as **[Fe-Fe*]**$^+$ and **[Fe'-Fe*]**$^+$.

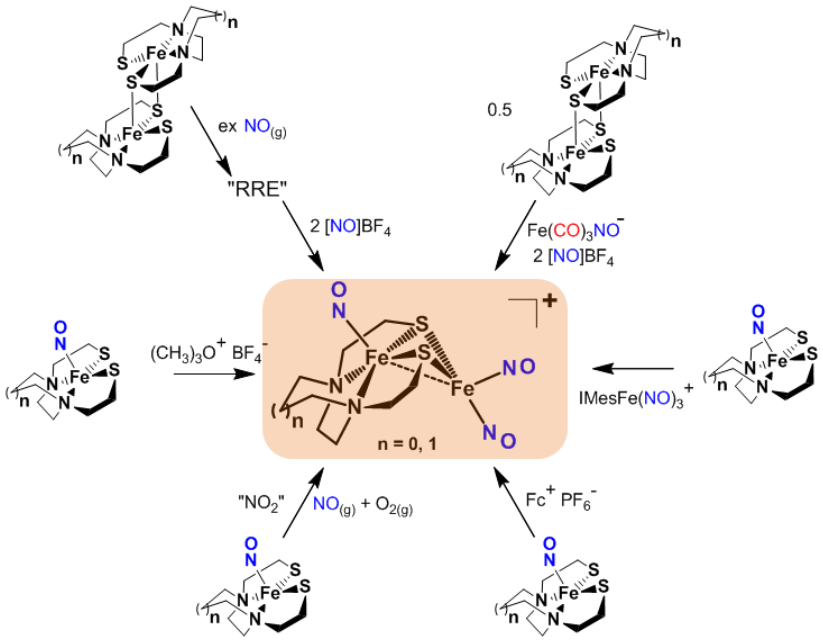

Figure VII-2. Reaction scheme showing six synthetic routes for the formation of the oxidized diirontrinitrosyl complex with bme-dame (n=0) and bme-dach (n=1) ligands.

Previously reported procedures involved the reaction of a carbene stabilized trinitrosyliron complex, $[(IMes)Fe(NO)_3]^+$, with $(NO)FeN_2S_2$ nucleophile, led to the loss of a NO• followed by a NHC to form the oxidized complex.[96] A feasible one pot synthesis of the compound involved *in situ* generation of NO• and $[Fe(CO)_2(NO)_2]^+$, from $[Fe(CO)_3(NO)]^-$ and two equivalents of $[NO]BF_4$, which further reacted with the $[FeN_2S_2]_2$ dimer, leading to the latter's cleavage and product formation.[74] Both reactions showed almost quantitative yields, ~75-80 %, using the bme-dame and bme-dach ligands.

Cleavage of the $[FeN_2S_2]_2$ dimer with stoichiometric amount of NO_g forms $(NO)FeN_2S_2$.[77] Addition of excess NO_g, however, leads to a Roussin's Red Ester (RRE)

which shows signature ν(NO) bands, 1780, 1754 cm^{-1}. Although this species has not been structurally characterized, oxidation by $[NO]BF_4$ formed the diirontrinitrosyl complex in good yields, ~ 80 % with both the ligands. Likewise, oxidation by aerial oxygen in presence of excess NO_g led to the oxidized diirontrinitrosyl complex, albeit in low yields ~ 35 %. Formation of $\{Fe(NO)\}^7$-$\{Fe(NO)_2\}^9$ were also repeatedly observed in various reactivity studies with $(NO)FeN_2S_2$, under oxidizing conditions. Use of strong alkylating agents like tri-(ethyl/methyl)-oxonium tetrafluoroborate or ferrocenium salts, overtime produced the diirontrinitrosyl species; the isolated yields for these reactions were very low, less than 20 % involving both the N_2S_2 ligands. The latter pathways are expected to have lower yields due to the nature of atom efficiency as three NOs and two Fes are required, from a likely involvement of three $(NO)FeN_2S_2$ molecules to form one molecule of the product.

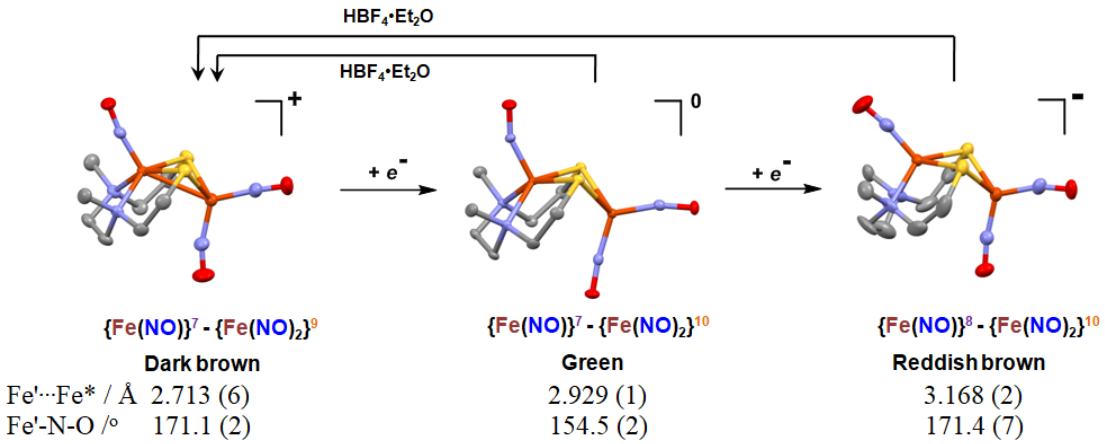

Figure VII-3. Reaction scheme showing the sequential reduction of **[Fe'-Fe*]**$^+$ to **[Fe'-Fe*]**^{0} and **[Fe'-Fe*]**$^-$ with select metric parameters, Fe'···Fe* distance and Fe'-N-O angles.

The reduction reaction of the oxidized diirontrinitrosyl complex, with the bme-dame tetradentate ligand, **[Fe'-Fe*]**$^{+}$, was carried out in presence of KEt_3BH in THF at 0 ^{o}C, Figure VII-3. Addition of one equivalent of KEt_3BH changed the color from dark brown to green with a concomitant hypsochromic shift in the ν(NO) stretching frequencies by ca. 110 cm^{-1}, Figure VII-4. The neutral compound, **[Fe'-Fe*]^{0}**, isolated as a green solid, showed an isotropic EPR spectrum, g = 2.023, for a S = 1/2 species.

The **[Fe'-Fe*]^{0}** and **[Fe-Fe*]^{0}** maintained an overall butterfly structure with distinct changes in structural features compared to its oxidized congener, **[Fe'-Fe*]^{0}** and **[Fe-Fe*]**$^{+}$, Table VII-1. With the bme-dach backbone, Elongation of the Fe•••Fe distance by 0.22 Å, shortening of the S•••S distance by 0.12 Å and the more pronounced out of plane displacement of the Fe(NO) from the average N_2S_2 plane by 0.03 Å, were some of the structural attributes of the neutral species. The fact that the two iron centers, buffered by the NOs, worked in concert to accommodate the added electron, was reflected in the moderate bending of the mononitrosyl-iron from 166^{o} to 155^{o}, *i.e.*, by ~11^{o}.[74]

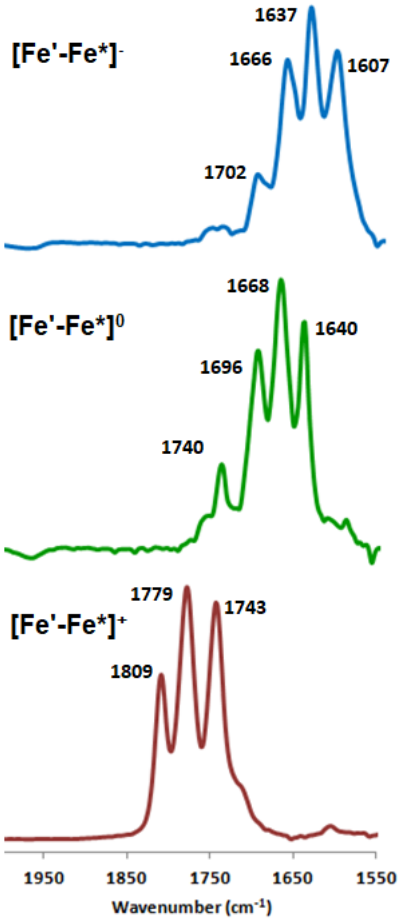

Figure VII-4. Stacked IR plots showing the ν(NO) stretching frequencies for the sequential reduction of **[Fe'-Fe*]**$^{+}$ to **[Fe'-Fe*]**^{0} and **[Fe'-Fe*]**$^{-}$, in THF.

Addition of two equivalents of KEt_3BH at -40 °C showed a further shift in the ν(NO) stretching frequencies to 1666, 1637, 1607 cm^{-1}, Figure VII-4. The anionic complex, **[Fe'-Fe*]**$^{-}$, was isolated at low temperatures and X-ray quality crystals were grown in THF/pentane at -35 °C as reddish-brown plates, Figure VII-5.

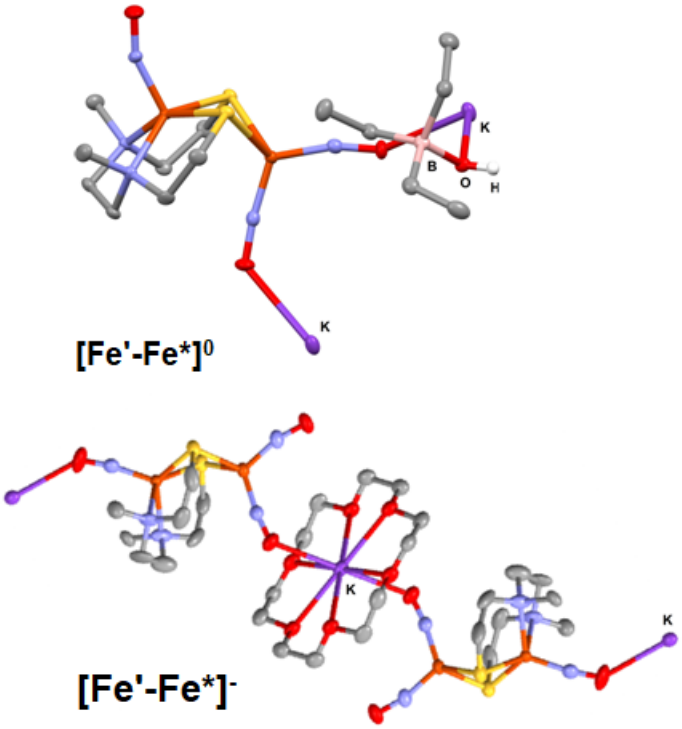

Figure VII-5. Thermal ellipsoid diagram of **[Fe'-Fe*]^{0}** (top) and **[Fe'-Fe*]$^{-}$** (bottom) showing interaction of oxygen atom of NOs with K^{+} in 18-crown-6 ether and BEt_3OH, at 50% probability level. The hydrogen atom on BEt_3OH is shown for clarity.

Comparison of metric parameters revealed marked elongation in the Fe•••Fe distance by 0.46 Å in the **[Fe'-Fe*]$^{-}$**. The mononitrosyl-iron angle, Fe-N-O, the most distinguishing feature of $\{Fe(NO)\}^{7}$ and $\{Fe(NO)\}^{8}$ couples in **[Fe'-Fe*]$^{+}$** and **[Fe'-Fe*]$^{-}$** complexes remained the same 171°; *i.e.*, the Fe-N-O angle was substantially linear in the $\{Fe(NO)\}^{8}$ state. While the out of plane displacement of the Fe(NO) from the average N_2S_2 plane for the **[Fe'-Fe*]$^{+}$** complex was 0.51 Å, it increased to 0.85 Å in **[Fe'-Fe*]$^{-}$**. The S•••S distance was almost invariant showing an elongation by 0.04 Å in the reduced complex. The difference in the Fe-N-O angles, in the $Fe(NO)_2$ moiety, are ~10° for **[Fe'-Fe*]$^{+}$** while it reduced to ~7° for **[Fe'-Fe*]$^{-}$**; a feature which can be related

to the interaction of the O atom in $Fe(NO)_2$ with the K^+ cation, Figure VII-5. The structural overalay of the oxidized cationic diiron trintrosyls and the reduced neutral diiron trintrosyls with different N_2S_2 ligands are shown in Figure VII-6. Comparison of the matrix parameters of **[Fe'-Fe*]$^{+/0/-}$** and **[Fe-Fe*]$^{+/0}$** are shown in Table VII-1.

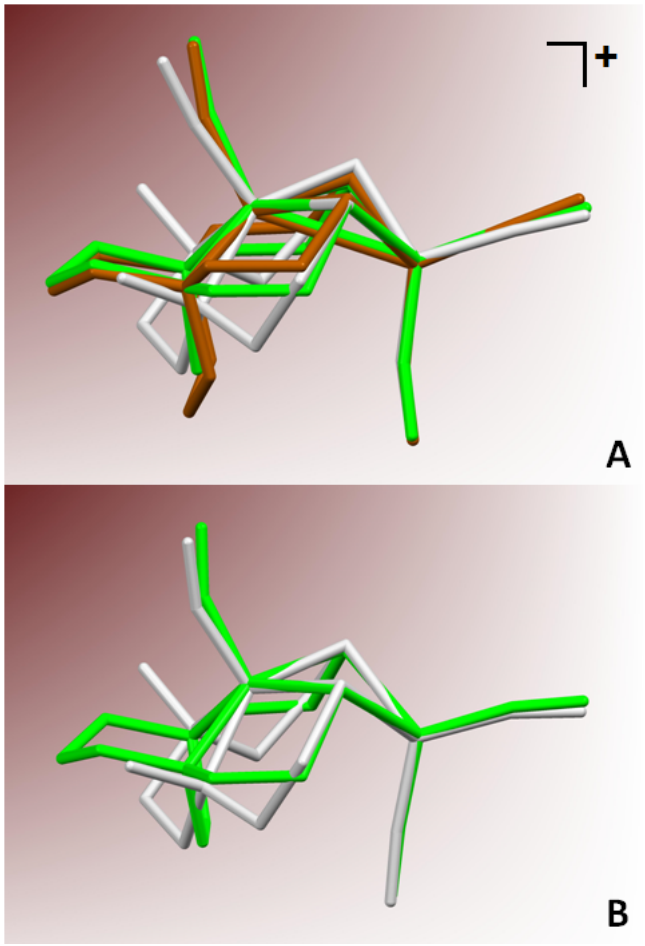

Figure VII-6. Structural overlay of A) the oxidized cationic diiron trintrosyls, B) the reduced neutral diiron trintrosyls with different N_2S_2 ligands; the overlays were done with respect to the $Fe(\mu\text{-}S)_2Fe$ butterfly core; color code: bme-daco (brown), bme-dach (green), bme-dame (silver).

Table VII-1. Select matrix parameters of **[Fe'-Fe*]$^{+/0/-}$** and **[Fe-Fe*]$^{+/0}$** complexes.

	[Fe'-Fe*]$^{+}$ ***[Fe-Fe*]$^{+}$*** [a]	**[Fe'-Fe*]^{0}** ***[Fe-Fe*]^{0}*** [a]	**[Fe'-Fe*]$^{-}$** ***[Fe-Fe*]$^{-}$*** [a]
Fe···Fe* / Å	2.713 (6) *2.786 (8)*	2.929 (1) *3.008 (1)*	3.168 (2)
$Fe_{(NO)disp.}$ [b] / Å	0.518 *0.524*	0.551 *0.548*	0.851
Fe-N_{NO} / Å	1.666 (2) *1.668 (2)*	1.692 (2) *1.692 (2)*	1.720 (7)
S···S / Å	3.150 (1) *3.253 (1)*	3.053 (8) *3.132 (2)*	3.189 (4)
$Fe_{(NO)}$-$S_{(avg)}$ / Å	2.241 (7) *2.251 (8)*	2.237 (7) *2.244 (1)*	2.361 (2)
Fe*-$S_{(avg)}$ / Å	2.255 (7) *2.249 (9)*	2.330 (6) *2.331 (1)*	2.367 (3)
Hinge [c] /°	115.41 *127.21*	119.41 *128.65*	130.22
Fe-N-O /°	171.1 (2) *165.8 (2)*	154.5 (2 *154.4 (2)*	171.4 (7)
Fe*-N-O /°	175.5 (3), 164.9 (3) *174.4 (2)*, *166.6 (2)*	173.4 (2), 165.4 (2) *175.0 (3)*, *168.0 (3)*	171.9 (6), 164.1 (7)
S-$Fe_{(NO)}$-S /°	89.28 (3) *95.52 (2)*	86.04 (2) *88.46 (3)*	84.88 (9)
S-Fe*-S /°	88.57 (3) *92.63 (2)*	82.00 (2) *84.36 (3)*	84.69 (9)

[a]Values in italics are for the bme-dach analogues.
[b]The angle between N_2S_2 and S_2Fe* best planes.
[c]Displacement of Fe_{NO} from N_2S_2 best plane.

Addition of $HBF_4.Et_2O$ to **[Fe'-Fe*]$^{-}$** or **[Fe'-Fe*]$^{+}$** resulted in the formation of **[Fe'-Fe*]$^{+}$** with release of H_2 showing stoichiometric reduction of protons. Comparison of {Fe(NO)}^{8} metric parameters of reported complexes, $[Fe(OEP)NO]^{-}$,[194]

$[Fe(TFPPBr_8)NO]^-$,[193] and $[Fe(NHC)NO]^+$[188] in LS states, with $[Fe'\text{-}Fe^*]^-$ in HS state, (where OEP = octaethylporphyrin, $TFPPBr_8$ = tetrakis(pentafluorophenyl) octabromoporphyrin and NHC = tetracarbene) are tabulated in Table VII-2.

Table VII-2. Comparison of metric parameters of $\{Fe(NO)\}^8$ in LS and HS states.

	$[Fe'\text{-}Fe^*]^-$	**$[Fe(OEP)NO]^-$** [194]	**$[Fe(TFPPBr_8)NO]^-$** [193]	**$[Fe(NHC)NO]^+$** [188]
Spin state	HS	LS	LS	LS
Fe-N-O / º	171.4 (7)	127.2 (2)	122.4 (3)	169.1
Fe_{NOdisp} [a]/ Å	0.85	0.198	0.167	0.56
Fe-N / Å	1.720 (7)	1.812 (3)	1.814 (4)	1.660
ν(NO) /cm^{-1}	1637	1445	1540	1590

[a]The Fe_{NO} disp. is calculated from the average N_2S_2 or N_4 or C_4(NHC) average plane.

Electrochemical Studies

The cyclic voltammogram of **$[Fe'\text{-}Fe^*]^+$** was recorded in CH_2Cl_2 at room temperature under argon containing 0.1 M $[^tBu_4N][PF_6]$ as supporting electrolyte using a glassy carbon working electrode. The CV scan at 200 mV/sec is shown in Figure VII-7 with assignments listed therein. The complex showed two single electron reversible events at -0.82 V and -1.43 V, which are assigned as the $\{Fe(NO)_2)\}^{9/10}$ and $\{Fe(NO)\}^{7/8}$ couples respectively. Similar redox events were recorded for **$[Fe\text{-}Fe^*]^+$** which were ca. 0.1 V more positive.[74]

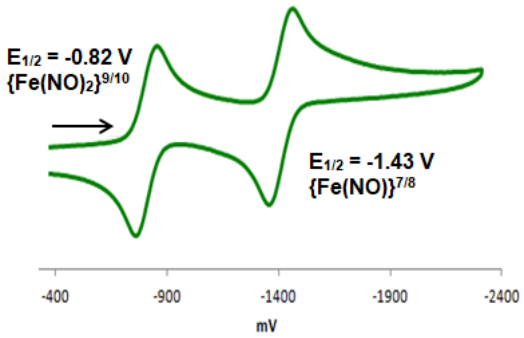

Figure VII-7. Cyclic voltammogram of **[Fe'-Fe*]**$^{+}$ as 2 mM CH_2Cl_2 solutions containing 0.1 M [$^{t}Bu_4N$][PF_6], referenced to $Fc^{0/+}$.

Addition of $HBF_4.Et_2O$ showed an increase in cathodic current at -0.82 V at the $\{Fe(NO)_2\}\}^{9/10}$ redox couple, Figure VII-8. The current enhancement is attributed to proton reduction, similar to the studies done on **[Fe-Fe*]**$^{+}$. Although studies involving bulk electrolysis for quantification of H_2 is in progress, preliminary studies accounted for a moderate TOF of 17.7 s^{-1}.

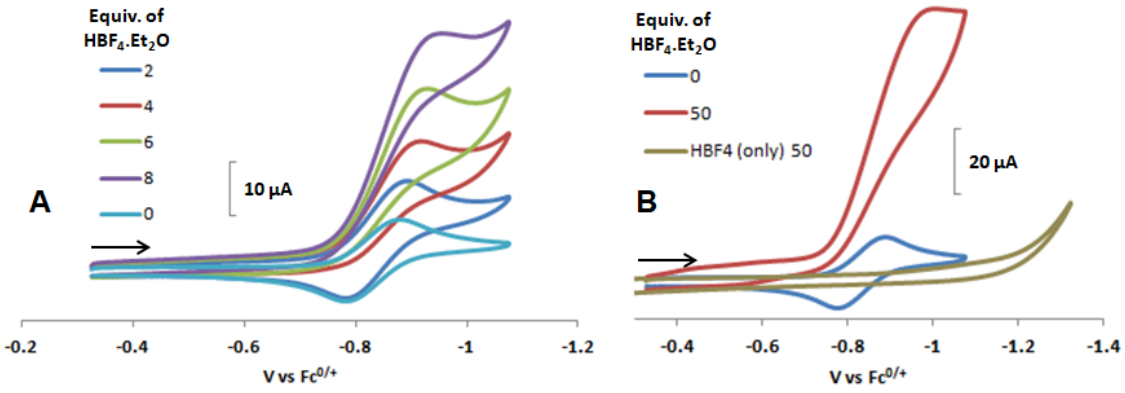

Figure VII-8. A) Cyclic voltammograms of **[Fe'-Fe*]**$^{+}$ as 2 mM CH_2Cl_2 solutions in presence of sequential additions of HBF_4•Et_2O. B) Overlay of catalytic current responses of **[Fe'-Fe*]**$^{+}$ in presence of 50 equivalents of HBF_4•Et_2O (red) and 50 equivalents of $HBF_4.Et_2O$ in absence of catalyst (grey).

Computational Report: Linear {Fe(NO)}^{8} in [Fe'-Fe*]$^-$ (Dr. Shengda Ding and Prof. Michael B. Hall)

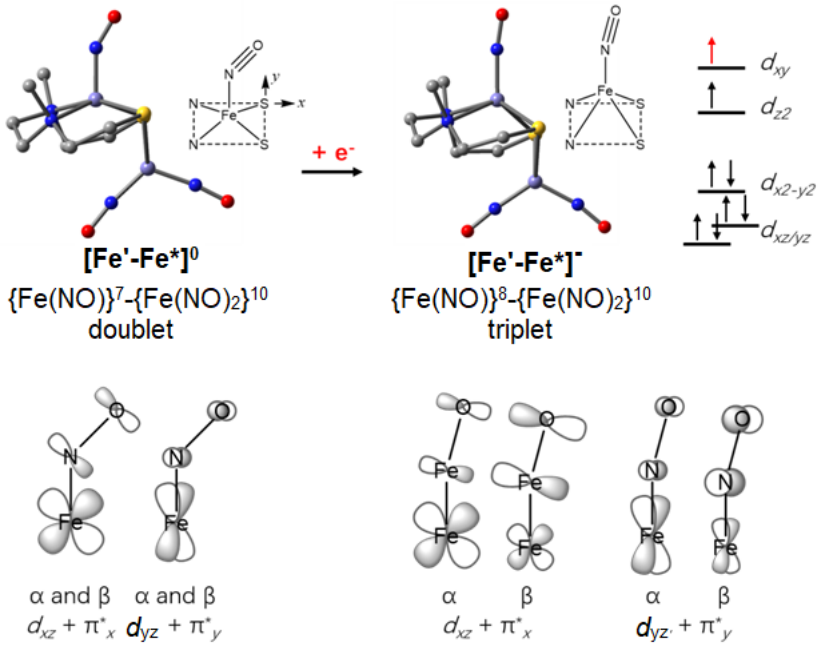

Figure VII-9. Electronic configuration and orbital overlap of d_{xz} and d_{yz} with π^*_x and π^*_y.

[Fe'-Fe*]$^-$ was calculated to be a triplet, with two unpaired electrons occupying d_{z2} and d_{xy} of the {Fe(NO)}^{8} moiety, respectively. (Note the coordination definition in Figure VII-9, is different from the convention.) Significant spin polarization occurs in the π-back-bonding orbitals formed by metals d_{xz}, d_{yz} and NO's π^*_x and π^*_y inside Fe(NO): the spin density of the iron is 2.958, larger than **[Fe'-Fe*]^0** and a spin density of – 1.178 is on its attached NO. The other iron containing moiety, {Fe(NO)$_2$}^{10} is saturated, however, spin-polarization also occurs in the unrestricted calculation. The difference is, the iron of {Fe(NO)$_2$}^{10} has negative spin density and (NO)$_2$ has positive spin density. Therefore, two irons are coupled antiferromagnetically while each of them

couples to its bound nitrosyl(s) antiferromagnetically as well. This kind of spin-polarization indicates nitrosyls are withdrawing electrons from irons to stabilize them and the electrons of the same spin localize to maximize exchange energy. In comparison, $\{Fe(NO)\}^7$ in **[Fe'-Fe*]^0**, which has less electron density, is less subject to spin-polarization. The corresponding singlet of **[Fe'-Fe*]$^-$**, which totally eliminates the spin-polarization and pairs the two above-mentioned unpaired electrons in d_{z2} of the $\{Fe(NO)\}^8$ unit, is 16.5 kcal/mol higher in energy.

During the reduction of doublet **[Fe'-Fe*]^0** into triplet **[Fe'-Fe*]$^-$**, the incoming electron is accommodated in the d_{xy} orbital, the anti-bonding with N_2S_2 σ-donation and is heavily destabilized. As an effort to stabilize the complex and lower the general energy level of iron's *d* orbital, the nitrosyl must provide subtantial back-bonding by overlapping both of its π* orbitals with the iron's d_{xz}, d_{yz} orbitals and therefore a linear Fe-N-O assembly is rendered. Bending of NO in x direction, for example, does not affect the π^*_y orbital but reduces the overlapping between π^*_x (which is primarily contributed by N p_x and O p_x) and d_{xz} while increases the overlap between π^*_x and d_{z2}. But the d_{z2} orbital is only singly occupied in contrast to the doubly occupied d_{xz} orbital in triplet **[Fe'-Fe*]$^-$**. Bending of NO is energetically rather unfavorable with a triplet configuration. In comparison, the singlet **[Fe'-Fe*]$^-$**, higher in energy, shows a much bent Fe-N-O angle of 131.1°, indicating a preference of the overlap between π^*_x and the now doubly occupied d_{z2} at the cost of the overlapping π^*_x and d_{xz}. The reasoning is d_{z2} is higher in energy than d_{xz} and it mixes better with ever-higher empty π^*_x orbital for back-bonding, which motivates the bending of NO. The neutral **[Fe'-Fe*]^0** featuring a

{Fe(NO)}^{7} unit with only one electron on d_{z2} and no electrons on d_{x2-y2}, shows a Fe-N-O angle in-between, 149.4°. Because it is so electronically pressured to relieve the crowdedness of electrons by adopting a linear or more bent geometry to maximize the back-bonding.

Despite the back-bonding contributed by NO, singly occupied d_{xy} of the Fe(NO) unit requires further stabilization, as reflected in the extended Fe-S (by 0.131 Å, avg) and Fe-N (by 0.252 Å, avg) bonds during the reduction from neutral **[Fe'-Fe*]^0** into triplet **[Fe'-Fe*]^0**, to reduce the orbital overlapping; the iron also goes out of the N_2S_2 mean plane (by 0.864 Å) to stagger the lobes of the d_{xy} orbitals with the σ-donation lobes from N_2S_2. In contrast, the singlet **[Fe'-Fe*]$^-$** does not have such pressure to stabilize d_{x2-y2} as evidence by marginal Fe-S (by 0.065 Å, avg) and Fe-N (by 0.014 Å, avg) length increases in the reduction with a smaller Fe displacement from N_2S_2 mean plane (by 0.585 Å).

In this report, the functional TPSSh instead of TPSS (the one used for closed chain **[Fe'-Fe*]$^+$**) was used to perform the calculations. TPSSh has Hartree-Fock exchange to ensure **[Fe'-Fe*]$^+$** has a broken-symmetry singlet ground state. TPSS fails to create a broken-symmetry singlet **[Fe'-Fe*]$^+$** and the probable cause might be the broken-symmetry singlet **[Fe'-Fe*]$^+$** is slightly higher in energy than the closed-shell singlet. In the optimization, a broken-symmetry guess gradually converges into a closed-shell wavefunction as the Fe-Fe distance decreases in the optimization. The geometry of **[Fe'-Fe*]$^+$** might be helpful in determining the electronic structure.

Conclusion

It is impressive to see how nitrosyls can buffer added negative charge. The non-innocence properties of NO are efficiently demonstrated in the isolation of a diiron complex in three different oxidation states. The fine structural variations observed in the molecular structures are signature features of the deft electronic delocalization through the $(NO)Fe(\mu\text{-}S)_2Fe(NO)_2$ core. Although DFT studies explain the linear/bent Fe-NO feature, Mossbauer and XES studies should be done to confirm the electronic nature in three redox levels. The stability of the diirontrinitrosyl complex in the oxidized cationic form was shown by its isolation from six different synthetic routes. The electrochemical response to acids should be quantified with constant potential coulometry studies.

CHAPTER VIII

METALLODITHIOLATE LIGANDS STABILIZING [$Fe^{I}Fe^{I}$], [Fe^{I}[Fe(NO)]^{II}] AND [(μ-H)$Fe^{II}Fe^{II}$] SYSTEMS: A FORAY IN [FeFe]-H_2ASE BIOMIMETICS

Introduction

The research for developing innovative ligands to meet specific stereo- and electrochemical requirements in catalysts, is of an imminent interest among chemists in academia and indistry. Subtle improvisations in ligand design allow mechanistic tweaks for a better understanding of the catalytic cycle. Several ligands have been utlilized by the synthetic chemists in the hydrogenase community to mimic the donor groups in the [FeFe]-H_2ase enzyme active site (EAS),[56-57] *e.g.*, substituted phosphines have been the major contributor in mimicing the cyanide ligands.[65] The donor properties of the phosphines are similar to that of cyanide, while, unlike the cyanides as ligands in the model systems, phosphines permit protons to reach the open site on the catalytically active distal Fe for proton reduction in homogeneous catalysis, without acting as a base.[65] The Rauchfuss group has extensively used the bidentate diphosphine ligands as donor groups in their model complexes.[56, 65] To achieve the "rotated structure"[201] the Darensbourg group has incorporared bulky carbene ligands (IMes), as well as substituents on the bridgehead of the S-R-S, in their models along with various phosphine ligands.[152, 201-202]

The enzyme active site of Acetyl-coA synthase (ACS) provides a Cys-Gly-Cys backbone that harbors a Ni^{II} center.[72-73] Similarly, the inactive form of the Iron Nitrile Hydratase (NHase)[203] contains Fe center, with an endogeneous NO as an axial fifth ligand, in a Cys-Ser-Cys motif. The dithiolate stabilized square planar Ni, in ACS, binds a catalytically active, second Ni center, through bridging cystenyl-sulfur, that allows organometallic transformations.[72] Such Cys-X-Cys tripeptide linkage provide inspirations for a tetradentate N_2S_2 ligand that can bind host of chelatable metals (M = Group 12, 11, 10 metals, $[(NO)Co]^{II}$, $[(NO)Fe]^{II}$, Ru^{II}, Mn^{II}, Mo^{IV}, $[V{\equiv}O]^{II}$ and some group 13 metals like Al^{III}, Ga^{III}, In^{III}).[162]

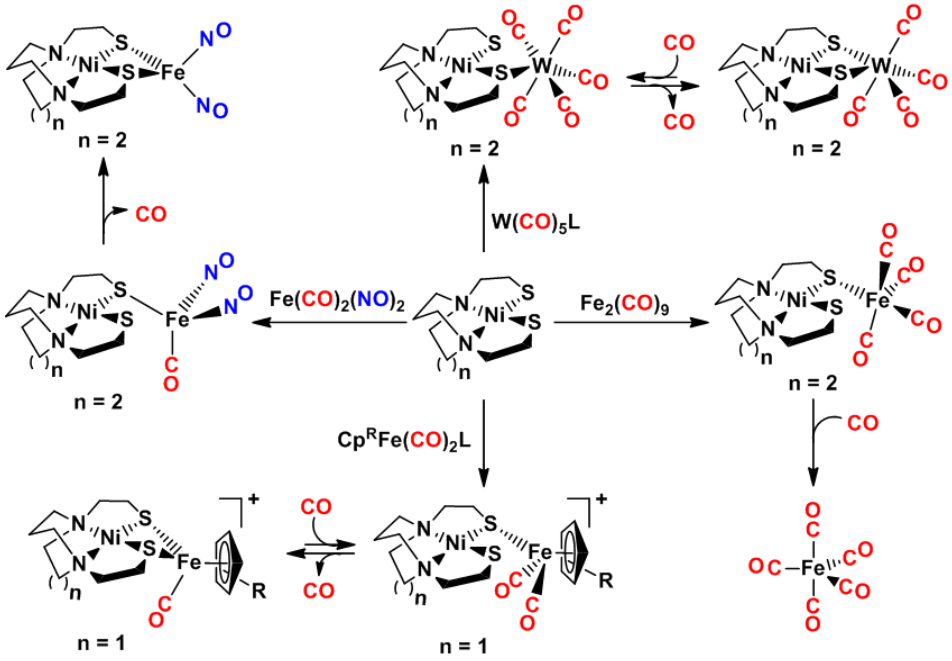

Figure VIII-1. NiN_2S_2 metallodithiolates displaying hemilability via mono- and dithiolate (M(μ-S)M'and M(μ-S)$_2$M') linkages.[162]

The Darensbourg group over the last two decades have synthesized several square planar (M = Ni^{II}) or square pyramidal (M = $[(NO)Fe]^{II}$ or $[(NO)Co]^{II}$) MN_2S_2 complexes that utilize *cis*-dithiolates as mono- (M(μ-S)M'), or bidentate donors (M(μ-$S)_2$M'), to bind exogenous carbonyl- or nitrosyl-stablilized low-valent metals.[162] These metallodithiolate-ligand stabilized heterometallics portray noteworthy chemical properties like ligand dependent chelation utilizing steric components, hemilability, redox and electronic donor properties involving '$W(CO)_{4/5}$', '$Fe(CO)_5$', '$Cp^RFe(CO)_{2/1}$' and '$Fe(CO)_{1/0}(NO)_2$' as the receiver units, Figure VIII-1.[160, 182, 204-206]

The art of developing efficient homogeneous catalysts typically lies in fine tuning the chemical environment of robust catalysts by incorporating subtle and appropriate steric and electronic modifications. Chemists are on the look-out for *de-novo* ligands that can be appended to the conventional and versatile organometallic ligand pool. In this regard, the MN_2S_2s represent an unique class of metallodithiolate ligands that illustrate controlled aggregation through bridging thiolates emulating electronic and steric requirements of the conventional phosphine or amine ligands. The bidentate/monodentate chelation (hemilability)[161], in presence of added CO[207] or electrons,[160] generates an unbound thiolate that has shown features to surrogate the pendant amine base of [FeFe]-H_2ase enzyme active site.[37] However, application of MN_2S_2's as metalloligands in the development of model complexes for [FeFe]-H_2ase enzyme active site have been little explored. Till date, $[(\mu\text{-pdt})Fe^I_2(CO)_5]_2$-M(sip) (where, sip = sulfanylpropyliminomethyl-pyridine and M = Fe and Ni in *Oh*

coordination), is the only example of a metallodithiolate binding to a $Fe^{I}Fe^{I}$ unit, stabilized by a propanedithiolate (pdt).[208]

The deceptively simple 1st generation model complex, (μ-pdt)$[Fe^{I}_2(CO)_6]$,[57] have been previously modified with an internal oxidant, $[NO]^+$, and H^+ to generate (μ-pdt)$[(CO)_3Fe^{I}(Fe(NO))^{II}(CO)L]^+$ and (μ-pdt)(μ-H)$[L(CO)_2Fe^{II}Fe^{II}(CO)_2L]^+$, respectively.[95, 97] Herein we report the synthesis and characterization of three different heterotrimetallics that employ MN_2S_2 binding to the aforementioned diiron scaffolds in three redox levels, $Fe^{I}Fe^{I}$•MN_2S_2, $Fe^{I}[Fe(NO)]^{II}$•MN_2S_2 and (μ-H)$Fe^{II}Fe^{II}$•MN_2S_2. The MN_2S_2s bind the diiron core with one thiolate, M(μ-SR)M', that allows the free unbound thiolate model features of a built-in pendant base to direct proton binding and promoting electrocatalysis for the hydrogen evolution reaction (HER).[182]

Synthesis and Characterization

Unlike the reactions using PMe_3, the reaction of NiN_2S_2 (N_2S_2 = bme-dach or bismercaptoethyldiazacycloheptane) with the parent (μ-pdt)$[Fe^{I}_2(CO)_6]$ complex showed negligible reaction even on heating. However, in presence of a decarbonylating agent, Me_3NO, there was an immediate solution color change from red to dark-brown with the formation of bubbles. Solution vibrational spectroscopy showed a shift in the *ν*(CO) stretching frequencies to lower wavenumbers, 2032(s), 1962(s), 1900(w), as expected upon binding an electron donating NiN_2S_2 to (μ-pdt)$[Fe^{I}_2(CO)_6]$ to form the trimetallic complex, **1a**, as shown in Figure VIII-2. The *ν*(CO) stretching frequencies in THF, matched an intensity ratio similar to phosphine substituted diiron pentacarbonyl species,

ensuring a monodentate binding through one bridging thiolate. Similar reactions were carried out for other diironhexacarbonyl complexes with substituted bridge-head groups, μ-$SCH_2C(CH_3)_2CH_2S$ (dmpdt), and μ-$SCH_2N(CH_3)CH_2S$ (NMe) forming trimetallics **1b** and **1c**, respectively, with similar pattern and slight variations in their ν(CO) stretching frequencies.

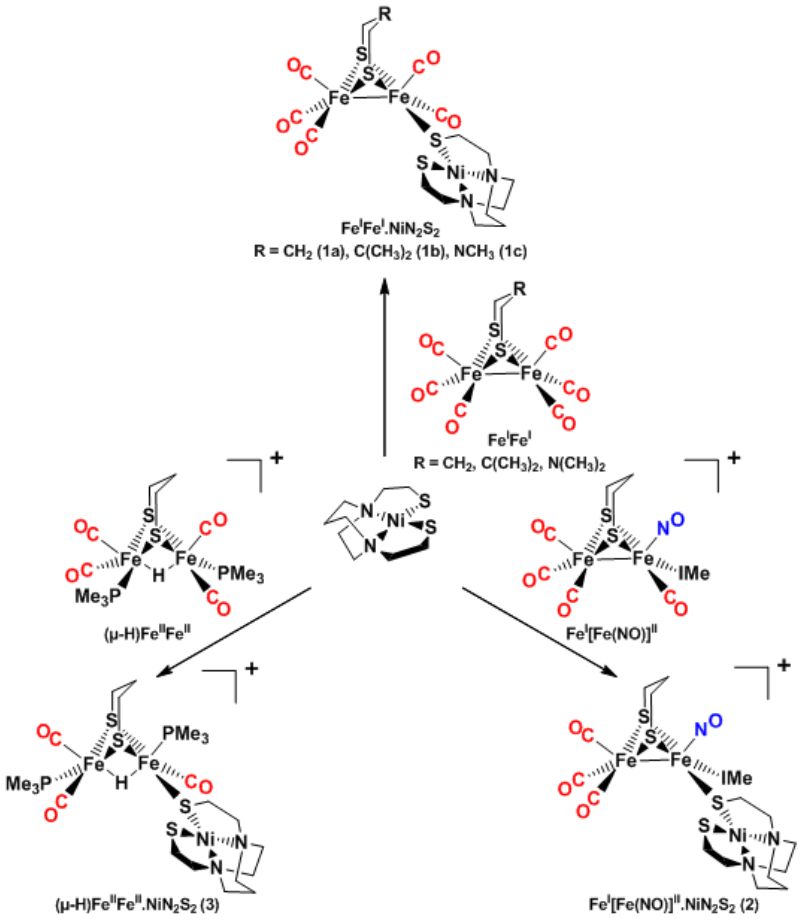

Figure VIII-2. Reaction of NiN_2S_2 with: 1) (μ-SRS)$[Fe^I_2(CO)_6]$, 2) (μ-pdt)$[(CO)_3Fe^I(Fe(NO))^{II}(CO)L]^+$, 3) (μ-pdt)(μ-H)$[L(CO)_2Fe^{II}Fe^{II}(CO)_2L]$

A list of ν(CO) stretching frequencies for the monosubstituted diiron pentacarbonyl complexes are shown in Table VIII-1. It is noteworthy, that the NiN_2S_2 metallodithiolates are better donors than the PMe_3 ligand as can be seen from the ν(CO) reporter units. These newly synthesized trimetallic compounds are diamagnetic and were characterized by ^1H and ^{13}C NMR spectroscopies.

As an interesting aside, reaction of NiN_2S_2 with carbonyl stabilized low-valent, golden colored $(THF)W^0(CO)_5$ synthon, resulted in a mono-thiolate bridged, Ni(μ-S)W, bimetallic complex **4** and a di-thiolate bridged, $Ni(\mu\text{-}S)_2W_2$, trimetallic complex **4"**. These complexes were purified using column chromatography and were recrystallized separately. The molecular structures of complexes **4** and **4"** are shown in Figure VIII-3.

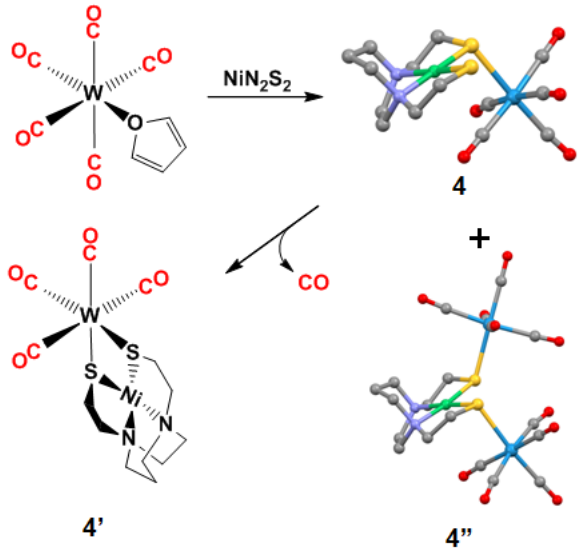

Figure VIII-3. Reaction of NiN_2S_2 with $(THF)W(CO)_5$ forming **4** and **4"**. **4** converts to **4'** upon photolysis. The molecular structures of **4** and **4"** are shown as ball and stick renditions.

Upon photolysis, complex **4** showed facile ring closure properties, *i.e.*, mono-dentate to bidentate conversion, with loss of a CO, forming complex **4'**, Figure VIII-3.[206] Similar reactions with substituted Ni(bme-daco), (where daco is bismercaptoethyldiazacyclooctane) has precedence in literature.[206]

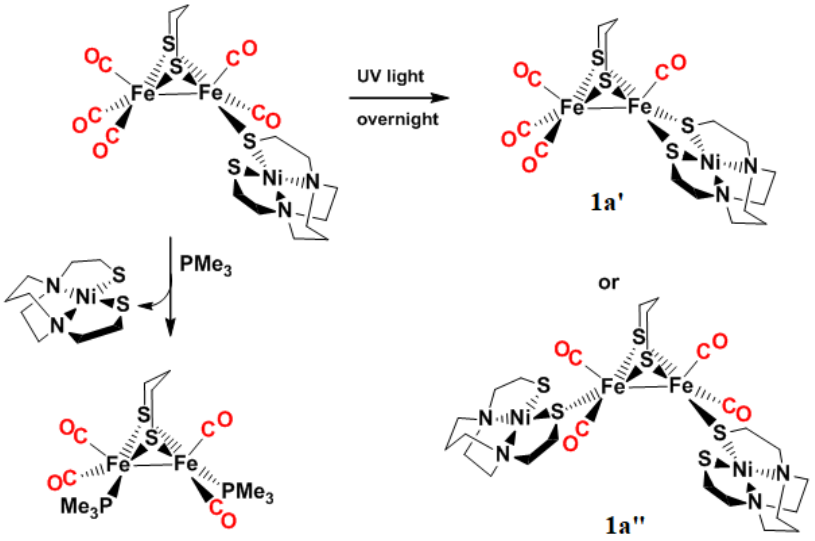

Figure VIII-4. Reactivity studies of complex **1** in presence of UV radiation and PMe_3.

Likewise, photolysis of **1a**, Figure VIII-4, resulted in a shift of the ν(CO) stretching frequencies to lower wavenumbers which matched the pattern of a diirontetracarbonyl species, Figure VIII-5; an intramolecular ring closure leads to **1a'** while an intermolecular nucleophilic substitution of a second CO forms **1a"**. Since the photolysis reaction is accompanied with significant decomposition of NiN_2S_2, formation of **1a"** is a possibility. However, the substituted complex could not be isolated to obtain X-ray quality crystals. It should be noted that addition of PMe_3 to **1a**, substitutes NiN_2S_2

to form a di-substituted complex, (μ-pdt)[$(CO)_2(PMe_3)Fe^IFe^I(CO)_2(PMe_3)$], Figure VIII-4.

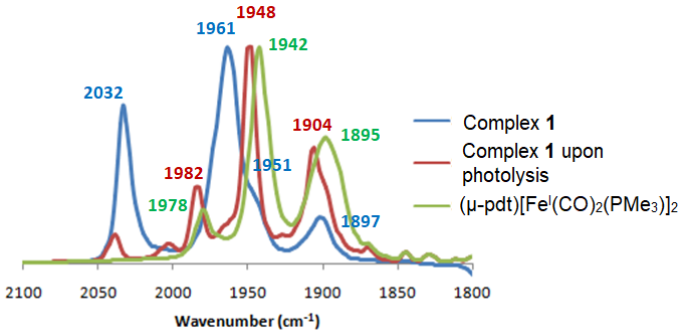

Figure VIII-5. Overlay of the normalized CH_3CN solution IR spectra of complex **1** (blue trace), complex **1** upon photolysis (red trace), and reaction of complex **1** in presence of PMe_3.

N-heterocyclic carbene (IMes or IMe) stabilized (μ-pdt)[$(CO)_3Fe^I(Fe(NO))^{II}(CO)L]^+$ complexes have been previously studied with respect to CO lability (in the [$(Fe(NO))^{II}$(CO)L] moiety) using PMe_3, CN^- or ^{13}CO exchange.[97] Stirring a suspension of NiN_2S_2 with (μ-pdt)[$(CO)_3Fe^I(Fe(NO))^{II}(CO)L]^+$ led to a clean conversion in ~1 h, forming complex **2**, Figure VIII-2. The reaction was monitored by IR in CH_2Cl_2 that showed a bathochromic shift in the *ν*(CO) and *ν*(NO) stretching frequencies. While the *ν*(NO) band shifts by ca. 60 cm^{-1}, the *ν*(CO) stretching frequencies move from 2084, 2057, 2017 cm^{-1} to 2056 and 1990 cm^{-1} with a concomitant change in the *ν*(CO) pattern resembling a pseudo C_{3v} geometry. The NiN_2S_2 proved a better donor than PMe_3 derivative[208] where the *ν*(CO)s and *ν*(NO) differed by ca. 6 and 15 cm^{-1}, respectively. Positive-ion ESI mass spectrum of complex **2** showed

characteristic signals at the molecular ion mass, *m/z* 703.94, with isotopic distribution patterns that closely matched the calculated bundle.

Likewise, photolysis of (μ-pdt)(μ-H)$[L(CO)_2Fe^{II}Fe^{II}(CO)_2L]^+$ in presence of NiN_2S_2 under a sunlamp formed (μ-H)$Fe^{II}Fe^{II}$•NiN_2S_2, complex **3**, over a period of 30 mins in CH_2Cl_2, Figure VIII-2.[95] Increase in electron density in the diiron construct, upon addition of NiN_2S_2, was amenable with the change in pattern and position of the vibrational spectrum with respect to *ν*(CO) reporters, from 2032, 1990 to 2023, 1968, 1929 cm^{-1}. A triphenylphosphine substituted complex, **3-PPh$_3$**, synthesized for comparison, displayed similar *ν*(CO) vibrational spectrum displaying a three band pattern which are slightly higher in wavenumbers than the NiN_2S_2 derivative. These diamagnetic compounds **3** and **3-PPh$_3$** were characterized by ^1H and ^{13}C NMR spectroscopy. Thus, the 'CO-substitution feature' was exploited by using a metallodithiolate ligand, NiN_2S_2, as has been established before using neutral or anionic σ-donor ligands. A list of *ν*(CO) and *ν*(NO) stretching frequencies of the substituted **$[Fe^IFe^I]$**, **$[Fe^I(Fe(NO))^{II}]$**, and **(μ-H)$[Fe^{II}Fe^{II}]$** trimetallic complexes are shown in Table VIII-1.

Table VIII-1. Comparison of solution *ν*(CO) and *ν*(NO) vibrational frequencies of substituted **[$Fe^{I}Fe^{I}$]**, **[$Fe^{I}(Fe(NO))^{II}$]**, and **(μ-H)[$Fe^{II}Fe^{II}$]** complexes.[95, 97, 208]

Complexes	**Diatomic vibrational frequencies (cm^{-1})[a]**
[$Fe^{I}Fe^{I}$]	
(μ-pdt)[$Fe^{I}_2(CO)_6$]	2072(m), 2037(s), 1990(s)[b]
(μ-pdt)[$(CO)_3Fe^{I}Fe^{I}(CO)_2(PMe_3)$]	2037(s), 1980(s), 1919(m)[b]
(μ-pdt)[$(CO)_3Fe^{I}Fe^{I}(CO)_2(PPh_3)$]	2044(s), 1984(s), 1931(m)[b]
(μ-pdt)[$(CO)_3Fe^{I}Fe^{I}(CO)_2$(IMe)]	2035(s), 1971(s), 1952(m), 1915(m)[c]
(μ-pdt)[$(CO)_3Fe^{I}Fe^{I}(CO)_2(NiN_2S_2)$]	2032(s), 1962(s), 1900(w)[c, d]
(μ-dmpdt)[$(CO)_3Fe^{I}Fe^{I}(CO)_2(NiN_2S_2)$]	2032(s), 1961(s), 1899(w)[c, d]
(μ-NMe)[$(CO)_3Fe^{I}Fe^{I}(CO)_2(NiN_2S_2)$]	2036(s), 1970(s), 1900(w)[c, d]
[$Fe^{I}(Fe(NO))^{II}$]	
(μ-pdt)[$(CO)_3Fe^{I}(Fe(NO))^{II}$(IMe)(CO)]$^+$	2085(s), 2058(s), 2018(s), <u>1809(s)</u>[c]
(μ-pdt)[$(CO)_3Fe^{I}(Fe(NO))^{II}(IMe)(PMe_3)$]$^+$	2061(s), 1996(s), <u>1759(m)</u>[c]
(μ-pdt)[$(CO)_3Fe^{I}(Fe(NO))^{II}$(IMe)(CN)]	2054(s), 1988(s), <u>1755(m)</u>[c]
(μ-pdt)[$(CO)_3Fe^{I}(Fe(NO))^{II}(IMe)(NiN_2S_2)$]$^+$	2056(s), 1990(s), <u>1740(m)</u>[c, d]
(μ-H)[$Fe^{II}Fe^{II}$]	
(μ-H)[$(PMe_3)(CO)_2Fe^{II}Fe^{II}(CO)_2(PMe_3)$]$^+$	2032(s), 1990(s)[c]
(μ-H)[$(PMe_3)(CO)_2Fe^{II}Fe^{II}(CO)(PMe_3)(PPh_3)$]$^+$	2026(s), 1976(m), 1951(m)[c, d]
(μ-H)[$(PMe_3)(CO)_2Fe^{II}Fe^{II}(CO)(PMe_3)(NiN_2S_2)$]$^+$	2023(s), 1968(m), 1929(m)[c, d]

[a]values underlined are for NO; [b]spectra measured in CH_3CN; [c]spectra measured in CH_2Cl_2; [d]this work.

Molecular Sructures

X-ray quality crystals of the complexes **1**, **2** and **3** were obtained by layering moderately concentrated solutions in CH_2Cl_2 with hexanes at -28 °C under nitrogen atmosphere. The NiN_2S_2 binds in a monodentate fashion, using one of the thiolates, from the basal position of the square pyramid, for complexes **1** and **2**, while from the apical position for complex **3**, Figure VIII-6.

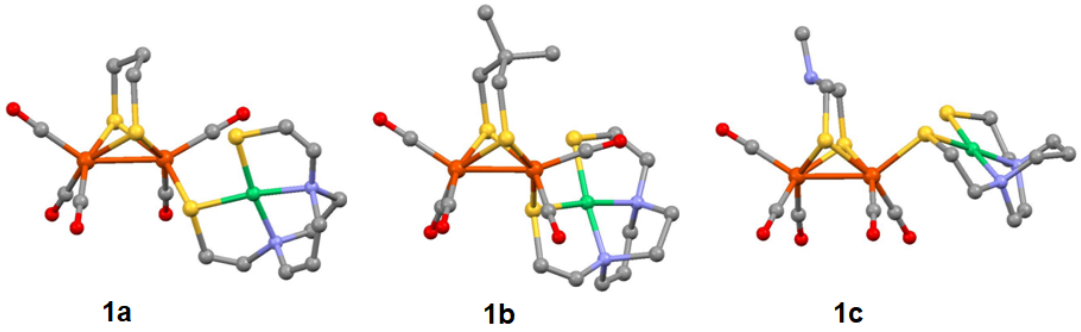

Figure VIII-6. Molecular structures of **1a**, **1b** and **1c** shown as ball and stick renditions.

Interestingly, $[(\mu\text{-pdt})Fe^{I}_2(CO)_5]_2$-M(sip),[208] and several phopsphine derivatives, $[(\mu\text{-pdt})Fe^{I}_2(CO)_5PR_3]$, show apical binding.[208] The bridging thiolate employs the divergent lobe of its *p*-type lone pair to bind the diiron unit such that the S_{NiN2S2}-Fe bond distance is within the limits of thioether derivatives (ca. 2.3 Å) while the S_{NiN2S2}•••Fe non-bonding distance is ~ 4 Å - a feature previously displayed by $[\kappa^1\text{-}NiN_2S_2\bullet FeCp(CO)_2]^+$ and $[\kappa^1\text{-}NiN_2S_2\bullet Fe(CO)(NO)_2]$ complexes.[160, 165, 168] The Ni^{II} in the metalloligand maintains a square planar geometry and the Ni•••Fe distances are 3.6 – 3.7 Å, that are significantly long to allow any bonding interaction.

The Fe-Fe distance of complexes **1a**, **1b** and **1c** shows a decreasing trend from ca. 2.54, 2.52 and 2.50 Å, respectively; this can be tentatively correlated with the additional steric bulk on the bridgehead. The boat conformation of the FeS_2C_3, created by the $\mu\text{-}SCH_2RCH_2S$ (where R = CH_2 or $C(CH_3)_2$), is on the NiN_2S_2 side of the diiron construct for complexes **1a** and **1b** while it is on the $Fe(CO)_3$ side for complex **1c**. This difference in orientation can be compared to the steric strain created by the apical binding of the NiN_2S_2 in complex **1c**. While the $FeS_2(C_{CO})_2S_{NiN2S2}$ moieties of **1a** and **1b**

are nearly perfect square pyramids (τ = 0.03 and 0.05, respectively), complex **1c** shows more distortion (τ = 0.12) due to steric restraints among basal C_{CO}, and $H_{\alpha\text{-}CH2}$ and $H_{\beta\text{-}CH2}$ of NiN_2S_2 that are around 2.7 Å. The average plane of NiN_2S_2 is moderately coplanar with the FeS_pFe (where S_p is the S of pdt, proximal to NiN_2S_2) plane for complexes **1a** and **1b**. Complex **1c** shows similar coplanarity with S_2Fe_p (where S_2 is the pdt-thiolates and Fe_p is proximal Fe to the NiN_2S_2) plane.

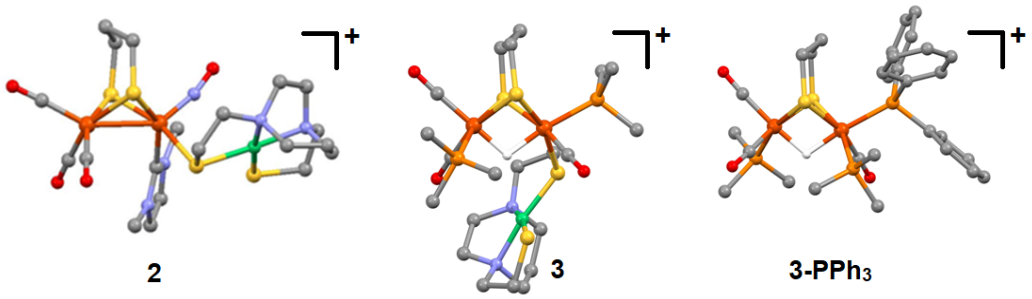

Figure VIII-7. Molecular structures of **2**, **3** and **3-PPh$_3$** shown as ball and stick renditions. The counter anions BF_4^- (**2**), $BArF^-$ (**3**), PF_6^- (**3-PPh$_3$**) and the hydrogen atoms, except the bridging hydride, are omitted for clarity.

The molecular structure of complex **2**, Figure VIII-7, shows that the NiN_2S_2 binds from the basal position which bears a close structural semblance with (μ-pdt)$[(CO)_3Fe^{I}(Fe(NO))^{II}(IMe)L]^{n+}$, where, L = PMe_3 (n = 1) or CN^- (n = 0).[97] The Fe-Fe distance shows a subtle elongation of ca. 0.03 Å with respect to the CN^- derivative. The flap angle created by the pdt and the slightly bent Fe-N-O angle, ca. 166°, are directed away from the substituted Fe for all. The torsion angle, defined by N_{ap} – Fe – Fe – C_{ap}, are ~ 7°, for complexes **2** and the CN^- derivative, while it is much lower, ~1°, for the PMe_3 derivative. Conversely, the τ value for the substituted Fe, shows a discernable

square pyramidal geometric distortion for complexes **2** and the PMe_3 derivative (0.22 and 0.26, respectively), while the CN^- substituted complex maintains a moderately regular square pyramid (τ = 0.1).[97] This can be attributed to the steric incumbencies created by the bulky PMe_3 and the metallodithiolate ligand compared to the linear diatomic cyanide. The Ni^{II}, present in a perfect square plane, is 3.4 Å away from the proximal Fe, negating any bonding interaction.

In complex **3**, **s**ubstituion of CO by NiN_2S_2 in (μ-pdt)(μ-H)$[L(CO)_2Fe^{II}Fe^{II}(CO)_2L]^+$ (L = PMe_3) repositions the PMe_3 ligands from trans-basal to apical-basal, minimizing the steric interactions between the NiN_2S_2 and PMe_3, Figure VIII-7.[95] On the contrary, PPh_3 substitutes the apical CO maintaining the trans-basal nature of the two PMe_3 ligands as seen in the starting material. In both **3** and **3-PPh3**, the flap created by the pdt is oriented towards the di-substituted iron. The face-bridged bioctahedra created by the bridging hydride, constricts the Fe•••Fe distance in complex **3** by 0.05 Å compared to **3-PPh3**. Unlike other complexes, NiN_2S_2 positions itself in a manner such that the N_2S_2 plane is oriented towards the diiiron scaffold in cmplex **3**. This shortens the free-thiolate to bridging-hydride distance to 3.06 Å. This feature serves as a potential structural facade to the 'free thiolate as a pendant base' thesis, such that the latter can bind a proton for a contiguous proton/hydride coupling for dihydrogen formation.

Electrochemistry

Complex **1** and **3** were chosen for electrochemical studies. The cyclic voltammograms were recorded in CH_3CN under argon at room temperature using a glassy carbon working electrode and 0.1 M $[^tBu_4N][PF_6]$ as supporting electrolyte.

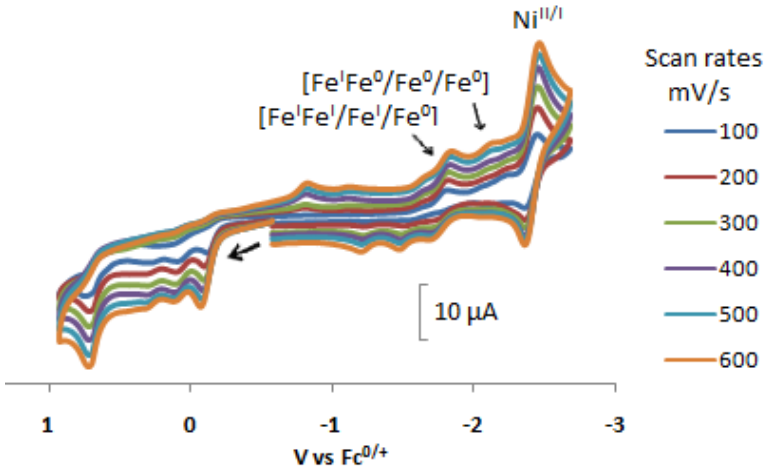

Figure VIII-8. Overlays of the scan rate dependence of the cyclic voltammograms of **1** as 2 mM CH_3CN solutions. The scans were initiated in the positive direction as indicated by the arrow.

Complex **1** and **3** in general showed three and two reduction events, respectively. Overlays of the voltamograms of **1** and **3,** showing scan rate dependance, are shown in Figure VIII-8 and 9, respectively. The irreversible reduction events of complex **1**, at -1.82 V and -2.1 V are assisgned for Fe^IFe^I/Fe^IFe^0 and Fe^IFe^0/Fe^0Fe^0 couples, respectively. Similar reduction events for the Fe^IFe^I/Fe^IFe^0 couple are shown by PR_3-substituted diironpentacarbonyl complexes that slightly differ by varying the donor groups on the phosphine.[208] Complex **3** showed one irreversible reduction event at -1.68

V which was assisgned for the $Fe^{II}Fe^{II}/Fe^{II}Fe^{I}$ couple. Both the complexes showed a $Ni^{II/I}$ quasi-reversible reduction event at -2.41 V and -2.46 V, respectively.

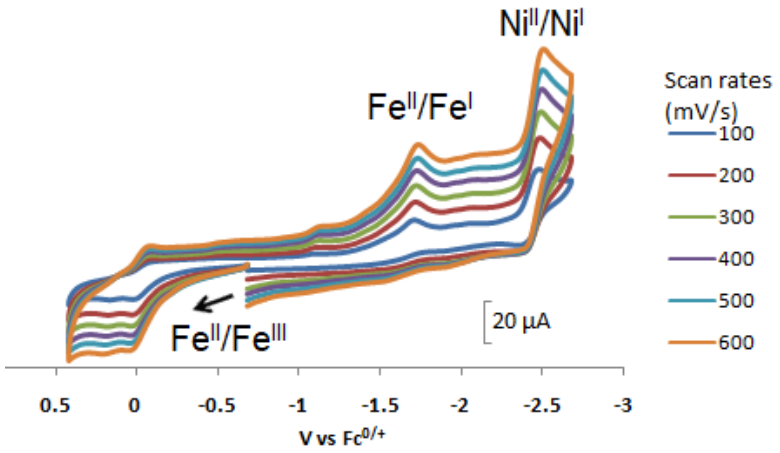

Figure VIII-9. Overlays of the scan rate dependence of the cyclic voltammograms of **3** as 2 mM CH_3CN solutions. The scans were initiated in the positive direction as indicated by the arrow.

Bimetallic complexes of the type 'metalloligand-Lewis acid adducts, (MN_2S_2-M')', in general, show a positive shift in the reduction potential of the metal center (M) in MN_2S_2-M', in comparison to free metalloligand (MN_2S_2). In contrast the reduction potential of the free metalloligand (Ni-bmedach) shows similar values with $Ni^{II/I}$ couple in complexes **1** and **3**, indicating no predominant shift in $Ni^{II/I}$ reduction event. This contrasting feature can be explained by recognizing the reduction potential of the free receiver moeity. If the receiver group undergoes reduction prior to the NiN_2S_2, the reduction of the former (in this case $Fe^{I}Fe^{I}/Fe^{I}Fe^{0}$ or $Fe^{II}Fe^{II}/Fe^{II}Fe^{I}$ couples) has minimal electrochemical effect on the $Ni^{II/I}$ reduction. The possibility of NiN_2S_2 dissociation can be obviated by the observation that repeated scans showed diminutive

deposition on the electrode. Similar features were shown by $[NiN_2S_2•Pd(dppe)]^{2+}$ and $[NiN_2S_2•Fe(NO)_2]^{+/0}$ complexes, where $Pd^{II/I}$ and $Pd^{I/0}$ reductions for the former, and $\{Fe(NO)_2\}^{9/10}$ reduction for the latter, were at higher potentials that allowed $Ni^{II/I}$ reduction at -2.48 V.[181-182]

Electrochemical Response to Added Acid

The effect of **1** as an electrocatalyst was tested by CV studies in the presence of trifluoroacetic acid (TFA) in CH_3CN, Figure VIII-10. Addition of TFA showed a consistent increase in the cathodic current at the first reduction potential, -1.82 V, for the Fe^IFe^I/Fe^IFe^0 couple. This catalytic current response is accompanied with a concomitant current event at -1.48 V that showed a steady increase in current upon further addition of TFA. It should be noted that free TFA shows a catalytic current response at -1.90 V.

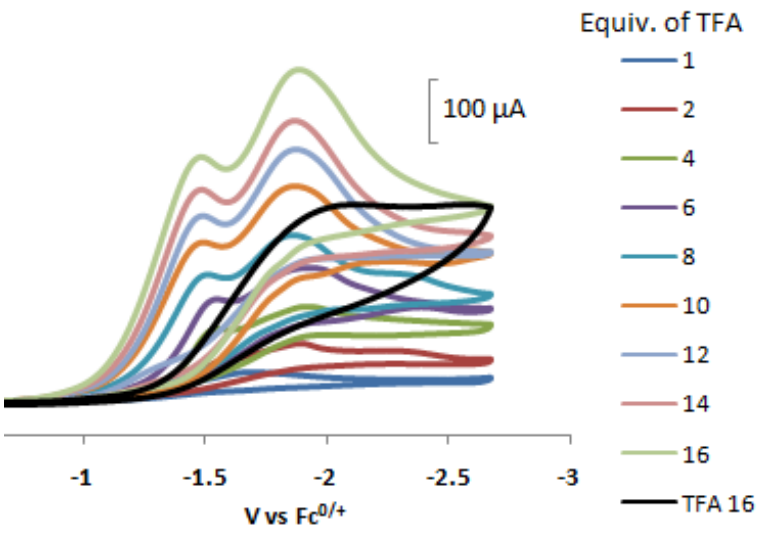

Figure VIII-10. Cyclic voltammograms of **1** in 2 mM CH_3CN solution with added equivalents of TFA. The black trace shows 16 equivalents of free TFA in absence of catalyst.

Contrasting the two major cathodic current events, we postulate the working mechanism, Figure VIII-11, as follows: The first step is the addition of an e^- at -1.82 V to form Fe^IFe^0, **1**$^-$. The species **1**$^-$ can bind H^+ at two potential basic sites: a) oxidative addition at the substituted iron as a potential hydride, or b) protonation at the unbound thiolate of NiN_2S_2, to form **1-SH**.

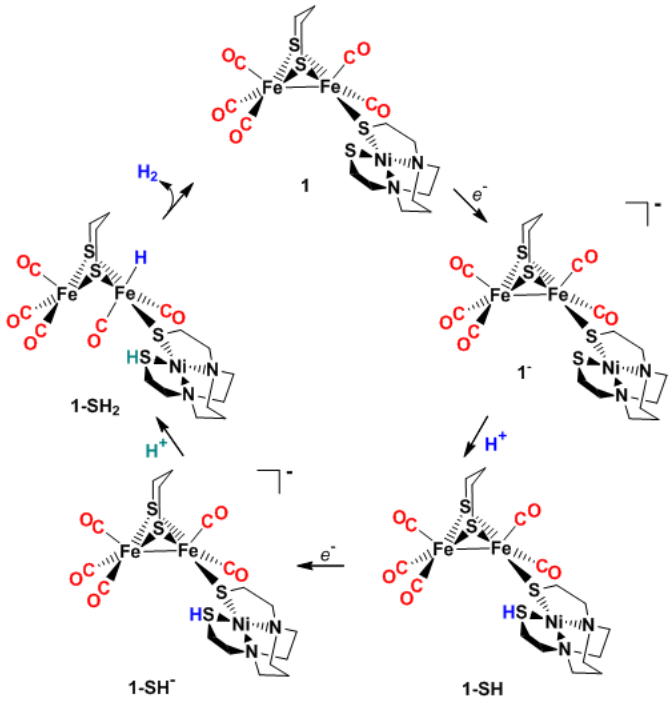

Figure VIII-11. Proposed catalytic cycle for H_2 production with complex **1** in presence of TFA.[160]

We postulate that the steady current event at -1.45 V is responsible for the formation of the latter, **1-SH.**[160] It should be noted that addition of TFA to **1** leads to decomposition, forming NiN_2S_2 and (μ-pdt)[$Fe^I_2(CO)_6$]. Hence electron addition precedes protonation. This is followed by the addition of a second e^- to form **1-SH**$^-$.

Transfer of the thiolate-bound proton to the substituted iron, as hydride, and re-protonation of the free thiolate of NiN_2S_2 creates the required $H^{-}\bullet\bullet\bullet H^{+}$ pair for a necessary hydride-proton coupling to form hydrogen.[160]

Conclusion

The metallodithiolate ligand (NiN_2S_2) efficiently surrogates phosphines or other pi-acid ligands like CN^- or CO in stabilizing the diiron scaffold in three redox states, $[Fe^{I}Fe^{I}]$, $[Fe^{I}[Fe(NO)]^{II}]$ and $[(\mu\text{-}H)Fe^{II}Fe^{II}]$. These trimetallics were characterized using IR, ESI-MS, X-ray crystallography. The *cis*-dithiolate, NiN_2S_2, displays monodentate binding using one sulfur that structurally emulates the cystenyl-thiolate in [FeFe]-Hyd A,[37] while the unbound thiolate brings forth its potency as a pendant base, modelling the bridge-head amine of the enzyme active site. Electrochemical studies in presence of trifluoraacetic acid showed a catalytic current response along with a shoulder that indicates the possible formation of the protonated thiolate. At this juncture, computational studies were not attempted for a full mechanistic understanding, nonotheless, a putative $Fe\text{-}H^{-}\bullet\bullet\bullet^{+}H\text{-}S$ coupling provides a *prima facie* mechanistic pathway for the catalytic proton reduction. The complex, $(\mu\text{-pdt})(\mu\text{-}H)[L(CO)_2Fe^{II}Fe^{II}(CO)(NIN_2S_2)L]^{+}$, provides opportunities for isotope exchange studies for characterizing the protonated-thiolate iron-hydride pair.

CHAPTER IX

CONCLUSIONS AND FUTURE PROSPECTS

In a broader perspective, over the past two decades, the pursuit of metallo-sulfur chemistry has become prevalent in the bioinorganic field, encompassing much variation in coordination chemistry, mechanisms, and reactivity. Specifically, the versatile organometallic type active sites in biology that harbor such metallo-sulfur units have been key inspirations for their synthetic development. During my graduate research years (2011-2017) significant advances were made in the understanding of salient features of such active sites via small molecule models from different research groups across the globe.

Synthetic small molecule models, with a thiolate-bridged hetero/homobimetallic core and emulating certain features of the [NiFe]-H_2ase active site, were developed as biomimetics. These efforts followed the report of details of the structure and their necessity for the catalytic mechanism. While a synthetic analogue truly faithful to the features of the active site has yet to be reported, ongoing research efforts that stem from newer and better understanding of the catalytic cycle continue to evolve. Certainly these models are not precise analogous to the active site, and it may not be possible to achieve this as the NiFe site is tied into the protein so carefully. However, distinct features may be explored that mimic the spectroscopically detected intermediates and computationally predicted transient species hitherto obscure under prevalent experimental conditions.

While [FeFe]- and [NiFe]-H_2ase have features in common, see Figure IX-1, the difference is the obvious pendant amine base between the S to S linker that is positioned propitiously on the open site of the distal Fe. The guide from this feature was adopted by Dan Dubois and his group at PNNL with spectacular success. This group incorporated a diphosphine-derivatized pendant amine into the second coordination sphere of a nickel catalyst and demonstrated its role in site directed proton relay. The phosphines were systematically tuned to provide steric encumbrance such that the overall result was remarkable, reaching a TOF for electrocatalytic proton reduction of 106,000 s^{-1}.[76] This result has steered much of the research in synthetic models of the [FeFe]-H_2ase.[56]

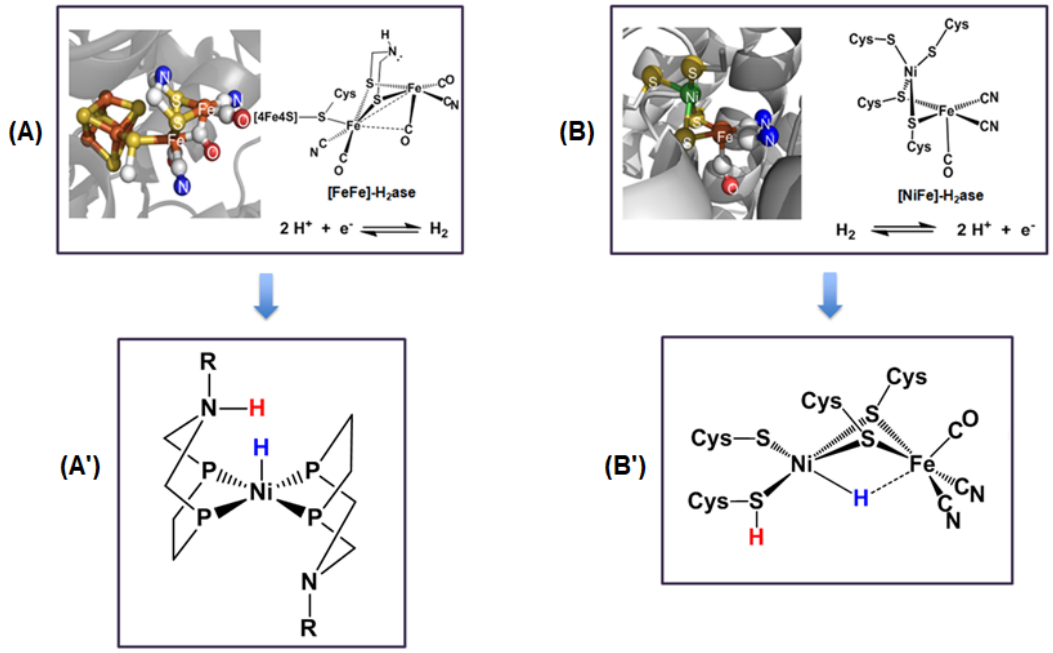

Figure IX-1. The top two panels, A and B, display the active sites of [FeFe]- and [NiFe]-H_2ase in their protein backbone, respectively; their chemdraw representations are shown alongside. The [FeFe]-H_2ase active site-inspired Dubois' catalyst showing the possible hydride and proton bound form, A'.[76, 102] The chemdraw representation of the Ni-R state in [NiFe]-H_2ase catalytic cycle with a protonated cysteinyl thiolate and a bridging hydride, by Ogata *et al.*, B'.[71]

The [NiFe]-H_2ase active site, on the contrary, has bridging dithiolates from protein cysteine residues and terminal cysteinyl groups, but no obvious pendant base, unless the terminal cysteinyl-sulfurs act in this capacity. In fact, a high resolution crystallographic evidence of a protonated cysteinyl thiolate and a bridging hydride in the Ni-R state by Ogata *et al*., supports this thesis.[71] Nevertheless, a plethora of heterobimetallic complexes have been synthesized, by various research groups, that possess only bridging dithiolates as structural models of the [NiFe]-H_2ase active site, Figure IX-2. Despite the lack of terminal thiolates, a significant number of such complexes show proton reduction electrocatalysis. Thus the general question is why/how does these bridging thiolate based electrocatalysts work? Specifically, how do the protons find their way into these compounds for the needed H^+/e^- coupling? Can such analysis lead to understanding of the efficacy of proton reduction electrocatalysis?

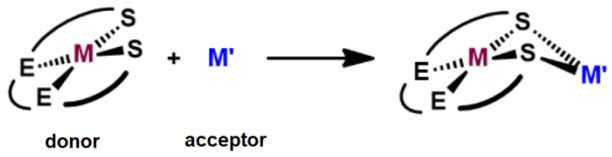

Figure IX-2. General strategy for synthesizing [NiFe]-H_2ase biomimetics; E can be nitrogen, sulfur or phosphorous atoms.

During the course of my research, I have pursued these questions in synthetic work and electrochemical analysis. A range of heterobimetallic complexes with varying donor and acceptor groups, were prepared and are presented in Chapters III, IV and V of my dissertation. We find that these complexes can be synthesized in bidentate and

monodentate forms, Figure IX-3. Thus it came as no surprise to us that computational analysis (performed by collaborators Prof. M. B. Hall and coworker Dr. Shengda Ding, TAMU Ph.D., 2017) of electrochemical events suggested that the catalytic mechanism should find rearrangement of these S-bridged bimetallics so as to guide the protons and electrons to perform a HER reaction. The computation-assisted mechanistic study revealed the generation of an electrochemically-induced pendant thiolate base (bidentate to monodentate conversion) that can bind a proton for an ultimate hydride-proton coupling.

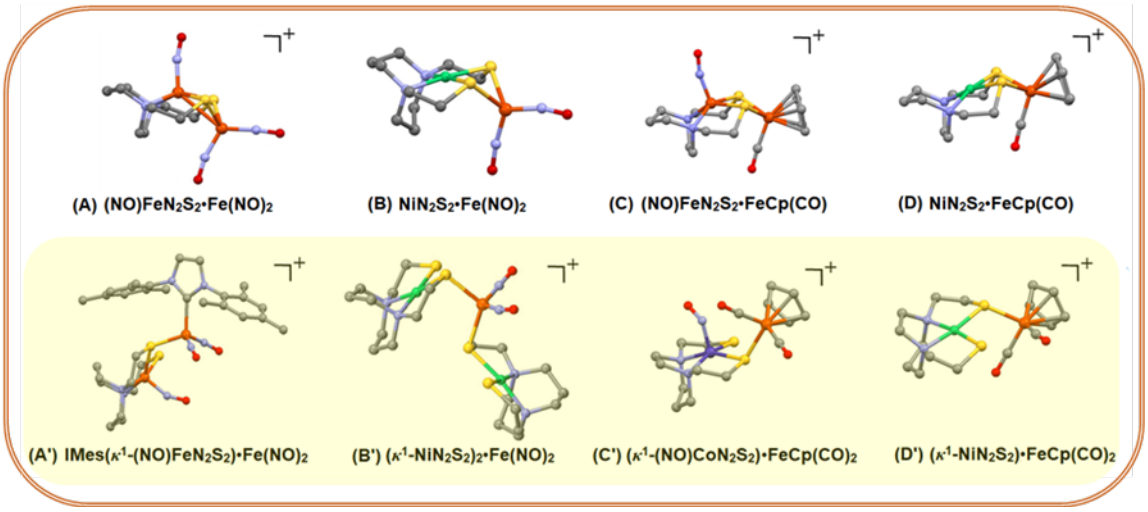

Figure IX-3. Molecular structures of electrocatalysts, showing mono- and bidentate S-bridged complexes; the bidentate complexes A, B, C and D were tested for HER; the N_2S_2 ligand is either bme-dach or bme-daco.

An open question is "can we isolate the protonated sulfur?" that are proposed by the computational studies. Thus the monodentate versions of the heterobimetallics based on the cis-dithiolate metalloligands, such as A', B', C', and D', were prepared and examined in Chapters V and VI for the possible isolation of a protonated terminal

thiolate. Although, such monodentate complexes displayed stoichiometric binding of protons and Ph_3PAu^+ (as a proton analogue), and other electrophiles, often leading to ligand displacement, it nevertheless showed possibilities to realize the synthetic goal. For example, spectroscopic evidence of a pinched proton, as postulated by computational studies in Chapter V, potentially mimics the protonated-thiolate in the native enzyme, shown in Figure IX-1B'. The versatility of the metallodithiolates ligands, as surrogates of conventional phosphines and carbenes, was also shown in their monodentate binding capabilities with $[Fe^IFe^I]$, $[Fe^I[Fe(NO)]^{II}]$ and $[(\mu\text{-}H)Fe^{II}Fe^{II}]$ systems, as [FeFe]-H_2ase bioinspired trimetallics, exhibiting a potential built-in base, described in Chapter VIII.

Another important facet that has not been structurally reproduced by the synthetic community is the Ni-centered hydride in NiFe bimetallics from first row transition metals as displayed in the native enzyme. Different research groups have synthesized NiM' bimetallics and isolated a hydride on the second receiver metal (M') using 2nd or 3rd row transition metals, like Ru^{II}, Ir^{III} etc.[56] Spectroscopic evidences of Ni-centered hydride have been shown by Artero *et al*. where redox active ligand bipyridyl plays an important role.[136]

Different from the MN_2S_2 metallodithiolate ligand concept, the Ni center in the [NiFe]-hydrogenase enzyme active site, is in a S_4 coordination due to four protein-bound cysteinyl-thiolates. These are not covalently bound to each other, unlike the active site coordination environments of ACS or Nitrile hydratase. The active site of ACS displays a cys-gly-cys, N_2S_2, tight binding motif that essentially holds abound Ni in a rigid square

planar geometry. The NiN_2S_2 acts as a metalloligand to support a second Ni center, with an open site, that allows organometallic type transformations. Whether the cis-dithiolates are involved in the reaction sequence as hemi-labile ligands acting as a base, is not yet understood.

Hence, development of catalysts that are inspired from the active site of [NiFe]-H_2ase should incorporate ligand features that would allow coordination flexibility at the Ni center. As shown in the Dubois catalysts, coordination flexibility, in turn, should stabilize low oxidation state Ni in pseudo tetrahedral coordination geometry. Chapter VIII showed the isolation of the doubly reduced, anionic diiron trinitrosyl complex, using flexible open chain N_2S_2 ligand. Ligand flexibility can be incorporated by increasing the carbon chain in the N to N linker. Low valent Ni can be further stabilized by the use of redox-active non-innocent ligands involving π-conjugation, as in dithiolene complexes.

Development of Electrocatalysts

Another important question is "how might we improve the synthetic catalysts"? From the work that I have done, I conclude that the efficiency of an electrocatalyst depends on:

1. the applied electropotential: the lower the potential the better
2. a low overpotential
3. the increase in cathodic current and TOF: the higher the better
4. the strength of the acid used

In the development of our $[MN_2S_2•Cp^RFe(CO)]^+$ or $[MN_2S_2•Fe(NO)_2]^{+/0}$ electrocatalysts, we have seen that the catalytic potential initiates at the first redox event. In case of the complexes with the hard $[Cp^RFe(CO)]^+$ receivers, the catalytic event was initiated at the reduction potential of the metal center in MN_2S_2, (E = <-1.64 V). Although the catalysts with the hard receivers were robust, this feature led to high overpotentials. The overpotentials were even higher in magnitude upon changing η^5-$C_5H_5$with η^5-C_5Me_5.

The overpotential problem was fixed to an extent when the hard receivers were replaced with soft receiver groups containing the electron-buffering NO ligand, $Fe(NO)_2$. The catalytic potentials were now initiated at the redox potentials of the receivers, E = -0.73 V, thus reducing the overpotential significantly. This change in molecular design, however, led to less robust catalysts with low catalytic current response. Moreover, it required strong acid $HBF_4•Et_2O$, instead of trifluoroacetic acid, for electrocatalysis, likely because of the absence of ready terminal thiolate and proton guidance system.

Thus, we have shown a rationale of choosing receiver units that would give rise to HER at low energy (electrochemical voltage), however, at the cost of efficiency. I hope that my work and this analysis will help advance future research regarding the stability of the electrocatalysts and increasing their TOF.

REFERENCES

1. Elsden, S. R., *Trends Biochem. Sci. (Pers. Ed.)* **1981,** *6*, 251.
2. Green, D. E.; Stickland, L. H., *Biochem. J.* **1934,** *28*, 898.
3. Pakes, W. C. C.; Jollyman, W. H., *J.Chem. Soc., Trans.* **1901,** *79*, 386.
4. Stephenson, M.; Stickland, L. H., *Biochem. J.* **1932,** *26*, 712.
5. Farkas, A.; Farkas, L.; Yudkin, J., *Proc. R. Soc. Lond. [Biol]*. **1934,** *115*, 373.
6. Kempner, W.; Kubowitz, F., *Biochem. Z.* **1933,** *265*, 245.
7. Kempner, W., *Biochem. Z.* **1933,** *257*, 41.
8. Pappenheimer, A. M.; Shaskan, E., *J. Biol. Chem.* **1944,** *155* (1), 265.
9. Lee, S. B.; Wilson, J. B.; Wilson, P. W., *J. Biol. Chem.* **1942,** *144*, 273.
10. Wyss, O.; Wilson, P. W., *Proc. Natl. Acad. Sci. U.S.A.* **1941,** *27*, 162.
11. Krasna, A. I.; Rittenberg, D., *J. Am. Chem. Soc.* **1954,** *76*, 3015.
12. Berlier, Y.; Lespinat, P. A.; Dimon, B., *Anal. Biochem.* **1990,** *188*, 427.
13. Krasna, A. I.; Riklis, E.; Rittenberg, D., *J. Biol. Chem.* **1960,** *235*, 2717.
14. Nicolet, Y.; Piras, C.; Legrand, P.; Hatchikian, E. C.; Fontecilla-Camps, J. C., *Struct. Fold. Des.* **1999,** *7*, 13.
15. Purec, L.; Krasna, A. I., *Proc.Natl. Acad. Sci.* **1967,** *57*, 1416.
16. Purec, L.; Krasna, A. I., *Biochemistry* **1968,** *7*, 51.
17. Coukoulis, H.; Campbell, L. L., *J. Bacteriol.* **1971,** *105*, 319.
18. Legall, J.; Dervartanian, D. V.; Spilker, E.; Lee, J.-P.; Peck, H. D., Curr. Microbiol. **1971,** *234*, 525.

19. Holm, R. H.; Lo, W., *Chem. Rev.* **2016,** *116*, 13685.

20. Holm, R. H.; Kennepohl, P.; Solomon, E. I., *Chem. Rev.* **1996,** *96*, 2239.

21. Nakos, G.; Mortenson, L., *Biochim. Biophys. Acta* **1971,** *227*, 576.

22. Beinert, H.; Kennedy, M. C.; Stout, C. D., *Chem. Rev.* **1996,** *96*, 2335.

23. Multani, J. S.; Mortenson, L. E., *Biochim. Biophys. Acta* **1972,** *256*, 66.

24. Smith, L. A.; Hill, S.; Yates, M. G., *Nature* **1976,** *262*, 209.

25. Lukoyanov, D.; Khadka, N.; Yang, Z.-Y.; Dean, D. R.; Seefeldt, L. C.; Hoffman, B. M., *J. Am. Chem. Soc.* **2016,** *138*, 1320.

26. Krasna, A. I., Oxygen-stable Hydrogenase and Assay. In *Methods in Enzymology*, Fleischer, S.; Packer, L., Eds. Academic Press: 1978; Vol. 53, pp 296-314.

27. Adams, M. W. W.; Hall, D. O., *Biochem. Biophys. Res. Commun.* **1977,** *77*, 730.

28. Schlegel, H. G.; Schneider, K., *Hydrogenases: Their Catalytic Activity, Structure and Function*, E. Goltze: Gottingen, 1978.

29. Lubitz, W.; Reijerse, E.; van Gastel, M., *Chem. Rev.* **2007,** *107*, 4331.

30. Schönheit, P.; Moll, J.; Thauer, R. K., *Arch. Microbiol.* **1979,** *123*, 105.

31. Albracht, S. P. J.; Graf, E. G.; Thauer, R. K., *FEBS Lett.* **1982,** *140*, 311.

32. Graf, E.-G.; Thauer, R. K., *FEBS Lett.* **1981,** *136*, 165.

33. Krüger, H. J.; Huynh, B. H.; Ljungdahl, P. O.; Xavier, A. V.; Der Vartanian, D. V.; Moura, I.; Peck, H. D.; Teixeira, M.; Moura, J. J.; LeGall, J., *J. Biol. Chem.* **1982,** *257*, 14620.

34. Moura, J. J. G.; Moura, I.; Huynh, B. H.; Krüger, H. J.; Teixeira, M.; DuVarney, R. C.; DerVartanian, D. V.; Xavier, A. V.; Peck, H. D.; LeGall, J., *Biochem. Biophys. Res. Commun.* **1982,** *108*, 1388.

35. LeGall, J.; Ljungdahl, P. O.; Moura, I.; Peck, H. D.; Xavier, A. V.; Moura, J. J. G.; Teixera, M.; Huynh, B. H.; DerVartanian, D. V., *Biochem. Biophys. Res. Commun.* **1982,** *106*, 610.

36. Yamazaki, S., *J. Biol. Chem.* **1982,** *257*, 7926.

37. Lubitz, W.; Ogata, H.; Rüdiger, O.; Reijerse, E., *Chem. Rev.* **2014,** *114*, 4081.

38. Adams, M. W.; Mortenson, L. E., *J. Biol. Chem.* **1984,** *259*, 7045.

39. Wang, G.; Benecky, M. J.; Huynh, B. H.; Cline, J. F.; Adams, M. W.; Mortenson, L. E.; Hoffman, B. M.; Münck, E., *J. Biol. Chem.* **1984,** *259*, 14328.

40. Teixeira, M.; Moura, I.; Xavier, A. V.; Huynh, B. H.; DerVartanian, D. V.; Peck, H. D.; LeGall, J.; Moura, J. J., *J. Biol. Chem.* **1985,** *260*, 8942.

41. Hom, S. S.; Graham, L. A.; Maier, R. J., *J. Bacteriol.* **1985,** *161*, 882.

42. Voordouw, G.; Walker, J. E.; Brenner, S., *Eur. J. Biochem.* **1985,** *148*, 509.

43. Thauer, R. K.; Klein, A. R.; Hartmann, G. C., *Chem. Rev.* **1996,** *96*, 303.

44. Fontecilla-Camps, J. C.; Volbeda, A.; Cavazza, C.; Nicolet, Y., *Chem. Rev.* **2007,** *107*, 4273.

45. Vignais, P. M.; Billoud, B., Occurrence, *Chem. Rev.* **2007,** *107*, 4206.

46. Higuchi, Y.; Yasuoka, N.; Kakudo, M.; Katsube, Y.; Yagi, T.; Inokuchi, H., *J. Biol. Chem.* **1987,** *262*, 2823.

47. Volbeda, A.; Charon, M.-H.; Piras, C.; Hatchikian, E. C.; Frey, M.; Fontecilla-Camps, J. C., *Nature* **1995,** *373*, 580.

48. Bagyinka, C.; Szokefalvi-Nagy, Z.; Demeter, I.; Kovacs, K. L., *Biochem. Biophys. Res. Commun.* **1989,** *162*, 422.

49. George, G. N.; Prince, R. C.; Stokley, K. E.; Adams, M. W.; Stockley, K. E., *Biochem. J.* **1989,** *259*, 597.

50. Adams, M. W.; Eccleston, E.; Howard, J. B., *Proc.Natl. Acad. Sci.* **1989,** *86*, 4932.

51. Seefeldt, L. C.; Arp, D. J., *J. Bacteriol.* **1989,** *171*, 3298.

52. Bagley, K. A.; Van Garderen, C. J.; Chen, M.; Woodruff, W. H.; Duin, E. C.; Albracht, S. P. J., *Biochemistry* **1994,** *33*, 9229.

53. Higuchi, Y.; Yasuoka, N.; Kakudo, M.; Katsube, Y.; Yagi, T.; Inokuchi, H., *J. Biol. Chem.* **1987,** *262*, 2823.

54. Cammack, R.; Frey, M.; Robson, R. *Hydrogen as a Fuel*, Taylor & Francis: London, 2001.

55. Lai, C.-H.; Lee, W.-Z.; Miller, M. L.; Reibenspies, J. H.; Darensbourg, D. J.; Darensbourg, M. Y., *J. Am. Chem. Soc.* **1998,** *120*, 10103.

56. Schilter, D.; Camara, J. M.; Huynh, M. T.; Hammes-Schiffer, S.; Rauchfuss, T. B., *Chem. Rev.* **2016,** *116*, 8693.

57. Li, Y.; Rauchfuss, T. B., *Chem. Rev.* **2016,** *116*, 7043.

58. Siegbahn, P. E. M.; Tye, J. W.; Hall, M. B., *Chem. Rev.* **2007,** *107*, 4414.

59. Peters, J. W.; Lanzilotta, W. N.; Lemon, B. J.; Seefeldt, L. C., *Science* **1998,** *282*, 1853.

60. Shima, S.; Thauer, R. K., *Chem. Rec.* **2007,** *7*, 37.

61. Vincent, K. A.; Parkin, A.; Armstrong, F. A., *Chem. Rev.* **2007,** *107*, 4366.

62. De Lacey, A. L.; Fernández, V. M.; Rousset, M.; Cammack, R., *Chem. Rev.* **2007,** *107*, 4304.

63. Lubitz, W.; Tumas, W., *Chem. Rev.* **2007,** *107*, 3900.

64. Arkadii, A. K.; Sergei, D. V., *Russ. Chem. Rev.* **1986,** *55*, 867.

65. Bethel, R. D.; Darensbourg, M. Y., The Bioorganometallic Chemistry of Hydrogenase. In *Bioorganometallic Chemistry*, Wiley-VCH Verlag GmbH & Co. KGaA: 2014; pp 239-272.

66. Parker, P. M., *Hydrogenase: Webster's Timeline History, 1942-2007*. ICON Group International, Inc.: San Diego, California, 2009.

67. Agrawal, A. G.; van Gastel, M.; Gärtner, W.; Lubitz, W., *J. Phys. Chem. B* **2006,** *110*, 8142.

68. Chapman, A.; Cammack, R.; Hatchikian, C. E.; McCracken, J.; Peisach, J., *FEBS Lett.* **1988,** *242*, 134.

69. Fan, C.; Teixeira, M.; Moura, J.; Moura, I.; Huynh Boi, H.; Le Gall, J.; Peck, H. D.; Hoffman, B. M., *J. Am. Chem. Soc.* **1991,** *113*, 20.

70. Whitehead, J. P.; Gurbiel, R. J.; Bagyinka, C.; Hoffman, B. M.; Maroney, M. J., *J. Am. Chem. Soc.* **1993,** *115*, 5629.

71. Ogata, H.; Nishikawa, K.; Lubitz, W., *Nature* **2015,** *520*, 571.

72. Can, M.; Armstrong, F. A.; Ragsdale, S. W., *Chem. Rev.* **2014,** *114*, 4149.

73. Darnault, C.; Volbeda, A.; Kim, E. J.; Legrand, P.; Vernede, X.; Lindahl, P. A.; Fontecilla-Camps, J. C., *Nat. Struct. Mol. Biol.* **2003,** *10*, 271.

74. Hsieh, C.-H.; Ding, S.; Erdem, O. F.; Crouthers, D. J.; Liu, T.; McCrory, C. C. L.; Lubitz, W.; Popescu, C. V.; Reibenspies, J. H.; Hall, M. B.; Darensbourg, M. Y., *Nat. Commun.* **2014,** *5*, 3684.

75. Tye, J. W.; Hall, M. B.; Darensbourg, M. Y., *Proc. Natl. Acad. Sci. U.S.A.* **2005,** *102*, 16911.

76. Helm, M. L.; Stewart, M. P.; Bullock, R. M.; DuBois, M. R.; DuBois, D. L., A *Science* **2011,** *333*, 863.

77. Chiang, C.-Y.; Lee, J.; Dalrymple, C.; Sarahan, M. C.; Reibenspies, J. H.; Darensbourg, M. Y., *Inorg. Chem.* **2005,** *44*, 9007.

78. Hess, J. L.; Conder, H. L.; Green, K. N.; Darensbourg, M. Y., *Inorg. Chem.* **2008,** *47*, 2056.

79. Golden, M.; Darensbourg, M.; Irwin, J.; Frost, B., 43. *Inorg. Synth.* **2014,** *36*, 231.

80. Jenkins, R. M.; Pinder, T. A.; Hatley, M. L.; Reibenspies, J. H.; Darensbourg, M. Y., *Inorg. Chem.* **2011,** *50*, 1849.

81. Mills, D. K.; Reibenspies, J. H.; Darensbourg, M. Y., *Inorg. Chem.* **1990,** *29*, 4364.

82. Mills, D. K.; Hsiao, Y. M.; Farmer, P. J.; Atnip, E. V.; Reibenspies, J. H.; Darensbourg, M. Y., *J. Am. Chem. Soc.* **1991,** *113*, 1421.

83. Tuntulani, T.; Reibenspies, J. H.; Farmer, P. J.; Darensbourg, M. Y., *Inorg. Chem.* **1992,** *31*, 3497.

84. Karlin, K. D.; Rabinowitz, H. N.; Lewis, D. L.; Lippard, S. J., *Inorg. Chem.* **1977,** *16*, 3262.

85. Karlin, K. D.; Lippard, S. J., *J. Am. Chem. Soc.* **1976,** *98*, 6951.

86. Catheline, D.; Astruc, D., *Organometallics* **1984,** *3*, 1094.

87. Reger, D. L.; Coleman, C., J. *Organomet. Chem.* **1977,** *131*, 153.

88. Suryaraman, M. G.; Viswanathan, A., J. Chem. Educ. **1949,** *26*, 594.

89. Winter, A.; Zsolani, L.; Huttner, G., *Naturforsch* **1982,** *37*, 1430.

90. Singleton, M. L.; Jenkins, R. M.; Klemashevich, C. L.; Darensbourg, M. Y., *C. R. Chim.* **2008,** *11*, 861.

91. Li, H.; Rauchfuss, T. B., *J. Am. Chem. Soc.* **2002,** *124*, 726.

92. Rampersad, M. V.; Jeffery, S. P.; Golden, M. L.; Lee, J.; Reibenspies, J. H.; Darensbourg, D. J.; Darensbourg, M. Y., *J. Am. Chem. Soc.* **2005,** *127*, 17323.

93. McBride, D. W.; Stafford, S. L.; Stone, F. G. A., *Inorg. Chem.* **1962,** *1*, 386.

94. Smith, C. R.; Zhang, A.; Mans, D. J.; RajanBabu, T. V., *Org. Synth.* **2008,** *85*, 248.

95. Zhao, X.; Georgakaki, I. P.; Miller, M. L.; Yarbrough, J. C.; Darensbourg, M. Y., *J. Am. Chem. Soc.* **2001,** *123*, 9710.

96. Hsieh, C.-H.; Darensbourg, M. Y., *J. Am. Chem. Soc.* **2010,** *132*, 14118.

97. Bethel, R. D.; Crouthers, D. J.; Hsieh, C.-H.; Denny, J. A.; Hall, M. B.; Darensbourg, M. Y., *Inorg. Chem.* **2015,** *54*, 3523.

98. Appel, A. M.; Helm, M. L., *ACS Catal.* **2014,** *4*, 630.

99. Wiese, S.; Kilgore, U. J.; Ho, M.-H.; Raugei, S.; DuBois, D. L.; Bullock, R. M.; Helm, M. L., *ACS Catal.* **2013,** *3*, 2527.

100. Felton, G. A. N.; Glass, R. S.; Lichtenberger, D. L.; Evans, D. H., *Inorg. Chem.* **2006,** *45*, 9181.

101. Bain, G. A.; Berry, J. F., *J. Chem. Educ.* **2008,** *85*, 532.

102. DuBois, D. L., *Inorg. Chem.* **2014,** *53*, 3935.

103. Wilson, A. D.; Shoemaker, R. K.; Miedaner, A.; Muckerman, J. T.; DuBois, D. L.; DuBois, M. R., *Proc. Natl. Acad. Sci. U.S.A.* **2007,** *104*, 6951.

104. Wilson, A. D.; Newell, R. H.; McNevin, M. J.; Muckerman, J. T.; Rakowski DuBois, M.; DuBois, D. L., *J. Am. Chem. Soc.* **2006,** *128*, 358.

105. Raugei, S.; Chen, S.; Ho, M.-H.; Ginovska-Pangovska, B.; Rousseau, R. J.; Dupuis, M.; DuBois, D. L.; Bullock, R. M., *Chem. Eur. J.* **2012,** *18* (21), 6493.

106. Stewart, M. P.; Ho, M.-H.; Wiese, S.; Lindstrom, M. L.; Thogerson, C. E.; Raugei, S.; Bullock, R. M.; Helm, M. L., *J. Am. Chem. Soc.* **2013,** *135*, 6033.

107. Liu, T.; DuBois, D. L.; Bullock, R. M., *Nat. Chem.* **2013,** *5*, 228.

108. Liu, T.; Wang, X.; Hoffmann, C.; DuBois, D. L.; Bullock, R. M., *Angew. Chem.* **2014,** *53*, 5300.

109. Liu, T.; Chen, S.; O'Hagan, M. J.; Rakowski DuBois, M.; Bullock, R. M.; DuBois, D. L., Synthesis, *J. Am. Chem. Soc.* **2012,** *134*, 6257.

110. Dementin, S.; Burlat, B.; De Lacey, A. L.; Pardo, A.; Adryanczyk-Perrier, G.; Guigliarelli, B.; Fernandez, V. M.; Rousset, M., *J. Biol. Chem.* **2004,** *279*, 10508.

111. Niu, S.; Hall, M. B., *Inorg. Chem.* **2001,** *40*, 6201.

112. Ogo, S.; Ichikawa, K.; Kishima, T.; Matsumoto, T.; Nakai, H.; Kusaka, K.; Ohhara, T., *Science* **2013,** *339*, 682.

113. Denny, J. A.; Darensbourg, M. Y., *Chem. Rev.* **2015,** *115*, 5248.

114. Nguyen, N. T.; Mori, Y.; Matsumoto, T.; Yatabe, T.; Kabe, R.; Nakai, H.; Yoon, K.-S.; Ogo, S., *Chem. Commun.* **2014,** *50*, 13385.

115. Yang, D.; Li, Y.; Su, L.; Wang, B.; Qu, J., Eur. J. *Inorg. Chem.* **2015,** *2015*, 2965.

116. Zhu, W.; Marr, A. C.; Wang, Q.; Neese, F.; Spencer, D. J. E.; Blake, A. J.; Cooke, P. A.; Wilson, C.; Schröder, M., *Proc.Natl. Acad. Sci. U.S.A.* **2005,** *102*, 18280.

117. Canaguier, S.; Field, M.; Oudart, Y.; Pecaut, J.; Fontecave, M.; Artero, V., *Chem. Commun.* **2010,** *46*, 5876.

118. Weber, K.; Erdem, Ö. F.; Bill, E.; Weyhermüller, T.; Lubitz, W., *Inorg. Chem.* **2014,** *53*, 6329.

119. Reynolds, M. A.; Rauchfuss, T. B.; Wilson, S. R., *Organometallics* **2003,** *22*, 1619.

120. Kim, K.; Matsumoto, T.; Robertson, A.; Nakai, H.; Ogo, S., *Chem. Asian J.* **2012,** *7*, 1394.

121. Kishima, T.; Matsumoto, T.; Nakai, H.; Hayami, S.; Ohta, T.; Ogo, S., *Angew. Chem. Int. Ed.* **2016,** *55*, 724.

122. Kure, B.; Sano, M.; Nakajima, T.; Tanase, T., *Organometallics* **2014,** *33*, 3950.

123. Kim, K.; Kishima, T.; Matsumoto, T.; Nakai, H.; Ogo, S., *Organometallics* **2013,** *32*, 79.

124. Chiang, C.-Y.; Miller, M. L.; Reibenspies, J. H.; Darensbourg, M. Y., *J. Am. Chem. Soc.* **2004,** *126*, 10867.

125. Smee, J. J.; Miller, M. L.; Grapperhaus, C. A.; Reibenspies, J. H.; Darensbourg, M. Y., *Inorg. Chem.* **2001,** *40*, 3601.

126. Fourmond, V.; Jacques, P.-A.; Fontecave, M.; Artero, V., *Inorg. Chem.* **2010,** *49*, 10338.

127. Smieja, J. M.; Benson, E. E.; Kumar, B.; Grice, K. A.; Seu, C. S.; Miller, A. J. M.; Mayer, J. M.; Kubiak, C. P., *Proc. Natl. Acad. Sci. U.S.A.* **2012,** *109*, 15646.

128. Cheng, T.-Y.; Bullock, R. M., *J. Am. Chem. Soc.* **1999,** *121*, 3150.

129. Surawatanawong, P.; Tye, J. W.; Darensbourg, M. Y.; Hall, M. B., *Dalton Trans.* **2010,** *39*, 3093.

130. Marenich, A. V.; Ho, J.; Coote, M. L.; Cramer, C. J.; Truhlar, D. G., *Phys. Chem. Chem. Phys.* **2014,** *16*, 15068.

131. Liu, Z.-P.; Hu, P., *J. Am. Chem. Soc.* **2002,** *124*, 5175.

132. Fan, H.-J.; Hall, M. B., *J. Am. Chem. Soc.* **2001,** *123*, 3828.

133. Liu, Z.-P.; Hu, P., *J. Chem. Phys.* **2002,** *117* , 8177.

134. Cao, Z.; Hall, M. B., *J. Am. Chem. Soc.* **2001,** *123*, 3734.

135. Berggren, G.; Adamska, A.; Lambertz, C.; Simmons, T. R.; Esselborn, J.; Atta, M.; Gambarelli, S.; Mouesca, J. M.; Reijerse, E.; Lubitz, W.; Happe, T.; Artero, V.; Fontecave, M., *Nature* **2013,** *499*, 66.

136. Esselborn, J.; Lambertz, C.; Adamska-Venkatesh, A.; Simmons, T.; Berggren, G.; Noth, J.; Siebel, J.; Hemschemeier, A.; Artero, V.; Reijerse, E.; Fontecave, M.; Lubitz, W.; Happe, T., *Nat. Chem. Biol.* **2013,** *9*, 607.

137. Siebel, J. F.; Adamska-Venkatesh, A.; Weber, K.; Rumpel, S.; Reijerse, E.; Lubitz, W., *Biochemistry* **2015,** *54*, 1474.

138. Esselborn, J.; Muraki, N.; Klein, K.; Engelbrecht, V.; Metzler-Nolte, N.; Apfel, U. P.; Hofmann, E.; Kurisu, G.; Happe, T., *Chem. Sci.* **2016,** *7*, 959.

139. Sun, N.; Liu, L. V.; Dey, A.; Villar-Acevedo, G.; Kovacs, J. A.; Darensbourg, M. Y.; Hodgson, K. O.; Hedman, B.; Solomon, E. I., *Inorg. Chem.* **2011,** *50*, 436.

140. Coetzee, J. F.; Padmanabhan, G. R., *J. Am. Chem. Soc.* **1965,** *87*, 5005.

141. Fourmond, V.; Jacques, P. A.; Fontecave, M.; Artero, V., *Inorg. Chem.* **2010,** *49*, 10338.

142. Artero, V.; Fontecave, M., *C. R. Chim.* **2008,** *11*, 926.

143. Luca, O. R.; Crabtree, R. H., *Chem. Soc. Rev.* **2013,** *42*, 1440.

144. Brazzolotto, D.; Gennari, M.; Queyriaux, N.; Simmons, T. R.; Pécaut, J.; Demeshko, S.; Meyer, F.; Orio, M.; Artero, V.; Duboc, C., *Nat. Chem.* **2016,** *8*, 1054.

145. Addison, A. W.; Rao, T. N.; Reedijk, J.; van Rijn, J.; Verschoor, G. C., *J. Chem. Soc., Dalton Trans.* **1984,** 1349.

146. Hammond, G. S., A Correlation of Reaction Rates. *J. Am. Chem. Soc.* **1955,** *77*, 334.

147. Simmons, T. R.; Artero, V., *Angew. Chem. Int. Ed.* **2013,** *52*, 6143.

148. Ogo, S., Electrons from hydrogen. *Chem. Commun.* **2009,** 3317.

149. Gloaguen, F.; Rauchfuss, T. B., *Chem. Soc. Rev.* **2009,** *38*, 100.

150. Grapperhaus, C. A.; Darensbourg, M. Y., *Acc. Chem. Res.* **1998,** *31*, 451.

151. Enemark, J. H.; Feltham, R. D., *Coord. Chem. Rev.* **1974,** *13*, 339.

152. Hsieh, C.-H.; Erdem, O. F.; Harman, S. D.; Singleton, M. L.; Reijerse, E.; Lubitz, W.; Popescu, C. V.; Reibenspies, J. H.; Brothers, S. M.; Hall, M. B.; Darensbourg, M. Y., *J. Am. Chem. Soc.* **2012,** *134*, 13089.

153. Mealli, C.; Rauchfuss, T. B., *Angew. Chem. Int. Ed.* **2007,** *46*, 8942.

154. Kishima, T.; Matsumoto, T.; Nakai, H.; Hayami, S.; Ohta, T.; Ogo, S., *Angew .Chem. Int. Ed.* **2016,** *55*, 822.

155. Matsumoto, T.; Kabe, R.; Nonaka, K.; Ando, T.; Yoon, K.-S.; Nakai, H.; Ogo, S., *Inorg. Chem.* **2011,** *50*, 8902.

156. Ichikawa, K.; Matsumoto, T.; Ogo, S., *Dalton Trans.* **2009,** 4304.

157. Ogo, S.; Kabe, R.; Uehara, K.; Kure, B.; Nishimura, T.; Menon, S. C.; Harada, R.; Fukuzumi, S.; Higuchi, Y.; Ohhara, T.; Tamada, T.; Kuroki, R., *Science* **2007,** *316*, 585.

158. Ogo, S., *Coord. Chem. Rev.* **2017,** *334*, 43.

159. Kim, K.; Matsumoto, T.; Robertson, A.; Nakai, H.; Ogo, S., *Chem. Asian J.* **2012,** *7*, 1118.

160. Ding, S.; Ghosh, P.; Lunsford, A. M.; Wang, N.; Bhuvanesh, N.; Hall, M. B.; Darensbourg, M. Y., *J. Am. Chem. Soc.* **2016,** *138*, 12920.

161. Jeffrey, J. C.; Rauchfuss, T. B., *Inorg. Chem.* **1979,** *18*, 2658.

162. Denny, J. A.; Darensbourg, M. Y., *Chem. Rev. (Washington, DC, U. S.)* **2015,** *115*, 5248.

163. Tye, J. W.; Darensbourg, M. Y.; Hall, M. B., *Inorg. Chem.* **2006,** *45*, 1552.

164. Denny, J. A.; Darensbourg, M. Y., *Coord. Chem. Rev.* **2016,** *324*, 82.

165. Ghosh, P.; Quiroz, M.; Wang, N.; Bhuvanesh, N.; Darensbourg, M. Y., *Dalton Trans.* **2017,** *46*, 5617.

166. Silakov, A.; Wenk, B.; Reijerse, E.; Lubitz, W., *Phys.Chem. Chem. Phys.* **2009,** *11*, 6592.

167. Liaw, W.-F.; Chiang, C.-Y.; Lee, G.-H.; Peng, S.-M.; Lai, C.-H.; Darensbourg, M. Y., *Inorg. Chem.* **2000,** *39*, 480.

168. Hsieh, C.-H.; Chupik, R. B.; Brothers, S. M.; Hall, M. B.; Darensbourg, M. Y., *Dalton Trans.* **2011,** *40*, 6047.

169. Osterloh, F.; Saak, W.; Haase, D.; Pohl, S., *Chem. Commun.* **1997,** 979.

170. Verhagen, Johanna A. W.; Lutz, M.; Spek, Anthony L.; Bouwman, E., *Eur. J. Inorg. Chem.* **2003,** *2003*, 3968.

171. Hsieh, C.-H.; Brothers, S. M.; Reibenspies, J. H.; Hall, M. B.; Popescu, C. V.; Darensbourg, M. Y., *Inorg. Chem.* **2013,** *52*, 2119.

172. Sanina, N. A.; Rudneva, T. N.; Aldoshin, S. M.; Chekhlov, A. N.; Morgunov, R. B.; Kurganova, E. V.; Ovanesyan, N. S., *Russ. Chem. Bull.* **2007,** *56*, 28.

173. Pinder, T. A.; Montalvo, S. K.; Lunsford, A. M.; Hsieh, C.-H.; Reibenspies, J. H.; Darensbourg, M. Y., *Dalton Trans.* **2014,** *43*, 138.

174. Hay, B. P.; Hancock, R. D., *Coord. Chem. Rev.* **2001,** *212*, 61.

175. Crouthers, D. J.; Ding, S.; Denny, J. A.; Bethel, R. D.; Hsieh, C.-H.; Hall, M. B.; Darensbourg, M. Y., *Angew. Chem., Int. Ed.* **2015,** *54*, 11102.

176. Hall, M. B., *Inorg. Chem.* **1978,** *17*, 2261.

177. Baldo, M. A.; Stortini, A. M.; Moretto, L. M.; Ongaro, M.; Roman, M.; Ugo, P., *Talanta* **2017,** *172*, 133.

178. Ding, S.; Ghosh, P.; Darensbourg, M. Y.; Hall, M. B., *Accepted in Proc. Nat. Aca. Sci. U.S.A.* **2017**.

179. Bethel, R. D.; Darensbourg, M. Y., *Nature* **2013,** *499*, 40.

180. Hsieh, C.-H.; Chupik, R. B.; Pinder, T. A.; Darensbourg, M. Y., *Polyhedron* **2013,** *58*, 151.

181. Zhao, T.; Ghosh, P.; Martinez, Z.; Liu, X.; Meng, X.; Darensbourg, M. Y., *Organometallics* **2017,** *36*, 1822.

182. Ghosh, P.; Ding, S.; Chupik, R. B.; Quiroz, M.; Bhuvanesh, N.; Hall, M. B.; Darensbourg, M. Y., *Chem. Sci.* **2017**. DOI: 10.1039/C7SC03378H

183. Pinder, T. A.; Montalvo, S. K.; Hsieh, C.-H.; Lunsford, A. M.; Bethel, R. D.; Pierce, B. S.; Darensbourg, M. Y., *Inorg. Chem.* **2014,** *53*, 9095.

184. Nagano, T.; Yoshimura, T., *Chem. Rev.* **2002,** *102*, 1235.

185. Butler, A. R.; Williams, D. L. H., *Chem. Soc. Rev.* **1993,** *22*, 233.

186. Li, L.; Li, L., *Coord. Chem. Rev.* **2016,** *306*, 678.

187. Berto, T. C.; Speelman, A. L.; Zheng, S.; Lehnert, N., *Coord. Chem. Rev.* **2013,** *257*, 244.

188. Kupper, C.; Rees, J. A.; Dechert, S.; DeBeer, S.; Meyer, F., *J. Am. Chem. Soc.* **2016,** *138*, 7888.

189. Lancon, D.; Kadish, K. M., *J. Am. Chem. Soc.* **1983,** *105*, 5610.

190. Choi, I. K.; Liu, Y.; Feng, D.; Paeng, K. J.; Ryan, M. D., *Inorg. Chem.* **1991,** *30*, 1832.

191. Wei, Z.; Ryan, M. D., *Inorg. Chem.* **2010,** *49*, 6948.

192. Pellegrino, J.; Bari, S. E.; Bikiel, D. E.; Doctorovich, F., *J. Am. Chem. Soc.* **2010,** *132*, 989.

193. Hu, B.; Li, J., *Angew. Chem. Int. Ed.* **2015,** *54*, 10579.

194. Kundakarla, N.; Lindeman, S.; Rahman, M. H.; Ryan, M. D., *Inorg. Chem.* **2016,** *55*, 2070.

195. Hauser, C.; Glaser, T.; Bill, E.; Weyhermüller, T.; Wieghardt, K., *J. Am. Chem. Soc.* **2000,** *122*, 4352.

196. Serres, R. G.; Grapperhaus, C. A.; Bothe, E.; Bill, E.; Weyhermüller, T.; Neese, F.; Wieghardt, K., *J. Am. Chem. Soc.* **2004,** *126*, 5138.

197. Berto, T. C.; Hoffman, M. B.; Murata, Y.; Landenberger, K. B.; Alp, E. E.; Zhao, J.; Lehnert, N., *J. Am. Chem. Soc.* **2011,** *133*, 16714.

198. Goodrich, L. E.; Roy, S.; Alp, E. E.; Zhao, J.; Hu, M. Y.; Lehnert, N., *Inorg. Chem.* **2013,** *52*, 7766.

199. Confer, A. M.; McQuilken, A. C.; Matsumura, H.; Moënne-Loccoz, P.; Goldberg, D. P., A Nonheme, *J. Am. Chem. Soc.* **2017,** *139*, 10621.

200. White, C. J.; Lehnert, N., Proc. Natl. Acad. Sci. U.S.A. **2016,** *113*, 14474.

201. Liu, T.; Darensbourg, M. Y., *J. Am. Chem. Soc.* **2007,** *129*, 7008.

202. Singleton, M. L.; Bhuvanesh, N.; Reibenspies, J. H.; Darensbourg, M. Y., *Angew. Chem., Int. Ed.* **2008,** *47*, 9492.

203. Nagashima, S.; Nakasako, M.; Dohmae, N.; Tsujimura, M.; Takio, K.; Odaka, M.; Yohda, M.; Kamiya, N.; Endo, I., *Nat. Struct. Mol. Biol.* **1998,** *5*, 347.

204. Jeffery, S. P.; Singleton, M. L.; Reibenspies, J. H.; Darensbourg, M. Y., *Inorg. Chem.* **2007,** *46*, 179.

205. Lai, C.-H.; Reibenspies, J. H.; Darensbourg, M. Y., *Angew. Chem., Int. Ed. Engl.* **1996,** *35*, 2390.

206. Phelps, A. L.; Rampersad, M. V.; Fitch, S. B.; Darensbourg, M. Y.; Darensbourg, D. J., *Inorg. Chem.* **2006,** *45*, 119.

207. Hu, M.-Q.; Wen, H.-m.; Ma, C.-B.; Li, N.; Yan, Q.-Y.; Chen, H.; Chen, C.-N., *Dalton Trans.* **2010,** *39*, 9484.

208. Li, P.; Wang, M.; He, C.; Liu, X.; Jin, K.; Sun, L., *Eur. J. Inorg. Chem.* **2007,** *2007*, 3718.